Bivalent Ni, Pd, Pt, and Zn Complexes of Some Chemodiverse Ligands: Structure, Biophysical Study, and Catalytic Activity

A Dissertation Submitted in
Partial Fulfillment for the Degree of
Doctor of Philosophy in Chemistry

by

Amlan Ranjan Rayasingh

(Roll No: 196122003)

Thesis Supervisor: Prof. Vadivelu Manivannan

Department of Chemistry
Indian Institute of Technology Guwahati
Guwahati, Assam, INDIA, 781039

October 2025

DEDICATED
TO
MY PARENTS

कर्मण्यकर्म यः पश्येदकर्मणि च कर्म यः।
स बुद्धिमान् मनुष्येषु स युक्तः कृत्स्नकर्मकृत्॥

One who perceives inaction in action and action in inaction is truly wise among humans; inwardly harmonized and united with divine consciousness, such a person acts without attachment and thus perfects all actions.

Bhagavad Gita, Chapter 4, Sloka 18

Indian Institute of Technology Guwahati

Department of Chemistry

DECLARATION

I do hereby declare that the research work embodied in this thesis entitled "**Bivalent Ni, Pd, Pt, and Zn Complexes of Some Chemodiverse Ligands: Structure, Biophysical Study, and Catalytic Activity**" is the outcome of research work carried out by me under the supervision of Prof. V. Manivannan, at the Department of Chemistry, Indian Institute of Technology Guwahati, Assam, India, 781039.

In keeping with the general practice of reporting scientific observations, due acknowledgments have been made wherever the work described is based on the findings of other investigators.

IIT Guwahati
AUGUST, 2025

Amlan Ranjan Rayasingh
Roll No: 196122003

भारतीय प्रौद्योगिकी संस्थान गुवाहाटी
Indian Institute of Technology Guwahati

Prof. Vadivelu Manivannan

Department of Chemistry, Indian Institute of Technology, Guwahati, Assam, INDIA-781039, Ph: +91 361 258 2306 (O), E-mail: mani@iitg.ac.in

CERTIFICATE

This is to certify that the research work presented in this thesis entitled "**Bivalent Ni, Pd, Pt, and Zn Complexes of Some Chemodiverse Ligands: Structure, Biophysical Study, and Catalytic Activity**" is an authentic record of the results obtained from the research work carried out by **Amlan Ranjan Rayasingh** under my supervision in the Department of Chemistry, Indian Institute of Technology Guwahati, India. This work is original and has not been submitted elsewhere for a degree.

IIT Guwahati
AUGUST, 2025

Prof. V. Manivannan
(Thesis Supervisor)

भारतीय प्रौद्योगिकी संस्थान गुवाहाटी
Indian Institute of Technology Guwahati

Acknowledgments

I am deeply indebted to Prof. V. Manivannan, my respected supervisor, for his steadfast guidance, scholarly insight, and continual encouragement throughout the tenure of my PhD. His thoughtful mentorship, constructive feedback, and enduring patience were invaluable in shaping the direction and outcome of my research. It has been both an honor and a privilege to conduct my research under his mentorship, and I remain sincerely obliged for his pivotal role in my academic growth.

My doctoral committee members, Prof. Anil Kumar Saikia (chairman), Prof. Kalyan Raidongia (member) and Prof. Kingsuk Mahata (member) are also highly acknowledged for their valuable suggestion and comments during annual progress evaluation.

I would like to express my deepest gratitude to all those who have directly or indirectly supported and inspired me throughout my PhD journey. This path has been both intellectually enriching and personally transformative, and it would not have been possible without the presence and encouragement of many individuals.

I am immensely thankful to my mentors, colleagues, friends, and labmates, whose unwavering support and cooperation served as a constant source of motivation.

I am deeply grateful to my family for their unwavering blessings, patience, and faith in me throughout this long journey.

A special thanks to the staffs of Central Instruments Facility, Indian Institute of Technology Guwahati, for providing various instrumental facilities. The financial support from the Ministry of Education, government of India is duly acknowledged.

Each contribution whether academic, emotional, or moral has left a lasting impact on my growth as a researcher and as an individual. Their support gave me strength in moments of doubt and reminded me of the value and purpose behind this pursuit.

Finally, I offer my humble pranāms at the lotus feet of Bhagavān, whose divine grace, boundless blessings, and eternal presence have guided and protected me throughout this journey. Jay Jagannath.

Amlan Ranjan Rayasingh

Abbreviations

T	Temperature	NMR	Nuclear magnetic resonance
h	Hours	HOMO	Highest occupied molecular orbital
mL	Milliliter	LUMO	Lowest unoccupied molecular orbital
(m)mol	(mili)mole	ORTEP	Oak Ridge Thermal Ellipsoid Plot
°C	Degree celcius	CCDC	Cambridge crystallographic data center
a	Unit cell dimension *a*	HRMS	High resolution mass spectrometry
b	Unit cell dimension *b*	ESI	Electron spray ionization
c	Unit cell dimension *c*	SCXRD	Single crystal X-Ray diffraction
α	Interfacial angle in a unit cell	UV-Vis	Ultraviolet-Visible
β	Interfacial angle in a unit cell	FDA	Food and Drug Adminstration
γ	Interfacial angle in a unit cell	THF	Tetrahydrofuran
Z	Unit cell formula unit	DMSO	Dimethyl sulfoxide
δ	Chemical shift in NMR	DMF	N,N-Dimethylformamide
g, mg	Gram, miligram	FESEM	Field Emission Scanning Electron Microscope
ppm	Parts Per Million		
(M)Hz	(Mega)Hertz	DFT	Density Functional Theory
Vs	Versus	EWG	Electron withdrawing group
m/z	Mass to charge ratio	EDG	Electron donating group
J	Spin-Spin coupling constant	DCM	Dichloromethane
s	Singlet	DNA	Deoxyribonucleic acid
d	Doublet	BSA	Bovine serum albumin
t	triplet	HSA	Human serum albumin
m	Multiplet	PoV-Ray	Persistence of Vision Raytracer
dd	Doublet of doublet	TBAB	Tetra-butyl ammonium bromide
td	Triplet of doublet	ADC	Acceptorless dehydrogenative coupling
ddd	Doublet of doublet of doublet	CDC	Cross-dehydrogenative coupling
RT	Room temperature	NHC	N-Heterocyclic carbene
Eq.	Equivalents	PEPPSI	Pyridine Enhanced Precatalyst Preparation Stabilization and Initiation
Via	Through		

Preface

The Thesis entitled "**Bivalent Ni, Pd, Pt, and Zn Complexes of Some Chemodiverse Ligands: Structure, Biophysical Study, and Catalytic Activity**" is divided into five chapters.

Chapter 1: A Thematic Review on Bivalent Ni, Pd, Pt and Zn Complexes: Evolution, Catalytic Versatility and Bioactivity

In this Chapter, literature reports have been reviewed to provide a perceptive view on synthesis and application of some bivalent Ni, Pd, Pt, and Zn complexes of several structurally and electronically diverse ligands. From a detailed analysis, this Chapter concluded the confines and opportunities of further study of bivalent group 10 complex especially for catalytic and biomedical application. This Chapter also includes general methods, material, and instrumentation used in experimental works.

Chapter 2: Palladium(II) and Platinum(II) Complexes of Disubstituted Imidazo[1,5-*a*]Pyridine and Imidazolylpyridine: Coordination Chemistry, Versatile Catalysis, and Biophysical Study

This Chapter contained synthetic process of some well characterized pincer type mono-, di- and poly-nuclear Pd(II) and Pt(II) complexes bearing ligands of imidazo[1,5-a]pyridine and imidazolylpyridine moiety. Distorted square planar geometry around the bivalent palladium and platinum in all complexes was established by single crystal X-ray diffraction studies. These Pd(II) complexes displayed high catalytic activity in Suzuki-Miyaura cross-coupling reaction, transfer hydrogenation reaction, and alkyne homocoupling. Also, interaction study of all the complexes with calf thymus DNA (CT-DNA) and bovine serum albumin (BSA) were investigated using electronic spectroscopy where intercalative binding mode was observed by all complexes through displacement of ethidium bromide (EB) in EB-DNA. The complexes were also displayed high binding affinity toward BSA confirmed by emission, synchronous fluorescence, and steady state fluorescence anisotropy measurement. Moreover, the pharmacokinetic properties of two bioactive compounds (**3s** and **3t**) obtained from Suzuki coupling reaction were calculated and to evaluate their activity as leukotriene A4 hydrolase (LTA_4H) inhibitor, these molecules were docked with human LTA_4H enzyme.

Chapter 3: Group 10 Complexes of Some Chemodiverse N-, O-, P- Donor Ligands: Structural Artistry, Versatile Catalytic Activity, and ct-DNA/BSA Interaction

Syntheses, characterization, and molecular structures of a series of bivalent group 10 complexes of containing benzothiazole viiiyridineviii, coumarin fused pyrrole and imidazo[1,5-*a*]pyridine nucleus with N/O/P-donor are discussed in this Chapter. The Ni(II) complexes were applied as catalysts in imine/viiiyridin formation *via* acceptorless dehydrogenative coupling (ADC) of alcohol and amine/diamine. Only 1.0 mol% of Ni(II) catalyst excellently produced imines/diimines in toluene (110 ºC, 12 h). In Heck coupling, Pd(II) catalysts were adeptly produced alkene in 98% yield in ethanol under significantly milder condition than traditional protocols relying on DMF/DMSO at higher temperatures. Among all complexes, NNP-NiCl complex (**1a**) and NNO-PdCl complex (**2h**) were found as superior catalyst in their respective conversion. Versatility of Pd(II) catalysts was also performed in a model reaction of cross dehydrogenative coupling (CDC) of thiophene-2-carbaldehyde. The Pt(II) complexes were examined for their interactions with CT-DNA and BSA wherein NNO-PtCl (**3e**) exhibited highest binding affinity which was also visualized through molecular docking with CT-DNA and BSA.

Chapter 4: Dinuclear Pd(II) Complexes of N-(imidazo[1,5-*a*]viiiyridine-1-yl)picolinimidamides: Pd···Pd distance *vs* Reactivity in C-C/P Bond Formation

In this Chapter, the facile syntheses and characterization of five dinuclear palldium(II) complexes of substituted imidazo[1,5-a]pyridinylpicolinimidamides were explored and their molecular structure was established using single crystal X-ray diffraction. All ligands coordinated with palladium center through pseudo-pincer type mode, Pd(II) possessed distorted square planar geometry and an eight-membered metallic cavity was observed in all complexes. These dinuclear Pd(II) complexes effectively viiiyridineviii copper-free Sonogashira coupling reactions under mild reaction conditions with excellent functional group tolerance. Also, they were employed as catalyst in C–P bond formation reaction. High catalytic activity of these complexes was accredited to cooperativity and synergic effect of two Pd(II) center present with in optimum proximity.

Chapter 5: Zinc(II) Complexes of Some 2-Cyanopyridine Derived Nitrogen-Rich Ligands: Catalysts for Cycloaddition of CO2 and Epoxide into Cyclic Carbonate

Synthetic methods of twelve mono- and two tri- nuclear zinc(II) complexes using some imidazo[1,5-*a*]pyridine, triazine, and imidazolylpyridine moieties containing ligands are described in this Chapter. The new ligands and all zinc complexes were thoroughly characterized using several spectroscopic techniques and molecular structure of some ligands and all zinc complexes were established by single crystal X-ray diffraction. The imidazo[1,5-*a*]pyridine and imidazolylpyridine nucleus containing ligands yielded both mono and trinuclear complexes while only mononuclear complexes were produced by the pincer triazine ligands. The geometry of tetra coordinated Zn(II) centres were observed as distorted tetrahedral while a distorted square pyramidal and trigonal bipyramidal environment was observed in penta-coordinated complexes as conferred from Houser and Addison geometry index values. All the zinc(II) complexes were employed as catalyst in the conversion of carbon dioxide and styrene epoxide into styrene carbonate, yielded excellently in a mild and solvent free condition using CO_2 balloon. Among all the Zn(II) catalysts, trinuclear analogous were found as superior catalyst as compared to their mononuclear congeners.

Contents

Chapter-1

A Thematic Review on Bivalent Ni, Pd, Pt and Zn Complexes: Evolution, Catalytic Versatility and Bioactivity

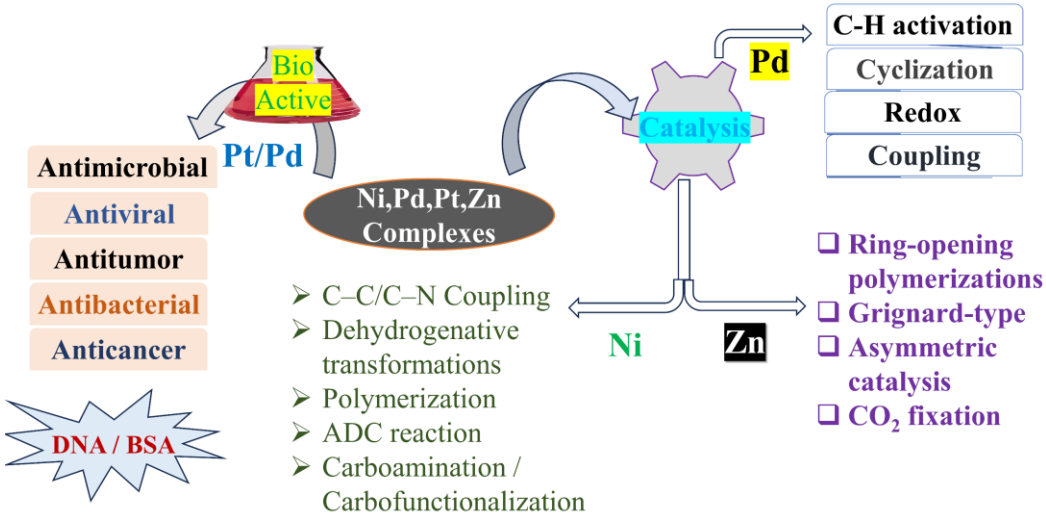

1.1 Introduction

Transition metal complexes, particularly those involving nickel, palladium, platinum, and zinc have played transformative role in both synthetic chemistry and biomedical science. In the field of catalysis, though palladium have dominated in the landscape, increasing attention has shifted toward more earth abundant and sustainable options such as Ni and Zn, shown excellent potential as catalysts in diverse chemical reactions. The use of nickel in catalysis dates back to the early 20th century, notably with the Raney nickel catalyst developed in 1926 and became a pillar in industrial hydrogenation processes.[1–4] In the homogeneous catalysis arena, Reppe's pioneering work in the 1950s identified the capability of nickel in alkyne trimerization and hydrocyanation reactions.[5,6] Palladium's rise began with Tsuji and Heck's work in the 1960s,[7,8] which ultimately culminated in the 2010 Nobel Prize[9] in chemistry awarded to Heck,[10] Suzuki,[11–13] and Negishi[14] for developing Pd-catalyzed cross-coupling reactions, now a cornerstone in the construction of complex molecules.[15–17] Platinum, in contrast, found its revolutionary applications not in catalysis but in medicine. In anti-cancer activity, the serendipitous discovery of cisplatin in the 1960s unbolted a new frontier in chemotherapy.[18–25] Since then, several Pt-based drugs like carboplatin and oxaliplatin have become backbones in oncology, showcasing the metal's biological relevance.[26–33] Early use of zinc in catalysis dates to the 20th century, notably in the Frankland reaction and early organometallic Grignard-type additions involving zinc halides.[34–38] However, the real turning point came with the employment of zinc complexes as catalyst in value addition of CO_2,[39–41] ring-opening polymerizations,[41–44] and asymmetric catalysis.[45–47]

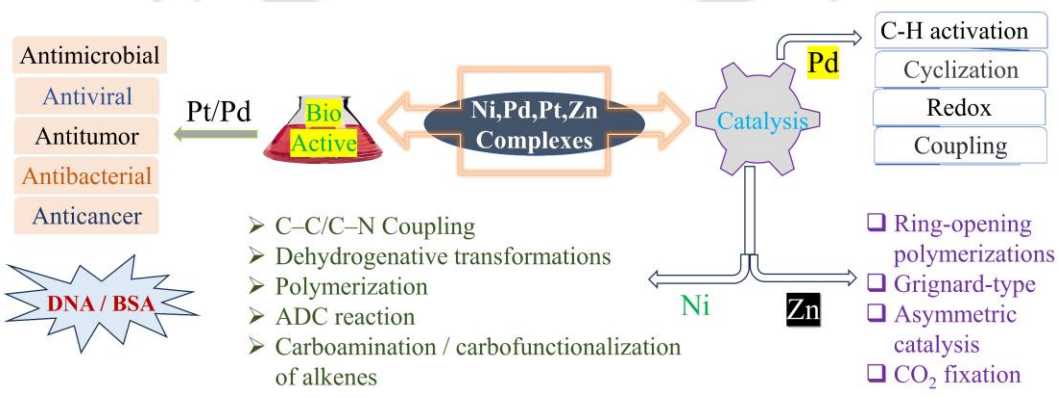

Figure 1.0: Application of Ni, Pd, Pt and Zn complexes.

Over the decades, advances in ligand design, mechanistic understanding, and sustainability have further refined the efficiency and selectivity of these metal catalysts, extending their use into greener transformations and industrial scale syntheses.

In sum, the multifaceted roles of Ni, Pd, Pt and Zn complexes in organic transformations to life-saving medicine, emphasize their profound impact on modern science. This thesis explores their cutting-edge design and useful applications with a focus on advancing rational design for future innovation.

1.2 Progress in palladium catalysis

Palladium catalysts have been witnessed remarkable evolution since its inception, shaping the landscape of modern synthetic chemistry. The journey began with the work of Tsuji, evolved by the discoveries of Mizoroki and Heck and laid the groundwork for a series of transformative cross-coupling reactions.

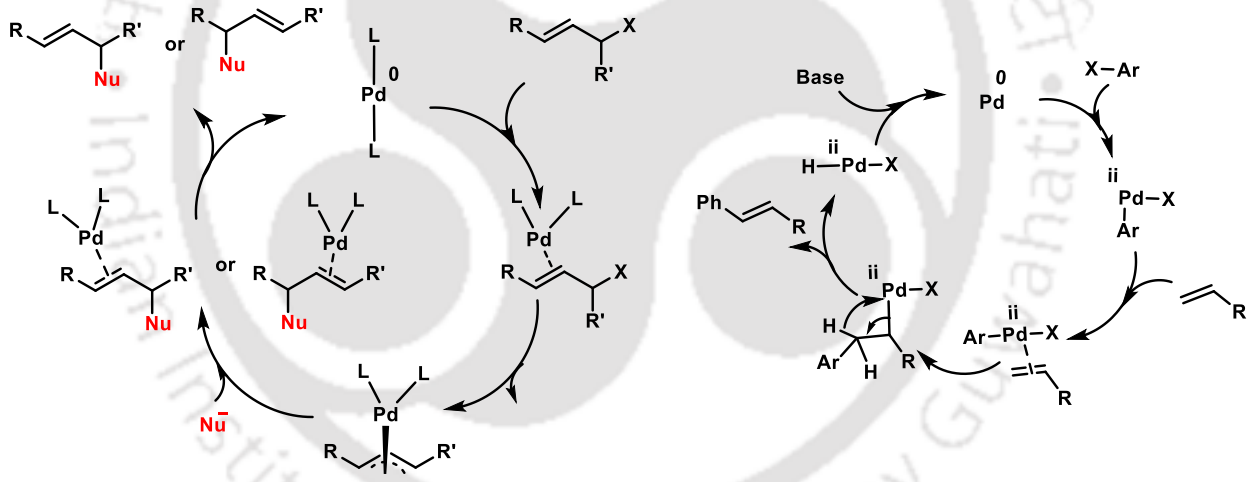

Scheme 1.0: Tsuji allylic alkylation (left) and Mizoroki-Heck (right)reaction catalytic cycle.

The field rapidly expanded with the development of the Suzuki, Negishi, Stille, Sonogashira, and Kumada reactions, each utilizing palladium as the central catalytic system with various organometallic partners.[48–54] Over the years, many developments on palladium catalysts were evolved including:

- The development of bulky, electron-rich phosphine ligands that greatly enhanced catalytic activity, selectivity, stability, and broad substrates scope.

- Air and moisture stable, heterogeneous, and recyclable Pd catalysts allow catalytic conversion under ambient conditions and in aqueous-phase reactions, align with the goals of sustainable chemistry.
- Pd catalysis has moved beyond classical cross-coupling to comprehend C–H activation, oxidative couplings, and asymmetric transformations, offering atom- and step-economical synthetic routes to complex molecules.
- Theoretical studies and spectroscopic techniques have deepened the understanding of mechanistic cycles, enabling rational design of catalysts and predictive reactivity models.

1.2.1 Recent advances in the design and reactivity of palladium(II) complexes

Modern strategies have increasingly shifted toward ligand-controlled reactivity, low-loading protocols, and environmentally benign conditions.[55–57] A series of recent studies discussed in this section collectively highlight innovations in structure, electronic tuning, and sustainable applications of Pd(II) complexes.

Santillan and coworker explored dinuclear Pd(II) complexes (**Pd1** and **Pd2**) supported by di- and tritriazol-5-ylidene ligands.[58] These complexes were evaluated in Sonogashira and Suzuki couplings, showing notable activity and stability under mild reaction conditions (Scheme 1.1).

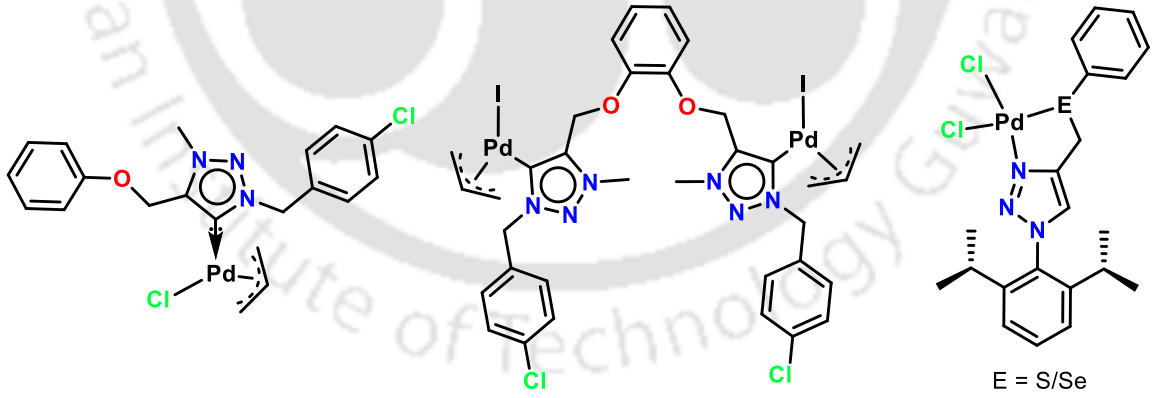

Pd1 **Pd2** **Pd3**

Scheme 1.1: Some reported Pd catalyst used in Suzuki–Miyaura and Sonogashira reactions.

Singh and co-worker developed triazole-based organosulfur and selenium ligand containing Pd(II) complexes (**Pd3**) that catalyzed both Suzuki–Miyaura and Sonogashira reactions in water.[59] The presence of bulky 2,6-diisopropylphenyl substituent on triazole core and the

nature of chalcogen was responsible for the catalytic activity by which the sulfur-based complex showed superior activity as compared to the Se-analogues (Scheme 1.1). Dehury *et al.* reported dinuclear Pd(II) complexes (**Pd4** – **Pd7**) supported by tetrapyrazolyl ligands,[60] which catalyzed tandem transfer hydrogenation/Suzuki coupling of fluoroarylketones. Their study provided insights into the effects of intermetallic Pd−Pd distances where **Pd6** (shorter Pd–Pd separations) produced higher yield than other (Scheme 1.2). The system was selective toward fluoroaryl substrates. Notably, mononuclear Pd analog displayed lower tandem activity, reinforcing the potential of spatially cooperative bimetallic catalysts.

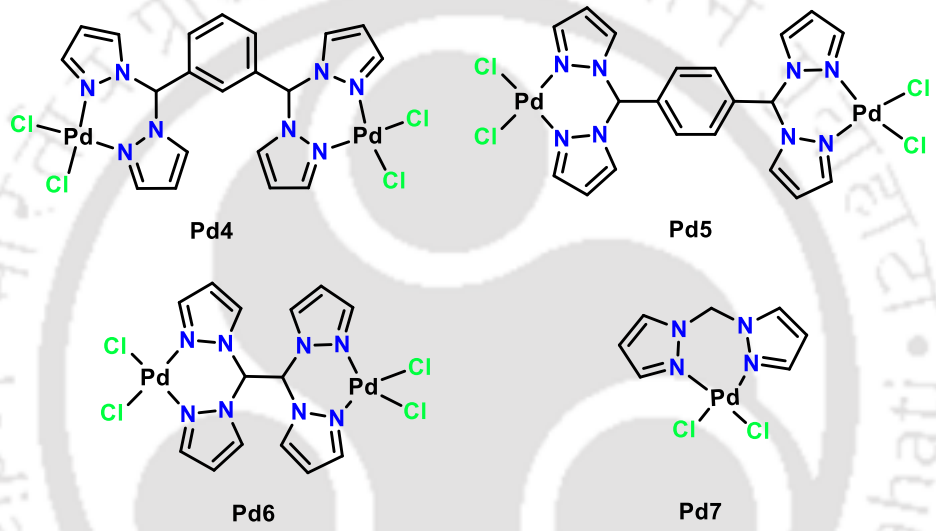

Scheme 1.2: Pd catalysts previously reported and used in tandem catalysis.

Moving into Heck-type C–C cross-coupling, Schroeter *et al.* synthesized and characterized an anionic Pd complex, [NBu$_4$][Pd(DMSO)Cl$_3$] (**Pd8**),[61] active in the Mizoroki–Heck reaction without stabilizing ligands. The mechanism, consistent with an Amatore–Jutand-type cycle, operated under Jeffery conditions and displayed excellent activity toward aryl chlorides in aqueous media. Lang and co-workers synthesized a library of mono- and binuclear Pd(II) complexes (**Pd9 – Pd12**, **Pd13 – Pd17**) based on N,N'-disubstituted imidazole-2-thiones and demonstrated their efficacy in Suzuki and copper-free Sonogashira couplings.[62] These phosphine-free systems were structurally diverse, ranging from trans dichloride to μ-thione bridged bis-Pd cores and exhibited tunable reactivity depending on steric and electronic properties of the substituents. DFT studies supported that the larger ligands promoted higher activity by stabilizing favorable transition states and elongating Pd–S bonds (Scheme 1.3).

In 2018, a key mechanistic insight emerged from the detailed mechanistic characterization by Toledo *et al.,* where an oxidase-type behavior was elucidated for aerobic Pd-catalyzed homocoupling of terminal alkynes.[63] Their study highlighted the central role of a low-ligated Pd(0) anionic intermediate, which undergoes oxygenation to form a (κO, κO-peroxo) palladium(II) species. The peroxo intermediate then proceeds *via* protonolysis and second alkyne metalation steps to deliver the 1,3-diyne. This coupling was mechanistically distinct due to the intertwined -

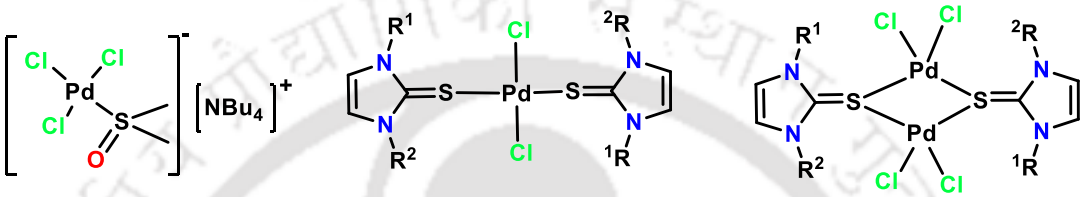

Scheme 1.3: Some previously reported anionic (**Pd8**), mono- and dinuclear Pd catalysts.

nature of catalyst oxidation and substrate transformation, a deviation from classical Pd(II)/Pd(0) redox cycles (Scheme 1.4).

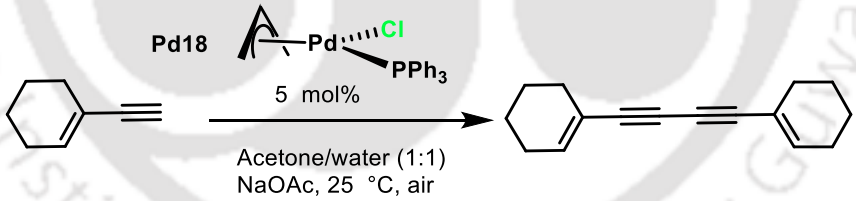

Scheme 1.4: A reported Pd catalyst used for homocoupling of alkynes.

Pirkl *et al.* reported a novel class of diiodo-bridged NHC–Pd(I) dimers, served as precatalysts for cross-coupling reactions such as Suzuki–Miyaura and Sonogashira, operating effectively under mild conditions with low catalyst loading.[64] Unlike traditional Pd(0) or Pd(II) systems that often require external activators or ligands, these Pd(I) dimers directly generated catalytically active species, offering practical advantages in scalability (Scheme 1.5).

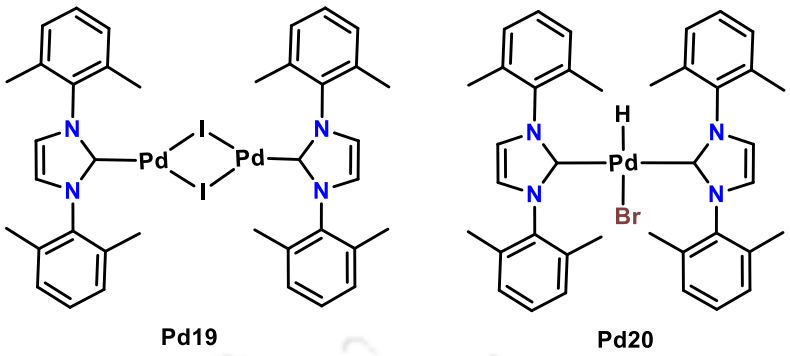

Scheme 1.5: Reported Pd catalysts used for C-C coupling reactions.

Ray *et al.* introduced a Pd(II) Schiff-base complex immobilized within a zeolite-Y framework (**Pd21**).[65] The encapsulated form showed enhanced thermal stability and reusability, outperforming the homogeneous analogue in Heck-type couplings. The zeolite matrix along with electron withdrawing substituents imparted distinct steric and electronic influences that subtly modulated catalytic performance (Scheme 1.6). In a parallel contribution, Singh and co-workers designed chalcogenated Schiff-base Pd(II) complexes (**Pd22**–**Pd24**) supported on an anthracene backbone.[66] These catalysts enabled base-free transfer hydrogenation and N-alkylation reactions under mild conditions. The redox-active chalcogen donor groups played a key role in hydrogen atom transfer processes. Lindsay's group introduced dinuclear benzimidazolyl Pd(II) complexes as bifunctional, air-stable catalysts for C–C coupling at low loadings in alcoholic solvent.[67] Their ambidentate ligands enabled internal base assistance, streamlining the (trans)metalation step in cross-coupling and enabling green reaction conditions with excellent yields (Scheme 1.6).

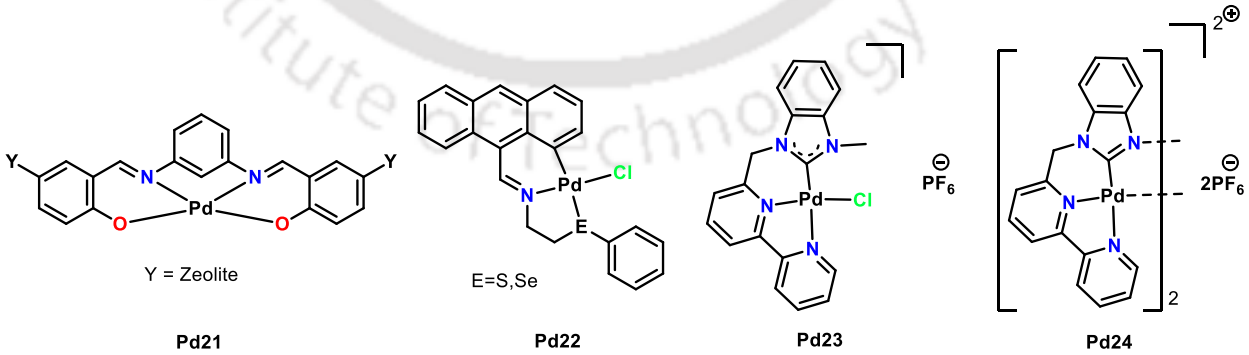

Scheme 1.6: Some reported Pd complexes used as catalysts.

Balakrishna's team explored Pd(II) pincer complexes (**Pd25** and **Pd26**) supported by bisphosphine-triazole ligands and delivered excellent catalytic efficiency in Mizoroki–Heck reactions.[68] Their study provided insight into phosphine-rich coordination environments (Scheme 1.7). The role of Pd–NHC scaffolds was further refined by Song *et al.,* by developing unsymmetrical Pd-PEPPSI-NHC complexes for hetero-arylation under ambient conditions.[69] These catalysts effectively produce 2-methyl-5-(4-nitrophenyl)furan with a low loading (0.05 mol%) at 130 °C in 12 h. However, increasing the steric hindrance by introducing isopropyl groups in place of methyl groups lessened the product yield. The findings underscored how flexible methyl groups can significantly influence catalytic activity (Scheme 1.7).

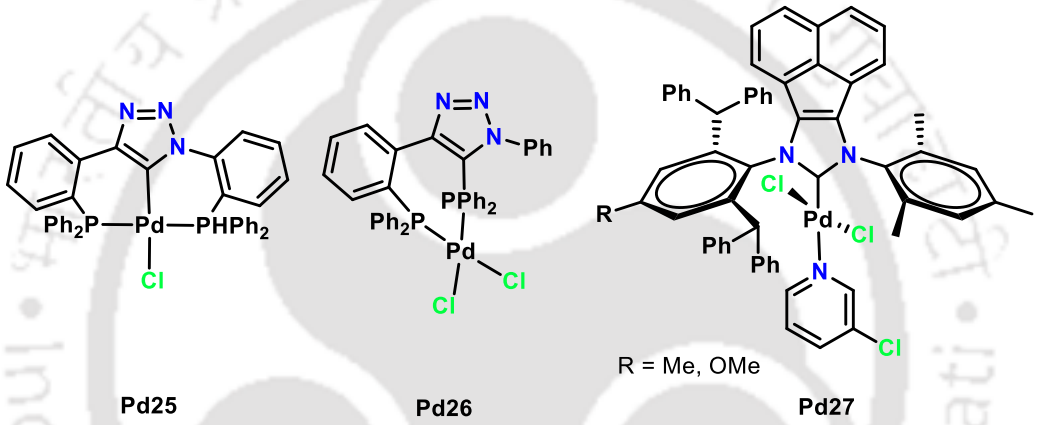

Scheme 1.7: Some reported phosphine and carbene Pd complexes used as catalysts.

In the domain of oxidative transformations, Joshi and coworkers developed NNN- and CNN-pincer Pd(II) complexes (**Pd28**–**Pd31**) for cross-dehydrogenative couplings (CDC) of heteroarenes.[70] Their air- and moisture-stable systems activated C–H bonds without external oxidants and showed compatibility with a variety of functional groups with minimal catalytic degradation over four cycles. The *in situ* generated acetate analogue of Pd catalyst was found as active catalyst for the conversion (Scheme 1.8).

In 2020, Kletskov *et al.* reported phosphine-free binuclear Pd(II) complexes made from N,N,N-pincer mimicked pyrimidinyl-azole carboxamide scaffolds.[71] These complexes (**Pd32**–**Pd35**) exhibited remarkable activity in aqueous-phase Suzuki, Mizoroki–Heck, and Sonogashira reactions, achieving high turnover frequencies using 0.1 mol% catalyst. Ravikanth and coworker reported a bis-Pd(II) complex (**Pd35**) derived from a pyrrole–benzimidazole–dipyrrin ligand framework.[72] The complex exhibited unique geometric and

spectroscopic properties and preliminary studies showing catalytic activity in Suzuki coupling reaction (Scheme 1.9).

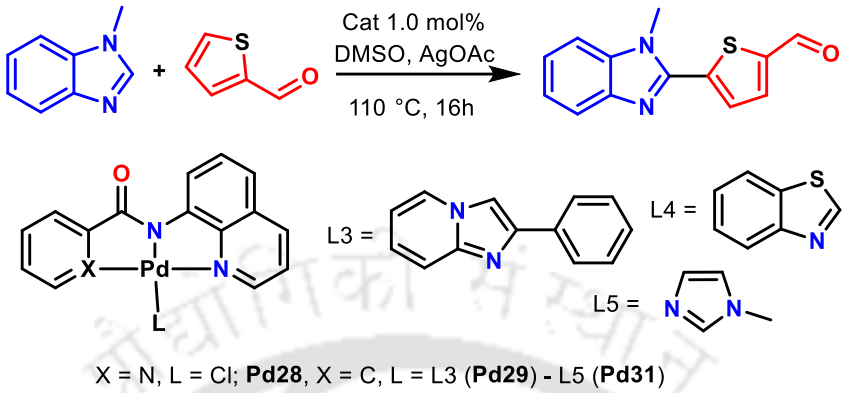

Scheme 1.8: Some reported NNN/CNN Pd complexes used as catalysts in Cross Dehydrogenative Coupling reaction.

In 2020, Kletskov *et al.* reported phosphine-free binuclear Pd(II) complexes made from N,N,N-pincer mimicked pyrimidinyl-azole carboxamide scaffolds.[71] These complexes (**Pd32**–**Pd35**) exhibited remarkable activity in aqueous-phase Suzuki, Mizoroki–Heck, and Sonogashira reactions, achieving high turnover frequencies using 0.1 mol% catalyst. Ravikanth and coworker reported a bis-Pd(II) complex (**Pd35**) derived from a pyrrole–benzimidazole–dipyrrin ligand framework.[72] The complex exhibited unique geometric and spectroscopic properties and preliminary studies showing catalytic activity in Suzuki coupling reaction (Scheme 1.9).

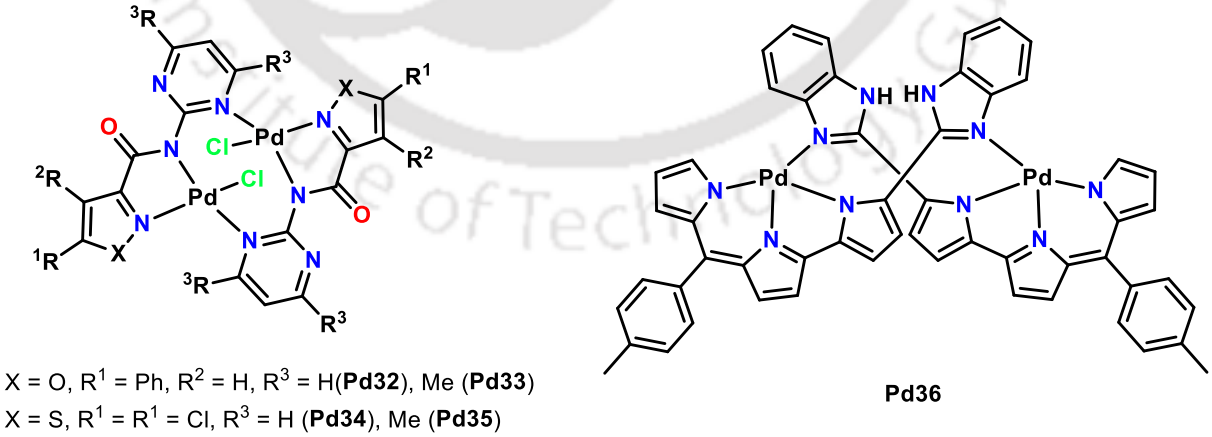

Scheme 1.9: Some previously reported dinuclear Pd catalysts.

In 2021, Chakrabortty *et al.* developed a bis(BICAAC) Pd(II) complex (**Pd37**) featuring a robust carbene framework based on a bicyclo[2.2.2]octane skeleton.[73] The enhanced σ-donating and π-accepting capabilities of BICAAC stabilized the Pd–carbene bond, enabling efficient Heck and Suzuki reactions at low catalyst loadings under open-air conditions. McIntosh's team reported amine-bisphenolate Pd complexes (**Pd38** – **Pd42**) competent in Suzuki–Miyaura couplings under phosphine-free conditions.[74] The maximum yield (88 %) in 1-acetylbiphenyl was observed using 1.0 mol% **Pd40** in MeOH at 40 °C for 24h providing environmentally benign protocols (Scheme 1.10).

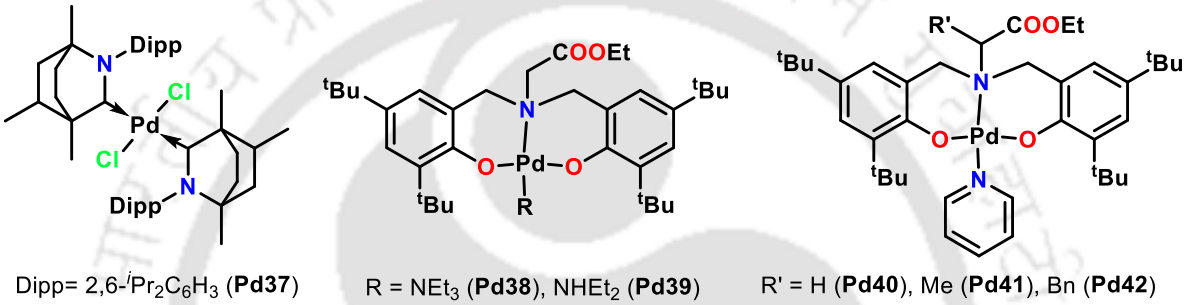

Dipp= 2,6-$^{i}Pr_2C_6H_3$ (**Pd37**) R = NEt_3 (**Pd38**), $NHEt_2$ (**Pd39**) R' = H (**Pd40**), Me (**Pd41**), Bn (**Pd42**)

Scheme 1.10: Some previously reported palladium catalysts used in Heck and Suzuki reactions.

In a structurally distinct system, Panchavarnam and coworkers prepared a Pd(II) complex (**Pd43**) of α-formyl pyrrolyl dipyrromethene.[75] The metal center exhibited a square planar geometry coordinated to three pyrrolic nitrogen and a water molecule, stabilized via hydrogen bonding. Despite the absence of conventional phosphine or carbene ligands, this complex exhibited substantial catalytic activity in Suzuki coupling, particularly for aryl bromides. Szostak and co-workers used the renewable alkaloid caffeine to prepare NHC–Pd(II) PEPPSI complexes **Pd44** – **Pd46** (Scheme 1.11), marking a unique convergence of sustainable ligand sourcing with robust catalysis.[76] The resulting catalysts performed efficiently across Suzuki, Heck, and Sonogashira reactions. These findings established caffeine-based NHCs as credible alternatives to traditional imidazol-2-ylidenes in Pd(II) chemistry.

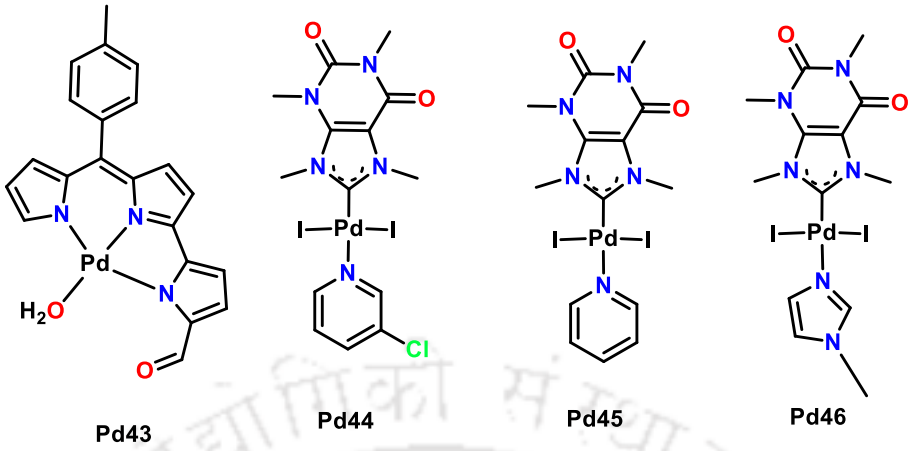

Scheme 1.11: Some previously reported palladium complexes used as catalyst.

In a separate work, Szostak and coworkers developed a family of Pd(II) complexes (**Pd47**–**Pd50**) featuring imidazo[1,5-a]pyridine-based NHC ligands those demonstrated high selectivity in Suzuki coupling via C–NO_2 bond activation.[77]

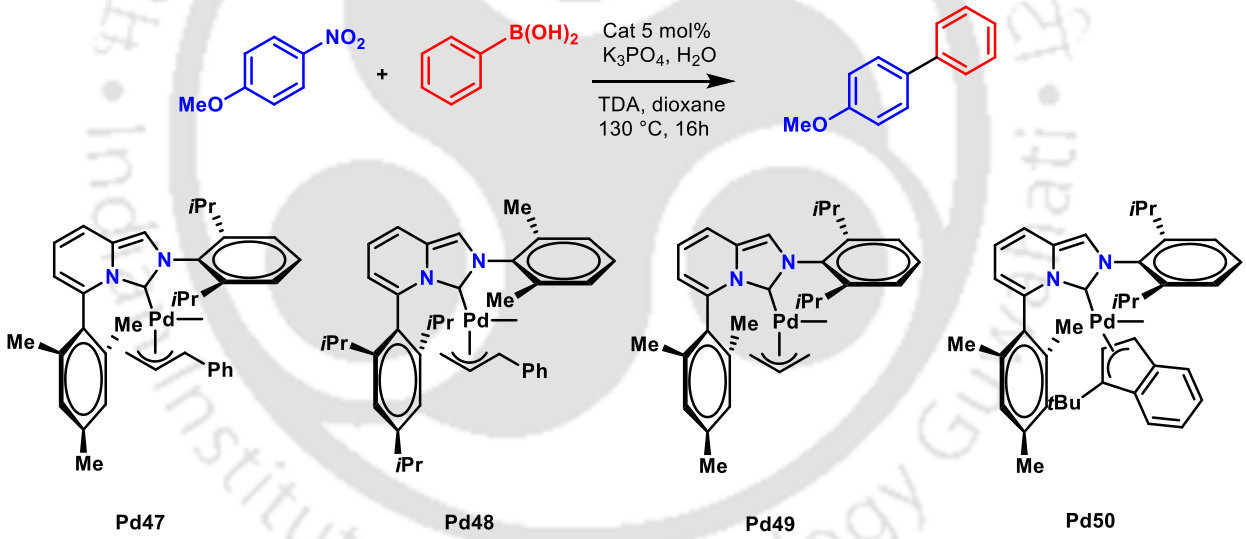

Scheme 1.12: Some previously reported NHC-Pd catalyst used in C–NO2 bond activation.

Their rigid NHC environment not only enhanced catalytic turnover but also broadened the accessible substrate scope in nitroarene functionalization (Scheme 1.12).

In 2023, Chang's group reported Pd(II) complexes (**Pd51**–**Pd52**) bearing PPh3-stabilized, di(1-adamantyl)phosphinous-acid ligands and exploring their reactivity in Hirao-type couplings.[78] Their system successfully activated aryl halides for P–C bond formation using dialkyl phosphites, marking a significant step toward sustainable phosphorus containing

molecule synthesis. Their findings highlighted the careful tuning of the ligand field around Pd(II) for selectivity, turnover frequency, and tolerance to functional groups (Scheme 1.13).

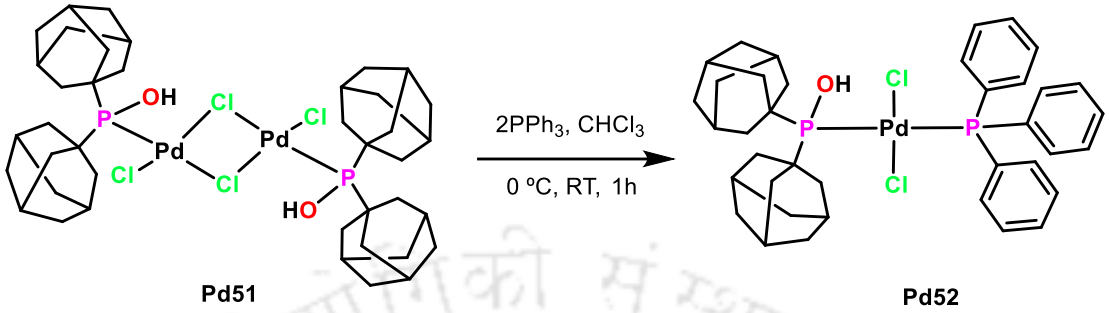

Pd51 **Pd52**

Scheme 1.13: Previously reported Phosphene-Pd catalyst used in C–P bond formation.

Patricio-Rangel *et al.* reported MIC-Pd(II)-PEPPSI complexes (**Pd53** and **Pd54**) functionalized with 2-/4-mercaptopyridine motifs.[79] Among them, complex **Pd53** displayed high catalytic activity in Suzuki coupling may be due to the presence 2-mercaptopyridine which coordinated with Pd^0 and stabilized intermediate. Further, the hydroamination of anilines and phenylacetylene was also conducted by a dicationic Pd complexes (**Pd55**) derived from **Pd53** (Scheme 1.14).

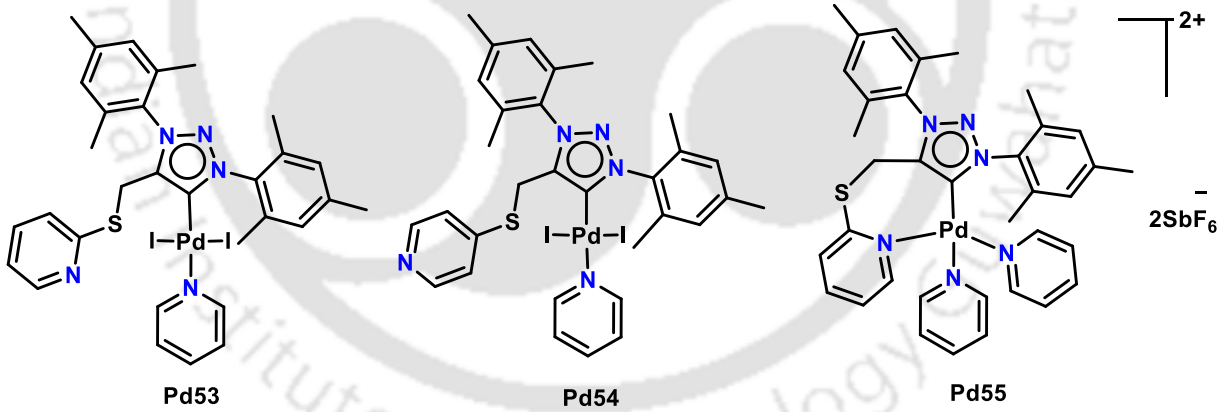

Pd53 **Pd54** **Pd55**

Scheme 1.14: Some reported MIC-Pd(II)-PEPPSI catalysts.

King et.al introduced a metalla-GAP strategy for homogeneous Pd catalysis in SM couplings, enabling catalyst recyclability without compromising activity.[80] The design exploits phosphinamide based ligands (**Pd56**–**Pd57**) to merge homogeneity with separability, preserving high turnover while facilitating facile recovery, a significant stride towards green catalysis (Scheme 1.15). Ananikov's group investigated how halogen substitution on aryl ligands affects the electronic structure and reactivity of Pd–NHC complexes (**Pd58** – **Pd70**).[81]

The incorporation of electron-withdrawing groups such as CF_3 and Br at meta or para positions led to enhanced catalytic activity and stability. The reactivity order of the halogen substituent was Br > F > Cl and *m*-X, *p*-X > *o*-X in Heck coupling and this structural property insight has broad implications for rational ligand design (Scheme 1.15).

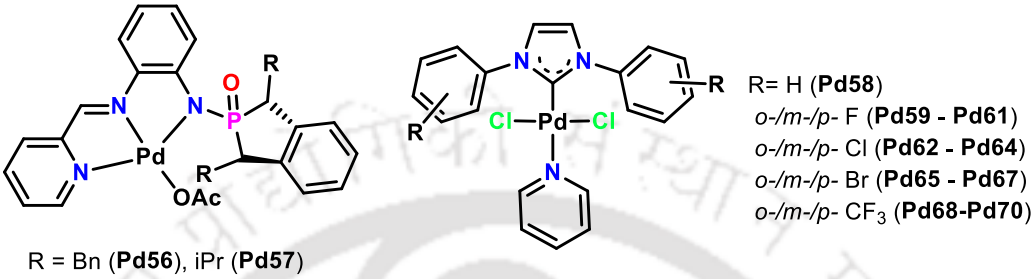

Scheme 1.15: Some reported palladium catalysts used in Suzuki and Heck coupling.

Recently, Hey-Hawkins and coworkers examined the reactivity of Pd(II) complexes (**Pd71** and **Pd72**) coordinated to phosphine aldehyde ligands in Cu-free Sonogashira and Suzuki–Miyaura reactions.[82] Their work revealed versatile coordination behavior and chelate-assisted C–H activation pathways and diversifying the ligand compatibility with Pd catalysis (Scheme 1.16).

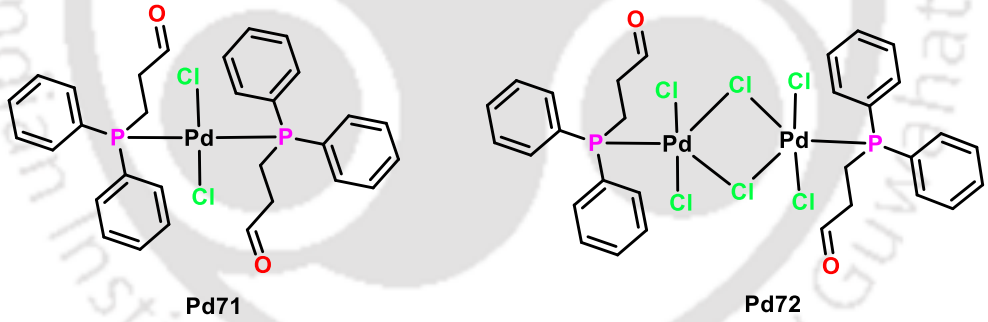

Scheme 1.16: Some Pd catalysts used in Cu-free Sonogashira and Suzuki–Miyaura reactions

1.3 Progress in platinum/palladium complexes in bioactivity

In 1965, Barnett Rosenberg discovered that platinum ions from electrodes inhibited E. coli cell division. Further study identified cis-diamminedichloroplatinum(II) (cisplatin) as the active compound, marked a breakthrough in medicinal chemistry and approved by the FDA in 1978 for treating testicular and ovarian cancers. Though its success (Figure 1.1) transformed platinum into a central figure in cancer therapy, its side effects have driven the search for safer and more effective metallodrugs. Among them, Pd(II) complexes stand out for their structural

similarity to Pt(II) complexes, while offering faster hydrolysis, higher ligand-exchange rates, and better water solubility.

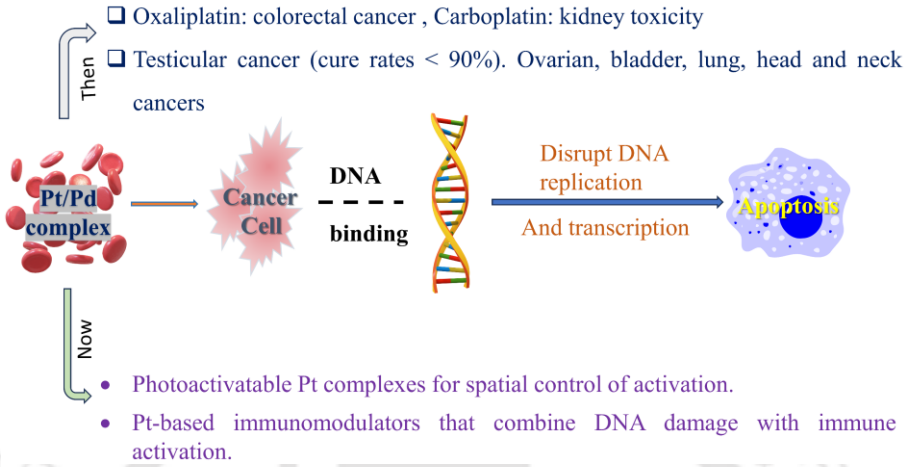

Figure 1.1: Mechanism and evolution of Pd/Pt complexes in bioactivity.

1.3.1 Emerging trends in bioactive Pt(ii) and Pd(ii) complexes

Recent efforts have aimed to improve selectivity, overcome resistance, and reduce toxicity in metallodrugs through structural innovations such as polynuclear architectures, redox-active ligands, and targeted delivery strategies. This review highlights key developments in platinum complexes, focusing on DNA/protein binding. It also discusses the growing interest in palladium complexes as promising alternatives to platinum drugs, owing to their versatile coordination chemistry, tunable reactivity, and better hydrophilicity.

Jovanović *et al.* reported some dinuclear Pd(II)/Pt(II) complexes (**Pt1** – **Pt3**)[83] bridged through pyrazine ligands and demonstrated significant DNA and BSA binding capabilities, and **Pt1** showed noticeable cytotoxicity toward melanoma and cervical cancer cells. Their structure-reactivity studies emphasized the decomposition pathways upon nucleophilic substitution (Scheme 1.17).

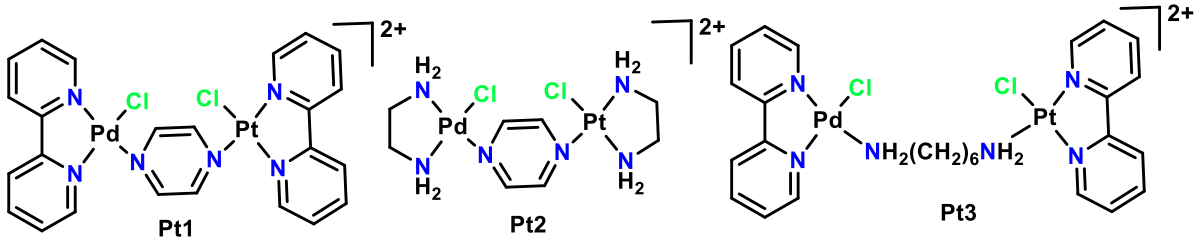

Scheme 1.17: Some bioactive Pt(II)/Pd(II) complexes. Counter ions are Cl– and ClO_4^-

Kašpárkova and co-workers reported an approach that combine platinum(II) centers with diclofenac, a nonsteroidal anti-inflammatory drug possessing both COX (cyclooxygenase)-dependent and COX-independent anticancer effects.[84] With a variation in co-ligands, they attained enhanced lipophilicity, increasing cellular uptake and allowing simultaneous DNA cross-linking by Pt and metabolic disruption *via* diclofenac. Thus, exhibited superior potency to cisplatin, demonstrating the clinical potential of dual-function metallodrugs (Scheme 1.18).

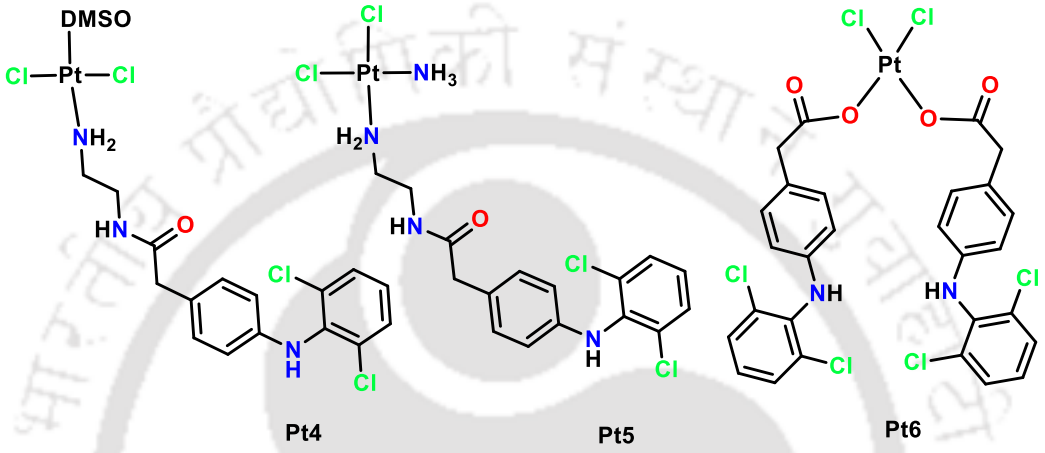

Scheme 1.18: Some reported Pt(II) complexes of diclofenac.

In a separate track, Icsel *et al.* synthesized saccharinate based Pt(II)/Pd(II) complexes (**Pt7** – **Pt10, Pd73** – **Pd76**) with diphosphine ligands.[85] The complexes caused reactive oxygen species (ROS) mediated apoptosis and S-phase arrest in colon cancer cells. The charge of the ligands suggestively enhanced water solubility and cellular uptake. Mansour and Shehab reported lysozyme and DNA interactions of N,N-pyridylbenzimidazole-coordinated Pd(II)/Pt(II) complexes (**Pt11**, **Pt12**, **Pd77** and **Pd78**).[86] The conjugation of alkylated phosphonium groups modulated DNA/lysozyme binding and showed antifungal and anticancer properties (Scheme 1.19).

Aseman *et al.* introduced cycloplatinated(II) complexes (**Pt13**–**Pt18**) integrating 6-mercaptopurine (6-MP) as a bioactive ligand.[87] The rigid C^N cyclometalated scaffold communicated high kinetic stability, while the 6-MP fragment offered DNA intercalation and protein-binding potential.

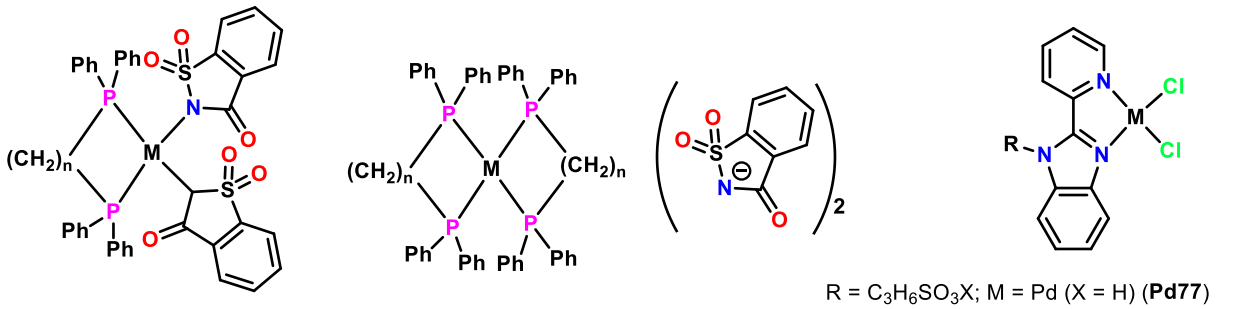

Scheme 1.19: Some reported Pt(II)/Pd(II) complexes.

Biophysical assessment confirmed strong interaction with human serum albumin (HSA) and efficient ct-DNA binding. Cytotoxicity assays discovered activity against leukemia cells, demonstrating the effectiveness of amalgamation of robust organometallic complex with biological relevance pharmacophores (Scheme 1.20).

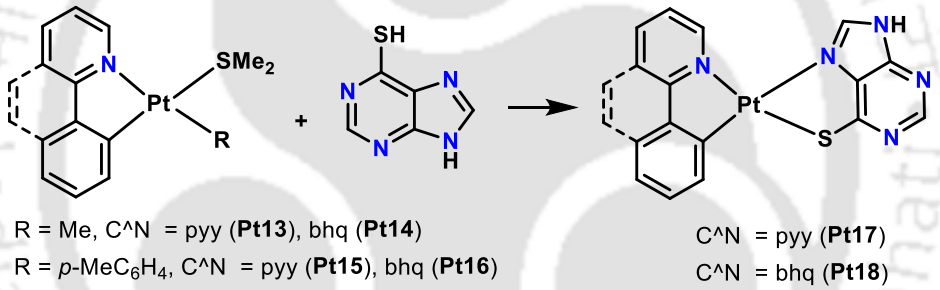

Scheme 1.20: Reported platinum complexes showing DNA/HAS interaction.

Petrović and coworker reported homo- and hetero-dinuclear Pt(II)/Pd(II) complexes (**Pd79**, **Pt19** and **Pt20**) that comprehended distinct substitution kinetics, strong DNA/BSA binding and inhibited autophagy, suggesting efficient anticancer potential (Scheme 1.21).[88]

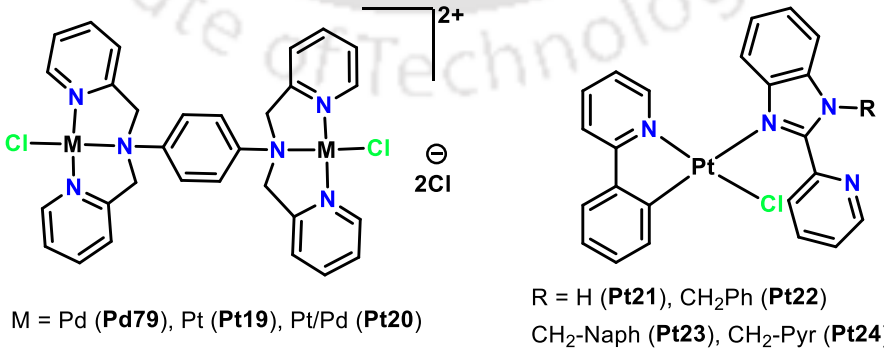

Scheme 1.21: Some reported Pd(II)/Pt(II) complexes displayed DNA interaction.

Incorporation of luminescent ligands such as 2-(2 Pyridyl)benzimidazoles in Pt(II) complexes (**Pt21**–**Pt24**) was reported by Vaquero *et al.,* displayed strong DNA interaction and luminescent properties in aqueous media that also exhibited micromolar level cytotoxicity with potential imaging capability valuable for clinical application (Scheme 1.21).[89] With a similar technique, Zamora *et al.* developed cyclometalated platinum complexes (**Pt25** – **Pt28**) for DNA recognition, adopting intercalation (**Pt26** – **Pt27**) and minor-groove interaction mode.[90] Their extended π-ligands enabled sequence selectivity, excimer emission "switch-on" with DNA, and sustained anticancer activity even in 3D tumor spheroids (Scheme 1.22).

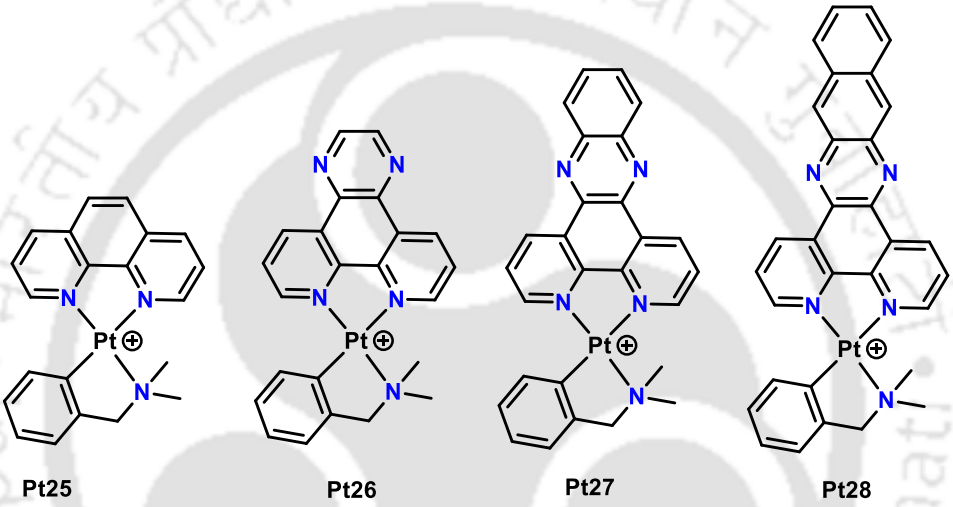

Scheme 1.22: Library of Pt complexes (NO_3^- ion present as counter ion).

The work forwarded by Gupta's group with some multinuclear platinum complexes (**Pt29** – **Pt32**) based on luminescent terpyridine ligands and employed for DNA detection.[91] By using radiant ligands, they shaped a platform for selective and sensitive DNA sensing, bridging therapeutic and diagnostic applications an emerging concept in metallodrug development (Scheme 1.23).

Chen and co-workers stated a mononuclear (**Pt34**) and a star-shaped trinuclear platinum(II) complex (**Pt33**) showed strong anticancer activity against TNBC cells.[92] The complex effectively disturbed DNA and mitochondria of the cell and induces apoptosis through p53-mediated pathways and better than cisplatin (Scheme 1.24). Yang and coworkers successfully synthesized Pt(II) Schiff base complexes (**Pt35** – **Pt40**) that well target cisplatin resistant lung cancer cells.[93] Among the complexes, particularly **Pt40** confirmed cell death through DNA damage by suppressing drug resistance mechanisms like P-glycoprotein overexpression.

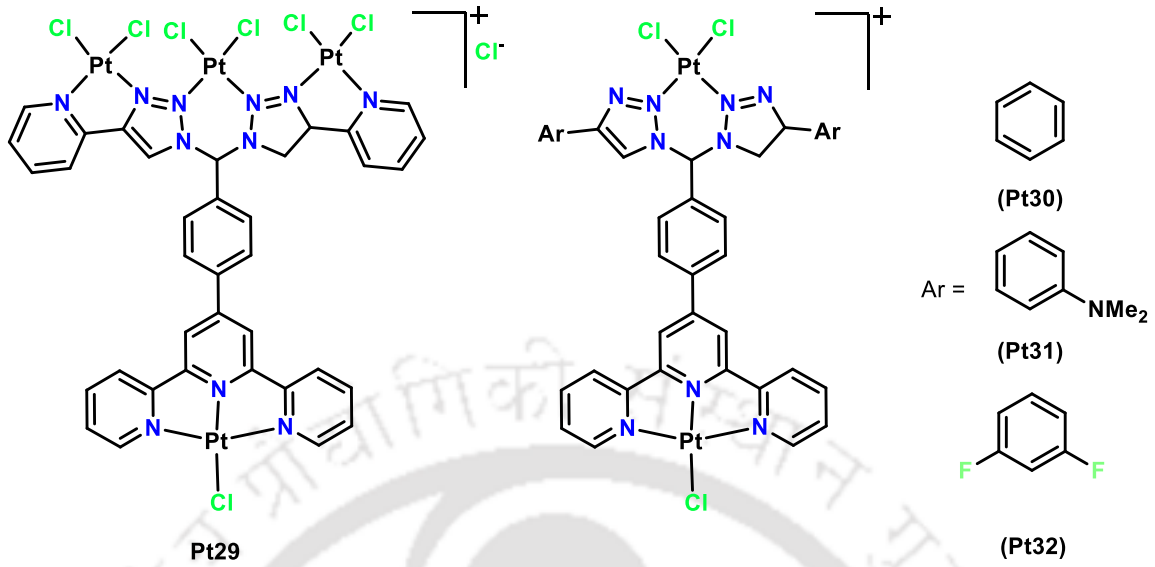

Scheme 1.23: Luminescent terpyridine based ligand containing reported Pt(II) complexes.

The study presented a proficient approach to overcome cisplatin resistance with less side effects (Scheme 1.24). Gushchin and Babak's team synthesized and characterized square planar Pt(II) and Pd(II) complexes of redox active bis(diisopropylphenyl)iminoacenaphtene (dpp-Bian) based ligand (Scheme 1.24).[94] Unlike Pd complexes (**Pd80** and **Pd21**), their platinum analogues (**Pt41** and **Pt42**) exhibited high anticancer activity against breast cancer cell lines surpassing cisplatin. The combination of DNA intercalation and ROS induction was credited to their superior anticancer effects.

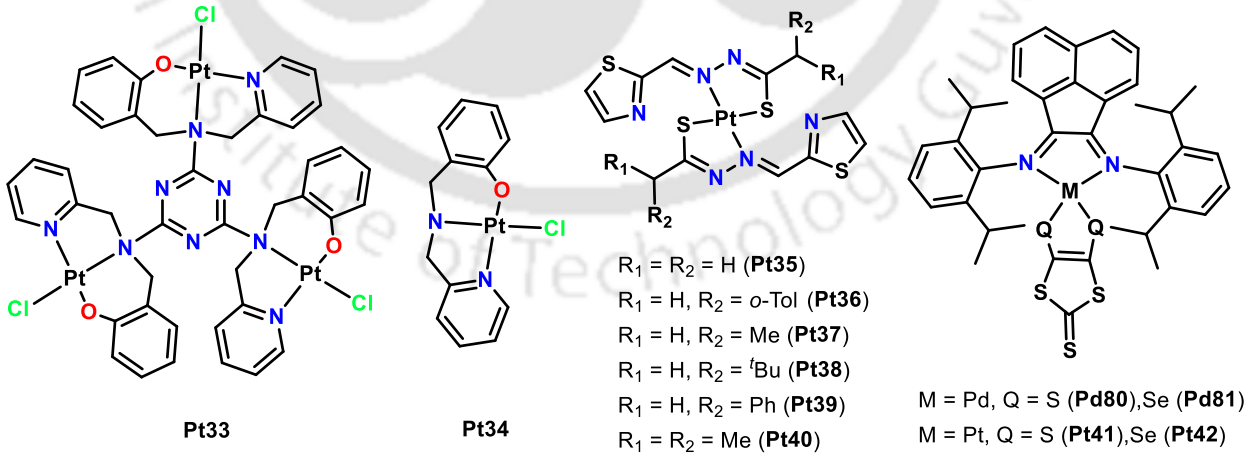

Scheme 1.24: Some reported Pt(II)/Pd(II) complexes used for DNA damage.

In 2024, Vilar's group explored Pt(II) complexes (**Pt43** – **Pt45**) of salphen based ligands as selective G-quadruplex DNA binders.[95] Their modular design permitted finetuning of

planarity, charge, and substituents to achieve excellent binding affinity and sequence selectivity. Cellular assays displayed significant inhibition and apoptosis induction similar to quadruplex targeting mechanism (Scheme 1.25).

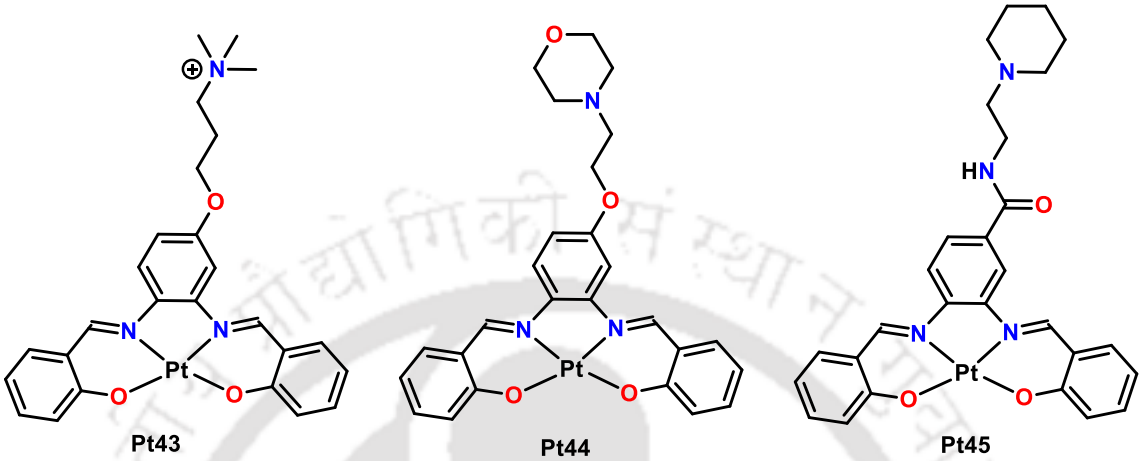

Scheme 1.25: Salphen based Pt(II) complexes reported by Vilar's group

The work by Mondal and team involved with two Pd(II) and Pt(II) complexes (**Pt46** and **Pd82**) of an ONS- donor azo-thioether pincer ligand.[96] The complexes exhibited strong binding affinity with DNA (via intercalation) and BSA. Also, the *in vitro* tests revealed potent anticancer activity that was more effective for Pt(II) complex than the Pd(II) analogue. Very recently, Qin's group contributed in the synthesis of two new Pt(II) complexes of 8-hydroxyquinoline (**Pt47** – **Pt48**).[97] The compounds displayed effective action against MDA-MB-231 breast cancer cells where the selectivity was higher than cisplatin and **Pt47** was more effective than **Pt48** (Scheme 1.26).

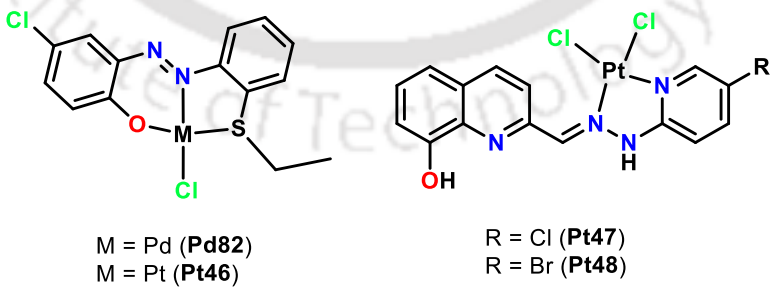

Scheme 1.26: Some reported Pt(II)/Pd(II) complexes exhibited DNA interaction

1.4 Progress in nickel catalysis

From the discovery of Raney nickel catalyst till date, Ni catalysts have been laid the groundwork for many catalytic conversions beyond cross-coupling chemistry (Figure 1.2).

Figure 1.2: Importance and use of Nickel catalyst.

Over the past years, as a low-cost alternative to palladium, nickel catalysis has undergone many developments that include:

- Nickel has proven valuable for challenging substrates and excels in reductive coupling for C–C bonds, carboamination/carbofunctionalization of alkenes, and C–H functionalization.
- Recent advancements have shown that Ni can engage in dual catalytic cycles, combining with photo redox or electrochemical systems enabling milder conditions.
- Ni catalysis has entered the domain of enantioselective synthesis, contributing to chiral drug development and total synthesis.

1.4.1 Recent advances in the design and reactivity of nickel(II) complexes

The exploration of nickel-based catalysts has advanced substantially over the past decade, driven by a need to replace expensive noble metals. A review discussed in this section highlighting key developments in nickel catalysis over last decade.

Monfette and coworker reported a robust and air-stable Ni(II) precatalyst, NiCl(*o*-tolyl)(TMEDA) (**Ni1**),[98] that matched the performance of commonly used $Ni(cod)_2$ in Suzuki, Kumada, and Heck-type cross-coupling reactions (Scheme 1.27). The work highlighted solid-

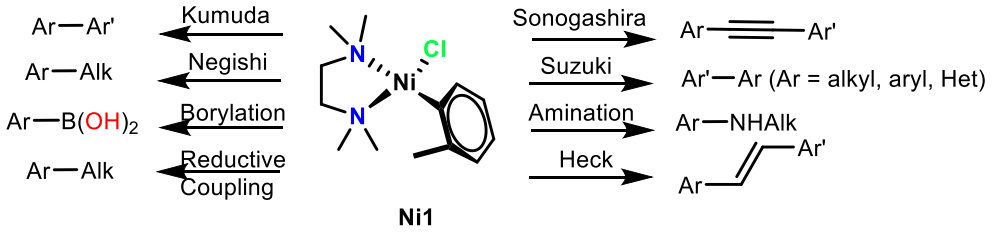

Scheme 1.27: A Nickel catalyst used in various reactions

state stability and glovebox-free handling for high scale induststrial and pharmaceutical synthesis. Some di- and tri- nuclear nickel complexes (**Ni2**–**Ni10**) of tridentate Schiff-base ligands was developed by Ko's group in 2016.[99] These complexes exhibited remarkable activity and selectivity in the alternating copolymerization of carbon dioxide with cyclohexene oxide, yielding highly ordered polycarbonates with ≥ 99% carbonate linkages (Scheme 1.28). Their study offered the role of Ni catalysis beyond traditional cross-couplings into sustainable polymer chemistry.

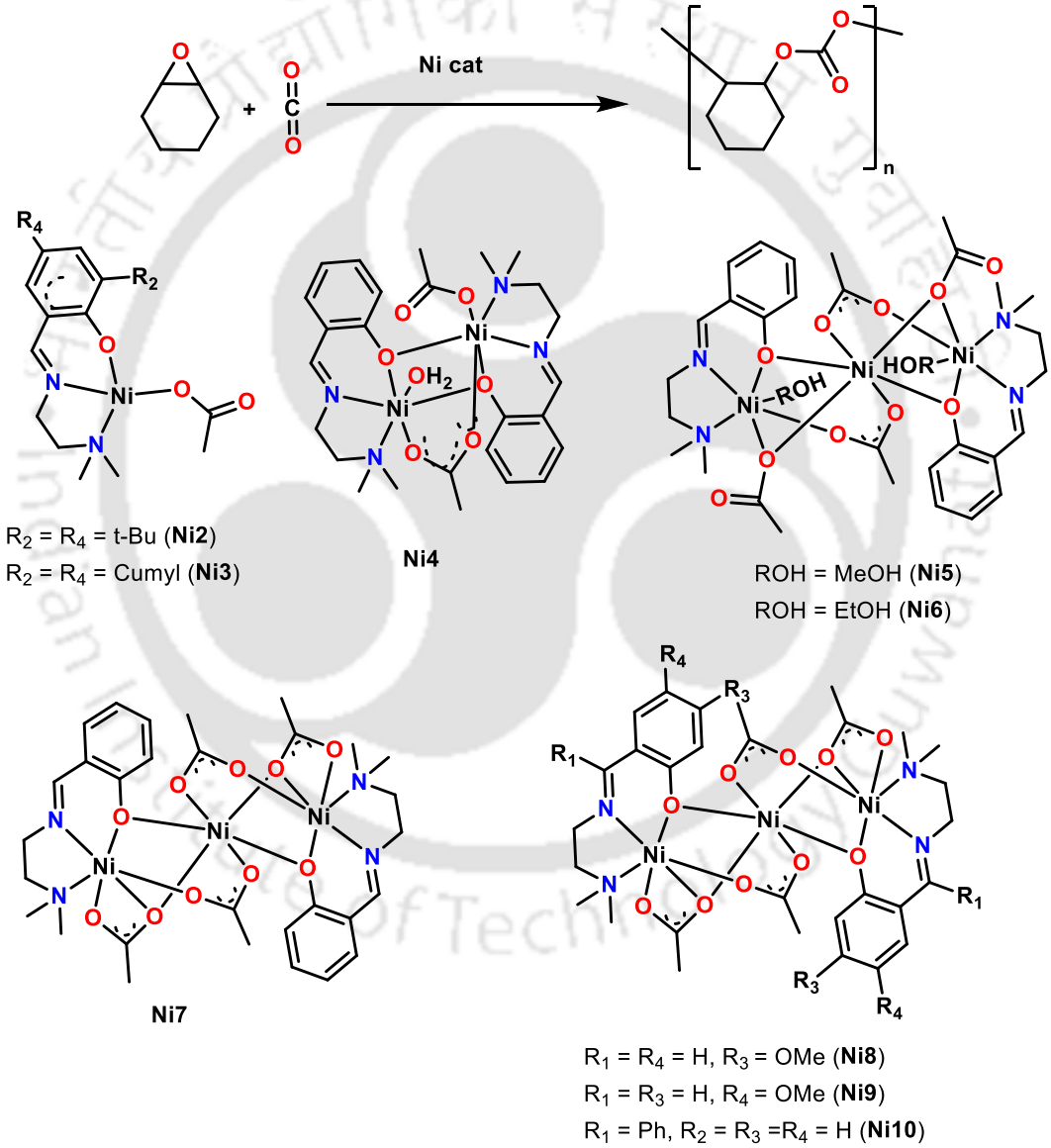

Scheme 1.28: Some previously reported Ni catalyst used for polymerization.

Wang *et al.* developed N-heterocyclic carbene (NHC) based hydrido Ni(II) pincer complexes (**Ni11**–**Ni16**) that effectively catalyze hydrodehalogenation of aryl and alkyl halides.[100] Their method relied on generating Ni–H species through reduction of Ni–Br complexes with silanes or $NaBH_4$. Complex **Ni15** exhibited superior activity, even at low catalyst loadings, particularly for substrates containing electron-withdrawing groups. Mechanistic experiments pointed to a radical pathway involving Ni(I) intermediates, supported by reactivity with iodoalkanes and trapping studies. Their work develops the mechanistic understanding of nickel mediated hydrogen atom transfer (HAT) processes and expands the catalytic utility of Ni–H species in reductive transformations (Scheme 1.29). The potential of imidazolin-2-imine based aryloxide ligands to design Ni(II) complexes (**Ni17**–**Ni19**) for efficient copolymerization of norbornene with polar monomers was introduced by Eisen and co-workers (Scheme 1.29).[101] The structural rigidity and strong σ-donating nature of the imidazolin-2-imine framework proved beneficial for enhancing thermal stability and catalytic activity, achieving highest polymerization activities for **Ni17** (26.88×10^6 g of Polynorborane (mol of **Ni17**)$^{-1}$ h^{-1}).

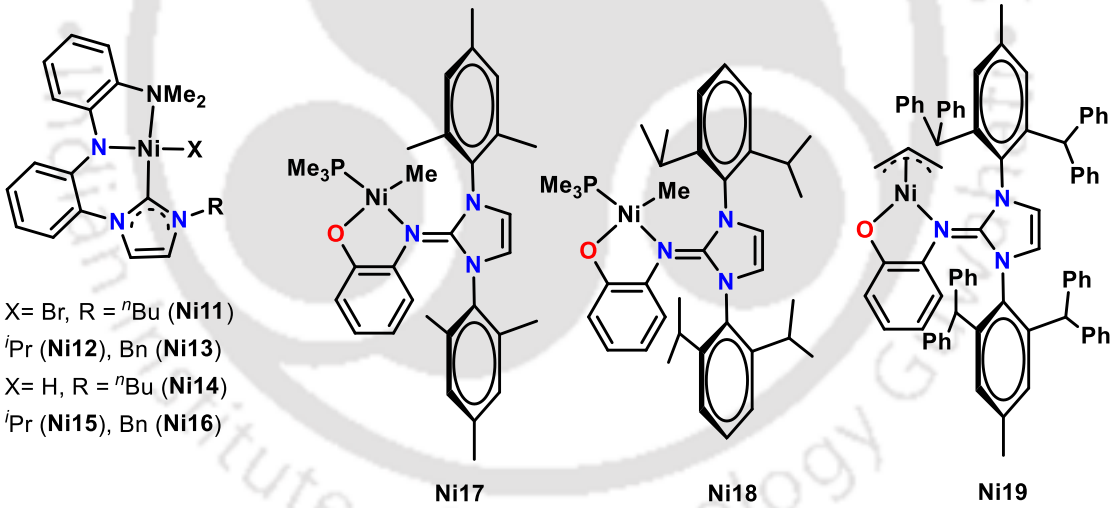

Scheme 1.29: Some previously reported nickel catalyst used in hydrodehalogenation (**Ni11** – **Ni16**) copolymerization of norbornene (**Ni17** – **Ni19**).

The Yamaguchi group reported pincer Ni(II) catalysts (**Ni20** – **Ni22**) bearing acetylacetonato based ONN-, ONP-, and NNN- donor ligandscatalyzed Kumada-type cross-couplings of aryl chlorides with Grignard reagents where the ONP- ligated complex (**Ni21**) delivered the most favorable performance.[102] Their investigation on electronic properties of the complexes

revealed the effect of ligand donor type and geometry on key mechanistic steps in activating the inert C–Cl bonds (Scheme 1.30).

Another polymerization reaction, coupling of carbon dioxide and ethylene to form acrylates under relatively mild conditions was reported by Hopkins *et al.* using a bis(di-iso-propylphosphino)benzene nickel complex (**Ni23**).[103] These findings marked a key step in the valorization of greenhouse gases into industrial monomers using nickel catalyst and provide a platform for acrylate synthesis from CO_2 (Scheme 1.30).

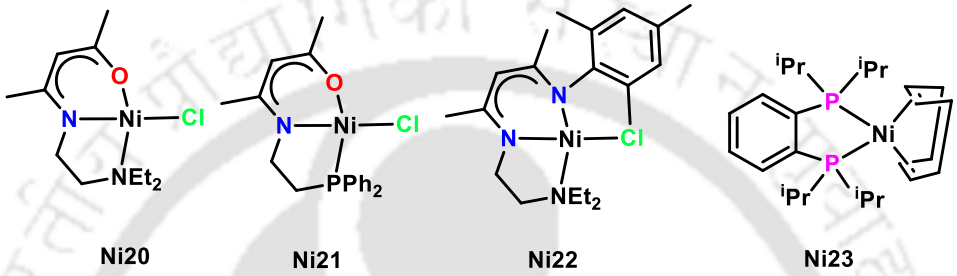

Scheme 1.30: Some previously reported nickel catalyst used in various coupling reaction.

Balaraman's group developed NNN pincer Ni(II) complexes (**Ni24** and **Ni25**) and employed in direct N-alkylation of amines using secondary alcohols.[104] This work extended the hydrogen autotransfer (HA) strategy into previously inaccessible substrate scope. Base metal nickel was seen as a substitute of expensive metal catalyst in HA type conversion (Scheme 1.31).

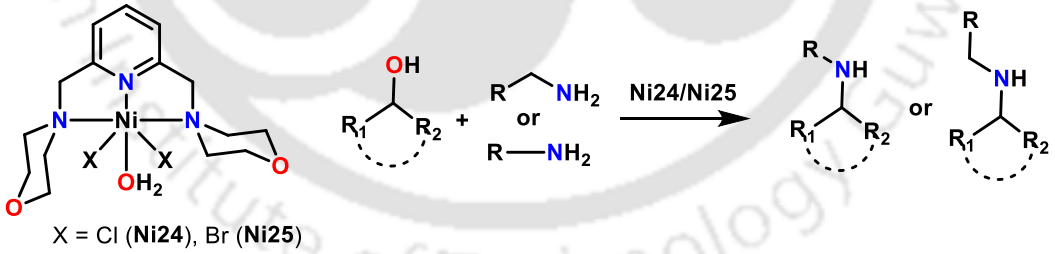

Scheme 1.31: Previously reported NNN-Ni catalyst used in hydrogen autotransfer reaction.

Nickel's capability on borrowing hydrogen and dehydrogenative coupling reactions was reported by Adhikari's group in 2020. They synthesized a phosphine-free Ni(II) catalyst (**Ni26**) for the formation of quinolines and quinoxalines (Scheme 1.32).[105] Avoiding classical metal-hydride intermediates and operating under aerobic conditions, this system delivered

synthetically valuable heterocycles with excellent yields and minimized waste, an eco-friendly substitute to traditional Friedländer-type annulations.[106–112]

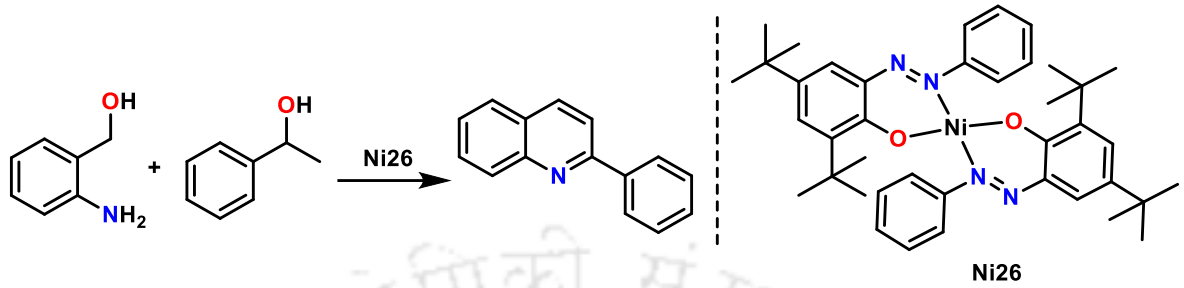

Scheme 1.32: A reported Ni catalyst used in the synthesis of quinoline.

A further evolution on borrowing hydrogen strategy for C–N bond formation was carried out Balamurugan *et al.* who synthesized azo-phenolate Ni(II) complexes (**Ni27** – **Ni29**).[113] Notably, these systems utilized ligand redox activity rather than metal-centered redox processes to facilitate the N-alkylation of amines with alcohols. This mechanistic development has opened the door for designing redox-cooperative ligand frameworks in nickel chemistry (Scheme 1.33). In 2024, Singh *et al.* provided a compelling case for multielectron redox capability in nickel catalysis using an iminosemiquinonate based pincer ligand (Scheme 1.33).[114] Their dinuclear Ni complex (**Ni30**) effectively catalyzed Kumada-type C–C coupling via a single-electron radical pathway supported by radical trapping and DFT studies.

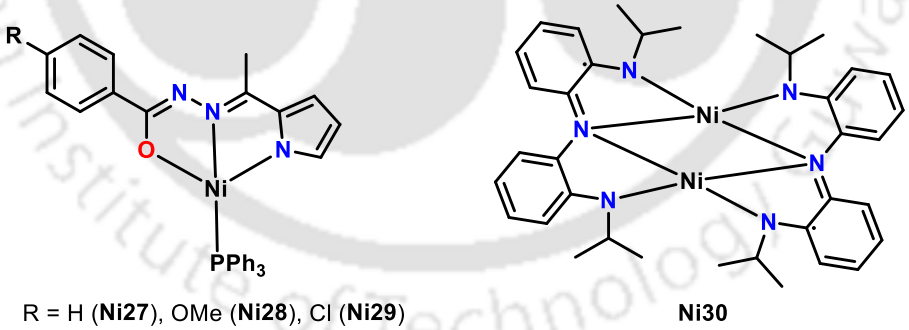

Scheme 1.33: Some reported Ni complexes used as catalyst.

Zhang *et al.* reported three phosphine free and air-stable nickel acetate complexes (**Ni31**–**Ni33**) having NNO- pincer type salicylaldiminato ligands.[115] The complexes were employed as catalyst in the synthesis of imines/diimines using primary alcohols and amines/diamines *via* ADC under mild reaction condition with excellent functional group tolerance. The study

delivered implementation of simple Schiff base Ni(II) complex as sustainable catalyst in C=N bond formation under sustainable conditions (Scheme 1.34).

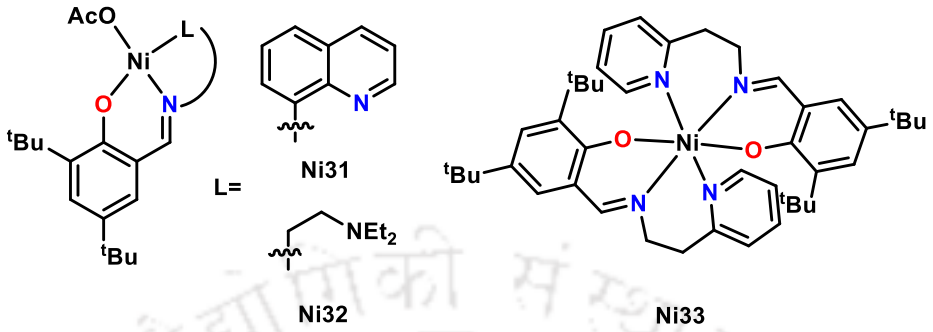

Scheme 1.34: Some reported Ni complexes used as catalyst.

Without using base, Mani and co-workers synthesized a family of bis(phosphine) ligands and their pincer carbene Ni(II) complexes (**Ni34**–**Ni39**).[116] These complexes were used as catalysts in the hydrosilylation of aldehydes, ketones, and nitro containing compounds. The phenyl substituent containing nickel thiolates **Ni36** and **Ni37** produced higher yield than the chloride and hydride analogous may be due to coordinated thiolate ligand and favorable steric factor (Scheme 1.35).

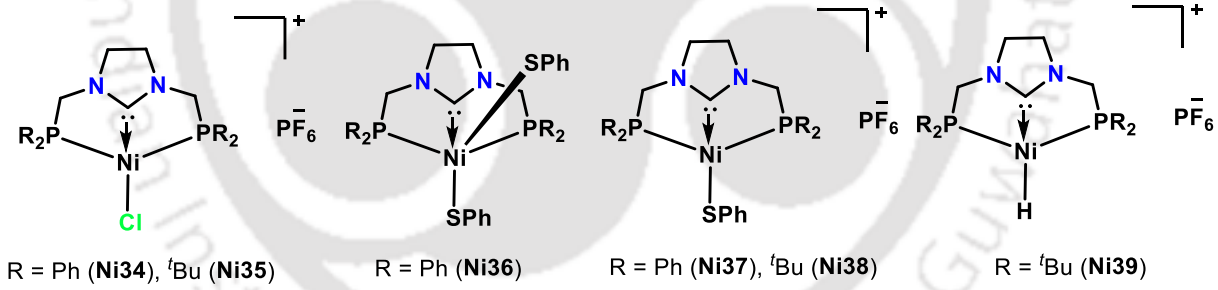

R = Ph (**Ni34**), ^{t}Bu (**Ni35**) R = Ph (**Ni36**) R = Ph (**Ni37**), ^{t}Bu (**Ni38**) R = ^{t}Bu (**Ni39**)

Scheme 1.35: Some reported Ni complexes used as catalyst in hydrosilylation reaction.

Kukreti *et al.* reported Ni-catalyzed multicomponent synthetic methods for 2-pyrazolines *via* acceptorless dehydrogenation of aryl primary alcohols (Scheme 1.36).[117] They employed two air-stable Ni(II) complexes (**NI40** and **Ni41**) anchored by NNN pincer type bis(imino)pyridine ligands and attained 93%, yield with **Ni41**. The method addressed key limitations in traditional heterocycle synthesis such as poor atom economy and multistep procedures.

Recently, Balakrishna and co-workers reported a bipincer Ni(II) complex of bisphosphine (PNN) based ligand. The complex **Ni42** was much capable to catalyze acceptorless

dehydrogenative coupling between 2-aminobenzyl alcohols and ketones, and α-alkylation of ketones.[118]

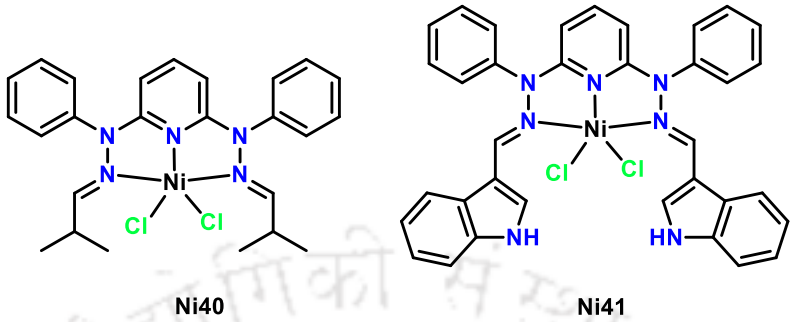

Scheme 1.36: Reported Ni complexes used as catalyst in the synthesis of 2-pyrazolines.

This straightforward methodology is economical and effective in wide range of both primary and secondary alcohols and ketones to produce high yields of quinoline and α-alkylated ketones respectively (Scheme 1.37).

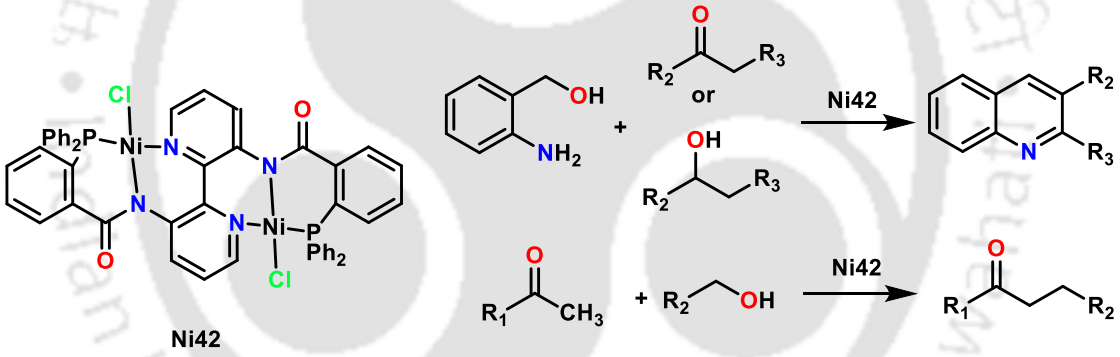

Scheme 1.37: Reported PNN-Ni complex used as catalyst in the synthesis of quinolines and α-alkylation of ketones.

1.5 Progress in zinc catalysis

Zinc, long regarded as a biologically essential and redox-inactive metal, has gradually emerged as a practical alternative to noble metals in catalysis (Figure 1.3). Since its early applications as Grignard-type additions, zinc has gained increasing attention due to its low toxicity, cost-effectiveness, versatile coordination behavior, and sustainable alternatives to noble metal catalysts.

Over the years, zinc catalysis has broadened significantly that include:

- Zn(II) catalysts have been used in ring-opening polymerizations (ROP) of lactides, carbonates, and cyclic esters, copolymerization, and selective bond activation.
- Zinc complexes are now widely investigated for converting CO_2 into cyclic carbonates and carbamates, suitable for carbon capture and utilization (CCU) strategies.
- Till date, zinc-based catalysts have been applied in selective bond-forming reactions, including alkylation, hydroboration, Michael additions, and aza-Diels–Alder reactions.

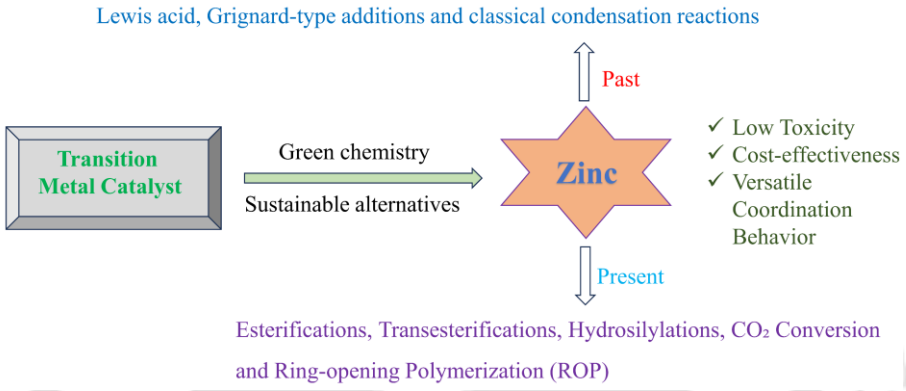

Figure 1.3: Importance and application of Zn complexes in catalysis.

1.5.1 Emerging trends in catalytic activity of zinc complexes

Meng's group designed some mono- and tri- nuclear zinc complexes (**Zn1** – **Zn7**) using Schiff base ligands, used as catalyst in CO_2 and epoxide copolymerization.[119] Trimetallic species displayed superior activity, with steric bulk and electron density on the zinc centers directly influencing polymer microstructure (Scheme 1.38).

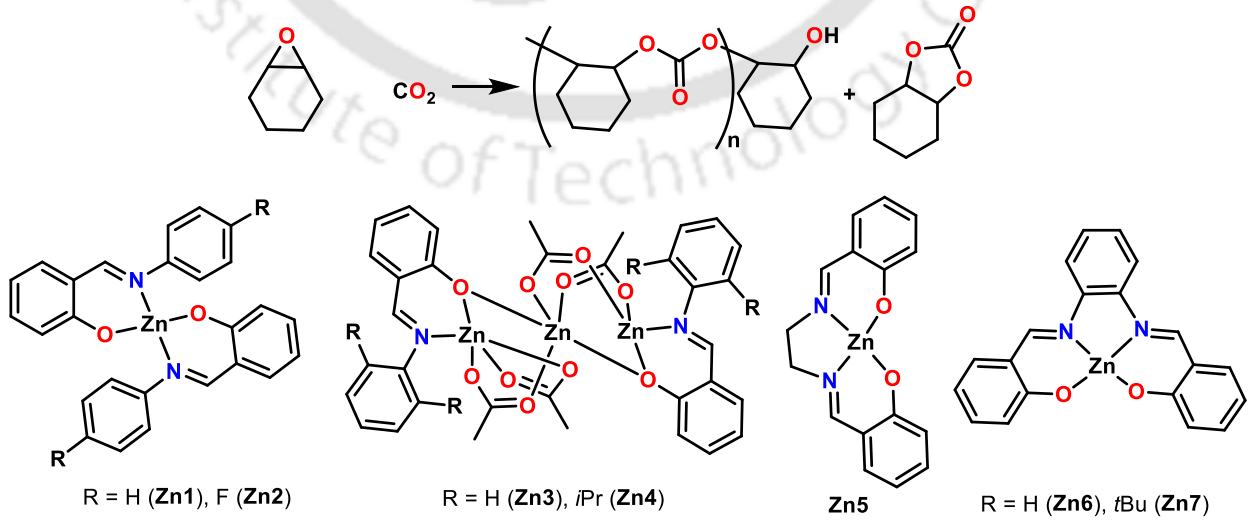

Scheme 1.38: Some reported zinc complex used as catalyst in polymerization.

Zhou and coworker devised a tetraoxo-coordinated 2-hydroxypyridine N-oxide zinc complex (**Zn8)** used in the reaction of epoxides and CO_2 and produced cyclic carbonate (22,000 h^{-1}, 120 °C, 3.0 MPa CO2) in the presence of tetra butyl ammonium iodide (TBAI).[120] Synthetic method of the catalyst design was easy and recovered up to 5 times without decreasing the product yield significantly (Scheme 1.39).

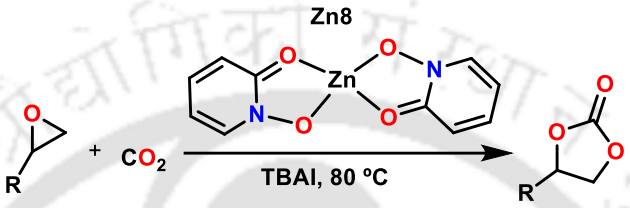

Scheme 1.39: A reported zinc catalyst used in the coupling of CO_2 and epoxide

Williams and co-worker focused on the application of Zn and Mg catalysts (**Zn9** – **Zn10**) for the synthesis of polycarbonate polyol using CO_2 derived from power station.[121] This catalyst was remarkably tolerant to impurities such as S–H (H_2S, octadecanethiol), N−H (diethylamine, MEA), and O−H (H_2O, MEA, SO_2). They established industrial feasibility for producing poly(cyclohexylene carbonate) without negotiating polymer properties (Scheme 1.40). Fuchs *et al.* prepared an easy-to-use salen-type zinc complex (**Zn11**) to produce cyclic carbonates in high yields.[122] During the substrate scope exploration, the catalyst was found to produce maximum yield with propylene oxide under mild reaction condition and low-level catalyst loading. The use of co-catalyst also affected the product formation where TBAB and TBAI majorly produced cyclic carbonates but TBA-Cl and PPN-Cl yielded alternating polycarbonates (Scheme 1.40).

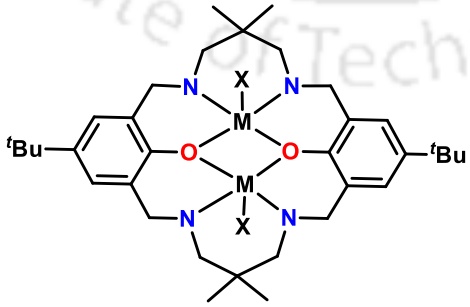

X = OAc (**Zn9**), O_2CF_3 (**Zn10**)

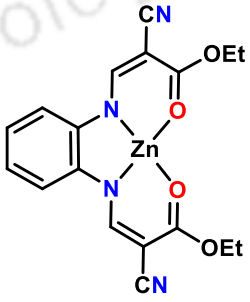

Zn11

Scheme 1.40: Some reported zinc complexes used as catalyst in CO_2 value addition.

Huang *et al.* developed a zinc complex (**Zn12**) that mimic the active site of carbonic anhydrase.[123] The complex exhibited remarkable catalytic activity in the hydrolysis of *p*-nitrophenylacetate (*p*-NPA) and *p*-nitrophenylbutyrate (*p*-NPB) and preparation of $CaCO_3$ using carbon dioxide. This bio-inspired Zn-complex synthesis bridged enzymatic principles with synthetic design (Scheme 1.41).

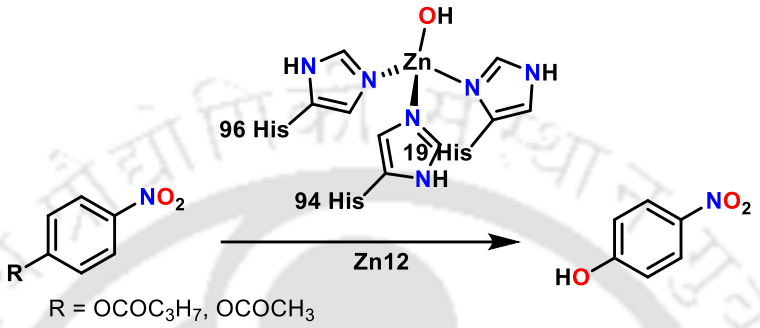

Scheme 1.41: A reported zinc catalyst mimicking carbonic anhydrase

Martínez *et al.* synthesized bimetallic zinc catalysts (**Zn13**–**Zn15**) having heteroscorpionate ligands with −NR2 group (Scheme 1.41).[124] The catalysts were proficient to catalyze alternating ring-opening copolymerization (ROCOP) of cyclohexene oxide and carbon dioxide where **Zn15** was found as superior catalyst. The bimetallic design allowed for tunable polymer microstructures, broadening the scope of sustainable polyester synthesis (Scheme 1.42). Yi's group reported N-oxide ligand containing zinc complexes (**Zn17**–**Zn18**) which effectively catalyzed Michael addition reactions of thiols and α,β-unsaturated carbonyls using only 0.01 mol% of the catalyst[125]. Exploring the mechanistic investigation, they found that the ligand substitution by thiolate ion produce the active catalyst which was responsible for the excellent catalytic activity of these zinc complexes (Scheme 1.42).

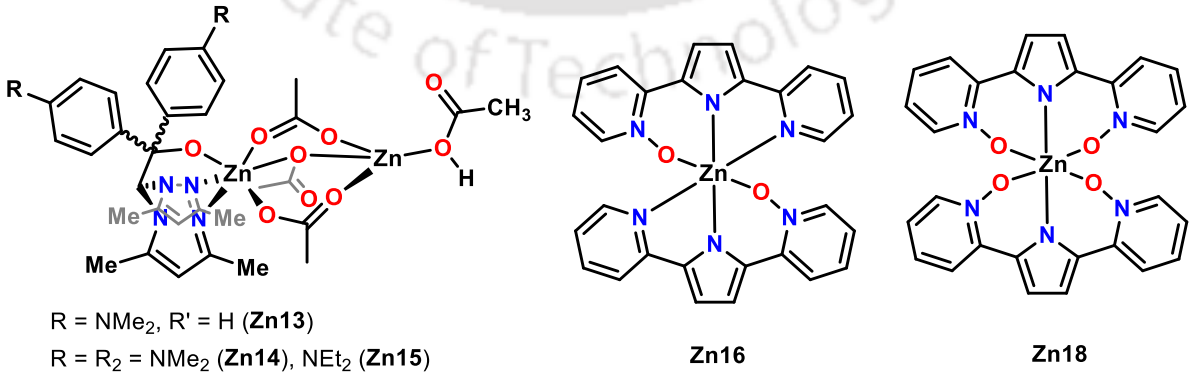

Scheme 1.42: Some reported zinc complexes used as catalyst in ROCOP

With the evolution in cyclic carbonate formation strategy, Nayak *et al.* developed tetradentate zinc salen complexes (**Zn19**–**Zn20**) for coupling CO_2 with epoxides under blue light irradiation.[126] The ligand framework provided an optimal balance of rigidity and flexibility, ensuring both substrate activation and product release. Wavelength of light was also very crucial for product formation as the catalyst was less active under UV light (Scheme 1.43). Kumar *et al.* reported three zinc complexes (**Zn21**–**Zn23**) supported by N-benzhydryl-1-(pyridine 2-yl)methanimine employed for hydroboration of esters and nitriles using pinacolborane and delivered high yields across a broad substrate range under ambient conditions (Scheme 1.43).[127] The transfer of hydride from boron to ester was found to proceed through a cyclic six-membered intermediate.

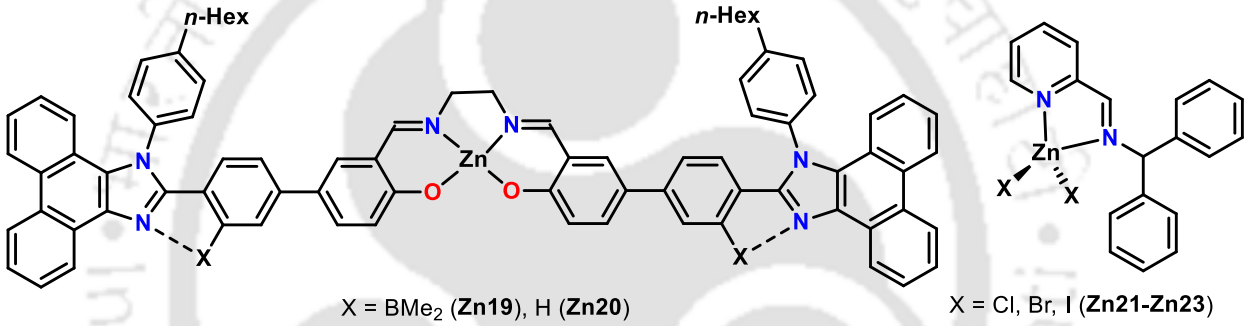

Scheme 1.43: Some reported zinc complexes used as catalyst in CO_2 valorization.

Lamberti's team compared mono- and binuclear Schiff-base zinc complexes (**Zn24** – **Zn26**) (Scheme 1.44).[128] The complexes successfully catalyzed the of lactides and ε-caprolactone and the ring opening copolymerization of cyclohexene oxide and phthalic anhydride. The binuclear catalyst **Zn24** displayed highest catalytic activity in the polymerization of *l*- and rac- lactide while **Zn25** outperformed in both the polymer synthesis.

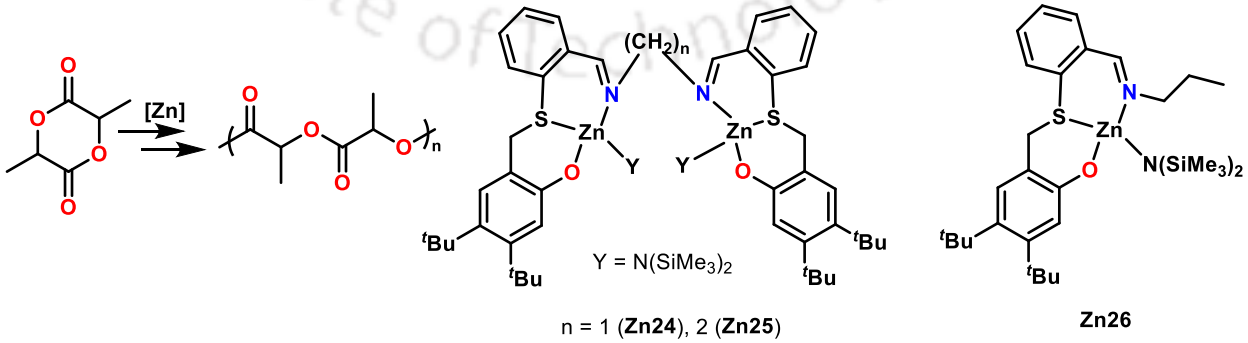

Scheme 1.44: Some reported zinc complexes used as catalysts in synthesis of polyester.

Sun and co-workers presented a series of Zn-N4 complexes (**Zn27**–**Zn31**) utilizing N4 aminopyridine ligands.[129] Using these catalysts, they fixed carbon dioxide with epoxides under solvent and cocatalyst conditions as well as reused for five times with significant loss in product yield. The complex **Zn28**, featuring a DAP ligand, exhibited a remarkable multifunctionality by coordinating Lewis acidic zinc and uncoordinated pyridine that assists in CO_2 activation (Scheme 1.45).

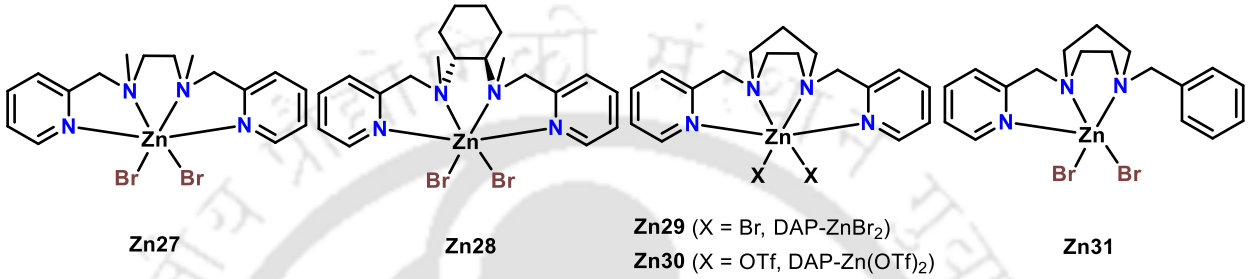

Scheme 1.45: Previously reported zinc complex used as catalyst in CO_2 valorization.

In 2024, Navarro *et al.* reported an enantiopure NNN- donor heteroscorpionate zinc complex (**Zn32**) that excelled in the ring-opening polymerization (ROP) of *rac*-lactide, achieving an isotacticity parameter of 0.88, comparable to the best-known zinc initiators.[130] Notably, the same complexes catalyzed the cycloaddition of CO_2 to epoxides under solvent-free, mild conditions, demonstrating multifunctionality rooted in stereogenic N-donor ligands (Scheme 1.46). Recently, Chen and co-workers reported five zinc complexes (**Zn33**–**Zn37**) based on fluorenylimine supported alkyl ligands and deployed as catalyst for selective hydroboration of aldehydes and ketones with pinacolborane and performed excellently with wide substrate scope (Scheme 1.46).[131] Among all zinc catalysts, **Zn37** gave maximum yield under mild reaction condition, using only 0.8 mol% catalyst loading.

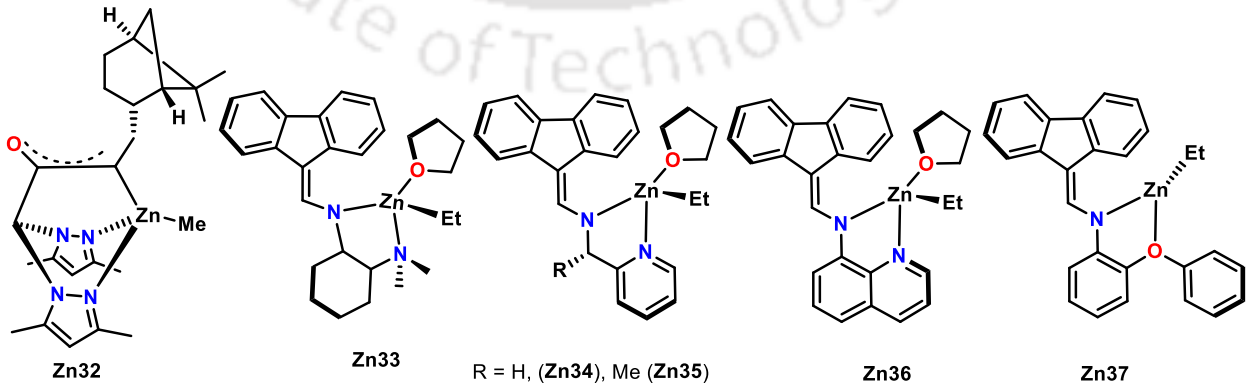

Scheme 1.46: Recently reported zinc catalysts used in ROP and hydroboration.

Very recently, Cruz and Veiros reported bis(κ2-borohydride) zinc complexes (**Zn32**–**Zn36**) of borane containing heteroscorpionate ligands (Scheme 1.47).[132] As a catalyst, these complexes were used for hydroboration of CO_2, tert-butyl isocyanate, and ethyl benzoate. Also, they were efficient in dihydroboration of diphenylacetonitrile at 60 °C with 1 mol% of catalyst loading. The borane tethered complexes **Zn41** and **Zn42** boosted the catalytic activity up to 5-fold as compared to non-borane analogues **Zn39** and **Zn40**. From the experimental and theoretical investigation, it was confirmed from their mechanistic study that the reactivity of the catalysts relied on removal of BH_3 from borohydride ligands.

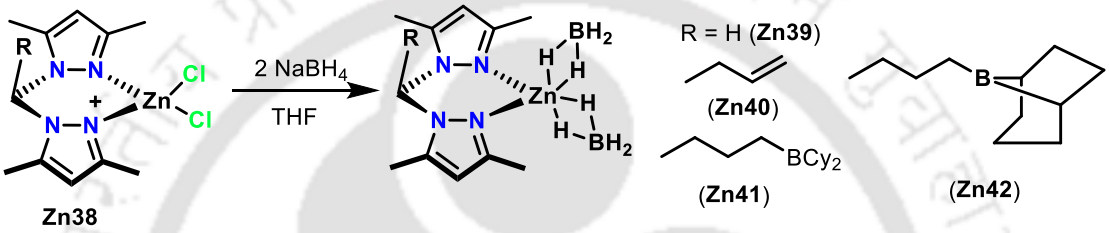

Scheme 1.47: Reported zinc complexes used as catalyst in hydroboration reaction

1.6 Challenges and need for further research

Although Pd, Ni, and Zn complexes displayed excellent catalytic performance and Pt complexes gained popularity in medicine, they have been facing challenges including the use of carbene and phosphene-based ligands, expensivePd/Pt, complicated catalyst synthesis, toxic solvents and byproducts, harsh reaction conditions, and tedious separation methods.[67,133–136] Several other challenges also persist that includes:

- Residual Pd contamination in active pharmaceutical ingredients (APIs) is strictly regulated and requires ultra-clean catalysis or heterogeneous systems that minimize leaching.
- Mechanistic understanding is limited in some Pd catalysts, especially those follow redox-neutral or dual-metal pathways, as seen in Zn due to undetectable intermediates, while versatile redox chemistry of Ni promotes off-cycle or radical routes, lowering selectivity. Thus, it requires specialized ligand design for better control.
- Air/moisture sensitivity of many Ni and Zn complexes drives the search for robust, stable. and a highly efficient catalyst.

- Many cancers cells' resistance to cisplatin arose due to DNA repair, efflux transporters, and intracellular detoxification.
- Metabolic fate needs better understanding because of limited efficacy in certain cancers due to poor penetration, resistance, and tumor selectivity.

Addressing these challenges requires the design of easily synthesized, multifunctional, and recyclable catalytic systems that operate in green solvents under mild reaction conditions, delivering high selectivity, broad substrate scope, and optimal atom economy while minimizing time, energy, and waste.

1.7 Objectives

From the above discussed literature review and considering the current challenges, this thesis focuses on the design of advanced Ni, Pd, Pt, and Zn complexes to enhance catalytic efficiency, broaden application scope, and improve sustainability in catalysis and biophysical chemistry with the following key objectives:

- ❖ Synthesize complexes by tailoring ligand environments for fine-tuning electronic properties of the metal center to boost catalytic activity under sustainable and mild reaction conditions.
- ❖ Exploring the novel 1,3-disubstituted imidazo[1,5-*a*]pyridine ligands to synthesize bivalent Ni, Pd, and Zn complexes for catalytic utility. Also, compared the effect of these ligands with other N-/O-/P- donor ligands.
- ❖ Investigate mono-, di-, and multinuclear complexes for making multifunctional catalysts.
- ❖ Explore ct-DNA and BSA binding affinity of Pt(II)/Pd(II) congeners within unified ligand framework for therapeutic relevance.

1.8 Why imidazo[1,5-*a*]pyridine based ligands were chosen

The first reported uses of imidazo[1,5-*a*]pyridine ligands in coordination chemistry date back to the early 2000s, where they were initially explored for their optical and medicinal properties due to unique structural and electronic characteristics (Figure 1.4).[137–141] Literature contained a few reports of various metal (Ni, Fe, Co, Pd, Ir, Rh and Ru) complexes having imidazo[1,5-*a*]pyridine moieties employed as catalysts and more exploration remained as a key goal.[142–152] Though there are many reports available for the synthesis of imidazo[1,5-*a*]pyridine moiety containing compounds,[153–156] synthetic methods for 1,3-disubstituted derivatives are

inadequate, which is crucial for metal complex design *via* N-coordination. In this facet, this thesis explored the bivalent Ni, Pd, Pt and Zn complexes of disubstituted imidazo[1,5-*a*]pyridine ligands reported by Manivannan and coworker[157,158] considering their unique architecture and facile synthetic method.

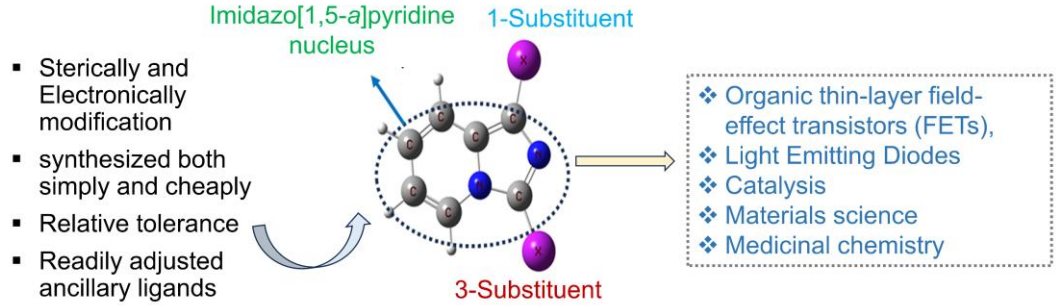

Figure 1.4: Importance and application. of imidazo[1,5-*a*]pyridine compound.

1.9 General Methods, Material, and Instrumentation

The solvents were purchased from commercial sources, chemicals used in this report were of reagent grade, obtained from Sigma-Aldrich and TCI, used without any further purification unless otherwise stated. The catalytic products were purified by preparative thin layer chromatography using ethyl acetate and hexane as eluting agents. Fourier Transform Infrared (FT-IR) measurements were recorded by using a Perkin–Elmer attenuated total reflection infrared (ATR-IR) spectrophotometer (4000–400 cm^{-1}). NMR spectra were recorded on Bruker 400MHz, 500 MHz, and 600 MHz instruments. FESEM images of the dry powder sample were taken on a Sigma 300 FESEM instrument (Carl Zeiss). Electronic spectra were recorded using Perkin Elmer Lambda-35 UV–visible and Fluoromax spectrophotometer. A varioMACROcube instrument was used for CHN analysis. Electrospray ionization high resolution mass spectra (ESI-HRMS) were recorded on an Agilent MS Model G6546A (Serial Number SG2242E201) Q-TOF mass spectrometer and the simulated spectra were calculated by using MestReNova software. All known compounds were characterized by using NMR spectroscopy and compared with the literature.

1.10 References

1. L. W. Covert and H. Adkins, *J. Am. Chem. Soc.*, 1932, **54 (10)**, 4116–4117.
2. S. H. Tucker, *J. Chem. Educ.*, 1950, **27**, 489.

3. D. S. Tarbell and A. T. Tarbell, *J. Chem. Educ.*, 1977, **54 (1)**, 26–28.
4. Seymour, R.B., 1986. Introduction to History of Polyolefins. In History of Polyolefins: The World's Most Widely Used Polymers (pp. 1-7). Dordrecht: Springer Netherlands.
5. W. Reppe and H. Vetter, *Justus Liebigs Ann. Chem.*, 1953, **582**, 133–161.
6. W. Reppe, O. Schlichting, and H. Meister, *Justus Liebigs Ann. Chem.*, 1948, **560**, 104–116.
7. B. M. Trost and T. J. Fullerton, *J. Am. Chem. Soc.*, 1973, **95**, 292–294.
8. J. Smidt, W. Hafner, R. Jira, R. Sieber, J. Sedlmeier and A. Sabel, *Angew. Chem.*, 1962, **74**, 93–102.
9. *Press release: NobelPrize.org*, 2010.
10. E. Negishi, *J. Organomet. Chem.*, 1999, **576**, xv–xvi.
11. N. Miyaura, K. Yamada and A. Suzuki, *Tetrahedron Lett.*, 1979, **20**, 3437–3440.
12. N. Miyaura, T. Yanagi and A. Suzuki, *Synth. Commun.*, 1981, **11**, 513–519.
13. A. Suzuki, *J. Organomet. Chem.*, 1999, **576**, 147–168.
14. E. Negishi, A. O. King and N. Okukado, *J. Org. Chem.*, 1977, **42**, 1821–1823.
15. V. M. Chernyshev and V. P. Ananikov, *ACS Catal.*, 2022, **12**, 1180–1200.
16. L. C. Campeau and N. Hazari, *Organometallics*, 2019, **38**, 3–35.
17. C. C. C. Johansson Seechurn, M. O. Kitching, T. J. Colacot and V. Snieckus, *Angew. Chem., Int. Ed.*, 2012, **51**, 5062–5085.
18. L. Galluzzi, L. Senovilla, I. Vitale, J. Michels, I. Martins, O. Kepp, M. Castedo and G. Kroemer, *Oncogene*, 2012, **31**, 1869–1883.
19. S. Dasari, *Eur. J. Pharmacol.*, 2014, **740**, 364–378.
20. D. J. Stewart, *Crit. Rev. Oncol. Hematol.*, 2007, **63**, 12–31.
21. K. Barabas, R. Milner, D. Lurie and C. Adin, *Vet. Comp. Oncol.*, 2008, **6**, 1–18.
22. *Oncologist*, 2006, **11**, 316–317.
23. T. Boulikas and M. Vougiouka, *Oncol. Rep.*, 2003, **10**, 1663–1682.
24. P. Loehrer and L. H. Einhorn, *Ann. Intern. Med.*, 1984, **100**, 704–713.
25. R. A. Alderden, M. D. Hall and T. W. Hambley, *J. Chem. Educ.*, 2006, **83**, 728–734.
26. R. S. Vardanyan and V. J. Hruby, *Synth. Essent. Drugs*, 2006.
27. A. H. Calvert, D. R. Newell, L. A. Gumbrell, S. O'Reilly, M. Burnell, F. E. Boxall, Z. H. Siddik, I. R. Judson, M. E. Gore and E. J. Wiltshaw, *J. Clin. Oncol.*, 1989, **7**, 1748–1756.

28. R. Canetta, M. Rozencweig and S. K. Carter, *Cancer Treat. Rev.*, 1985, **12**, Suppl. A, 125–136.
29. D. Lebwohl and R. Canetta, *Eur. J. Cancer*, 1998, **34**, 1522–1534.
30. D. Cunningham, N. Starling, S. Rao, T. Iveson, M. Nicolson, F. Coxon, G. Middleton, F. Daniel, J. Oates and A. R. N. Norman, *N. Engl. J. Med.*, 2008, **358**, 36–46.
31. M. G. Apps, E. H. Y. Choi and N. J. Wheate, *Endocr. Relat. Cancer*, 2015, **22**, R219–R233.
32. H. Ehrsson, I. Wallin and J. Yachnin, *Med. Oncol.*, 2002, **19**, 261–265.
33. N. J. Wheate, S. Walker, G. E. Craig and R. Oun, *Dalton Trans.*, 2010, **39**, 8113–8127.
34. F. Langer, L. Schwink, A. Devasagayaraj, P. Y. Chavant and P. Knochel, *J. Org. Chem.*, 1996, **61**, 8229–8243.
35. L. C. McCann, H. N. Hunter, J. A. C. Clyburne and M. G. Organ, *Angew. Chem., Int. Ed.*, 2012, **51**, 7024–7027.
36. P. R. Markies, G. Schat, O. S. Akkerman, F. Bickelhaupt and A. L. Spek, *J. Organomet. Chem.*, 1992, **430**, 1–13.
37. A. Krasovskiy, V. Malakhov, A. Gavryushin and P. Knochel, *Angew. Chem., Int. Ed.*, 2006, **45**, 6040–6044.
38. D. Seyferth, *Organometallics*, 2001, **20**, 2940–2955.
39. Monfared, R. Mohammadi, A. Hosseinian, S. Sarhandi and P. K. Nezhad, *RSC Adv.*, 2019, **9**, 3884–3899.
40. R. Jianming, X. Anguo, W. Hongwei and Y. Hailin, *Des. Monomers Polym.*, 2014, **17**, 345–355.
41. C. A. Montoya, C. F. Gómez, A. B. Paninho, A. V. M. Nunes, K. T. Mahmudov, V. Najdanovic-Visak, L. M. D. R. S. Martins, M. F. C. Guedes da Silva, A. J. L. Pombeiro and M. J. Nunes da Ponte, *J. Catal.*, 2016, **335**, 135–140.
42. Y. Wu, Y. Jiang, H. Yin, X. Chen, N. Wang and Z. Wang, *Mater. Today Sustain.*, 2025, **31**, 101148.
43. K. Żółtowska, M. Sobczak and E. Olędzka, *Molecules*, 2015, **20**, 2816.
44. S. Abbina and G. Du, *ACS Macro Lett.*, 2014, **3**, 689–692.
45. H. Pellissier, *Coord. Chem. Rev.*, 2021, **439**, 213926.

46. J. Álvarez-Valle, P. García-Martínez, L. A. López and J. Santamaría, *Eur. J. Org. Chem.*, 2025, **28**, e202401271.
47. H. D. Bishop, Q. Zhao and C. Uyeda, *J. Am. Chem. Soc.*, 2023, **145**, 20152–20157.
48. A. Biffis, P. Centomo, A. Del Zotto and M. Zecca, *Chem. Rev.*, 2018, **118**, 2249–2295.
49. N. Kambe, T. Iwasaki and J. Terao, *Chem. Soc. Rev.*, 2011, **40**, 4937–4947.
50. C. E. I. Knappke and A. J. von Wangelin, *Chem. Soc. Rev.*, 2011, **40**, 4948–4962.
51. Muzammil, A. F. Zahoor, B. Parveen, S. Javed, R. Akhtar and S. Tabassum, *Chem. Pap.*, 2024, **78**, 3399–3430.
52. P. J. Anju, M. Neetha and G. Anilkumar, *ChemistrySelect*, 2022, **7**, e202103564.
53. K. P. S. Cheung and V. Gevorgyan, *Acc. Chem. Res.*, 2025, **58**, 861–876.
54. V. Farina, *Adv. Synth. Catal.*, 2004, **346**, 1553–1582.
55. C. S. Horbaczewskyj and I. J. S. Fairlamb, *Org. Process Res. Dev.*, 2022, **26**, 2240–2269.
56. M. J. West and A. J. B. Watson, *Org. Biomol. Chem.*, 2019, **17**, 5055–5059.
57. A. K. Cooper, P. M. Burton and D. J. Nelson, *Synthesis*, 2020, **52**, 565–573.
58. D. Mendoza-Espinosa, R. González-Olvera, G. E. Negrón-Silva, D. Ángeles-Beltrán, O. R. Suárez-Castillo, A. Álvarez-Hernández and R. Santillan, *Organometallics*, 2015, **34**, 4529–4542.
59. S. Kumar, F. Saleem and A. K. Singh, *Dalton Trans.*, 2016, **45**, 11445–11458.
60. N. Dehury, N. Maity, S. K. Tripathy, J. M. Basset and S. Patra, *ACS Catal.*, 2016, **6**, 5535–5540.
61. F. Schroeter, J. Soellner and T. Strassner, *ACS Catal.*, 2017, **7**, 3004–3009.
62. L. M. Zhang, H. Y. Li, H. X. Li, D. J. Young, Y. Wang and J. P. Lang, *Inorg. Chem.*, 2017, **56**, 11230–11243.
63. A. Toledo, I. Funes-Ardoiz, F. Maseras and A. C. Albéniz, *ACS Catal.*, 2018, **8**, 7495–7506.
64. N. Pirkl, A. Del Grosso, B. Mallick, A. Doppiu and L. J. Gooßen, *Chem. Commun.*, 2019, **55**, 5275–5278.
65. S. Kumari, B. Das and S. Ray, *Dalton Trans.*, 2019, **48**, 15942–15954.
66. P. Dubey, S. Gupta and A. K. Singh, *Organometallics*, 2019, **38**, 944–961.
67. J. Zhu and V. N. G. Lindsay, *ACS Catal.*, 2019, **9**, 6993–6998.

68. L. Radhakrishna, H. S. Kunchur, P. K. Namdeo, R. J. Butcher and M. S. Balakrishna, *Dalton Trans.*, 2020, **49**, 3434–3449.
69. A. X. Song, X. X. Zeng, B. B. Ma, C. Xu and F. S. Liu, *Organometallics*, 2020, **39**, 3524–3534.
70. V. N. Shinde, N. Bhuvanesh, A. Kumar and H. Joshi, *Organometallics*, 2020, **39**, 324–333.
71. V. Kletskov, N. A. Bumagin, S. K. Petkevich, E. A. Dikusar, A. S. Lyakhov, L. S. Ivashkevich, I. A. Kolesnik and V. I. Potkin, *Inorg. Chem.*, 2020, **59**, 10384–10388.
72. S. Panchavarnam, R. Sengupta and M. Ravikanth, *Inorg. Chem.*, 2021, **60**, 15686–15694.
73. S. Chakrabortty, M. Kaur, M. Adhikari, K. K. Manar and S. Singh, *Inorg. Chem.*, 2021, **60**, 6209–6217.
74. E. Fazekas, D. T. Jenkins, A. A. Forbes, B. Gallagher, G. M. Rosair and R. D. McIntosh, *Dalton Trans.*, 2021, **50**, 17625–17634.
75. S. Panchavarnam, R. Sengupta and M. Ravikanth, *Dalton Trans.*, 2022, **51**, 5587–5595.
76. M. M. Rahman, J. Zhang, Q. Zhao, J. Feliciano, E. Bisz, B. Dziuk, R. Lalancette, R. Szostak and M. Szostak, *Organometallics*, 2022, **41**, 2281–2290.
77. T. Zhou, P. Gao, E. Bisz, B. Dziuk, R. Lalancette, R. Szostak and M. Szostak, *Catal. Sci. Technol.*, 2022, **12**, 6581–6589.
78. L. H. Hong, W. J. Feng, W. C. Chen and Y. C. Chang, *Dalton Trans.*, 2023, **52**, 5101–5109.
79. E. B. Patricio-Rangel, K. González-Silva and D. Mendoza-Espinosa, *Organometallics*, 2023, **42**, 2893–2901.
80. A. K. King, A. Brar, G. Li and M. Findlater, *Organometallics*, 2023, **42**, 2353–2358.
81. R. O. Pankov, D. O. Prima, A. Y. Kostyukovich, M. E. Minyaev and V. P. Ananikov, *Dalton Trans.*, 2023, **52**, 4122–4135.
82. S. Baweja, T. Gabler, P. Lönnecke and E. Hey-Hawkins, *Dalton Trans.*, 2023, **52**, 6494–6500.
83. S. Jovanović, K. Obrenčević, Ž. D. Bugarčić, I. Popović, J. Žakula and B. Petrović, *Dalton Trans.*, 2016, **45**, 12444–12457.
84. F. P. Intini, J. Zajac, V. Novohradsky, T. Saltarella, C. Pacifico, V. Brabec, G. Natile and J. Kasparkova, *Inorg. Chem.*, 2017, **56**, 1483–1497.

85. C. Icsel, V. T. Yilmaz, M. Aygun, B. Cevatemre, P. Alper and E. Ulukaya, *Dalton Trans.*, 2018, **47**, 11397–11410.
86. A. M. Mansour and O. R. Shehab, *Dalton Trans.*, 2018, **47**, 3459–3468.
87. M. D. Aseman, S. Aryamanesh, Z. Shojaeifard, B. Hemmateenejad and S. M. Nabavizadeh, *Inorg. Chem.*, 2019, **58**, 16154–16170.
88. D. Cócíć, S. Jovanović-Stević, R. Jelić, S. Matić, S. Popović, P. Djurdjević, D. Baskić and B. Petrović, *Dalton Trans.*, 2020, **49**, 14411–14431.
89. M. Vaquero, N. Busto, N. Fernández-Pampín, G. Espino and B. García, *Inorg. Chem.*, 2020, **59**, 4961–4971.
90. A. Zamora, E. Wachter, M. Vera, D. K. Heidary, V. Rodríguez, E. Ortega, V. Fernández-Espín, C. Janiak, E. C. Glazer, G. Barone and J. Ruiz, *Inorg. Chem.*, 2021, **60**, 2178–2187.
91. Das and P. Gupta, *Dalton Trans.*, 2021, **50**, 10225–10236.
92. Y. Wu, D. Zhao, J. Shang, W. Huang and Z. Chen, *Dalton Trans.*, 2022, **51**, 10930–10942.
93. M. Jiang, T. Yang, Y. Chu, Z. Zhang, H. Sun, H. Liang and F. Yang, *Dalton Trans.*, 2022, **51**, 5257–5270.
94. N. F. Romashev, P. A. Abramov, I. V. Bakaev, I. S. Fomenko, D. G. Samsonenko, A. S. Novikov, K. K. H. Tong, D. Ahn, P. V. Dorovatovskii, Y. V. Zubavichus, A. A. Ryadun, O. A. Patutina, M. N. Sokolov, M. V. Babak and A. L. Gushchin, *Inorg. Chem.*, 2022, **61**, 2105–2118.
95. M. Bartlett, J. Burke, P. Sherin, M. K. Kuimova, M. Barahona and R. Vilar, *Chem. Eur. J.*, 2024, **30**, e202402465.
96. A. Das, M. Saha, S. Mandal, S. Das, K. Das Saha and T. K. Mondal, *New J. Chem.*, 2023, **47**, 4931–4943.
97. R. C. Wu, J. M. Zhang, X. Q. Huang, Q. M. Li, Z. Zhou, H. Liang, M. X. Tan and Q. P. Qin, *New J. Chem.*, 2025, **49**, 6561–6567.
98. J. Magano and S. Monfette, *ACS Catal.*, 2015, **5**, 3120–3123.
99. C. Y. Tsai, F. Y. Cheng, K. Y. Lu, J. T. Wu, B. H. Huang, W. A. Chen, C. C. Lin and B. T. Ko, *Inorg. Chem.*, 2016, **55**, 7843–7851.
100. Z. Wang, X. Li, H. Sun, O. Fuhr and D. Fenske, *Organometallics*, 2018, **37**, 539–544.
101. M. Li, Z. Cai and M. S. Eisen, *Organometallics*, 2018, **37**, 4753–4762.

102. E. Asano, Y. Hatayama, N. Kurisu, A. Ohtani, T. Hashimoto, Y. Kurihara, K. Ueda, S. Ishihara, H. Nagao and Y. Yamaguchi, *Dalton Trans.*, 2018, **47**, 8003–8012.
103. M. N. Hopkins, K. Shimmei, K. B. Uttley and W. H. Bernskoetter, *Organometallics*, 2018, **37**, 3573–3580.
104. M. Subaramanian, S. P. Midya, P. M. Ramar and E. Balaraman, *Org. Lett.*, 2019, **21**, 8899–8903.
105. A. K. Bains, V. Singh and D. Adhikari, *J. Org. Chem.*, 2020, **85**, 14971–14979.
106. P. Friedländer and C. F. Gohring, *Ber.*, 1883, **16**, 1833–1839.
107. P. Friedlaender, *Ber.*, 1882, **15**, 2572–2575.
108. R. Varala, R. Enugala and S. R. Adapa, *Synthesis*, 2006, 3825–3830.
109. C. S. Jia, Z. Zhang, S. J. Tu and G. W. Wang, *Org. Biomol. Chem.*, 2006, **4**, 104–110.
110. R. H. Manske, *Chem. Rev.*, 1942, **30**, 113–144.
111. J. Wu, H. G. Xia and K. Gao, *Org. Biomol. Chem.*, 2006, **4**, 126–129.
112. A. Shaabani, E. Soleimani and Z. Badri, *Synth. Commun.*, 2007, **37**, 629–635.
113. G. Balamurugan, R. Ramesh and J. G. Malecki, *J. Org. Chem.*, 2020, **85**, 7125–7135.
114. V. Singh, H. Jain, S. Nath and D. Adhikari, *Chem. Eur. J.*, 2024, **30**, e202303189.
115. X. Zhang, J. Zhang, Z. Hao, Z. Han, J. Lin and G. L. Lu, *Organometallics*, 2021, **40**, 3843–3853.
116. A. Kumar, R. Gupta and G. Mani, *Organometallics*, 2023, **42**, 732–744.
117. P. Kukreti, R. Chauhan, A. Panwar and K. Ghosh, *Org. Biomol. Chem.*, 2024, **22**, 8273–8278.
118. A. Pandey and M. S. Balakrishna, *New J. Chem.*, 2024, **48**, 19549–19560.
119. Y. Xu, M. Xiao, S. Wang, M. Pan and Y. Meng, *Polym. Chem.*, 2014, **5**, 3838–3846.
120. R. Ma, L. N. He and Y. B. Zhou, *Green Chem.*, 2015, **18**, 226–231.
121. A. M. Chapman, C. Keyworth, M. R. Kember, A. J. J. Lennox and C. K. Williams, *ACS Catal.*, 2015, **5**, 1581–1588.
122. M. A. Fuchs, S. Staudt, C. Altesleben, O. Walter, T. A. Zevaco and E. Dinjus, *Dalton Trans.*, 2014, **43**, 2344–2347.
123. Y. Huang, S. Zhang, H. Chen, L. Zhao, Z. Zhang, P. Cheng and Y. Chen, *Inorg. Chem.*, 2019, **58**, 9916–9921.

124. F. De La Cruz-Martínez, M. Martínez De Sarasa Buchaca, J. Martínez, J. Tejeda, J. Fernández-Baeza, C. Alonso-Moreno, A. Rodríguez, J. A. Castro-Osma and A. Lara-Sánchez, *Inorg. Chem.*, 2020, **59**, 8412–8423.
125. X. F. Mo, C. F. Xiong, Z. W. Chen, C. Liu, P. He, H. X. Tong and X. Y. Yi, *Dalton Trans.*, 2020, **49**, 12365–12371.
126. P. Nayak, A. C. Murali, P. K. Pal, U. D. Priyakumar, V. Chandrasekhar and K. Venkatasubbaiah, *Inorg. Chem.*, 2022, **61**, 14511–14516.
127. G. S. Kumar, R. Kumar, A. Sau, V. Chandrasekhar and T. K. Panda, *J. Org. Chem.*, 2023, **88**, 12613–12622.
128. F. Santulli, F. Tufano, M. Cozzolino, I. D'Auria, M. Strianese, M. Mazzeo and M. Lamberti, *Dalton Trans.*, 2023, **52**, 14400–14408.
129. B. Wang, L. Wang, J. Lin, C. Xia and W. Sun, *ACS Catal.*, 2023, **13**, 10386–10393.
130. M. Navarro, S. Sobrino, I. Fernández, A. Lara-Sánchez, A. Garcés and L. F. Sánchez-Barba, *Dalton Trans.*, 2024, **53**, 13933–13949.
131. B. Wei, Z. Qin, H. Miao, C. Wang, M. Huang, C. Liu, C. Bai and Z. Chen, *Dalton Trans.*, 2025, **54**, 3427–3436.
132. T. F. C. Cruz and L. F. Veiros, *Dalton Trans.*, 2025, **54**, 4244–4254.
133. S. Santoro, F. Ferlin, L. Luciani, L. Ackermann and L. Vaccaro, *Green Chem.*, 2017, **19**, 1601–1612.
134. S. McCarthy, D. C. Braddock and J. D. E. T. Wilton-Ely, *Coord. Chem. Rev.*, 2021, **442**, 213925.
135. P. Srinivas, K. Srinivas, P. R. Likhar, B. Sridhar, K. V. Mohan, S. Bhargava and M. L. Kantam, *J. Organomet. Chem.*, 2011, **696**, 795–801.
136. Amit and M. Sen, *Sustainable Green Catalytic Processes*, 2024, 1–27.
137. G. Volpi, G. Magnano, I. Benesperi, D. Saccone, E. Priola, V. Gianotti, M. Milanesio, E. Conterosito, C. Barolo, G. Viscardi, *Dyes Pigm.*, 2017, **137**, 152–164.
138. N. Kundu, S. M. T. Abtab, S. Kundu, A. Endo, S. J. Teat and M. Chaudhury, *Inorg. Chem.*, 2012, **51**, 2652–2661.
139. S. Pischedda, S. Stoccoro, A. Zucca, G. Sciortino, F. Ortu and G. J. Clarkson, *Dalton Trans.*, 2021, **50**, 4859–4873.

140. C. Garino, T. Ruiu, L. Salassa, A. Albertino, G. Volpi, C. Nervi, R. Gobetto and K. I. Hardcastle, *Eur. J. Inorg. Chem.*, 2008, **23**, 3587–3591.
141. Y. Imada, S. Mukai, K. Tahara, N. Kozai, M. Itaya, Y. Yoshida, S. Ueta, Y. Arakawa, K. Minagawa and F. Yagishita, *Inorg. Chim. Acta*, 2023, **555**, 121584.
142. X. Zhang, C. He, X. Yang, Q. Zhang, Y. Li and J. Yao, *New J. Chem.*, 2022, **46**, 141.
143. G. A. Ardizzoia, D. Ghiotti, B. Therrien and S. Brenna, *Inorg. Chim. Acta*, 2018, **471**, 384–390.
144. J. Dong, M. Li and B. Wang, *Organometallics*, 2019, **38**, 3786–3795.
145. J. Dong, D. Yang and B. Wang, *Eur. J. Inorg. Chem.*, 2021, **45**, 4661–4668.
146. F. Han, Y. Xie, X. Xie, S. I. Ivlev and E. Meggers, *Synlett*, 2022, **34**, 1403–1408.
147. T. Samanta, S. K. Seth, S. K. Chattopadhyay, P. Mitra, V. Kushwah and J. Dinda, *Inorg. Chim. Acta*, 2014, **411**, 165–171.
148. M. Nonnenmacher, D. Kunz, F. Rominger and T. Oeser, *J. Organomet. Chem.*, 2007, **692**, 2554–2563.
149. X. Yang, B. Wang and Y. Li, *Appl. Organomet. Chem.*, 2025, **39**, e7934.
150. X. Yang, C. Dou, B. Wang, Q. Zhang and Y. Li, *J. Mol. Struct.*, 2025, **1325**, 141015.
151. T. Murai, E. Nagaya, F. Shibahara, T. Maruyama and H. Nakazawa, *J. Organomet. Chem.*, 2015, **794**, 76–80.
152. F. Yagishita, K. Nomura, S. Shiono, C. Nii, T. Mino, M. Sakamoto and Y. Kawamura, *ChemistrySelect*, 2016, **1**, 4560–4563.
153. J. Wang, L. Dyers, R. Mason, P. Amoyaw and X. R. Bu, *J. Org. Chem.*, 2005, **70**, 2353–2356.
154. M. R. Reddy, C. M. Darapaneni, R. D. Patil and H. Kumari, *Org. Biomol. Chem.*, 2022, **20**, 3440–3468.
155. K. Zeng, R. Mei, X. C. Zhang, L. B. Andreas and K. Zhang, *Chem. Commun.*, 2022, **58**, 1060.
156. M. Li, Y. Xie, Y. Ye, Y. Zou, H. Jiang and W. Zeng, *Org. Lett.*, 2014, **16**, 6232–6235.
157. V. K. Fulwa and V. Manivannan, *Tetrahedron*, 2012, **68**, 3927–3931.
158. V. K. Fulwa, R. Sahu, H. S. Jena and V. Manivannan, *Tetrahedron Lett.*, 2009, **50**, 6264–6267.

Chapter-2

Palladium(II) and Platinum(II) Complexes of Disubstituted Imidazo[1,5-*a*]Pyridine and Imidazolylpyridine: Coordination Chemistry, Versatile Catalysis, and Biophysical Study*

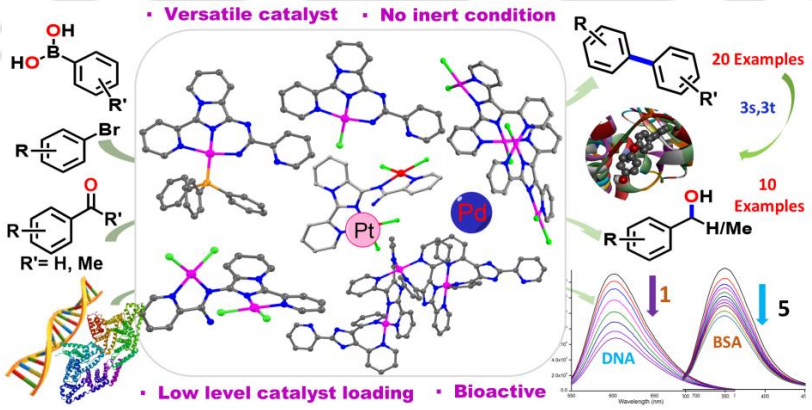

* This work has been published in

A. R. Rayasingh and V. Manivannan, *Dalton Trans.* 2025, ***54*** (19), 7741–7752.

Abstract

Some pincer type mono- and poly-nuclear Pd(II) and Pt(II) complexes bearing imidazo[1,5-a]pyridine and imidazolylpyridine moiety were synthesized and characterized by using several spectroscopic methods. Determination of molecular structures of all complexes by single crystal X-ray diffraction studies revealed a distorted square planar geometry around the bivalent palladium and platinum in all complexes. These Pd(II) complexes have been observed to display high catalytic activity in various reaction such as Suzuki-Miyaura cross-coupling reaction, transfer hydrogenation reaction, and alkyne homocoupling. The theoretical study was also well matched with experimental data of all catalysts. Substantial deviations in the catalytic activity were observed by changing the co-ligand, binding mode of the ligand and the number of metal centre. Under optimal conditions, Suzuki cross-coupling and the transfer hydrogenation reaction were accomplished proficiently with wide functional group possibility by taking only 0.1 mol% of tetranuclear Pd(II) complex (**5**) as catalyst. Intermediates in Suzuki coupling reaction were also detected by using mass spectroscopy. Among all studied complexes, the tetra nuclear palladium complex exhibited high catalytic activity. Further Pd(II) complexes were tested in a model reaction of homocoupling of phenylacetylene and produce diphenylbutadiyne in excellent yield. Also, interaction study of all the complexes with calf thymus DNA (CT-DNA) and bovine serum albumin (BSA) were investigated using electronic spectroscopy Absorption study showed minor groove binding of DNA with these complexes while intercalative binding was observed by all complexes through displacement of ethidium bromide (EB) in EB-DNA by quenching of fluorescence intensity. The complexes were also displayed high binding affinity toward BSA confirmed by emission, synchronous fluorescence, and steady state fluorescence anisotropy measurement. Moreover, the pharmacokinetic properties of two bioactive compounds (**3s** and **3t**) obtained from Suzuki coupling reaction were calculated and to evaluate their activity as leukotriene A4 hydrolase (LTA_4H) inhibitor, these molecules were docked with human LTA_4H enzyme.

2.1 Introduction

In transition metal catalysis, palladium complexes have emerged as highly effective and versatile tools in organic transformation such as coupling reactions, transfer hydrogenation of carbonyl compounds, homo coupling of alkynes and many more.[1–8] The coupling

reactions play a key role in the production of pharmaceuticals,[9] plastics, agrochemicals,[10] and other synthetic chemicals. A well-known transformation in organic synthesis is metal catalysed transfer hydrogenation process, in which conversion of carbonyl group to alcohol achieved by transfer of hydrogen from alcoholic solvent to the carbonyl group.[11–13] From a comprehensive literature survey in Chapter 1, it was concluded that there are some limitations posed by palladium catalysts such as expensive synthesis of catalyst, carbene and phosphene based ligands, noxious byproduct, toxic solvent, inert conditions, and tedious separation.[14] To overcome these drawbacks faced by the homogeneous palladium catalyst, the development of innovative and simply made protean catalytic systems are supposedly desirable[15] intending the execution of multiple reactions by means of minuscule amounts of recyclable catalyst in harmless solvents, ordinary conditions, atom economy with diminution of time, energy, and waste.[16] To overcome the prevailing expensive, lethal, and unstable carbene or phosphine-based ligands,[17] there has been an incremental necessitate for alternate ligand systems. Also, in recent years bi- and tri-nuclear palladium complexes have appeared as an attractive system in organic conversions.[18,19]

In this facet, nitrogen rich imidazo[1,5-*a*]pyridine and imidazolylpyridine based multidentate ligands turns to be an upright option as these ligand embedded catalyst systems are relatively rare.[20,21] Imidazo[1,5-*a*]pyridine based heterocycles have engrossed a lot of attention due to their fascinating biological,[22] photophysical[23] and medicinal properties.[22–27] This unique ligand architecture imparts specific properties to the resulting PdII) complex, making it an attractive candidate for catalytic applications.[21] Metal complexes bearing multi-substituted imidazoles have been widely employed in catalysis, biomimetic studies and as photoluminescent materials.[28–31] The effect of various groups on the imidazole rings was observed to be responsible for the catalytic activity by altering the donor capability of imidazole ring.[32]

Ravikanth and co-worker synthesized biphenyls up to 86% yield in 5 h using 5 mol% of α-formyl pyrrolyl dipyrromethene based Pd(II) complex in toluene at 90 °C.[33] Suzuki coupling catalyzed by mono and dinuclear Pd(II) complexes bearing phosphine aldehyde ligand was recently reported by Hey-Hawkins and coworker.[34] However, they used 1,1,3,3-tetramethylguanidine as base, in toluene at 100 °C for 5 h and got about 47–57 % yield which was amplified to 84% by increasing boronic acid quantity.

Other than catalytic activity, Pd(II) and Pt(II) complexes are known for significant biological applications such as anticancer agents as they interact with DNA, RNA, and proteins, disturb the tumour microenvironment that cause apoptosis.[35] Some side effects of well-known anticancer drug, cisplatin, inspired researcher to design an alternative, non-toxic and effective metallodrugs. In this regard, Pd(II) complexes have also gained specific attention due to resemblance to Pt(II) complex, along with some more advantages such as faster hydrolysis, high ligand-exchange rate, and better water solubility than Pt(II) complexes. For delivery of drugs to the targeted area, their binding with serum albumins is essential because serum albumins are the main drug transporter present in blood.[36] Bovine serum albumin (BSA) is commonly employed in binding studies due to its similarity with human serum albumin (HSA).[37] Hence, DNA and BSA binding study is an important part to investigate therapeutic effectiveness,[38] antitumour activity and pharmacological response of metallodrug.[39]

This Chapter described the synthesis and characterization of two pincer(II) and each of one binuclear PdII) and Pt(II) complexes bearing *N*-(3-(pyridin-2-yl)imidazo[1,5-*a*]pyridin-1-yl)picolinimidamide (**L1H**) along with a tri- and tetra- nuclear palladium(II) complex using 2,2',2"-(1H-imidazole-2,4,5-triyl)tripyridine (**L2H**). The Pd(II) complexes were employed as catalyst in Suzuki coupling and transfer hydrogenation reaction while all complexes were evaluated for their interaction with ct-DNA and BSA.

Also, two bioactive molecules (**3s** and **3t**) were synthesized using the Pd(II) catalyst under Suzuki condition. Their adsorption, distribution, metabolism, excretion, and toxicity (ADMET) properties were calculated and inhibition properties for human leukotriene A4 hydrolase (LTA4H) enzyme were computed using molecular docking. The conversion of leukotriene A4 into leukotriene B4 (LTB_4) by LTA_4H[40,41] has been known to cause several diseases [42–45] and thus, LTA_4H inhibitors play a great role in diminishing LTB_4 production.[46] These computational calculations not only mitigate the risk factor but also minimize the animal trials.[47-49]

2.2 Results and Discussion

2.2.1 Synthesis, characterization, and coordination chemistry of all complexes

Both **L1H** and **L2H** were synthesized by following the reported procedure.[50] Using ligand **L1H**, mononuclear palladium complexes of composition [Pd(**L1**)Cl] (**1**) and [Pd(**L1**)(PPh_3)]PF_6 (**2**) were synthesized by the 1:1 reaction with $PdCl_2$ and $Pd(PPh_3)_2Cl_2$ in acetonitrile and methanol respectively. The complex **1** got precipitated from the reaction mixture, while cationic complex **2** was precipitated by stirring with KPF_6 (Scheme 2.1).

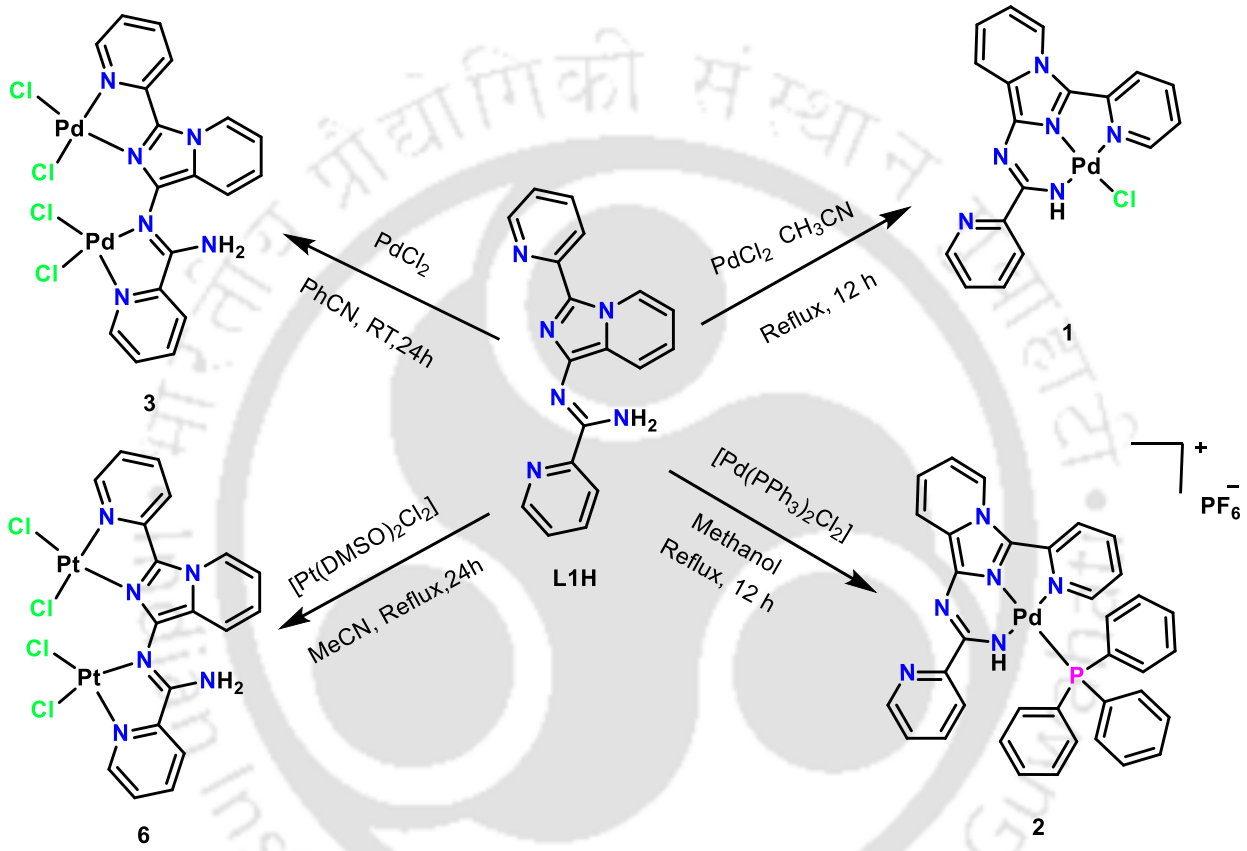

Scheme 2.1: Synthetic outline for complexes **1** – **3** and **6**.

The ^1H and ^{13}C NMR spectra of **1** and **2** matched correctly and **2** displayed a singlet at δ = 32.9 ppm in ^{31}P NMR confirmed the palladium bonded phosphorous (Figure 2.1). Two characteristic triplets at δ = 6.81 and 6.85 *ppm* in the ^1H NMR of due to imidazopyridine ring in **L1H** was observed to be shifted respectively to 7.31 and 7.20 – 7.14 as triplet and multiplet in **1** due to coordination. Similar downfield shift of signals due to these protons in ^1H NMR spectrum of **2** was also observed (Figure S2.1 and S2.2). The peaks due to [Pd(**L1**)(CH_3CN)]$^+$ and [Pd(**L1**)(PPh_3)]$^+$ ions appeared as the base peak in their mass spectra (Figure S2.5A and S2.6B). Molecular structure of **1** and **2** has been established

further by the single crystal X-ray diffraction method and crystallized in orthorhombic Pbca and monoclinic $P2_1/n$ space group respectively (Table S2.1). Ligand **L1H** has five potential N-binding sites and has been found to coordinate in anionic (**L1**$^-$) tridentate manner in **1** and **2**, spanning three coordination sites in pincer-type mode.

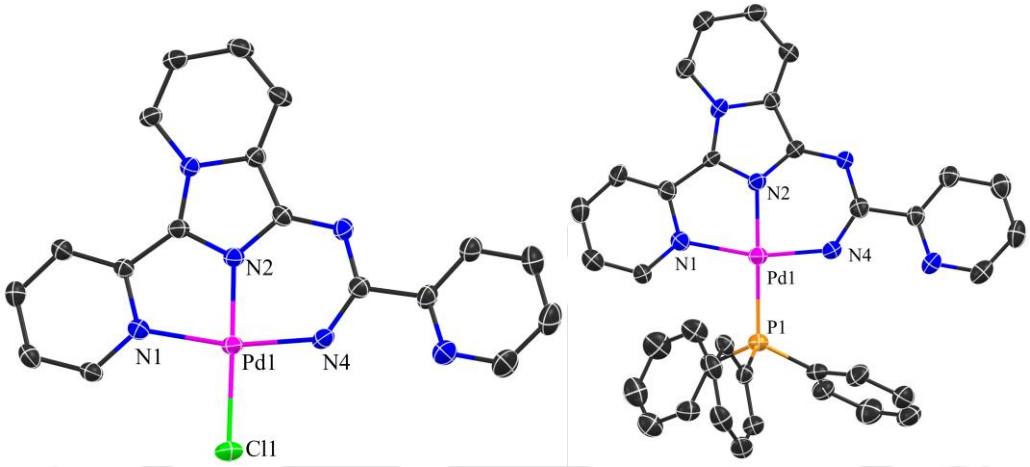

1 **2**

Figure 2.1: POV-Ray rendered ORTEP diagrams (30% probability level) of **1** and **2**. Hydrogen atoms are omitted for clarity.

The fourth site being occupied respectively by chloride ion in **1** and by PPh_3 in **2**. As a result, the whole molecule of **1** was planar in nature while **2** was non-planar due to bulky PPh_3. The imidazo[1,5-*a*]pyridine-N (N_I) lie trans to Cl and P, with the N_I–Pd bond length being shorter by ~0.028(4) Å in **1** compared to that of in **2**. The nitrogen from 2-pyridyl ring (N_P) that is attached with imidazo[1,5-*a*]pyridine nucleus lie trans to the nitrogen from –NH^- (N_A) of 2-picolinamide moiety. The five-membered chelate ring was formed by N_I–Pd–N_P and six-membered chelate ring was formed by N_I–Pd–N_A. In general, the trend in the bond length Pd-N_I < Pd-N_A < Pd-N_P has been observed in **1** and **2**. The Pd1-P1 bond length value of 2.284 (16) Å, was comparable with reported complex,[49] but shorter than Pd1–Cl1 and the Pd–N_I bond length found in **2** and was longer as that of in **1**. The palladium center in both **1** and **2** has displayed a distorted square planar geometry (Figure 2.1, Table S2.1–S2.4).

Two isostructural binuclear palladium and platinum complexes of composition [M_2(**L1H**)Cl_4] {M = Pd(II) (**3**), Pt(II) (**6**)} were obtained by altering the reaction condition

and by using stoichiometric ratio of **L1H** to metal precursor as 1:2. Orange coloured complex **3** was isolated using $PdCl_2$ in benzonitrile at room-temperature and using $PtCl_2(DMSO)_2$ in acetonitrile under reflux produced yellow powder of **6**. HRMS spectra of **3** and **6** contained base peaks corresponding to $[Pd_2(\mathbf{L1})Cl_2(CH_3CN)]^+$ and $[Pt_2(\mathbf{L1H})Cl_3(CH_3CN)]^+$ respectively (Figure S2.7A, S2.7B and S2.12). Both **3** and **6** crystallised in triclinic $P\bar{1}$ space group, contained two molecules in the asymmetric unit and the structure of one of them has been described here as the bond parameter in both units were nearly identical. The ligand **L1H** sequestered two M(II) ions and was found to exist in its neutral form with the denticity changed to a bis-bidentate fashion compared to tridentate in **1** and **2**. The Pd1/Pt1 and Pd2/Pt2 centre contained each of one five-membered chelate ring formed using N_I, N_P and nitrogen atoms from imine (N_E) and 2-picolinamide ring (N_D) in *cis* fashion (Figure 2.2).

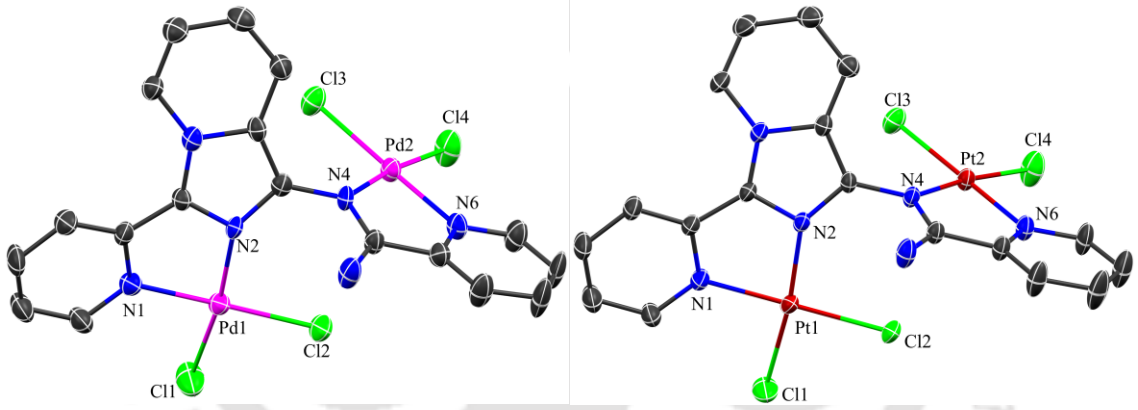

Figure 2.2: POV-Ray rendered ORTEP diagrams (30% probability level) of **3** and **6**. Hydrogen atoms are omitted for clarity.

The Pd2/Pt2 was chelated by pair of nitrogen atoms from imine (N_E) and 2-picolinamide ring (N_D), in *cis* fashion. Other two coordination sites in **3** and **6** were occupied by two chloride ligands alike cisplatin type geometry with each metal centre having a distorted square planar coordination geometry (Table S2.5–S2.8). The non-bonded intramolecular Pd···Pd and Pt···Pt distance was 4.588(1) Å and 4.696(1) Å respectively and Pd/Pt coordinated nitrogen and chloride distances in **3** and **6** (Table 2.1) were matched well with the literature values.[26]

Table 2.2: Selected bond distance (Å) in complex **3** and **6**.

	M1-N1	M1-N2	M1-Cl1	M1-Cl2	M2-N4	M2-N6	M2-Cl3	M2-Cl4
3: M=Pd	2.030(4)	2.048(4)	2.2722(15)	2.2819(14)	2.028(4)	2.031(4)	2. 2765(14)	2.2984(15)
6: M=Pt	2.027(4)	2.020(4)	2.2754(15)	2.2825(13)	2.014(4)	2.010(4)	2.2773(13)	2.2981(15)

The ligand **L2H** can be a potential tetradentate ligand in the neutral form and pentadentate in the anionic form and may lead to diverse binding modes. The reaction of **L2H** and $PdCl_2$ in 2:1 ratio at room temperature in acetonitrile, a mononuclear Pd-complex having two neutral ligand units was expected. Captivatingly, an unusual discrete trinuclear $[Pd_3(\mathbf{L2})_2(\mathbf{L2H})_2](\mathbf{L2})Cl_3$ (**4**) complex was harvested as orange colour crystals upon slow evaporation of reaction solution, in which a free $\mathbf{L2}^-$ served as the anion outside the coordination sphere (Scheme 2.2).

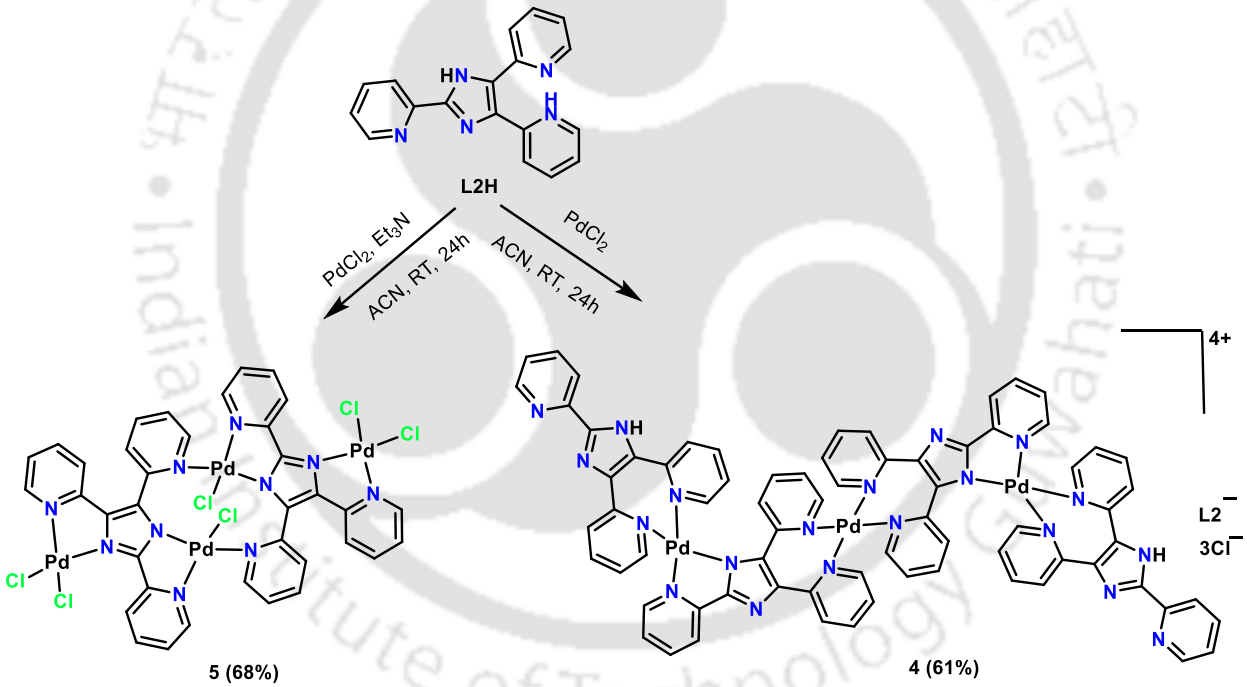

Scheme 2.2: Synthetic outline for complexes **4** and **5**.

By reversing the molar ratio of **L2H** and $PdCl_2$ to 1:2 and using few drops of triethylamine to facilitate the deprotonation, a tetranuclear complex of composition $[Pd_4(\mathbf{L2})_2Cl_6]$ (**5**) was isolated as squash coloured powder, crystals were obtained by slow evaporation of DMF solution. The complex **4** crystallized in monoclinic $P2_1/n$ while **5** in trigonal $P3_221$ space group. In complex **4** three Pd(II) ions were embedded by two equivalents each of anionic

L2^{-} and neutral **L2H**. One free uncoordinated anionic ligand along with three chloride ions were present outside the coordination sphere to balance the charge on complex cation. Coordination environment of palladium centres was quite infrequent in **4**, the anionic **L2**$^{-}$ behaved as bis-bidentate ligand bound to both central and two terminal palladium centres while neutral **L2H** coordinated in bidentate fashion bound only to the terminal Pd(II) centre.

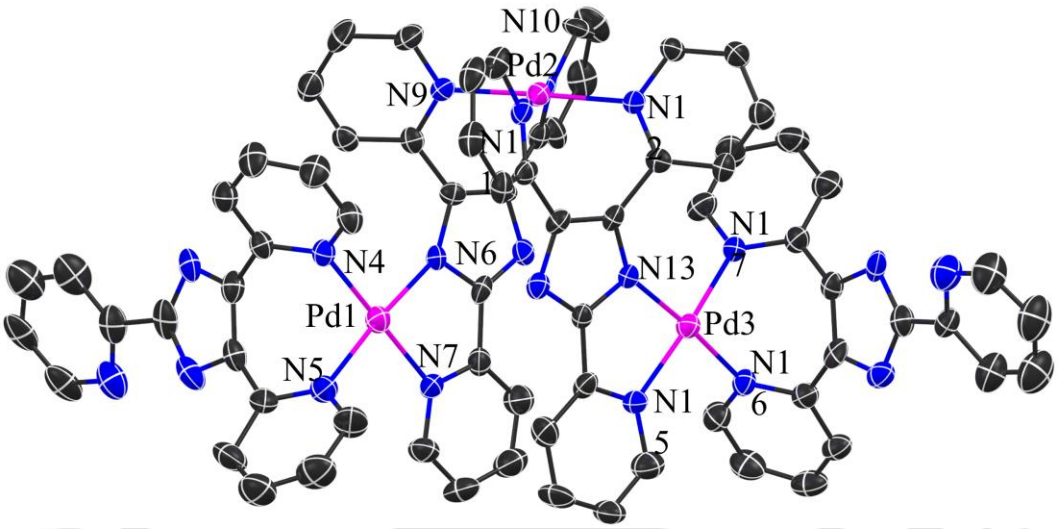

4

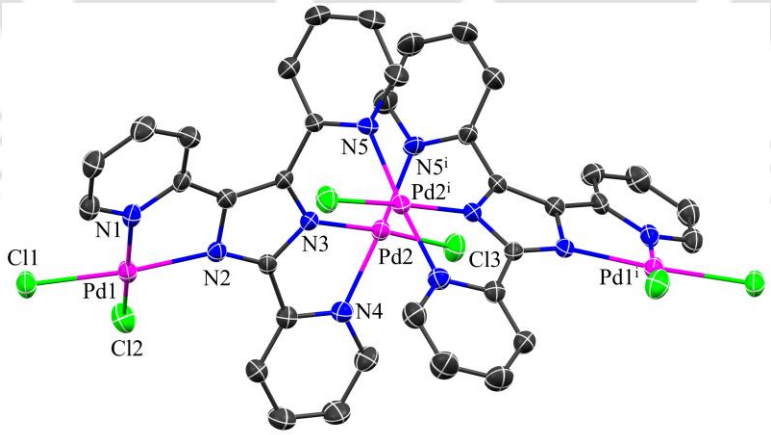

5

Figure 2.3: POV-Ray rendered ORTEP diagrams (30% probability level) of **4** and **5**. Hydrogen atoms are omitted for clarity.

Terminal Pd1 and Pd3 displayed same framework (Figure 2.3) by forming a five-membered chelate ring with imidazolate-N (N_T) and pyridine-N (N_Y) of **L2**$^-$ and a seven membered chelate ring with pyridine-N situated at 4 and 5 positions of **L2H**. These two terminal palladium units acted as a reverse folding hand, approached the central palladium Pd2 and built two seven membered chelate rings with free pyridyl nitrogen from **L2**$^-$ of Pd1 and Pd3 components and concluded the trinucleation. The chelate bites of five- and seven-membered chelate rings lie respectively in the range 80.8(3)°–81.6(3)° and 87.2(3)°–88.1(3)°. All palladium centre in **4** displayed a distorted square planar geometry (Figure S2.9 and S2.10). The presence of readily detachable strained seven membered chelate ring in **4**, make it unstable in solution as two fragments of **4** were observed along with the trinuclear entity [**4**-2Cl-**L2**$^-$]$^{3+}$ in HRMS(ESI) spectrum (Figure S2.8A–S2.10).

The asymmetric unit of complex **5** contained half of the molecule with a two-fold rotational axis passing through the center of **5**, along with a DMF molecule in the lattice. All the palladium centre in **5** possessed one 5-membered chelate ring and the two terminal Pd(II) centers had N_2Cl_2 while the central two had N_3Cl coordination environments. Among coordinated nitrogen atoms N_{PY} and N_{IM} {N_{PY} = pyridine-N; N_{IM} = imidazolate-N} were linked to the terminal Pd(II) center, while two N_{PY} and one N_{IM} were linked to the two central Pd(II) center. The non-bonded Pd1···Pd2 and Pd2···Pd2^i distances were respectively 5.974(1) and 3.836(1) Å and all the four Pd(II) centers had distorted square planar geometry around all palladium centre (Figure 2.3, Table S2.11,S2.12). The non-bonded Pd1···Pd2 distance observed in **5** was in agreement with reported dinuclear Pd(II) catalyst[50] and the Pd2···Pd2^i distance was also comparable with reported Pd(II) bifunctional catalyst.[15] The HRMS (ESI) spectrum of **5** contained peak at *m*/*z* 1198.6702 that can be assigned to the composition [Pd_4(**L2**)$_2$$(Cl)_5$]$^+$ (calcd. *m*/*z* = 1198.6767) indicated stability in solution (Figure S2.11A–S2.11C).

The electronic absorption spectrum of all complexes was recorded in DMF and the major peak values observed at λ_{max}, nm (ε, $M^{-1}cm^{-1}$) for **1**: 488 (14600), **2**: 491 (5050), **3**: 461 (5890), **4**: 324 (9090), **5**: 361 (18000), and **6**: 430 (7100) (Figure S2.14A), all may be due to MLCT. Field emission scanning electron microscope (FESEM) images were taken to understand the morphology of **1** – **6** and the smooth surface images without any pores established existence of

molecular packing in elevated order (Figure S2.14B). Significantly, all these palladium complexes crystallized without lattice water, were found to be air stable and non-hygroscopic for prolonged duration in solid state and hence they can be employed as catalysts without dehydration.

2.2.2 Assessment of Suzuki coupling catalysed by palladium complexes 1 – 5

Considering the ever-increasing need of palladium catalyst in Suzuki Miyaura cross coupling reaction, the catalytic activity of **1**–**5** was investigated. The reaction condition was optimized by varying solvents, base, and the temperature by taking phenylboronic acid and 4-bromo nitrobenzene as a model reaction (Table 2.4). From the base screening experiments, it was found that the highest yield of product was obtained in the presence of K_2CO_3 which may be due to the ability of K_2CO_3 to enhance the intramolecular trans-metalation process during catalytic cycle. Bearing in mind the effect of solvents on the Suzuki-Miyaura cross coupling reaction, in the model reaction carried out with methanol, ethanol, toluene, acetonitrile and chloroform, ethanol was found to be the finest solvent. The best yield of biphenyl was found with ethanol as solvent and potassium bicarbonate as base (Table S2.4, entry 5) using catalyst **1** at 80 °C in 4h. To check the temperature effect on catalytic activity of **1**, the model reaction was examined at various temperature and optimum temperature was found to be 80 °C and the yield declined at high temperature (120 °C) may be due to homo coupling of boronic acid. A time dependent experiment was also executed to optimize the effect time on conversion percentage (Figure 2.6b) and maximum yield was noticed in 4h. The hot filtration test was also carried out to check the homogeneity of catalyst **1** and no significant decrease in product yield indicated the homogenous nature of the catalyst. It was revealed form recycle experiment that catalyst **1**

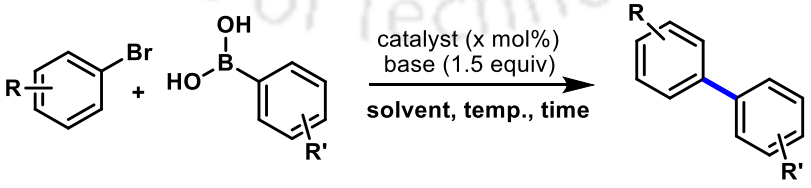

Table 2.4: Optimization table for Suzuki cross-coupling reaction

Entry	catalyst (mol%)	base	solvent	T/ °C	Time (h)	Yield (%) [a]
1	**1** (1)	KOH	EtOH	80	4	62

2	**1** (1)	K_2CO_3	Toluene	80	4	14
3	**1** (1)	K_2CO_3	CH_3CN	80	4	84.5
4	**1** (1)	K_2CO_3	$CHCl_3$	80	4	60
5	1 (1)	K_2CO_3	EtOH	80	4	98.5
6	**1** (1)	NaOH	EtOH	80	4	60
7	**1** (1)	Et_3N	EtOH	80	4	44
8	**1** (1)	^tBuOK	EtOH	80	4	58
9	**1** (1)	K_2CO_3	EtOH	RT	4	5
10	**1** (1)	K_2CO_3	EtOH	50	4	52
11	**1** (1)	K_2CO_3	EtOH	120	4	68.5
12	**2** (1)	K_2CO_3	EtOH	80	4	88
13	**3** (1)	K_2CO_3	EtOH	80	4	86
14	**4** (1)	K_2CO_3	EtOH	80	4	81
15	**5** (1)	K_2CO_3	EtOH	80	4	99
16	**5 (0.1)**	**K_2CO_3**	**EtOH**	**80**	**4**	**99**
17	**5** (0.01)	K_2CO_3	EtOH	80	4	72
18	**1** (0.1)	K_2CO_3	EtOH	80	4	64
19	**1** (0.01)	K_2CO_3	EtOH	80	4	27
20	**1** (0.1)	K_2CO_3	EtOH	80	4	82[b]
21	**1** (0.1)	K_2CO_3	EtOH	80	4	42[c]

[a] NMR yield determined by using 1,4-dimethoxybenzene as internal standard. [b]1-iodo-4-methoxybenzene and [c]4-chlorobenzaldehyde was used.

effectively produced 67% coupled product for the fifth cycle (Figure 2.6a). Evaluation of reactivity of complexes **1**–**5** under the optimized conditions uncovered a notable variance in catalytic activity. Only 1.0 mol% of **1** gave the coupled product in excellent yield, while the complex **2** and **3** resulted in a diminution of the product yield. The transformation was also affected while dropping the catalyst loading of 1.0 to 0.1 mol % with lesser yield. The important variance in catalytic productivity perceived for catalysts **1**−**5** can be credited to several aspects. In **1**, the pincer palladium is bonded with chloride which facilitate the reduction of Pd(II)

to Pd(0) while in cationic complex **2**, the PPh_3 group may hinder the reduction as well as further oxidative addition, as it may be present on Pd(0) centre during the catalytic cycle.

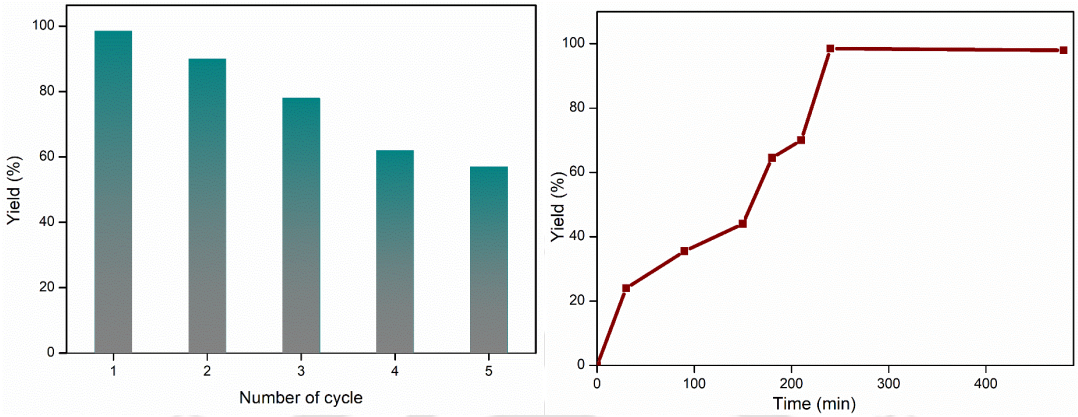

a b

Figure 2.6: (a) Reusability of palladium catalyst **1** in Suzuki coupling, (b) time dependent yield of 4-nitro-1,1'-biphenyl

The natural bonding orbital (NBO) analysis also supported this assumption as the palladium center in **1** (+0.49136) and **2** (+0.13098) displayed variation in charge led to more nucleophilic Pd center in complex **1** than **2**. In bis-palladium complex **3**, though there are two metal centres present but the catalytic activity was not excellent as that of **1** may be due to intramolecular long Pd···Pd distance which may vary due rotation about C–N bond. Though high conversion was anticipated from catalyst **4**, but a moderated yield was observed which may be attributed to the low palladium percentage in the complex and the coordination environment around Pd(II) in **4** due to involvement of seven membered chelate ring. Tetranuclear catalyst **5** produced biphenyls in excellent yield even in very less catalyst loading of 0.1 mol% and made it superior catalyst among all complexes (Table 2.4, entry 16). This exceptional high reactivity of **5** may be due to presence of four palladium centres. The Pd···Pd distance between both central palladium center in **5** was in optimal range of 3.836(1) Å, which maximize the cooperative effect, work together in concerted substrate activation, stabilize transition state, and boost the catalytic activity. With these refined Suzuki cross-coupling conditions, a diversity of substrates was evaluated to ascertain the general applicability of the process by taking various aryl halides having electron withdrawing and donating groups as well as diverse phenylboronic acids with all producing moderate to high yield.

Scheme 2.3. Substrate scope in the Suzuki coupling reaction catalyzed by **5**.

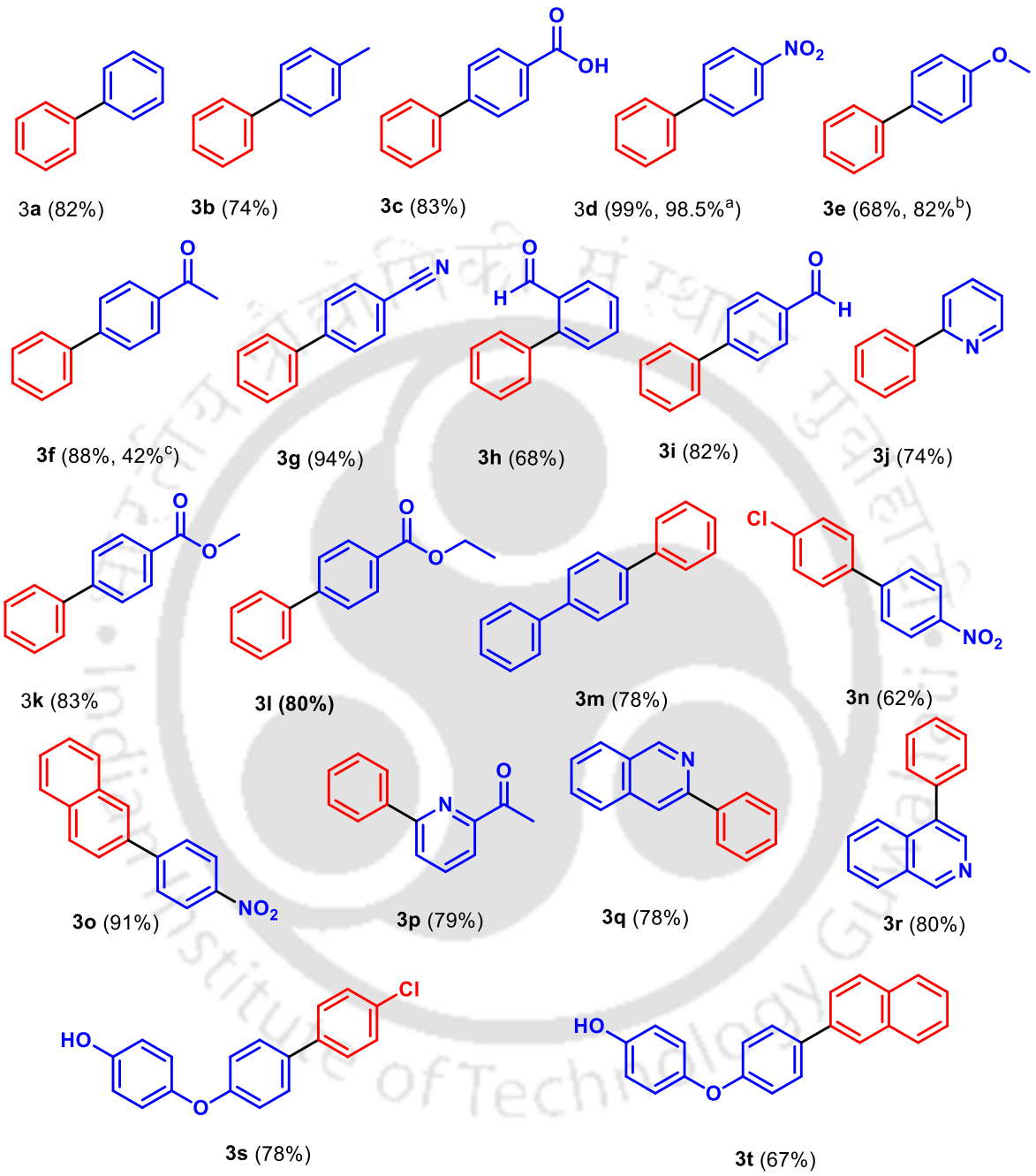

Reaction conditions: Aryl halide (1.0 mmol), Aryl boronicacid (1.2 mmol), K_2CO_3 (1.5mmol), catalyst **5** (1 mol%), ethanol (10 mL), temperature (80 °C) and time (4 h). Isolated yields. [a]NMR yield was determined by using 1,4-dimethoxybenzene as internal standard. [b]1-iodo-4-methoxybenzene was taken. [c]4-chlorobenzaldehyde was used.

The Suzuki-Miyaura cross-coupling reactions of aryl bromides containing electron-withdrawing groups (EWGs) such as -NO_2, -COOH, -COOR, -COH, and -CN with phenylboronic acid proceeded with high to excellent yields. This may be due to increased electrophilicity and ease of C–halide bond breaking during oxidative addition step. The reactions of less reactive aryl bromides containing electron-donating groups such as -Me, -OMe, -Ph also proceeded efficiently and furnished respective biphenyls in good yields. Among aryl halides, conversion was better for bromides and iodide but lesser product was obtained for chloride. The noted yields for heterocyclic bromides were also good. The HRMS(ESI) analyses of model reaction mixture in the mid of the reaction (peak observed at *m/z* 542.0578) confirmed the oxidative addition with the formation of 4-nitrophenyl bonded palladium(II) intermediate complex (IM1, Scheme 2.4). In the spectrum of reaction mixture taken after 4 h, the peak observed at *m/z* 497.0717 due to phenyl bonded palladium intermediate (Figure 2.7 and 2.8). However, no peak was observed for both phenyl and 4-nitrophenyl bonded complex (IM3, Scheme 2.4) which may be an indicative of faster reductive elimination step.

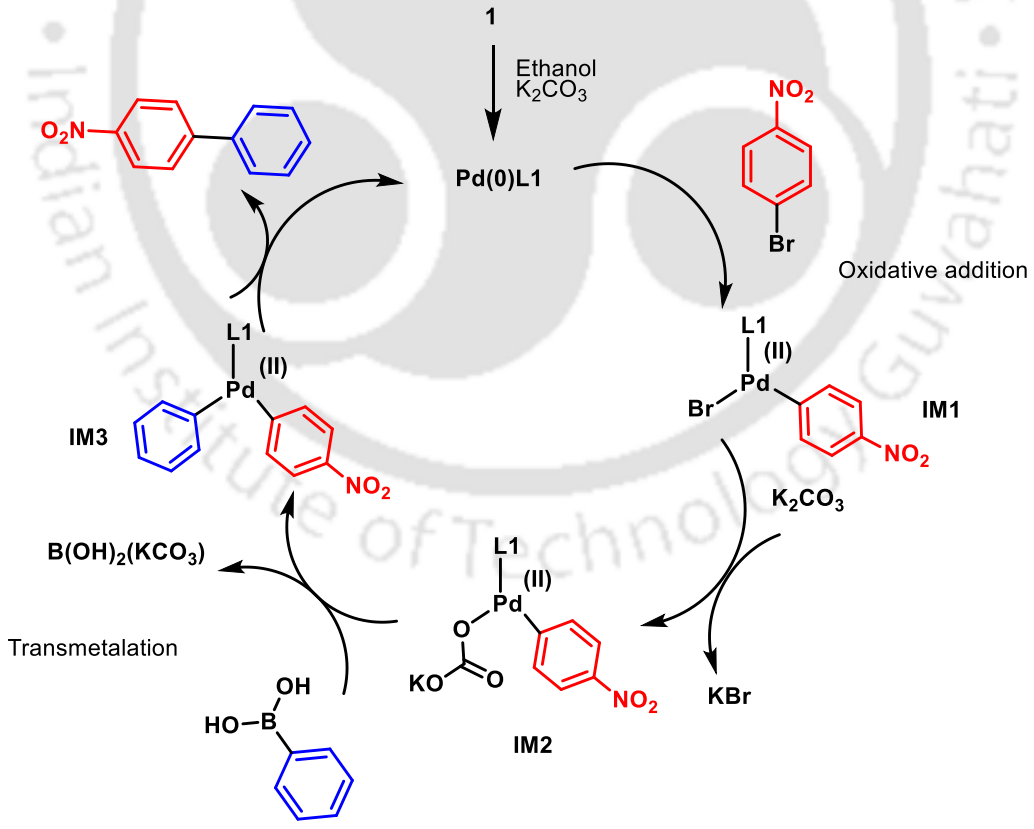

Scheme 2.4. Proposed mechanism of Suzuki-Miyaura coupling reaction for phenyl boronic acid and 4-nitrobromobenzene catalyzed by **1**.

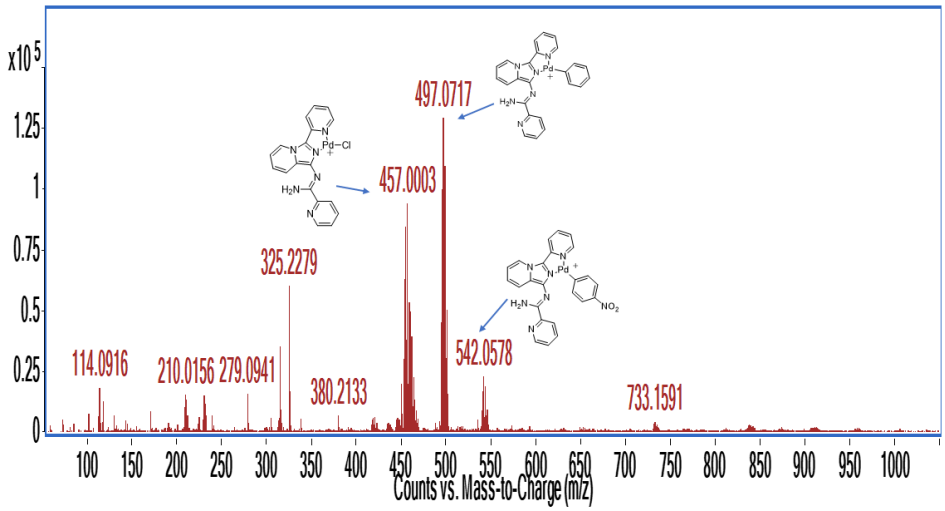

Figure 2.7: HRMS(ESI) spectra of Suzuki coupling reaction (catalyzed by **1**) mixture after 2h.

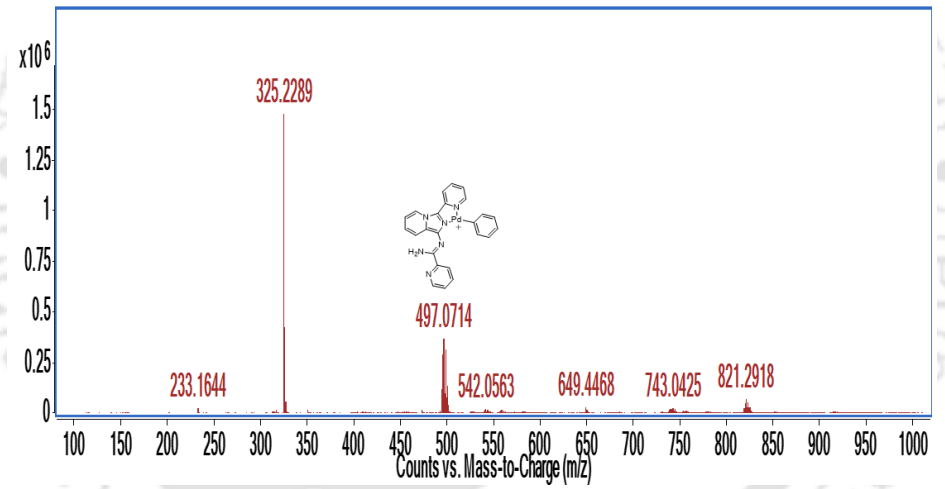

Figure 2.8: HRMS(ESI) spectra of Suzuki coupling reaction (catalyzed by **1**) mixture after 4h.

2.2.3 Assessment of transfer hydrogenation activities by palladium complexes 1 – 5

The complexes **1**−**5** were also employed for their catalytic activity in hydrogen transfer reaction for the conversion of carbonyl compounds to alcohols. The reaction conditions were optimized with the variation of several factors including temperature, base, and solvent (as the source of hydrogen). The conversion of carbonyl compound into alcohol was not established in any non-alcoholic solvents and in the absence of strong base (Table 2.5). Secondary alcohol such as ^{i}PrOH was found to be the best solvent as compared to the primary analogous and KOH was ascertained as the best base. From the time regulated

evaluation, maximum yield was noticed in 16 hours (Figure 2.9a). The conversion was also monitored at various temperature and the suitable temperature was observed to be 80 °C. Catalytic activities were also monitored with the palladium precursors $PdCl_2$ and $Pd(PPh_3)_2Cl_2$ which produced lower yield of alcohol as compared to the palladium complexes **1**–**5**. However, unlike Suzuki coupling reaction, here all the catalyst exhibited comparatively excellent yield which may be due to hydride addition to metal centre (Scheme 2.7). Here also, **5** was found as superior catalyst (entry 13, Table 2.5) as compared to **1**–**4** and efficiently produced alcohols in very low catalyst loading (0.1 mol%).

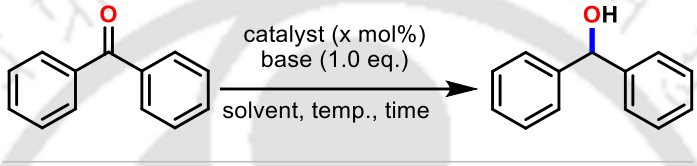

Table 2.5: Optimization data of transfer hy drogenation reaction

Entry	Catalyst (mol %)	Base	Solvent	T/ °C	Time (h)	Yield (%)[a]
1	**1** (1)	KOH	EtOH	80	16	nd
2	**1** (1)	K_2CO_3	^{i}PrOH	80	16	54
3	**1** (1)	KOH	^{i}PrOH	30	16	nd
4	1 (1)	KOH	^{i}PrOH	80	16	99
5	**1** (1)	KOH	^{i}PrOH	60	16	87
6	**1** (1)	KOH	MeOH	80	16	nd
7	**1** (1)	KOH	$PhCH_2OH$	80	16	nd
8	**1** (1)	-	iPrOH	80	16	nd
9	**2** (1)	KOH	^{i}PrOH	80	16	95
10	**3** (1)	KOH	^{i}PrOH	80	16	98
11	**4** (1)	KOH	^{i}PrOH	80	16	98
12	**5** (1)	KOH	^{i}PrOH	80	16	98
13	**5 (0.1)**	**KOH**	**^{i}PrOH**	**80**	**16**	**99**
14	**-**	Et_3N	^{i}PrOH	80	16	nd

15	**1**(0.1)	KOH	^{i}PrOH	80	16	82
16	$(PPh_3)_2PdCl_2$	KOH	^{i}PrOH	80	16	nd
17	$PdCl_2$	KOH	^{i}PrOH	80	16	16

[a] NMR yield determined by using 1,4-dimethoxybenzene as internal standard. nd= not detected

Scheme 2.5: Substrate scope in the transfer Hydrogenation reaction catalyzed by **5**.

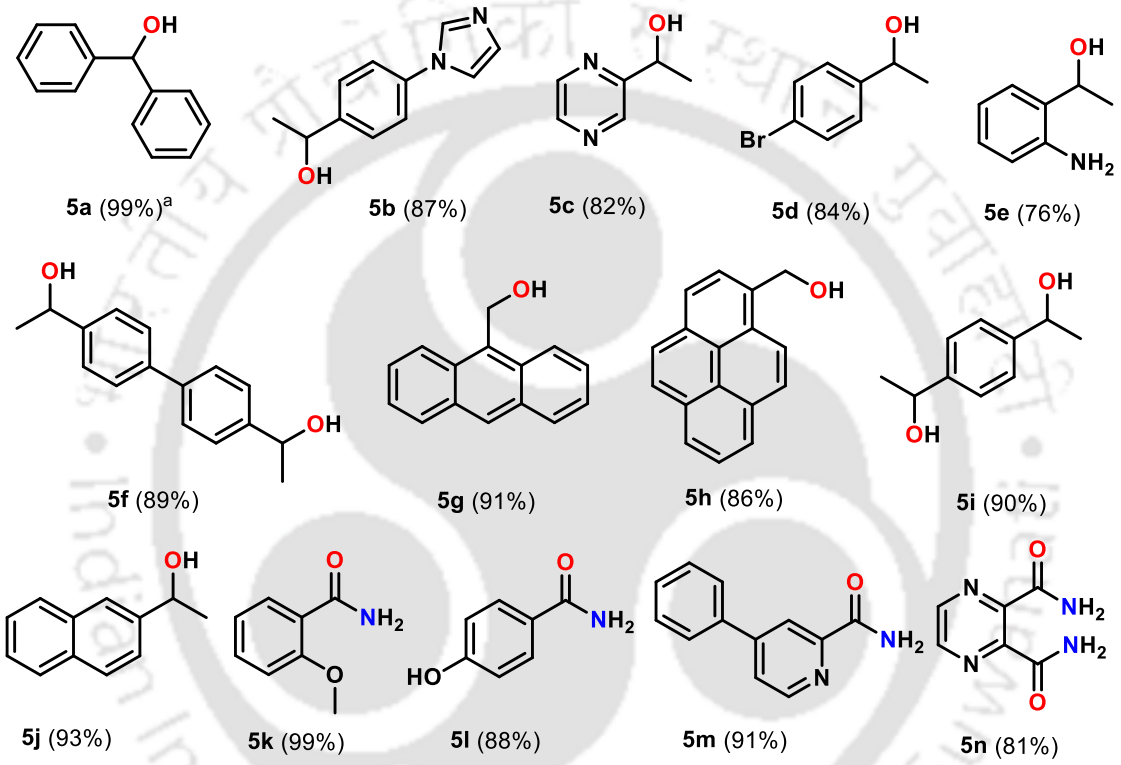

Reaction conditions: Aryl aldehydes/ketone/nitriles (1.0 mmol), KOH (1.0 mmol), catalyst **5** (0.1 mol%), ^{i}PrOH (10 mL), temperature (80 °C), time (16 h). Isolated yields. [a]NMR yield determined by using 1,4-dimethoxybenzene as internal standard.

With the optimum conditions in hand, a variety substrate of aldehydes and ketones including heterocyclic ketone were utilized to assess the hydrogen transfer activity. In case of 2- aminoacetophenone, yield was decreased which may be due to the intramolecular interaction of amino and keto group present in the molecule. It was also noticed that under the optimal conditions, only aldehyde and ketone function got reduced to alcohol but

competitive hydrodehalogenation were not observed. Attempt to prepare primary amines (-CH_2NH_2) using nitriles were failing as it produced amides in high yield.

It was noticed that after formation of 4-acetylbiphenyl, the reduction ensues to keto centre, also there was no hydrogen transfer till first one hour of the reaction. After 4-acetylbiphenyl reached a maximum yield, the transfer hydrogenation step started with a decrease of yield in 4-acetylbiphenyl (Figure 2.9b). Thus, the transfer hydrogenation process is slower than the Suzuki coupling reaction as reported in the literature.[55]

Scheme 2.6: Tandem Suzuki coupling/transfer hydrogenation process catalyzed by **1**.

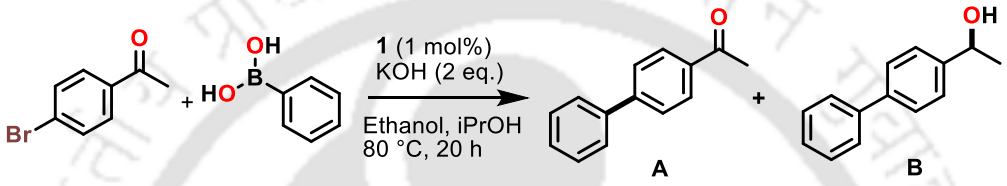

Reaction conditions: 4-bromo acetophenone (1.0 mmol), $PhB(OH)_2$ (1.0 mmol), KOH (2.0 mmol), catalyst **1** (1 mol%), ethanol + ^{i}PrOH (5+5 mL), temperature (80 °C) and time (20 h).

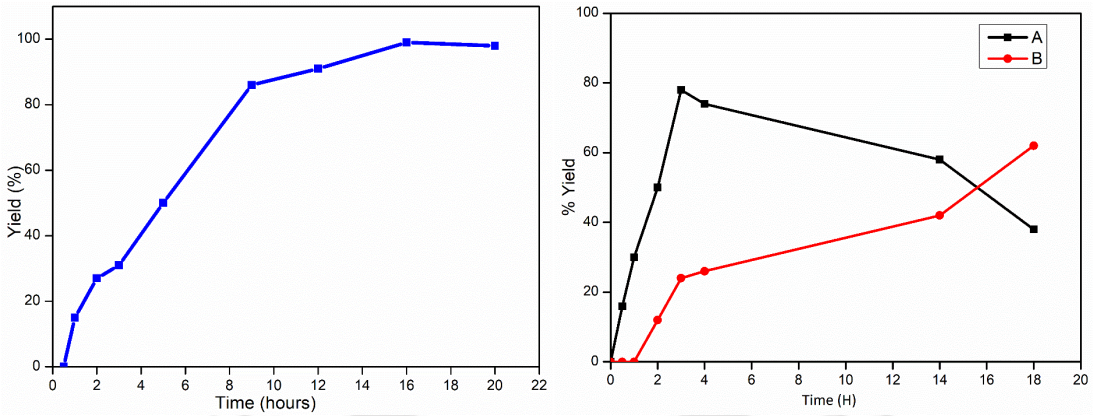

(a) (b)

Figure 2.9: (a) Time dependent yield of diphenylmethanol. (b) Time-dependent formation of 1-([1,1'-biphenyl]-4-yl)ethan-1-one (A) and 1-([1,1'-biphenyl]-4-yl)ethan-1-ol (B).

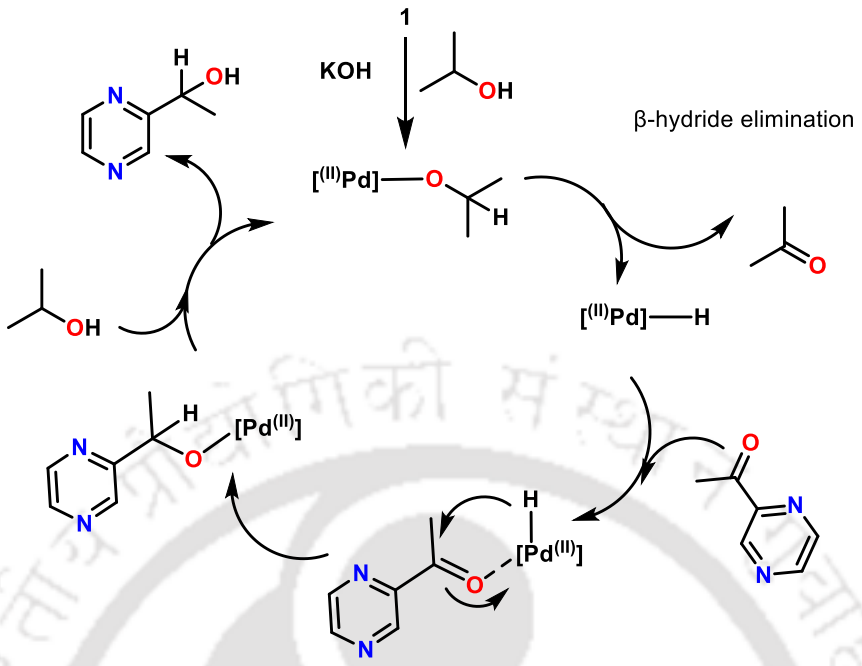

Scheme 2.7: Proposed mechanism of transfer hydrogenation reaction for **5c** catalyzed by **1**.

To explore versatility in catalytic application of these Pd(II) complexes, they were examined in a model reaction of homocoupling of phenylacetylene (Scheme 2.8). Complexes **1** – **5** produced moderate to excellent yield of 1,4-diphenylbuta-1,3-diyne using potassium carbonate in ethanol at 70 °C for 8h (Table 2.6).

Scheme 2.8: Homocoupling of phenylacetylene

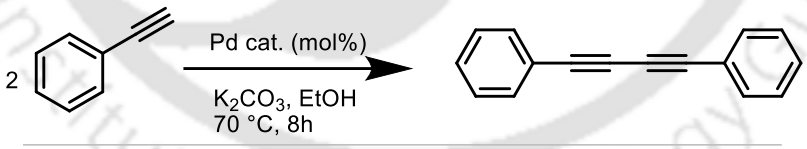

Table 2.6: Homocoupling of phenylacetylene

Complex	**1**	**2**	**3**	**4**	**5**
Catalyst mol %	1	1	1	1	1, 0.1
Yield (%)	95	90	88	77	99, 98

2.2.4 Bioactivity studies

2.2.4.1 DNA binding study

Deoxyribonucleic acid (DNA) is the prime target for most of the anticancer drugs such as metallodrug due to their binding affinity with cancer cell DNA and prevents from proliferating which lead to cell death. The binding mode may be covalent or non-covalent bonding between DNA and metal complexes. In covalent bonding, a nitrogen atom (N7) of guanine in DNA forms covalent bond with metal complex. Non-covalent binding mode may be intercalative, electrostatic, and groove binding. In intercalation, planar metal complexes insert between DNA base pair and disturb the helical structure and thus inhibits replication and transcription. Electrostatic binding is possible with cationic complex but this is weak and reversible. To know the type of binding between a metal complex and DNA, UV-Vis and fluorescence spectroscopic techniques are widely used. Hypochromism and bathochromic shift in UV titration study indicates intercalative mode of binding while hyperchromism suggests groove binding. Further, in fluorescence spectroscopy, metal complexes are used as quencher to decrease fluorescence intensity of ethidium bromide (EB)–DNA adduct as the intercalator EB fluoresces when bind to DNA.

All the complexes **1** – **6** was seen to exhibit a hypochromic shift upon gradual increase of the CT-DNA concentration confirmed the intercalative mode of binding (Figure 2.10 and S2.20). The UV spectral data were also analysed using Wolfe-Shimmer equation (Eq. 2.1) and the intrinsic binding constant (K_b) values of all complexes were calculated and listed in Table 2.7. The values were in the range of 10^4 M^{-1}, indicated high affinity of the complexes towards DNA.

$$\frac{[DNA]}{(\varepsilon_a - \varepsilon_f)} = \frac{[DNA]}{(\varepsilon_b - \varepsilon_f)} + \frac{1}{K_b(\varepsilon_b - \varepsilon_f)} \qquad \text{(Eq. 2.1)}$$

Where [DNA] is the concentration of DNA in base pairs, ε_a is the extinction coefficient for complex in presence of DNA, ε_f is the extinction coefficient for the unbound complex and ε_b is the extinction coefficient for the complex in the fully bound form. The binding constant K_b can be obtained from the plot [DNA]/($\varepsilon_a - \varepsilon_f$) versus [DNA].

Also, the Gibbs free energy (ΔG) was calculated using equation 2.2 and the binding of these complexes with DNA was seen as a spontaneous process due to the negative ΔG.

$$\Delta G = -RT \ln Kb \qquad \text{(Eq. 2.2)}$$

Table 2.7: K_b and ΔG values from UV-Vis titration of CT–DNA with all complexes individually.

Complexes	**1**	**2**	**3**	**4**	**5**	**6**
$K_b\ M^{-1}$	4.17×10^5	1.77×10^5	1.4×10^5	3.23×10^4	2.03×10^5	3.31×10^5
ΔG (Kcal mol^{-1})	-32.062	-29.939	-29.358	-25.724	-30.278	-31.49

Further, all the complexes were tested using fluorescence titration method for their DNA binding ability. The emission spectra of EB–DNA adduct with the gradual addition of each complex individually were taken. All the complexes efficiently diminished the fluorescence intensity which unveiled that these complexes are capable to displace EB from EB-DNA adduct (Figure 2.10 and S2.22). All the emission spectra were also processed using Stern−Volmer equation (eq. 2.3) and Scatchard equation (eq. 2.4) to calculate Starn−Volmer and bimolecular quenching (K_q and K_{SV}) constants using equations S3 and S4, values were listed in Table 2.8.

$$\frac{I_0}{I} = 1 + K_{SV}[Q] = 1 + K_q\tau_0[Q] \qquad \text{(Eq. 2.3)}$$

$$log(\frac{I_0 - I}{I}) = logKb + nlog[Q] \qquad \text{(Eq. 2.4)}$$

where I_0 and I represent the fluorescence intensities in absence and presence of the quencher 'Q' (here Q is complexes **1**–**6**) respectively. [Q] is the quencher concentration, and K_{SV} denotes the Stern– Volmer quenching constant calculated from the plot of I_0/I *vs* [Q]. K_q is the biomolecular quenching constant and τ_0 is the mean lifetime of the fluorophore = 23 ns. The binding constant K_b is the intercept of log (I_0 - I)/I *vs* log [Q] plot. The number of binding sites per nucleotide is n.

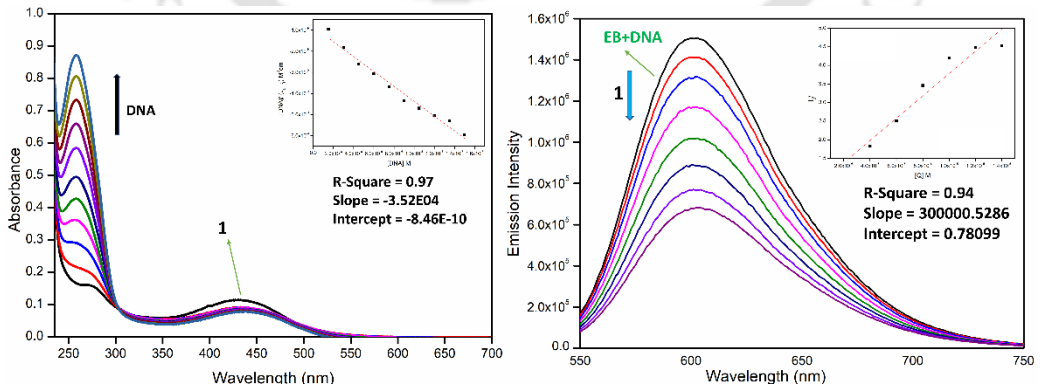

(a) (b)

Figure 2.10: (a) Absorption spectra of **1** upon gradual addition of CT-DNA. (b) Emission spectra of EB-DNA adduct with incremental addition of complex **1**.

The K_q values (~10^{12}) were greater than that of the scattering collision quenching constant (2×10^{10}) for the biopolymer, suggesting that a static quenching process is present. Quenching constant order was **1** > **2** > **4** > **5** > **6** > **3**. Complex **1** displayed very high K_{SV} values (3.0×10^5 M^{-1}) may be due to the planar structure which enhances the intercalating property. Thus, the high K_{SV} values indicated that the complexes can displace EB from the EB–DNA adduct.

Table 2.8: K_{SV}, K_q, K_b, and n values from EB–DNA titration with **1–6** individually.

complexes	$K_{SV} \times 10^4$ M^{-1}	$K_q \times 10^{12}$ M^{-1} s^{-1}	K_b M^{-1}	ΔG (kJ mol^{-1})	n
1	9.77	4.25	3.71×10^7	-43.182	1.55
2	8.89	3.86	8.44×10^7	-45.218	1.23574
3	1.31	0.57	1.15×10^4	-23.166	0.99403
4	2.29	1	2.67×10^3	-19.548	0.80156
5	1.47	0.64	7.4×10^4	-27.778	1.16226
6	1.37	0.6	5.97×10^2	-15.836	0.71183

2.2.4.2 BSA Binding Study:

Serum albumins (SA) are basically used to study the interaction of drugs or metal complexes due to their importance in the transportation of ions and drugs to cells and tissues through the bloodstream. Thus, the binding affinities of metallodrugs towards albumin is very crucial. One of the extensively studied albumins is bovine serum albumin (BSA) due to its high structural similarity with human serum album (HSA). BSA has two tryptophan, Trp-134 and Trp-213 present in the IA and IIA subdomains respectively as there are three α-helical domains I, II, III and each domain is further subdivided into A and B present in BSA. The intrinsic fluorescence nature of BSA is primarily due to the tryptophan alone though it contains three fluorophores, tryptophan, tyrosine, and phenylalanine. This is due to that phenyl alanine has a very low quantum yield and the fluorescence of tyrosine is almost totally quenched when close to tryptophan residue or amino group, carbonyl group or ionized. After the addition of some bioactive molecule, the fluorescence intensity of the of BSA decreases due to interactions on a certain fluorophore. Various kinds of molecular interactions such as molecular excitation, rearrangements, energy transfer, ground-state

complex formation, and collision quenching are responsible to reduce the fluorescence intensity.

Here, different types of fluorescence spectroscopic techniques such as emission, synchronous, and steady-state anisotropy studies were implemented to study the binding of these complexes with BSA**.**

Emission Study.

Gradually addition of studied complexes individually into a BSA solution in HEPES buffer, a linear quenching in fluorescence intensity was observed (figure 2.11 and S2.25) which may be due to the structural modification in the protein. All the emission spectra were processed using equation 2.3 and 2.4 to calculate K_{SV}, K_q, K_b, and n (Table 2.9). It was observed that the binding affinity follows the order: **5** > **4** > **6** > **1** > **3** > **2**. This trend can be explained based on polycentric, planarity and type of metal.

The calculated K_q values of these complexes were in the range of 4.3 – 15.8 × 10^{12} M^{-1} s^{-1} which are > 200 times higher than the scatter collision quenching constant (2.0 × 10^{10} M^{-1} s^{-1}) values known for various quenchers with biomolecules. Thus, it can be concluded that these complexes induced a static quenching mechanism during the interactions with BSA. Comparable K_b values (~10^3 – 10^5 M^{-1}) were observed like reported Pd/Pt complexes in the literature.[56] The binding constants were also not very high to foil the release of the complex upon being delivered to the intended cells. The number of binding sites (n) was close to 1, indicating the single binding site present in BSA for each complex.

Table 2.9: K_{SV}, K_q, K_b, and n values of BSA for all complexes individually.

complexes	K_{SV} × 10^4 M^{-1}	K_q × 10^{12} M^{-1} s^{-1}	K_b M^{-1}	n
1	12.31	5.25	6.3×10^3	0.75099
2	9.90	4.3	4.7 ×10^3	0.74387
3	11.22	4.87	6.38 ×10^4	0.95412
4	26.69	11.6	2.88 ×10^4	0.82011
5	36.33	15.79	7.54 ×10^5	1.0641
6	14.37	6.2	1.7 ×10^4	0.83034

Synchronous Fluorescence Experiment

The synchronous fluorescence study was performed to investigate the conformational changes around the tryptophan (Trp) and tyrosine (Tyr) residues of the BSA microenvironment. To monitor the interactions in tryptophan and tyrosine residues of BSA, the monochromators of excitation and emission were kept at constant wavelength interval of $\Delta\lambda = 60$ and 15 nm respectively. All the complexes (0–1.5 μM) were titrated individually with a fixed concentration of BSA (1.5 μM) in both offsets and displayed a significant decline in fluorescence intensity along with a red shift for tryptophan residue at $\Delta\lambda = 60$ nm while only complexes **1**, **3** and **4** exhibited decreases in fluorescence intensity at tyrosine environment (Figure 2.11 and S2.28). Thus, it is confirmed that all the complexes interacted strongly with tryptophan residue of BSA while complex **1** and **3** moderately interact with tyrosine and complex **4** strongly decrease the intensity by binding with tyrosine in the microenvironment. Further all the synchronous spectra were analysed to calculate K_{SV}, K_q, K_b, and n (Table 2.10).

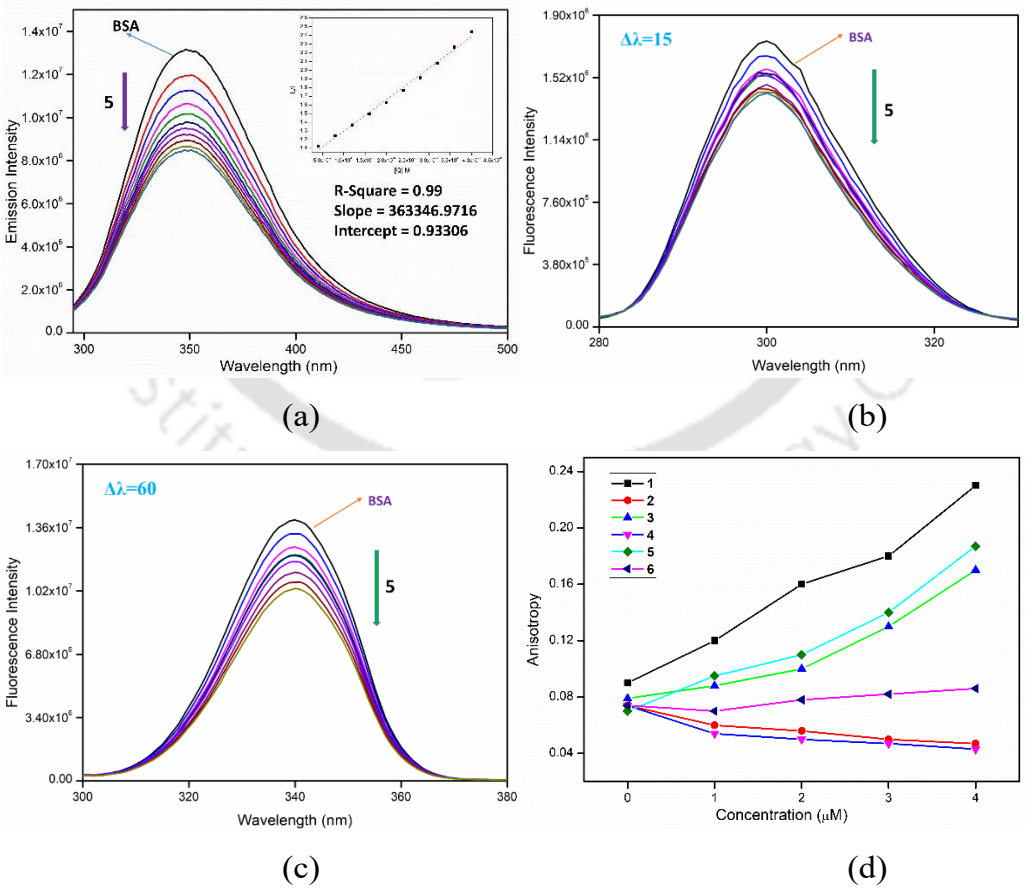

Figure 2.11: (a) Emission spectra of BSA upon gradual addition of **5**. Synchronous fluorescence spectra of BSA in presence **5** at (b) $\Delta\lambda = 5$ and (c) $\Delta\lambda = 60$ nm. (d) Fluorescence anisotropy of BSA in presence of complexes **1** – **6**.

Table 2.10: K_{SV}, K_q, K_b, and n values of BSA (synchronous fluorescence data) for all complexes individually.

Complexes	Δλ (nm)	K_{SV} (M^{-1})	$K_q \times 10^{12}$ M^{-1} s^{-1}	K_b (M^{-1})	n
1	15	5.88×10^4	2.56	3.64×10^1	0.37434
	60	1.18×10^5	5.16	4.63×10^2	0.54023
2	15	2.46×10^4	1.07	9.27×10^0	0.3222
	60	4.59×10^4	1.99	9.18×10^3	0.74737
3	15	1.02×10^5	4.44	2.01×10^4	0.86172
	60	1.71×10^5	7.4	3.51×10^5	1.0572
4	15	2.81×10^5	12.26	2.33×10^6	1.17507
	60	2.89×10^5	12.59	1.60×10^6	1.1441
5	15	5.17×10^4	2.25	3.56×10^3	0.77643
	60	9.74×10^4	4.24	2.25×10^4	0.89174
6	15	5.37×10^4	2.34	1.02×10^3	0.68072
	60	1.16×10^5	5.06	3.82×10^4	0.91286

Steady-state fluorescence anisotropy

In the absence and presence of **1**–**6**, the fluorescence anisotropy of BSA was recorded to investigate the interaction of complexes with BSA. This technique tracks the alteration in the rotational diffusion or Brownian motion of the molecule present in solution. The infusion of the metal complexes into the albumin solution produces a BSA-complex adduct leading to more rigid structure or make any structural modification of the protein backbone which slows down the overall rotational motion, as a result, anisotropy value increases. Sometimes if the molecule increase flexibility of BSA skeleton due to partial unfolding, then internal motion of the protein increases and thus anisotropy decreases. The anisotropy (r) values of BSA with different studied complex were recorded and plotted as anisotropy *vs* concentration (Figure 2.11d) by using the following equation (Eq. 2.4).

$$r = (I_{VV} - GI_{VH})/(I_{VV} + 2GI_{VH}) \quad \text{(Eq. 2.4)}$$

$$G = I_{VH}/I_{HH}$$

Where G is the instrumental grating factor, I_{VV} and I_{VH} denotes the intensities obtained with the excitation polarizer in the vertical position and the emission polarizer in both the horizontal and vertical positions, respectively.

The result revealed that all complexes effectively altered the BSA microenvironment and confirmed the binding with BSA. However, it was also seen that cationic complexes **2** and **6** diminished the net anisotropy value while all other neutral complexes effectively increased the BSA anisotropy.

2.2.5 Bioactivity of compound 3s and 3t

Two new compounds **3s** {4-((4'-chloro-[1,1'-biphenyl]-4-yl)oxy)phenol} and **3t** {4-(4-(naphthalen-2-yl)phenoxy)phenol} obtained for the first time from Suzuki coupling using **5** as catalyst, can be potential inhibitor for Leukotriene A_4 Hydrolase (LTA_4H) since their phenyl analogue (4-(4-(phen-4-yl)phenoxy)phenol)[57] was reported to exhibit inhibition. So, ADMET properties of **3s** and **3t** were calculated and *in silico* molecular docking study were carried out with as LTA_4H (PDB id-5fwq) to evaluate their inhibition properties. From the calculated results, the physicochemical values, lipophilicity, drug-likeness,[58] and medicinal chemistry properties of both **3s** and **3t** were found to be compatible with drug development. To check the similarities in properties of existing drugs, a drug-likeness test of **3s** and **3t** was calculated for all five filters (Lipinski, Muegge, Ghose, Veber, and Egan). However, **3s** had one Lipinski and Muegge violation, and **3t** also had one violation of each Lipinski, Muegge, Ghose, and Egan. The bioavailability score was 55% for both **3s** and **3t** and they were not against the biological assays in the Pan-assay interference compounds (PAINS), and Brenk filter. The pharmacokinetic properties of both molecules were compared with the known LTA_4H inhibitor SC-22716[59] and commercially available drug bestatin[60]. The GI (gastrointestinal) absorption rate of **3s** and **3t** was 94.42% and 93.08%, which is specified as appropriate for human intestinal absorption while it was only 37.07 % for bestatin. The blood-brain barrier (BBB) values of **3s** and **3t** were less than 1 (LogBB < 1), and thus, these are not dispersed to the brain.[61] As cytochrome P450 (CYP450) isomers are one of the significant drug-metabolizing enzymes, both molecules were subjected to

various CYP450 enzyme substrates/inhibitors and produced better results than SC-22716 and were comparable to bestatin.[62] Also, **3s** and **3t** tested negative in Ames test[63] and **3t** was found to be non-carcinogenic in 2 years carcinogenicity bioassay in mouse and rat while **3s** produced a positive result for mouse carcinogenicity. Molecules **3s** and **3t** were also assessed for more toxicity using ProTox-II[64] and both molecules were observed as non-toxic in most of the targets and found to be active in only two out of eighteen tests. Thus, from ADMET properties, the compounds **3s** and **3t** were found to be appropriate for most of the pharmacokinetic properties. All the calculated data are given in Table S2.13– 2.18 in Appendix I.

After ADMET assessment, all the compounds were run in Autodock 4.2.6 to predict their efficacy as the human Leukotriene A_4 hydrolase inhibitor. High binding free energy was found for **3s** and **3t** as compared to that of SC-22716 and bestatin. Both **3s** and **3t** displayed various nonbonding interaction (Table S2.19) with active side amino acid residues of the receptor to form a stable ligand-protein complex.

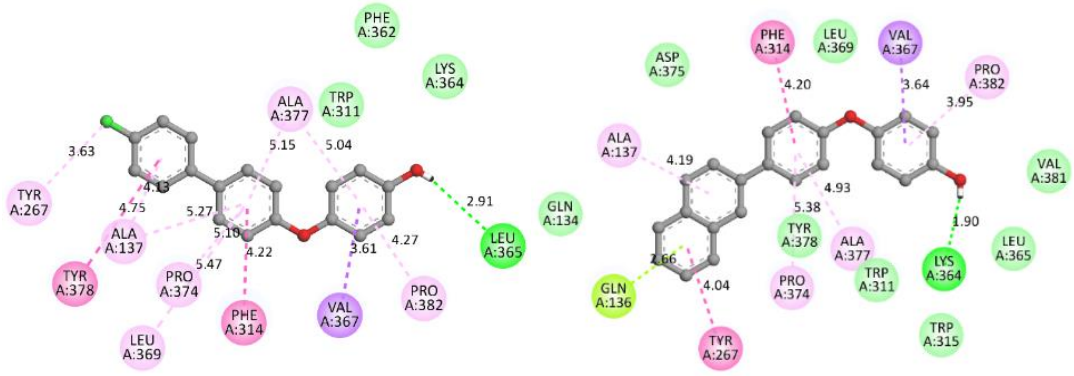

(a) (b)

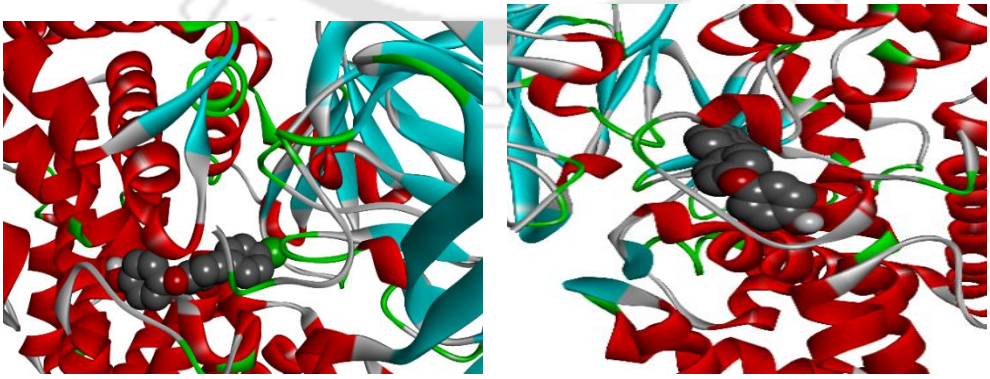

(c) (d)

Figure 2.12: 2D Interactions and 3D docking pose view of **3s** (a, c) and **3t** (b, d) with LTA4H (PDB ID: 5fwq).

The binding free energy of **3s** and **3t** was −12.73 kcal/mol and −12.42 kcal/mol respectively which was higher than that of SC-22716 (−10.45kcal/ mol) and bestatin (−7.32 kcal/mol) (Table 2.11). Many hydrophobic and a hydrogen bonding interaction were observed for **3s** and **3t** with active side residues of human Leukotriene A_4 hydrolase (Figure 2.12).

Table 2.11: Molecular docking energy of all molecules.

	Free Energy of Binding (kcal/mol)	Inhibition Constant (K_i)	Internal energy [a] (U) kcal/mol
3s	-12.42	783.56 pM	-9.26
3t	-12.73	463.17 pM	-9.45
SC-22716	-10.45	21.75 nM	-6.81
Bestatin	-7.32	4.28 µM	-4.90

[a] T= 298.15 K. pM = picomolar, nM = nanomolar, µM = micromolar.

2.3 Conclusions

In summary, we tale the design and characterization some pincer mono-, di- and poly-nuclear Pd(II) complexes bearing imidazo[1,5-*a*]pyridine and imidazolyl-pyridine ligands along with a cisplatin like dinuclear Pt(II) complexes bearing imidazo[1,5-*a*]pyridine ligands which showed resilience to both moisture and air. The Pd(II) complexes were proved as versatile and potent catalysts in Suzuki cross-coupling, transfer hydrogenation reaction, and alkyne homocoupling under environmentally apposite conditions. It has been observed that the denticity of **L1H** was found to be bis-bidentate or tridentate coordinated through nitrogen atoms by controlled stoichiometric ratio and reaction conditions. The exceptional coordination mode with formation of a seven membered chelate was observed in trinuclear Pd(II) complex of **L2H** and a tetranuclear complex was synthesized by reversing the molar ratio of ligand and $PdCl_2$. Based on X-ray diffraction study and spectroscopic results, the geometry around palladium center was observed to be distorted square planar. The binding mode of ligand and the co-ligand were found to be very crucial in their catalytic activity. The tridentate pincer palladium complex **1** was recognized as a better catalyst bearing imidazo[1,5-*a*]pyridine moiety while the tetranuclear palladium

complex of imidazolyl-pyridine ligand **L2H** was found as superior catalyst among all the catalyst. Notably, from the HRMS(ESI) analysis of Suzuki Miyaura cross coupling reaction mixture, intermediate (IM1) was identified. The interaction of all Pd(II) and Pt(II) complexes with calf thymus DNA were examined wherein all displayed intercalative mode of binding. Also complexes **1** – **6** showed high binding affinity with bovine serum albumin (BSA). From comprehensive ADMET calculations and molecular docking study, both **3s** and **3t** may act as potent LTA_4H inhibitors and thus paves the way for further experimental investigations as an effective anti-inflammatory candidate. The versatile reactivity of these palladium catalysts may unbolt more trails for the organic transformations and the biomolecule interaction properties instigate further investigations for *in vitro* anticancer activities.

2.4 Experimental Section

2.4.1 Synthesis of Ligands

The ligands **L1H** {N-(3-(pyridin-2-yl)imidazo[1,5-a]pyridin-1-yl)picolinimidamide} and **L2H** {2,2',2"-(1H-imidazole-2,4,5-triyl)tripyridine} were synthesized by following a previously reported procedure. For this, 2-picolylamine (0.976 g, 0.009 mol) and 2-cyanopyridine 1.880 g, 0.018 mol) were heated at 100 °C in an oil bath for 12 h. The resultant red gummy oil was suspended in 25 mL of water, and KOH (1.00 g, 0.18 mmol) was added with mechanical stirring for the next 12 h. The yellow solid obtained was filtered, washed with water, and dried in vacuum over fused $CaCl_2$. The dry solid was subjected to column chromatography using silica gel (60-120 mesh) with ethyl acetate–hexane (1:9) as eluent and the yellow fibrous solid of pure **L1H** ($C_{18}H_{14}N_6$) was obtained after removal of the solvent. Then, the filtrate was neutralized with 1N HCl to produce precipitate, which was filtered, dried, and recrystallized from dichloromethane to produce ligand **L2H** **(**$C_{18}H_{13}N_5$). All the spectroscopic data were in good agreement with the reported values.

2.4.2 Synthesis of complexes

[Pd(**L1**)Cl] (**1**):

Solid $PdCl_2$ (35.46 mg, 0.2 mmol) was refluxed (~2 h) in acetonitrile (10 mL) until all palladium chloride dissolved. To this hot solution, **L1H** (62.8 mg, 0.2 mmol) dissolved in acetonitrile (10 mL) was added dropwise and the resultant brownish orange solution was refluxed with continuous stirring for 12 h. It was allowed to cool to room temperature and precipitates were separated by

filtration, washed with diethyl ether, and dried in vacuum to yield pure **1**. Dark brown crystals suitable for X-ray crystallography were obtained by slow vapor diffusion of tetrahydrofuran into a concentrated solution of **1** in DMSO for several months. Yield: 74.6 mg, 82%. Anal. calcd for $C_{18}H_{13}N_6PdCl$: C 47.49, H 2.88, N 18.46; found: C 47.58, H 2.91, N 18.24. ATR-IR (neat, cm^{-1}) 3318, 1666, 1474, 1262, 1147, 996, 672, 542, 433. ^{1}H NMR (600 MHz, DMSO-d_6) δ 9.03 (d, J = 6.9 Hz, 1H), 8.77 (d, J = 4.3 Hz, 1H), 8.67 (d, J = 4.1 Hz, 1H), 8.61 (d, J = 7.8 Hz, 1H), 8.43 (s, 1H), 8.39 (d, J = 8.2 Hz, 1H), 8.18 (t, J = 7.7 Hz, 2H), 7.94 (s, CH, DMF), 7.97 (t, J = 7.0 Hz, 1H), 7.55 – 7.51 (m, 1H), 7.46 – 7.41 (m, 1H), 7.31 (t, J = 6.5 Hz, 1H), 7.20 – 7.14 (m, 1H), 2.88 (s, CH_3, DMF), 2.72 (s, CH_3, DMF), 2.06 (CH_3CN). ^{13}C NMR (151 MHz, DMSO-d_6) δ 149.9, 148.3, 148.4 144.1, 138.8, 137.4, 124.7, 124.3, 123.8, 121.4, 120.9, 119.5, 119.3, 119.2. HRMS(ESI) *m/z* calcd. for [Pd(**L1**)(CH_3CN)]$^+$: 460.0502, found 460.0505.

[Pd(**L1**)(PPh_3)]PF_6 (**2**):

To a hot methanolic solution of [Pd(PPh_3)$_2Cl_2$] (87.7 mg, 0.125 mmol), **L1H** (39.3 mg, 0.125 mmol) dissolved in methanol (10 mL) was added dropwise followed by few drops of triethylamine. Resultant dark red solution was heated at reflux for 12 h, cooled to room temperature and KPF_6 (23 mg, 0.125) was added and stirred. After few minutes, precipitates of **2** deposited were filtered and washed well with cold ethanol and diethyl ether. Methanol solution of **2** on slow evaporation produced deep red crystals suitable for X-ray crystallographic analysis. Yield: 73.4 mg, 71%. Anal. calcd for $C_{36}H_{28}N_6P_2F_6Pd$: C 52.22, H 3.53, N 10.15; found: C 52.37, H 3.48, N 10.08. ATR-IR (neat, cm^{-1}) 3275, 1519, 1476, 1295, 1147, 836, 751, 685, 556.5, 429. ^{1}H NMR (600 MHz, DMSO-d6) δ 9.22 (d, J = 7.1 Hz, 1H), 8.55 (dd, J = 13.6, 8.2 Hz, 2H), 8.37 (d, J = 8.9 Hz, 1H), 8.22 (d, J = 4.5 Hz, 1H), 8.17 (t, J = 7.9 Hz, 1H), 7.90 (dd, J = 11.9, 7.7 Hz, 6H), 7.87 – 7.82 (m, 1H), 7.79 (t, J = 7.4 Hz, 3H), 7.67 (dt, J = 7.9, 4.0 Hz, 6H), 7.64 (d, J = 5.8 Hz, 1H), 7.51 (t, J = 6.9 Hz, 1H), 7.43 (d, J = 10.9 Hz, 1H), 7.41 – 7.34 (m, 2H), 7.09 (t, J = 6.6 Hz, 1H), 5.72 (s, -CH_2, dichloromethane), 4.45 (t, J = 5.0 Hz, -OH ethanol), 4.20 (d, J = 5.2 Hz, -OH methanol), 3.42 (-CH_2 ethanol, merged with broad H_2O peak), 3.16 (d, J = 5.0 Hz, -CH_3 methanol), 1.05 (t, J = 7.0 Hz, -CH3 ethanol). ^{13}C NMR (151 MHz, DMSO-d_6) δ 151.8, 151.7, 147.7, 145.7, 139.7, 137.3, 134.7, 134.6, 132.8, 132.4, 130.1, 126.8, 126.0, 125.7, 124.9, 124.3, 122.1, 121.7, 121.3, 120.5, 120.3, 120.0, 56.2 (-CH3 ethanol), 54.9 (-CH_2, dichloromethane), 48.7 (-CH_3 methanol), 18.63 (-CH_2 ethanol). ^{31}P NMR (243 MHz, DMSO-d_6) δ 32.90, -144.22 (hept, J = 711.3 Hz, PF_6). HRMS(ESI) *m/z* calcd. for [Pd(**L1**)(PPh_3)]$^+$: 681.1148, found 681.1176.

$[Pd_2Cl_4(\mathbf{L1H})]$ (**3**):

Solid $PdCl_2$ (35.4 mg, 0.2 mmol) was heated (~1 h) in benzonitrile (10 mL) until all palladium chloride got dissolved. Solid **L1**H (31.4 mg, 0.1 mmol) was added to this solution at room temperature and stirred for 24 h. The precipitates of **3** deposited were separated by filtration, washed with diethyl ether, and dried in vacuum. Yellowish brown crystals suitable for X-ray crystallography were obtained by slow evaporation of DMF solution of **3** for several weeks. NMR spectra of the complex were not recorded due to poor solubility in common deuterated solvents. Yield: 48.0 mg, 72%. Anal. calcd for $C_{18}H_{14}Cl_4N_6Pd_2$: C 32.32, H 2.11, N 12.56; found: C 32.48, H 2.17, N 12.48. ATR-IR (neat, cm^{-1}) 3314. 1640, 1567, 1132, 1244, 1150, 681, 503, 424. HRMS(ESI) *m/z* calcd. for $[Pd_2(\mathbf{L1})Cl_2(CH_3CN)]^+$: 637.8918, found 637.8916.

$[Pd_3(\mathbf{L2})_2(\mathbf{L2H})_2](\mathbf{L2})Cl_3$ (**4**):

Solid $PdCl_2$ (35.4 mg, 0.2 mmol) was heated in acetonitrile (10 mL) till a clear solution was obtained and cooled to room temperature. To this solution, **L2H** (119.7 mg, 0.4 mmol) dissolved in acetonitrile (10 mL) was added and the resultant tangerine color solution was stirred for 12h at ambient temperature. Solvent was evaporated to ~2 mL, diethyl ether was added and formed solid was washed with diethyl ether, dried in vacuo. Dark orange crystals suitable for X-ray crystallography were obtained by slow evaporation of reaction solution. Yield: 78.2 mg, 61%. Anal. calcd for $C_{90}H_{62}Cl_3N_{25}Pd_3$: C 56.32, H 3.26, N 18.25; found: C 56.74, H 3.23, N 18.21. ATR-IR (neat, cm^{-1}) 3356, 1593, 1518, 1482,1155, 780, 744. ^{1}H NMR (600 MHz, DMSO-d_6) δ 8.91 (d, J = 4.1 Hz, 2H), 8.70 (d, J = 4.4 Hz, 1H), 8.49 (d, J = 7.7 Hz, 2H), 8.21 (d, J = 7.9 Hz, 1H), 8.17 (t, J = 7.3 Hz, 2H), 7.99 (t, J = 8.3 Hz, 1H), 7.65 – 7.60 (m, 2H), 7.53 – 7.48 (m, 1H). ^{13}C NMR (151 MHz, DMSO-d_6) δ 149.4, 147.4, 147.3, 140.5, 137.7, 127.0, 125.0, 124.6, 123.9, 123.2, 121.0. HRMS(ESI) *m/z* calcd. for $[Pd_3(\mathbf{L2})_2(\mathbf{L2H})_2Cl]^{3+}$: 516.3780, found 516.3751.

$[Pd_4(\mathbf{L2})_2Cl_6](\mathbf{5})$:

Solid $PdCl_2$ (35.4 mg, 0.2 mmol) was heated in acetonitrile (10 mL) till a clear solution was obtained and cooled to room temperature. To this solution, **L2H** (30.0 mg, 0.1 mmol) dissolved in acetonitrile (10 mL) was added followed by few drops of triethylamine and the resultant apricot color solution was stirred for 24 h at ambient temperature. Solvent was evaporated to ~5 mL and formed solid was filtered, washed with diethyl ether, dried in vacuo. Amber colored crystals suitable for X-ray crystallography were obtained by slow evaporation of **5** in DMF. Yield: 42.0

mg, 68%. Anal. calcd for $C_{36}H_{24}Cl_6N_{10}Pd_4$: C 35.01, H 1.96, N 11.34; found: C 35.12, H 2.01, N 11.23. ATR-IR (neat, cm^{-1}) 1603, 1485, 1454, 1256, 1157, 993, 778, 744, 891, 545, 425. ^{1}H NMR (600 MHz, DMSO-d_6) δ 9.00 (d, J = 5.4 Hz, 1H), 8.89 – 8.83 (m, 2H), 8.50 (d, J = 5.5 Hz, 1H), 8.11 (t, J = 7.5 Hz, 1H), 7.97 (d, J = 4.3 Hz, 2H), 7.94 (s, DMF), 7.88 (t, J = 7.9 Hz, 1H), 7.46 (t, J = 6.6 Hz, 1H), 7.40 (t, J = 6.8 Hz, 1H), 7.34 (d, J = 4.9 Hz, 1H), 6.88 – 6.83 (m, 1H), 2.88 (s, DMF), 2.73 (s, DMF). ^{13}C NMR (151 MHz, DMSO-d_6) δ 162.5(DMF), δ 155.58, 155.34, 151.91, 150.89, 149.93, 149.57, 148.18, 141.05, 140.18, 139.90, 137.53, 129.54, 129.25, 126.95, 126.74, 125.61, 123.87, 121.42, 35.89(DMF), 30.88(DMF). HRMS(ESI) *m/z* calcd. for $[Pd_4(\mathbf{L2})2Cl_5]^+$: 1198.6767, found 1198.6702.

$[Pt_2Cl_4(\mathbf{L1H})]$ (**6**):

Ligand **L1H** (31.4 mg, 0.1 mmol) and $PtCl_2(DMSO)_2$ (84.45 mg, 0.2 mmol) was taken in 10 mL acetonitrile solution and stirred for 12 h at reflux condition. The golden yellow precipitates of **6** were collected by filtration, washed with diethyl ether, and dried under vacuum. Golden yellow crystals suitable for X-ray crystallography were obtained by slow evaporation of **6** in DMF for few weeks. Yield: 60.0 mg, 71%. Anal. calcd for $C_{18}H_{14}Cl_4N_6Pt_2$: C 25.55, H 1.67, N 9.93; found: C 25.72, H 1.70, N 9.78. ATR-IR (neat, cm^{-1}) 3281. 1605, 1488, 1241, 1147, 748, 668, 428. HRMS(ESI) *m/z* calcd. for $[Pt_2(\mathbf{L1H})Cl_3(CH_3CN)]^+$: 851.9875, found 851.9992.

2.4.3 Crystallographic data

For the single crystal XRD data collection of the appropriate single crystals of complex **1**, **2** and **4**; a single source Super Nova CCD System from Agilent Technologies equipped with a fine focus 1.75 kW sealed tube with Mo-Kα radiation was used at room temperature. The data were reduced using CrysAlisPro and Autochem2.1 software. For complex **3**, **5**, and **6**, data was collected at room temperature using a Bruker D8 QUEST instrument equipped with SMART APEX CCD diffractometer with fine focus 1.75 kW sealed tube of Mo-Kα (λ = 0.71073 Å) X-ray source, with increasing ω (width of 0.3° per frame) at a scan speed of 3s–5s per frame. The SMART software was used for data acquisition and the SAINT software for data extraction. The structure solution and refinement were performed in APEX4 and Olex2-1.5 using the SHELXT, SHELXL programs.[65] All atoms except hydrogen atoms are tuned using anisotropic displacement parameters, whereas hydrogen atoms are tuned using relative isotropic parameters. Solvent molecules in **1**, **3** and **4** were SQUEEZED by solvent masking and disordered atoms were modeled

in olex2-1.5. PLATON was used for structure validation.[66] Mercury and ORTEP software were used to create a pictorial depiction linked to X-ray single crystal data.

2.4.4 Optimization of Suzuki cross coupling reaction

1-bromo-4-nitrobenzene (0.5 mmol), phenylboronic acid (0.6 mmol), 1,4-dimethoxybenzene (0.5 mmol) (internal standard), base (0.75 mmol), and catalyst (x mol%) were mixed in solvent (10 mL) and was stirred at specified temperature for a given time. After the completion of the reaction, the mixture was cooled, filtered through a short pad of celite, and washed with ethyl acetate. Further, water was added and the reaction mixture was extracted with ethyl acetate and dried over Na_2SO_4. The solvent was removed under reduced pressure, and the crude product was analyzed by using ^{1}H NMR spectroscopy to calculate the NMR yield.

2.4.5 Time dependent study

1-bromo-4-nitrobenzene (1.0 mmol), phenylboronic acid (1.2 mmol), 1,4-dimethoxybenzene (1.0 mmol) (internal standard), K_2CO_3 (1.5 mmol), and catalyst **1** (1 mol%) were taken in ethanol (20 mL) at 80 °C. Aliquots were taken at different time interval (0, 30, 90, 150, 210, 240, and 480 minutes), diluted with ethylacetate and filtered. After removing the volatiles, crude product was analyzed by ^{1}H NMR to calculate the yield.

2.4.6 General procedure for the Suzuki–Miyaura cross-coupling reaction

A mixture of aryl halide (0.5 mmol), aryl boronic acid (0.6 mmol), potassium carbonate (1.5 mmol), and catalyst **5** (0.1 mol%) in ethanol solution (10 mL) was stirred at 80 °C for 4 hours. After the completion of the reaction, the mixture was cooled, filtered through a short pad of celite, and washed with ethyl acetate. Further, water was added and the reaction mixture was extracted with ethyl acetate and dried over Na_2SO_4. The solvent was removed under reduced pressure and the residue was purified by preparative thin layer chromatography using ethyl acetate/hexane as the eluent to give the corresponding biphenyl products.

2.4.7 Characterization data for Suzuki coupling products 3a-3t

1,1'-biphenyl (3a)[67]

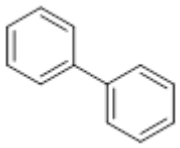

^{1}H NMR (400 MHz, Chloroform-*d*) δ 7.65 (d, *J* = 6.8 Hz, 4H), 7.49 (t, *J* = 6.8 Hz, 4H), 7.39 (t, *J* = 7.2 Hz, 2H).^{13}C NMR (125.78 MHz, Chloroform-*d*) δ 141.6, 129.1, 127.6, 127.5.

4-methyl-1,1'-biphenyl (3b)[68]

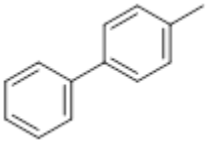

^{1}H NMR (400 MHz, Chloroform-*d*) δ 7.57 (d, *J* = 7.2 Hz, 2H), 7.49 (d, *J* = 8.0 Hz, 2H), 7.42 (t, *J* = 7.6 Hz, 2H), 7.31 (t, *J* = 7.3 Hz, 1H), 7.26 – 7.23 (m, 2H), 2.39 (s, 3H). ^{13}C NMR (125.78 MHz, Chloroform-*d*) δ 141.3, 138.5, 137.1, 129.6, 128.8, 127.1 (d, *J* = 2.6 Hz), 21.2.

[1,1'-biphenyl]-4-carboxylic acid (3c)[69]

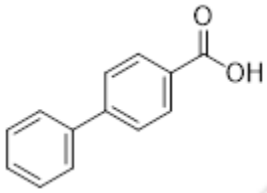

^{1}H NMR (400 MHz, Chloroform-*d*) δ 8.19 (d, *J* = 8.4 Hz, 2H), 7.71 (d, *J* = 8.4 Hz, 2H), 7.67 – 7.63 (m, 2H), 7.48 (t, *J* = 7.4 Hz, 2H), 7.41 (t, *J* = 6.8 Hz, 1H). ^{13}C NMR (125.78 MHz, Chloroform-*d*) δ 171.3, 146.6, 140.0, 130.9, 129.1, 128.4, 128.1, 127.4, 127.3.

4-nitro-1,1'-biphenyl (3d)[67]

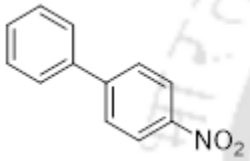

^{1}H NMR (400 MHz, Chloroform-*d*) δ 8.30 (d, *J* = 8.8 Hz, 2H), 7.74 (d, *J* = 8.8 Hz, 2H), 7.63 (d, *J* = 7.0 Hz, 2H), 7.53 – 7.44 (m, 3H). ^{13}C NMR (125.78 MHz, Chloroform-*d*) δ 147.7, 147.2, 138.9, 129.3, 129.0, 127.9, 127.5, 124.2.

4-methoxy-1,1'-biphenyl (3e)[68]

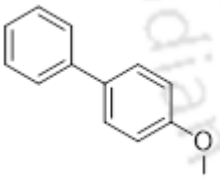

^{1}H NMR (400 MHz, Chloroform-*d*) δ 7.58 – 7.51 (m, 4H), 7.42 (t, *J* = 7.7 Hz, 2H), 7.31 (t, *J* = 7.4 Hz, 1H), 6.99 (d, *J* = 8.7 Hz, 2H), 3.86 (s, 3H). ^{13}C NMR (125.78 MHz, Chloroform-*d*) δ 159.3, 140.9, 133.9, 128.8, 128.3, 126.8, 126.7, 114.3, 55.4.

1-([1,1'-biphenyl]-4-yl)ethan-1-one (3f)[68]

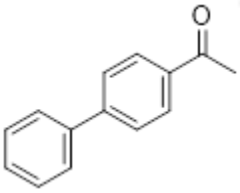

^{1}H NMR (400 MHz, Chloroform-*d*) δ 8.04 (d, *J* = 8.5 Hz, 2H), 7.69 (d, *J* = 8.5 Hz, 2H), 7.63 (d, *J* = 7.1 Hz, 2H), 7.47 (t, *J* = 7.4 Hz, 2H), 7.40 (t, *J* = 7.3 Hz, 1H), 2.64 (s, 3H). ^{13}C NMR (125.78 MHz, Chloroform-*d*) δ 197.9, 145.9, 140.0, 136.0, 129.0, 129.0, 128.3, 127.4, 127.3, 26.7.

[1,1'-biphenyl]-4-carbonitrile(3g)[68]

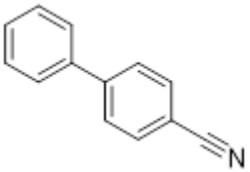

^{1}H NMR (400 MHz, Chloroform-*d*) δ 7.75 – 7.67 (m, 4H), 7.60 (d, *J* = 8.8 Hz, 2H), 7.49 (t, *J* = 7.6 Hz, 2H), 7.43 (t, *J* = 7.3 Hz, 1H). ^{13}C NMR (125.78 MHz, Chloroform-*d*) δ 145.8, 139.3, 132.7, 129.2, 128.8, 127.8, 127.3, 119.0, 111.0.

[1,1'-biphenyl]-2-carbaldehyde (3h)[70]

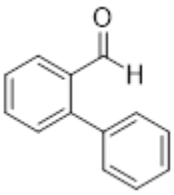

^{1}H NMR (400 MHz, Chloroform-*d*) δ 9.96 (s, 1H), 8.01 (d, *J* = 8.7 Hz, 1H), 7.59 (td, *J* = 7.5, 1.3 Hz, 1H), 7.43 (dt, *J* = 14.7, 7.5 Hz, 5H), 7.34 (dd, *J* = 7.6, 1.7 Hz, 2H). ^{13}C NMR (125.78 MHz, Chloroform-*d*) δ 192.4, 146.0, 137.7, 133.7, 133.6, 130.8, 130.1, 128.4, 128.1, 127.8, 127.6.

[1,1'-biphenyl]-4-carbaldehyde (3i)[68]

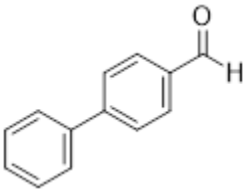

^{1}H NMR (400 MHz, Chloroform-*d*) δ 10.06 (s, 1H), 7.96 (d, *J* = 8.3 Hz, 2H), 7.76 (d, *J* = 8.2 Hz, 2H), 7.64 (d, *J* = 7.1 Hz, 2H), 7.49 (t, *J* = 7.4 Hz, 2H), 7.42 (t, *J* = 7.3 Hz, 1H). ^{13}C NMR (125.78 MHz, Chloroform-*d*) δ 192.1, 147.3, 139.8, 135.3, 130.4, 129.1, 128.6, 127.8, 127.5.

2-phenylpyridine (3j)[71]

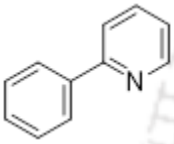

^{1}H NMR (400 MHz, Chloroform-*d*) δ 8.70 (d, *J* = 4.9 Hz, 1H), 8.00 (d, *J* = 7.1 Hz, 2H), 7.74 (dd, *J* = 6.3, 1.5 Hz, 2H), 7.48 (t, *J* = 7.3 Hz, 2H), 7.42 (t, *J* = 7.3 Hz, 1H), 7.23 (ddd, *J* = 6.8, 4.9, 2.2 Hz, 1H). ^{13}C NMR (125.78 MHz, Chloroform-*d*) δ 157.5, 149.6, 139.4, 136.7, 128.9, 128.7, 126.9, 122.1, 120.6.

Methyl [1,1'-biphenyl]-4-carboxylate(3k)[72]

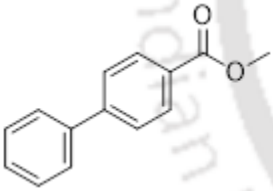

^{1}H NMR (400 MHz, Chloroform-d) δ 8.14 – 8.10 (m, 2H), 7.69 – 7.61 (m, 4H), 7.50 – 7.44 (m, 2H), 7.43 – 7.37 (m, 1H), 3.95 (s, 3H). ^{13}C NMR (125.78 MHz, Chloroform-d) δ 167.1, 145.7, 140.1, 130.2, 129.0, 128.2, 127.1, 52.2.

Ethyl [1,1'-biphenyl]-4-carboxylate(3l)[73]

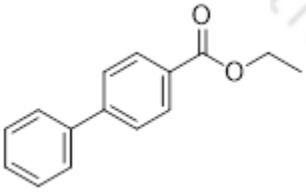

^{1}H NMR (400 MHz, Chloroform-d) δ 8.13 (d, J = 8.4 Hz, 2H), 7.65 (dd, J = 14.0, 7.9 Hz, 4H), 7.47 (t, J = 7.4 Hz, 2H), 7.40 (t, J = 7.3 Hz, 1H), 4.41 (q, J = 7.1 Hz, 2H), 1.43 (t, J = 7.1 Hz, 3H). ^{13}C NMR (125.78 MHz, Chloroform-d) δ 166.6, 145.6, 140.1, 130.1, 129.3, 129.0, 128.2, 127.3, 127.1, 61.0, 14.4.

1,1':4',1''-terphenyl (3m)[74]

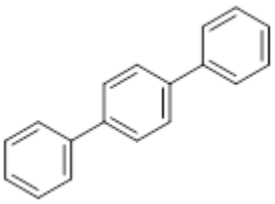

^{1}H NMR (400 MHz, Chloroform-*d*) δ 7.68 (s, 4H), 7.65 (d, *J* = 7.1 Hz, 4H), 7.46 (t, *J* = 7.6 Hz, 4H), 7.36 (t, *J* = 7.4 Hz, 2H). ^{13}C NMR (125.78 MHz, Chloroform-*d*) δ 140.8, 140.2, 128.9, 127.6, 127.4, 127.2.

4-chloro-4'-nitro-1,1'-biphenyl (3n)[75]

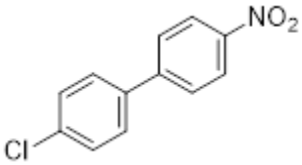

^{1}H NMR (400 MHz, Chloroform-*d*) δ 8.30 (d, *J* = 8.8 Hz, 2H), 7.71 (d, *J* = 8.9 Hz, 2H), 7.56 (d, *J* = 8.6 Hz, 2H), 7.47 (d, *J* = 8.6 Hz, 2H). ^{13}C NMR (125.78 MHz, Chloroform-*d*) δ 147.4, 146.4, 137.3, 135.4, 129.1, 128.7, 127.8, 124.3.

2-(4-nitrophenyl)naphthalene (3o)[76]

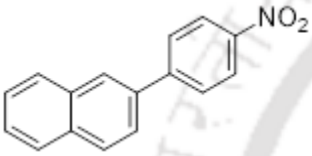

^{1}H NMR (400 MHz, Chloroform-*d*) δ 8.35 (d, *J* = 8.8 Hz, 2H), 8.10 (s, 1H), 7.99 – 7.86 (m, 5H), 7.75 (dd, *J* = 8.5, 1.8 Hz, 1H), 7.58 – 7.53 (m, 2H). ^{13}C NMR (125.78 MHz, Chloroform-*d*) δ 147.6, 147.1, 136.0, 133.4, 133.2, 129.0, 128.4, 128.0, 127.7, 126.9, 126.8, 124.9, 124.2.

1-(6-phenylpyridin-2-yl)ethan-1-one (3p)[77]

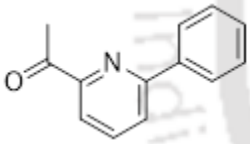

^{1}H NMR (400 MHz, Chloroform-*d*) δ 8.10 (d, *J* = 7.0 Hz, 2H), 7.96 (dd, *J* = 7.3, 1.3 Hz, 1H), 7.87 (dt, *J* = 15.2, 7.2 Hz, 2H), 7.50 (d, *J* = 7.5 Hz, 2H), 7.48 – 7.43 (m, 1H), 2.82 (s, 3H). ^{13}C NMR (125.78 MHz, Chloroform-*d*) δ 200.5, 156.4, 153.4, 138.4, 137.6, 129.5, 128.9, 126.9, 123.4, 119.8, 25.7.

3-phenylisoquinoline (3q)[78]

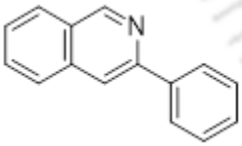

^{1}H NMR (400 MHz, Chloroform-*d*) δ 9.19 (d, *J* = 2.2 Hz, 1H), 8.27 (d, *J* = 1.7 Hz, 1H), 8.15 (d, *J* = 8.5 Hz, 1H), 7.85 (d, *J* = 8.1 Hz, 1H), 7.70 (d, *J* = 8.2 Hz, 3H), 7.59 – 7.48 (m, 3H), 7.42 (t, *J* = 7.4 Hz, 1H). ^{13}C NMR (125.78 MHz, Chloroform-*d*) δ 149.9, 147.3, 137.8, 133.8, 133.2, 129.43 129.2, 129.2, 128.1, 128.0, 127.4, 127.0.

4-phenylisoquinoline (3r)[79]

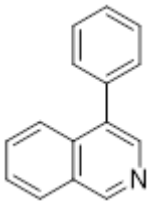

^{1}H NMR (400 MHz, Chloroform-*d*) δ 9.25 (s, 1H), 8.49 (s, 1H), 8.02 (d, *J* = 8.2 Hz, 1H), 7.91 (d, *J* = 8.3 Hz, 1H), 7.66 – 7.59 (m, 2H), 7.53 – 7.45 (m, 5H). ^{13}C NMR (125.78 MHz, Chloroform-*d*) δ 152.0, 142.8, 137.0, 134.2, 133.3, 130.5, 130.1, 128.6, 128.4, 127.9, 127.9, 127.2, 124.8.

4-((4'-chloro-[1,1'-biphenyl]-4-yl)oxy)phenol (3s)

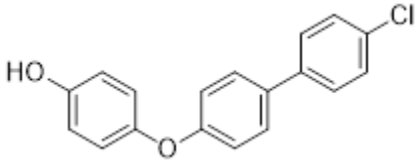

ATR-IR (neat, cm^{-1}) 3193, 2956, 2921, 1603, 1509, 1480, 1245, 1102, 817,490. ^{1}H NMR (400 MHz, Chloroform-*d*) δ 7.47 (dd, *J* = 8.7, 2.0 Hz, 4H), 7.38 (d, *J* = 8.5 Hz, 2H), 6.98 (dd, *J* = 12.5, 8.8 Hz, 4H), 6.84 (d, *J* = 8.9 Hz, 2H), 4.85 (s, 1H). ^{13}C NMR (125.78 MHz, Chloroform-*d*) δ 158.50, 152.14, 150.12, 139.21, 134.41, 133.14, 129.04, 128.33, 128.21, 121.31, 117.97, 116.55. HRMS (ESI) *m/z* calculated for [C_{18}H13ClO2–H]$^-$: 295.0531, found: 295.0530.

4-(4-(naphthalen-2-yl)phenoxy)phenol (3t)

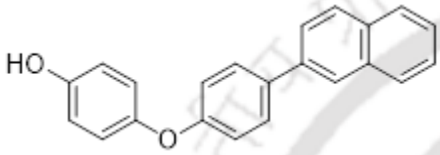

ATR-IR (neat, cm^{-1}) 3195, 2958, 2923, 1604, 1508, 1245, 1101, 818, 740, 475. ^{1}H NMR (400 MHz, Chloroform-*d*) δ 7.99 (s, 1H), 7.88 (q, *J* = 8.6 Hz, 3H), 7.71 (dd, *J* = 8.5, 1.8 Hz, 1H), 7.68 – 7.63 (m, 2H), 7.52 – 7.44 (m, 2H), 7.08 – 7.03 (m, 2H), 7.02 – 6.96 (m, 2H), 4.87 (s, 1H). ^{13}C NMR (125.78 MHz, Chloroform-*d*) δ 158.30, 152.06, 150.30, 138.08, 135.60, 133.86, 132.58, 128.74, 128.56, 128.24, 127.78, 126.45, 125.95, 125.56, 125.45, 121.25, 118.06, 116.54. HRMS (ESI) *m/z* calculated for [$C_{22}H_{16}O_2$+H]$^+$: 313.1224, found: 313.1210.

2.4.8 Optimization of transfer hydrogenation reaction

Benzophenone (1.0 mmol), base (1.0 mmol), catalyst (x mol%), and 1,4-dimethoxybenzene (1.0 mmol) (internal standard) were mixed in solvent (10 mL) and were stirred at a specified temperature for a given time. After the completion of reaction, the mixture was cooled, filtered through a short pad of celite, washed with ethyl acetate. The solvent was removed under reduced pressure, and the crude product was analyzed using ^{1}H NMR spectroscopy to calculate the NMR yield.

2.4.9 Time dependent study

To investigate the effect of time on formation of alcohol, we carried out a time dependent study. For this, benzophenone (1.0 mmol), KOH (1.0 mmol), catalyst **1** (1 mol%), and 1,4-dimethoxybenzene (1.0 mmol) (internal standard) were taken in isopropanol (20 mL) and was stirred at 80 °C. Aliquots were taken at different time interval (0.5, 1, 2, 3, 5, 9, 20, and 24 hours), diluted with ethylacetate, and filtered. After removing the solvents, ^{1}H NMR spectrum was analyzed to calculate the percent yield of diphenylmethanol.

2.4.10 General procedures of transfer Hydrogenation reaction.

A mixture of aryl ketone or aldehyde (1.0 mmol), potassium hydroxide (1.0 mmol), and catalyst **5** (0.1 mol%) in isopropanol (10 mL) was stirred at 80 °C for 16 hours. After the completion of the reaction, the mixture was filtered through a short pad of celite and washed with ethyl acetate. Further, water was added and the reaction mixture was extracted with ethyl acetate and dried over Na_2SO_4. The solvent was removed under reduced pressure and the residue was purified by preparative thin layer chromatography using ethyl acetate/hexane as the eluent to give the corresponding alcohol products.

2.4.11 Specific procedures and characterization data for Transfer Hydrogenation products (5a-5n)

diphenylmethanol (5a)[80]

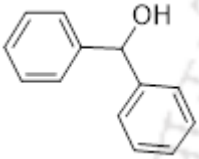

^{1}H NMR (400 MHz, Chloroform-*d*) δ 7.38 – 7.22 (m, 10H), 5.79 (s, 1H), 2.36 (s, 1H). ^{13}C NMR (125.78 MHz, Chloroform-*d*) δ 143.9, 128.5, 127.6, 126.6, 76.3.

1-(4-(1H-imidazol-1-yl)phenyl)ethan-1-ol (5b)[81]

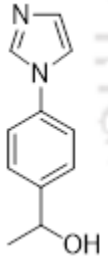

^{1}H NMR (400 MHz, Chloroform-*d*) δ 7.74 (s, 1H), 7.49 (d, *J* = 8.3 Hz, 2H), 7.33 (d, *J* = 8.4 Hz, 2H), 7.24 (s, 1H), 7.15 (s, 1H), 4.96 (q, *J* = 6.4 Hz, 1H), 2.83 (s, 1H), 1.52 (d, *J* = 6.5 Hz, 3H). ^{13}C NMR (125.78 MHz, Chloroform-*d*) δ 146.0, 136.3, 135.6, 130.0, 127.1, 121.5, 118.4, 69.5, 25.5.

1-(pyrazin-2-yl)ethan-1-ol (5c)[82]

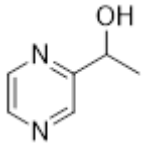

^{1}H NMR (400 MHz, Chloroform-*d*) δ 8.66 (s, 1H), 8.54 – 8.44 (m, 2H), 4.98 (q, *J* = 6.5 Hz, 1H), 3.72 (s, 1H), 1.55 (d, *J* = 6.6 Hz, 3H) ppm. ^{13}C NMR (125.78 MHz, Chloroform-*d*) δ 158.8, 143.4, 143.2, 142.5, 68.1, 24.0ppm.

1-(4-bromophenyl)ethan-1-ol (5d)[83]

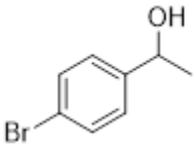

^{1}H NMR (400 MHz, Chloroform-*d*) δ 7.47 (d, *J* = 8.4 Hz, 2H), 7.25 (d, *J* = 8.3 Hz, 2H), 4.86 (q, *J* = 6.4 Hz, 1H), 1.90 (s, 1H), 1.47 (d, *J* = 6.5 Hz, 3H). ^{13}C NMR (125.78 MHz, Chloroform-*d*) δ 144.9, 131.7, 127.2, 121.3, 69.9, 25.3.

1-(2-aminophenyl)ethan-1-ol (5e)[84]

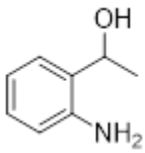

^{1}H NMR (400 MHz, Chloroform-*d*) δ 7.09 (t, *J* = 6.8 Hz, 2H), 6.73 (t, *J* = 7.4 Hz, 1H), 6.68 (d, *J* = 8.2 Hz, 1H), 4.94 (q, *J* = 6.6 Hz, 1H), 1.60 (d, *J* = 6.6 Hz, 3H). ^{13}C NMR (125.78 MHz, Chloroform-*d*) δ 145.2, 128.7, 128.4, 126.6, 118.2, 116.7, 69.7, 21.6.

1,1'-([1,1'-biphenyl]-4,4'-diyl)bis(ethan-1-ol) (5f)[85]

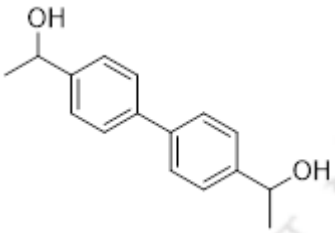

^{1}H NMR (400 MHz, Chloroform-*d*) δ 7.57 (d, *J* = 8.3 Hz, 4H), 7.44 (d, *J* = 8.1 Hz, 4H), 4.95 (q, *J* = 6.5 Hz, 2H), 1.76 (s, 2H), 1.54 (d, *J* = 6.5 Hz, 6H). ^{13}C NMR (125.78 MHz, Chloroform-*d*) δ 144.9, 140.2, 127.3, 126.0, 70.3, 25.3

anthracen-9-ylmethanol (5g)[86]

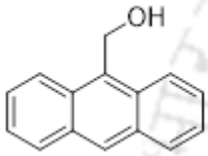

^{1}H NMR (400 MHz, Chloroform-*d*) δ 8.48 (s, 1H), 8.43 (d, *J* = 8.9 Hz, 2H), 8.04 (d, *J* = 8.4 Hz, 2H), 7.61 – 7.55 (m, 2H), 7.52 – 7.47 (m, 2H), 5.69 (s, 2H), 1.77 (s, 1H). ^{13}C NMR (125.78 MHz, Chloroform-*d*) δ 131.7, 131.1, 130.4, 129.3, 128.5, 126.6, 125.2, 124.0, 57.6.

pyren-1-ylmethanol (5h)[87]

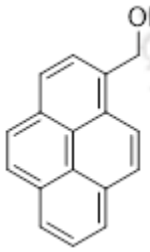

^{1}H NMR (400 MHz, Chloroform-*d*) δ 8.39 (d, *J* = 9.2 Hz, 1H), 8.20 (dd, *J* = 6.9, 5.5 Hz, 2H), 8.18 – 8.14 (m, 2H), 8.09 – 7.99 (m, 4H), 5.42 (s, 2H), 1.90 (s, 1H). ^{13}C NMR (125.78 MHz, Chloroform-*d*) δ 133.9, 131.4, 130.9, 129.0, 128.0, 127.6, 127.5, 126.2, 126.1, 125.4, 125.1, 124.9, 124.8, 123.1, 64.0.

1,1'-(1,4-phenylene)bis(ethan-1-ol) (5i)[88]

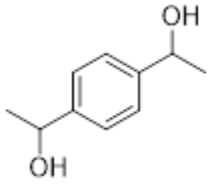

1H NMR (400 MHz, CDCl3): δ = 7.38 (s, 4H), 4.93 (q, J = 6.4 Hz, 2H), 2.03 (s, 2H), 1.52 (d, J = 6.4 Hz, 6H); 13C NMR (125.78 MHz, CDCl3): δ = 145.0, 125.5, 70.18 70.1, 25.1.

1-(naphthalen-2-yl)ethan-1-ol (5j)[83]

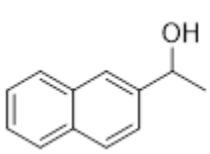

^{1}H NMR (400 MHz, Chloroform-*d*) δ 7.89 – 7.77 (m, 4H), 7.49 (dtt, *J* = 10.9, 7.2, 3.3 Hz, 3H), 5.07 (q, *J* = 5.6 Hz, 1H), 2.03 (s, 1H), 1.59 (d, *J* = 6.5 Hz, 3H). ^{13}C NMR (125.78 MHz, Chloroform-*d*) δ 143.3, 133.4, 133.0, 128.4, 128.0, 127.8, 126.2, 125.9, 123.9, 70.6, 25.2.

2-methoxybenzamide (5k)[89]

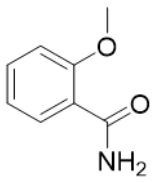

^{1}H NMR (400 MHz, Chloroform-*d*) δ 8.21 (d, *J* = 9.3 Hz, 1H), 7.72 (s, 1H), 7.47 (t, *J* = 8.7 Hz, 1H), 7.09 (d, *J* = 7.4 Hz, 1H), 6.99 (d, *J* = 8.3 Hz, 1H), 6.06 (s, 1H), 3.97 (s, 3H). ^{13}C NMR (125.78 MHz, Chloroform-*d*) δ 167.2, 157.9, 133.5, 132.7, 121.4, 120.9, 111.5, 56.0.

4-hydroxybenzamide (5l)[90]

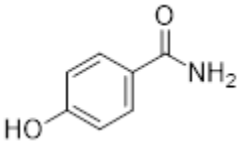

^{1}H NMR (400 MHz, DMSO-d_6) δ 10.04 (s, 1H), 7.75 (d, *J* = 8.7 Hz, 3H), 7.12 (s, 1H), 6.85 – 6.75 (m, 2H). ^{13}C NMR (126 MHz, Chloroform-*d*) δ 168.2, 160.41, 129.7, 125.0, 114.9

4-phenylpicolinamide (5m)

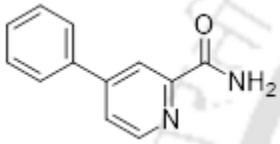

^{1}H NMR (400 MHz, DMSO-d_6) δ 8.61 (d, *J* = 5.0 Hz, 1H), 8.47 (s, 1H), 7.92 (s, 1H), 7.74 – 7.70 (m, 2H), 7.67 (dd, *J* = 5.1, 1.8 Hz, 1H), 7.54 – 7.44 (m, 3H), 5.80 (s, 1H). ^{13}C NMR (126 MHz, Chloroform-*d*) δ 167.3, 150.2, 150.0, 148.9, 137.5, 129.6, 129.4, 127.2, 124.2, 120.5.

pyrazine-2,3-dicarboxamide (5n)

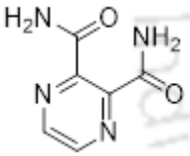

^{1}H NMR (400 MHz, Chloroform-*d*) δ 9.25 (s, 2H), 8.57 (s, 2H), 8.14 (s, 2H). ^{13}C NMR (126 MHz, DMSO-d_6) δ 167.16, 147.17, 144.69. Cas no 6164-78-9.

2.4.12 Homocoupling of phenylacetylene

Phenylacetylene (2 mmol), K_2CO_3(1.5 mmol), and catalyst **5** (0.1 mol%) were mixed in ethanol (10 mL) and were stirred at 70 °C for 8h. After the completion of reaction, the mixture was cooled, filtered through a short pad of celite, washed with ethyl acetate. The solvent was removed under reduced pressure, and the crude product was purified by preparative thin layer chromatography to produce isolated yield of **1,4-diphenylbuta-1,3-diyne**.[91] ^{1}H NMR (400 MHz, Chloroform-d) δ 7.56 – 7.51 (m, 4H), 7.35 (q, J = 7.2, 6.3 Hz, 6H). ^{13}C NMR (126 MHz, DMSO-d6) δ 132.65, 129.36, 128.59, 121.94, 81.69, 74.04.

2.4.13 Reusability of catalyst 1

1-bromo-4-nitrobenzene (1.0 mmol), phenylboronic acid (1.2 mmol), K_2CO_3 (1.5 mmol), and catalyst **1** (1 mol%) were taken in ethanol (20 mL) at 80 °C and stirred for 4 hours. Solvent was removed, water (10 mL) was added and extracted with ethylacetate. Organic phase was collected,

dried over anhydrous sodium sulfate and solids were collected after removal of solvent. The crude product was purified by preparative thin layer chromatography (5% EtOAc/hexane). The insoluble catalyst present in aqueous phase was collected by centrifuge, dried in an oven, and applied directly for next run.

2.4.14 Hot filtration test

To check the homogeneity of catalyst **1**, a hot filtration test was conducted. The reaction condition was same as for product **3d**. After 1.5 hours, the reaction solution was filtered quickly through a short pad of celite in hot condition. Then, the filtrate was allowed to stirring for next 2.5 hours. After the completion of reaction, the mixture was cooled, filtered through a short pad of celite, and washed with ethyl acetate. The solvent was removed under reduced pressure and the residue was purified by preparative thin layer chromatography using ethyl acetate/hexane (1:19) as the eluent to obtain pure 4-nitro-1,1'-biphenyl. The yield of the product was 96% while without filtration, it was 98.5% which confirmed the homogeneous nature of catalyst **1**.

2.4.15 DNA Binding Study:

The experiments were performed at room temperature in Tris-HCl buffer (5 mM Tris-HCl and 50 mM NaCl, pH = 7.2). The DNA stock solution was prepared in Tris-HCl buffer and the stock solution was stored at 4 °C in dark. The concentration was determined spectrophotometrically from the absorbance at 260 nm (molar extinction coefficient is 6600 M^{-1} cm^{-1}). Further, the absorbance of DNA stock solution at 260 and 280 nm gave a ratio of 1.8, signifying that the DNA was adequately protein free. The titration experiment was carried out with fixed complex concentration (15 μM) to which DNA (0−15 μM) was gradually added for absorption measurement. For emission experiments, stock solution of ethidium bromide (EB) was prepared in deionized water. A 5.0 μM of EB solution was mixed with 5.0 μM DNA solution and kept for 30 minutes. A 5.0 μM of EB–DNA mixed solution was titrated with variation of complex concentration (0–15 μM). EB-DNA adduct.

2.4.16 BSA Binding Study:

BSA stock solution was prepared by dissolving in HEPES buffer (10.0 mM, pH= 7.2) and concentration was determined from the absorbance at 278 nm (molar extinction coefficient 4.4 × 10^4 M^{-1} cm^{-1}). Stock solutions of all metal complexes were prepared in DMSO and diluted in HEPES buffer. Titration study was carried out with a constant BSA concentration (1.5 μM) and

gradually increasing concentration of metal complexes (0–3.0 μM). The excitation was set at 285 nm and emission spectra were collected in the range of 280–500 nm at 25 °C. For steady-state fluorescence anisotropy measurement, the excitation and emission slit were set at 5 nm and 10 nm. respectively. The system was excited at 350 nm and emission wavelength was fixed at 533 nm.

2.4.17 In silico ADMET properties and Molecular Docking study

The physicochemical properties, lipophilicity, drug-likeness scores, and medicinal chemistry data were calculated with the SwissADME database.[92] Pharmacokinetics properties were computed using pkCSM tool.[93] The Ames test and rodent carcinogenicity were predicted in PreADMET.[94] Molecular docking was executed using the Autoock4.2.6 and MGL Tools 1.5.6 programs.[95] The Apo structure of human LTA_4H was obtained from Protein Data Bank (PDB ID: 5fwq).[96] Then, it was cleaned by removing water and co-crystal molecules followed by the addition of polar hydrogens and atomic Kollman charges. A blind docking was carried out with grid box dimensions 148 × 236 × 200, grid points spaced 0.375 Å, and the receptor was kept inflexible during the study. Lamarckian Genetic Algorithm (GA) with a population size of 100 was used to generate the docked conformations with studied compounds. The docking results were visualized by using BIOVIA Discovery Studio Visualizer.[97]

2.4.18 Computational Study

For computational study, all calculations were performed by using Gaussian09 (G09) program and GaussView 5.0 was used for picturization.[98,99] The geometry of complexes **1**–**6** were optimized using B3LYP hybrid functional and 6-311g(d,p)/LanL2DZ basis set.[100,101] The natural bonding orbital (NBO) analysis was carried out to calculate natural atomic charges and electron configurations.[102,103] Frontier molecular orbital (FMO) analysis was also performed to calculate the chemical reactivity and stability in **1**–**6**.[104]

CCDC No. *2390283–2390286, 2422918, and 2422915* contain the crystallographic data for all complexes studied in this Chapter.

The ATR-IR, NMR and HRMS spectra of complexes, NMR spectra of catalytic products, electronic spectra of DNA/BSA interaction, and optimized structures, HOMO-LUMO orbitals, NBO analysis data and cartesian coordinates of all complexes can be found in Appendix I by using the following link:

https://drive.google.com/file/d/1NH8C4aVkmm2rxSCxNTd-MVQwWbqaTB7X/view?usp=sharing

2.5 References

1. H. Li, C. C. C. J. Seechurn and T. J. Colacot, *ACS Catal.*, 2012, **2**, 1147–1164.
2. N. Selander and K. J. Szabó, *Chem. Rev.*, 2011, **111**, 2048–2076.
3. C. Torborg and M. Beller, *Adv. Synth. Catal.*, 2009, **351**, 3027–3043.
4. L. C. Campeau and N. Hazari, *Organometallics*, 2019, **38**, 3–35.
5. C. A. Wang, M. M. Rahman, E. Bisz, B. Dziuk, R. Szostak and M. Szostak, *ACS Catal.*, 2022, **12**, 2426–2433.
6. A. Biffis, P. Centomo, A. Del Zotto and M. Zecca, *Chem. Rev.*, 2018, **118**, 2249–2295.
7. T. Ben Halima, W. Zhang, I. Yalaoui, X. Hong, Y.-F. Yang, K. N. Houk and S. G. Newman, *J. Am. Chem. Soc.*, 2017, **139**, 1311–1318.
8. D. Wang and D. Astruc, *Chem. Rev.*, 2015, **115**, 6621–6686.
9. D. G. Brown and J. Boström, *J. Med. Chem.*, 2016, **59**, 4443–4458.
10. P. Devendar, R.-Y. Qu, W.-M. Kang, B. He and G.-F. Yang, *J. Agric. Food Chem.*, 2018, **66**, 8914–8934.
11. S. Chakraborty, P. E. Piszel, W. W. Brennessel and W. D. Jones, *Organometallics*, 2015, **34**, 5203–5206.
12. M. Valencia, H. Müller-Bunz, R. A. Gossage and M. Albrecht, *Chem. Commun.*, 2016, **52**, 3344–3347.
13. R. H. Morris, *Chem. Soc. Rev.*, 2009, **38**, 2282–2291.
14. S. Santoro, F. Ferlin, L. Luciani, L. Ackermann and L. Vaccaro, *Green Chem.*, 2017, **19**, 1601–1612.

15. J. Zhu and V. N. G. Lindsay, *ACS Catal.*, 2019, **9**, 6993–6998.
16. M. Sen (ed.), *Sustainable Green Catalytic Processes*, John Wiley & Sons, 2024.
17. P. Srinivas, K. Srinivas, P. R. Likhar, B. Sridhar, K. V. Mohan, S. Bhargava and M. L. Kantam, *J. Organomet. Chem.*, 2011, **696**, 795–801.
18. S. Panchavarnam, R. Sengupta and M. Ravikanth, *Inorg. Chem.*, 2021, **60**, 15686–15694.
19. D. E. Herbert and O. V. Ozerov, *Organometallics*, 2011, **30**, 6641–6654.
20. F. Yagishita, K. Nomura, S. Shiono, C. Nii, T. Mino, M. Sakamoto and Y. Kawamura, *ChemistrySelect*, 2016, **1**, 4560–4563.
21. G. A. Ardizzoia, D. Ghiotti, B. Therrien and S. Brenna, *Inorg. Chim. Acta*, 2018, **471**, 384–390.
22. T. Scattolin, G. Andreetta, M. Mauceri, F. Rizzolio, N. Demitri, V. Canzonieri and F. Visentin, *J. Organomet. Chem.*, 2021, **952**, 122014.
23. N. Kundu, S. M. T. Abtab, S. K. Kundu, A. Endo, S. J. Teat and M. Chaudhury, *Inorg. Chem.*, 2012, **51**, 2652–2661.
24. G. Volpi, G. Magnano, I. Benesperi, D. Saccone, E. Priola, V. Gianotti, M. Milanesio, E. Conterosito, C. Barolo and G. Viscardi, *Dyes Pigm.*, 2017, **137**, 152–164.
25. C. Garino, T. Ruiu, L. Salassa, A. Albertino, G. Volpi, C. Nervi, R. Gobetto and K. I. Hardcastle, *Eur. J. Inorg. Chem.*, 2008, 3587–3591.
26. S. Pischedda, S. Stoccoro, A. Zucca, G. Sciortino, F. Ortu and G. J. Clarkson, *Dalton Trans.*, 2021, **50**, 4859–4873.
27. Y. Imada, S. Mukai, K. Tahara, N. Kozai, M. Itaya, Y. Yoshida, S. Ueta, Y. Arakawa, K. Minagawa and F. Yagishita, *Inorg. Chim. Acta*, 2023, **555**, 121584.
28. Y. Qin, Y. Chen, J. Liu, J. Zhao, D. Gao, Y. Li, W. Liu and W. Li, *Inorg. Chem. Commun.*, 2015, **56**, 58–61.
29. R. G. Gámez-Heredia, A. Cruz-Enríquez, R. Aceves, H. Höpfl, M. Parra-Hake, R. E. Navarro and J. J. Campos-Gaxiola, *Inorg. Chim. Acta*, 2019, **486**, 377–386.
30. C. Guo, M. Li, W. Yuan, K. Wang, B. Zou and Y. Chen, *J. Phys. Chem. C*, 2017, **121**, 27009–27017.
31. Y. Zhan, X. Wang, Y. Wang and Y. Xu, *Dyes Pigm.*, 2019, **167**, 1–9.
32. A. O. Eseola, D. Geibig, H. Görls, W. H. Sun, X. Hao, J. A. O. Woods and W. Plass, *J. Organomet. Chem.*, 2014, **754**, 39–50.

33. S. Panchavarnam, R. Sengupta and M. Ravikanth, *Inorg. Chem.*, 2021, **60**, 15686–15694.
34. S. Baweja, T. Gabler, P. Lönnecke and E. Hey-Hawkins, *Dalton Trans.*, 2023, **52**, 6494–6500.
35. S. Abedanzadeh, K. Karami, M. Rahimi, M. Edalati, M. Abedanzadeh, A. M. Tamaddon, M. D. Jahromi, Z. Amirghofran, J. Lipkowski and K. Lyczko, *Dalton Trans.*, 2020, **49**, 14891–14907.
36. C. Tan, J. Liu, H. Li, W. Zheng, S. Shi, L. Chen and L. Ji, *J. Inorg. Biochem.*, 2008, **102**, 347–358.
37. S. Jovanović, K. Obrenčević, Ž. D. Bugarčić, I. Popović, J. Žakula and B. Petrović, *Dalton Trans.*, 2016, **45**, 12444–12457.
38. D. Cócić, S. Jovanović-Stević, R. Jelić, S. Matić, S. Popović, P. Djurdjević, D. Baskić and B. Petrović, *Dalton Trans.*, 2020, **49**, 14411–14431.
39. M. A. Razzak, J. E. Lee and S. S. Choi, *Food Hydrocoll.*, 2019, **91**, 290–300.
40. T. D. Penning, N. S. Chandrakumar, B. B. Chen, H. Y. Chen, B. N. Desai, S. W. Djuric, S. H. Docter, A. F. Gasiecki, R. A. Haack, J. M. Miyashiro, M. A. Russell, S. S. Yu, D. G. Corley, R. C. Durley, B. F. Kilpatrick, B. L. Parnas, L. J. Askonas, J. K. Gierse, E. I. Harding, M. K. Highkin, J. F. Kachur, S. H. Kim, G. G. Krivi, D. Villani-Price, E. Y. Pyla, W. G. Smith and N. S. Ghoreishi-Haack, *J. Med. Chem.*, 2000, **43**, 721–735.
41. D. Moser, S. K. Wittmann, J. Kramer, R. Blöcher, J. Achenbach, D. Pogoryelov and E. Proschak, *J. Chem. Inf. Model.*, 2015, **55**, 284–293.
42. R. J. Griffiths, E. R. Pettipher, K. Koch, C. A. Farrell, R. Breslow, M. J. Conklyn, M. A. Smith, B. C. Hackman, D. J. Wimberly and A. J. Milici, *Proc. Natl. Acad. Sci. U.S.A.*, 1995, **92**, 517–521.
43. A. Stsiapanava, U. Olsson, M. Wan, T. Kleinschmidt, D. Rutishauser, R. A. Zubarev, B. Samuelsson, A. Rinaldo-Matthis and J. Z. Haeggström, *Proc. Natl. Acad. Sci. U.S.A.*, 2014, **111**, 4227–4232.
44. J. Z. Haeggström, *J. Biol. Chem.*, 2004, **279**, 50639–50642.
45. J. A. Mancini and J. F. Evans, *Eur. J. Biochem.*, 1995, **231**, 65–71.
46. S. Thangapandian, S. John, S. Sakkiah and K. W. Lee, *J. Chem. Inf. Model.*, 2011, **51**, 33–44.
47. T. Kennedy, *Drug Discov. Today*, 1997, **2**, 436–444.
48. I. Kola and J. Landis, *Nat. Rev. Drug Discov.*, 2004, **3**, 711–716.

49. G. Moroy, V. Y. Martiny, P. Vayer, B. O. Villoutreix and M. A. Miteva, *Drug Discov. Today*, 2012, **17**, 44–55.
50. V. K. Fulwa, R. Sahu, H. S. Jena and V. Manivannan, *Tetrahedron Lett.*, 2009, **50**, 6264–6267.
51. A. Ratnam, M. Bala, R. Kumar, U. P. Singh and K. Ghosh, *J. Organomet. Chem.*, 2018, **856**, 41–49.
52. N. Dehury, N. Maity, S. K. Tripathy, J. M. Basset and S. Patra, *ACS Catal.*, 2016, **6**, 5535–5540.
53. A. Zanardi, J. A. Mata and E. Peris, *J. Am. Chem. Soc.*, 2009, **131**, 14531–14537.
54. S. Gonell, M. Poyatos, J. A. Mata and E. Peris, *Organometallics*, 2012, **31**, 5606–5614.
55. N. Dehury, N. Maity, S. K. Tripathy, J. M. Basset and S. Patra, *ACS Catal.*, 2016, **6**, 5535–5540.
56. R. O. Omondi, N. R. S. Sibuyi, A. O. Fadaka, M. Meyer, D. Jaganyi and S. O. Ojwach, *Dalton Trans.*, 2021, **50**, 8127–8143.
57. World Intellectual Property Organization, PCT/US98/03926, 1998, 1–51.
58. C. Y. Jia, J. Y. Li, G. F. Hao and G. F. Yang, *Drug Discov. Today*, 2020, **25**, 248–258.
59. S. K. Wittmann, L. Kalinowsky, J. S. Kramer, R. Bloecher, S. Knapp, D. Steinhilber, D. Pogoryelov, E. Proschak and J. Heering, *Bioorg. Med. Chem.*, 2016, **24**, 5243–5248.
60. D. T. Muskardin, N. F. Voelkel and F. A. Fitzpatrick, *Biochem. Pharmacol.*, 1994, **48**, 131–137.
61. R. D. Cramer III, G. Redl and C. E. Berkoff, *J. Med. Chem.*, 1974, **17**, 533–535.
62. C. A. Kemp, J. U. Flanagan, A. J. van Eldik, J.-D. Maréchal, C. R. Wolf, G. C. K. Roberts, M. J. I. Paine and M. J. Sutcliffe, *J. Med. Chem.*, 2004, **47**, 5340–5346.
63. B. N. Ames, E. G. Gurney, J. A. Miller and H. Bartsch, *Proc. Natl. Acad. Sci. U.S.A.*, 1972, **69**, 3128–3132.
64. P. Banerjee, E. Kemmler, M. Dunkel and R. Preissner, *Nucleic Acids Res.*, 2024, **52**, W513–W520.
65. G. M. Sheldrick, *Acta Crystallogr. C Struct. Chem.*, 2015, **71**, 3–8.
66. A. L. Spek, *J. Appl. Crystallogr.*, 2003, **36**, 7–13.
67. J. H. Li, B. X. Tang, L. M. Tao, Y. X. Xie, Y. Liang and M. B. Zhang, *J. Org. Chem.*, 2006, **71**, 7488–7490.

68. T. Zhou, C. L. Ji, X. Hong and M. Szostak, *Chem. Sci.*, 2019, **10**, 9865–9871.
69. L. Liu, Y. Dong, B. Pang and J. Ma, *J. Org. Chem.*, 2014, **79**, 7193–7198.
70. L. S. Søbjerg, D. Gauthier, A. T. Lindhardt, M. Bunge, K. Finster, R. L. Meyer and T. Skrydstrup, *Green Chem.*, 2009, **11**, 2041–2046.
71. X. Li, D. Zou, F. Leng, J. Li, Y. Wu and Y. Wu, *Chem. Commun.*, 2013, **49**, 312–314.
72. A. Wang, J. Huang, C. Zhao, Y. Fan, J. Qian, Q. Chen, M. He and W. Zhou, *Green Chem.*, 2023, **26**, 353–361.
73. S. Yang, H. Li, X. Yu, J. An and M. Szostak, *J. Org. Chem.*, 2022, **87**, 15250–15260.
74. T. Kawamoto, A. Sato and I. Ryu, *Org. Lett.*, 2014, **16**, 2111–2113.
75. M. Al-Amin, M. Akimoto, T. Tameno, Y. Ohki, N. Takahashi, N. Hoshiya, S. Shuto and M. Arisawa, *Green Chem.*, 2013, **15**, 1142–1145.
76. S. Hachiya, K. Asai and G. I. Konishi, *Tetrahedron Lett.*, 2013, **54**, 1839–1841.
77. P. Gnanasekaran, Y. Yuan, C. S. Lee, X. Zhou, A. K. Y. Jen and Y. Chi, *Inorg. Chem.*, 2019, **58**, 10944–10954.
78. Y. N. Niu, Z. Y. Yan, G. L. Gao, H. L. Wang, X. Z. Shu, K. G. Ji and Y. M. Liang, *J. Org. Chem.*, 2009, **74**, 2893–2896.
79. I. Kazi, S. Guha and G. Sekar, *J. Org. Chem.*, 2019, **84**, 6642–6654.
80. P. V. Ramachandran, A. A. Alawaed and H. J. Hamann, *J. Org. Chem.*, 2022, **87**, 13259–13269.
81. R. Pothikumar, V. T. Bhat and K. Namitharan, *Chem. Commun.*, 2020, **56**, 13607–13610.
82. H. Zeng, J. Wu, S. Li, C. Hui, A. Ta, S. Y. Cheng, S. Zheng and G. Zhang, *Org. Lett.*, 2019, **21**, 401–406.
83. I. Khan, B. G. Reed-Berendt, R. L. Melen and L. C. Morrill, *Angew. Chem.*, 2018, **130**, 12536–12539.
84. Y. Zhao, B. Huang, C. Yang, Q. Chen and W. Xia, *Org. Lett.*, 2016, **18**, 5572–5575.
85. G. Zhang, R. Liu, Y. Chou, Y. Wang, T. Cheng and G. Liu, *ChemCatChem*, 2018, **10**, 1882–1888.
86. V. K. Jakhar, M. K. Barman and S. Nembenna, *Org. Lett.*, 2016, **18**, 4710–4713.
87. G. Zhang, J. Cheng, K. Davis, M. G. Bonifacio and C. Zajaczkowski, *Green Chem.*, 2019, **21**, 1114–1121.
88. S. Liu, H. Liu, H. Zhou, Q. Liu and J. Lv, *Org. Lett.*, 2018, **20**, 1110–1113.

89. N. Bandopadhyay, K. Paramanik, G. Sarkar, S. Roy, S. J. Panda, C. S. Purohit, B. Biswas and H. S. Das, *Dalton Trans.*, 2024, **53**, 13795–13804.
90. Y. Sim, S. J. Lee and S. H. Kim, *Chem. Sci.*, 2024, **136**, 56.
91. A. Sagadevan, V. P. Charpe and K. C. Hwang, *Catal. Sci. Technol.*, 2016, **6**, 7688–7692.
92. A. Daina, O. Michielin and V. Zoete, *Sci. Rep.*, 2017, **7**, 42717.
93. D. E. V. Pires, T. L. Blundell and D. B. Ascher, *J. Med. Chem.*, 2015, **58**, 4066–4072.
94. https://preadmet.qsarhub.com/toxicity
95. G. M. Morris, R. Huey, W. Lindstrom, M. F. Sanner, R. K. Belew, D. S. Goodsell, A. J. Olson, *J. Comput. Chem.* 2009, **30** (16), 2785-2791.
96. https://www.rcsb.org
97. BIOVIA Discovery Studio Visualizer, v21.1.0.20298. San Diego: Dassault Systèmes, 2020.
98. M. J. ea Frisch, G. W. Trucks, H. B. Schlegel, G. E. Scuseria, Ma. Robb, J. R. Cheeseman, G. Scalmani, V. Barone, G. A. Petersson and H. Nakatsuji, Gaussian, Inc. Wallingford, CT, 2016, preprint.
99. R. Dennington, T. A. Keith and J. M. Millam, Semichem Inc Shawnee Mission KS.
100. O. Treutler and R. Ahlrichs, *J. Chem. Phys.*, 1995, **102**, 346–354.
101. A. D. Becke, *J. Chem. Phys.*, 1993, **98**, 1372–1377.
102. L. Wei, Y. She, Y. Yu, X. Yao and S. Zhang, *J. Mol. Model.*, 2012, **18**, 2483–2491.
103. F. Weinhold and C. R. Landis, *Chem. Educ. Res. Pract.*, 2001, **2**, 91–104.
104. Y. Ruiz-Morales, *J. Phys. Chem. A*, 2002, **106**, 11283–11308.

Chapter-3

Group 10 Complexes of Some Chemodiverse Ligands: Structural Artistry, Catalytic Activity, and Biomolecule Interaction*

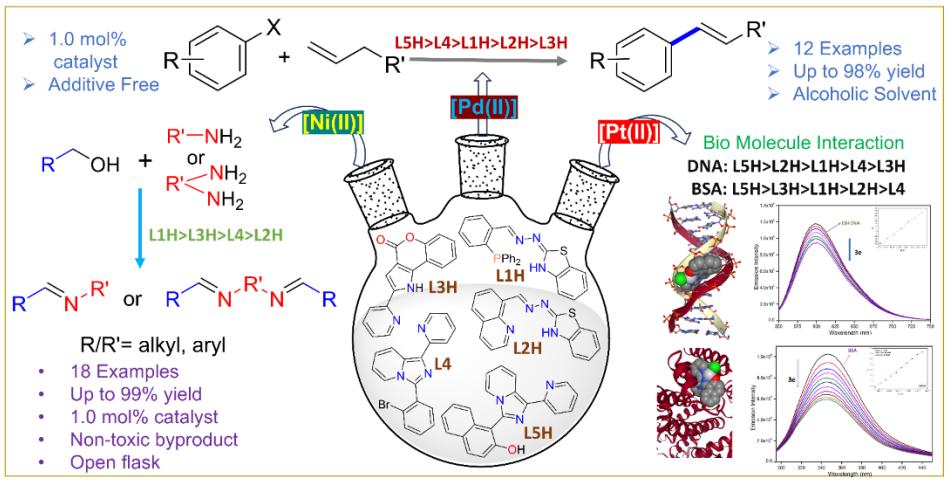

* Major part of this work has been accepted in

A. R. Rayasingh and V. Manivannan, *Dalton Trans.,* https://doi.org/10.1039/D5DT02077H

Abstract

A series of bivalent complexes of group 10 metals using various structurally and electronically diverse ligands (N/O/P-donor) were synthesized, characterized, and their structures were determined by SCXRD. Computational calculations were applied to optimize molecular geometries, evaluate the energies of frontier molecular orbitals (FMOs), NBO analysis and possible electronic transitions. The ligands featuring various donor sites revealed how they were responsible for the geometry of complexes; altered the catalytic and bioactivity. The Ni(II) complexes were applied as catalysts in imine/diimine formation *via* acceptorless dehydrogenative coupling (ADC) of alcohol and amine/diamine. Only 1.0 mol% of Ni(II) catalyst excellently produced imines/diimines in toluene (110 ºC, 12 h). In Heck coupling, Pd(II) catalysts were adeptly produced alkene in 98% yield in ethanol under significantly milder condition than traditional protocols relying on DMF/DMSO at higher temperatures. Among all complexes, **1a** and **2h** were found as superior catalyst in their respective conversion. Versatility of Pd(II) catalysts was also examined in a model reaction of cross dehydrogenative coupling (CDC) of thiophene-2-carbaldehyde. The Pt(II) complexes were examined for their interactions with CT-DNA and BSA wherein **3e** exhibited highest binding affinity. Binding mode of **3e** was visualized through molecular docking with CT-DNA and BSA.

3.1 Introduction

Group 10 metal complexes have been extensively used as catalysts and metallodrugs. Many types of organic transformations catalyzed by Pd(II) and Ni(II) complexes are much importance as well as powerful tool in research and synthetic industry.[1–4] In the history of homogeneous metal catalyst, palladium earned a special place due to its versatility, selectivity, high activity, mild reaction conditions and large functional group tolerance.[5–7] However, the high cost of palladium motivated the evaluation of cheaper and earth-abundant nickel as an alternate option for establishing the catalytic conversions.[8–10] In the era of metal catalyzed organic synthesis, design of a catalyst to catalyze more than one reaction is more desirable which diminished the requirement of multiple catalyst syntheses. Minimal use of solvents, reagents, reaction time, and energy during synthesis of both catalyst and reactions catalyzed by them are major advantages of these multifunctional catalysts.[11,12] Remarkably, the cutting-edge development of efficient, stable, and multifunctional catalysts that enhance their synthetic application are highly demanded.[13]

However, characteristics of the ligand plays a significant role in the catalytic activity at the metal site. In case of palladium, the selection of ligand to enhance the reactivity for a specific catalysis has become instinctive, but this ramification for nickel remains inherent. In some reports, it was observed that ligands specific for activity of Pd were found to be inactive for Ni.[14–17] Pincer ligands gain popularity due to their ability to form structurally predictable and highly robust complexes.[18] and N and P donors in the same chelate was a crucial combination to provide hemi-lability that support metal center in different oxidation states. [19,20] An important transition metal complex catalyzed chemical conversion is imine synthesis, and compounds containing the imine function have been widely used in various medical, agricultural, and other sectors.[21–26] Acceptorless dehydrogenative coupling (ADC) of alcohols with amine by using a catalyst has emerged as a greener strategy to produce imines. However, imine synthesis has been performed using precious metal catalyst.[21,26–29] Some pincer ruthenium complexes (**Ru3.1**, **Ru3.2**) were used by Nishibayashi and co-worker as catalyst to produce imine from amines and benzyl alcohol.[27] However, 48 h was required to achieve a maximum 86% imine in presence of NaO^{i}Pr and toluene. The Yao group reported some air-stable half-sandwich iridium complexes (**Ir3.1**–**Ir3.5**) and used as oxidation catalyst for imine synthesis using DMSO as solvent and under 1 atm oxygen.[22] A well-defined cobalt complex (**Co3.1**) was reported by Ding and coworkers and used to catalyze imine formation reaction *via* dehydrogenative coupling of amines with primary alcohols using 3.0 mol% of catalyst loading in 24 hours.[30] Very recently, Lin group reported ruthenium catalysts (**Ru3.3**–**Ru3.6**) for imine formation reaction.[31] (Scheme 3.1). Thus, development of earth abundant catalysts using simple ligands for imine synthesis via ADC would be significant.

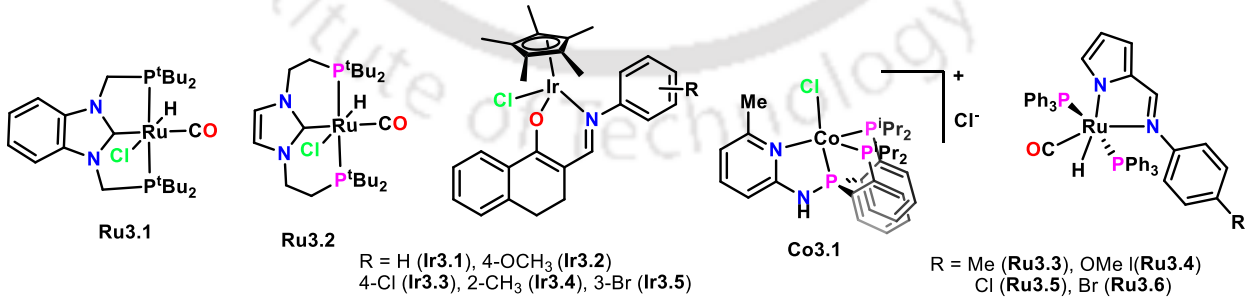

Scheme 3.1: Some reported metal catalysts used for imine synthesis from alcohol and amine.

Another most demanded C–C coupling reaction is Heck coupling which is very useful synthetic procedure in natural product synthesis, biomaterials, and fine chemical synthesis. Shao and

coworker successfully conducted Heck coupling between aryl bromide and n-butyl acrylate using CNC pincer type Pd(II) complexes (**Pd3.1**–**Pd3.3**) in DMSO at 110 °C.[32] A bis (BICAAC) palladium(II) complex (**Pd3.4**) was reported by Singh and coworker.[33] The enhanced σ-donating and π-accepting capabilities of BICAAC stabilized the Pd–carbene bond and catalyzed Heck reactions at 110 °C for 10-12 hours in DMA. Szostak group reported various C-C coupling reactions including Heck coupling in moderate yield by using Pd-PEPSSI N-heterocyclic caffeine complexes (**Pd3.5**–**Pd3.7**).[34] Recently Ananikov group showed that how halogen substitution on aryl ligands affects the electronic structure and reactivity of the Pd-NHC catalysts (**Pd3.8**–**Pd3.20**) in the Heck reaction .[35] The reactivity order of the halogen substituent was Br > F > Cl and *m*-X, *p*-X > *o*-X in Heck coupling. The presence of electron-withdrawing groups such as CF_3 and Br at meta or para positions led to enhanced catalytic activity and stability (Scheme 3.2).

As most of the Heck coupling used Pd(II) catalyst made from phosphene and carbene based ligands along with toxic solvents and high temperature, it would be noteworthy to develop sustainable reaction condition using alcoholic solvent and readily available ligand systems.

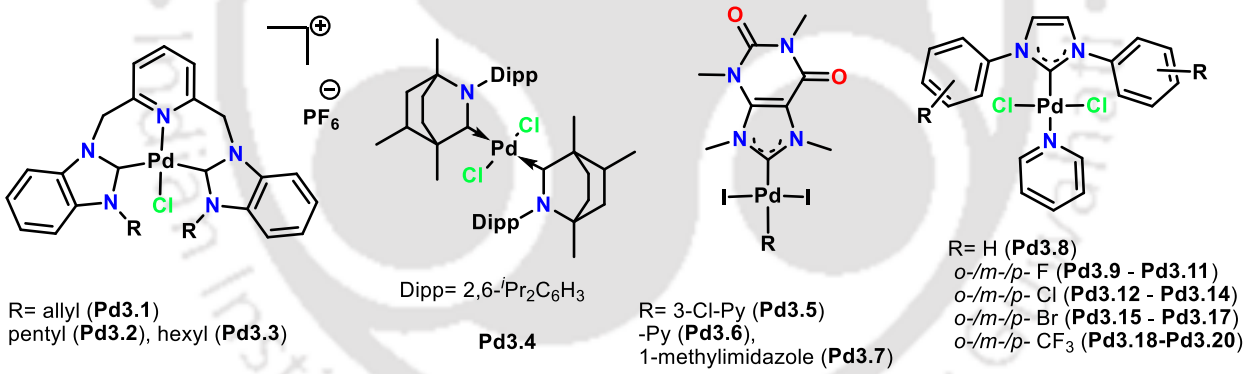

Scheme 3.2: Some reported Pd(II) catalysts used in Heck coupling reaction.

In addition to their well-known catalytic roles, group 10 metal complexes, particularly Pt(II) complexes have attracted considerable attention for their potential in biomedical applications, especially as anticancer agents.[36–39] Their ability to interact with key biomolecules such as deoxyribose nucleic acid (DNA) and serum proteins can disrupt the tumour microenvironment and trigger cell death (apoptosis).[40] A crucial aspect of any effective anticancer drug lies in its ability to reach the intended site of action. In this regard, binding to serum albumins is vital, as these proteins are the primary carriers of drugs in the bloodstream.[41] Bovine serum albumin (BSA) is frequently used in such studies because of its close structural resemblance to human serum albumin

(HSA).[42] Therefore, evaluating the binding affinity of these platinum(II) complexes to both DNA and BSA is essential for understanding their therapeutic potential, anticancer activity, and pharmacological behaviour.[43–46] With this in mind, we have investigated the interactions between the platinum(II) complexes of the synthesized ligands and biomolecules like calf thymus DNA (CT-DNA) and BSA.

Thus, from the above discussed literature results, it is concluded that there is necessity for development of robust and sustainable Ni and Pd catalyst which can overcome the various limitation faced by metal catalyzed imine synthesis and Heck coupling. This chapter discussed the synthesis of some benzothiazole hydrazone (NNP- and NNN- donor), coumarin fused pyrrole (NN- donor) and imidazo[1,5-*a*]pyridine (NN-, NNO- donor) based ligand systems and explored the catalytic activity of their nickel(II) and palladium(II) complexes and DNA, BSA interaction with Pt(II) congeners. The main objective of this chapter is to investigate how various fused ring moieties containing ligands with different donor sites influences structure and control reactivity of their group 10 complexes in both catalysis and biomolecule interaction.

3.2 Results and discussion

3.2.1 Synthesis and characterization of ligands

Ligands (*E*)-2-(2-(2-(diphenylphosphaneyl)benzylidene)hydrazineyl)benzo[d]thiazole (**L1H**) and (*E*)-2-(2-(quinolin-8-ylmethylene)hydrazineyl)benzo[d]thiazole (**L2H**) was prepared through a simple condensation reaction (Scheme 3.3). The NNP- donor ligand **L1H** was obtained from the reaction of 2-(diphenylphosphaneyl)benzaldehyde and 2-hydrazineylbenzo[*d*]thiazole in 92% yield, while **L2H** having NNN- coordinating sites was prepared from quinoline-8-carbaldehyde and 2-hydrazineylbenzo[d]thiazole with a yield of 88%. Both the ligands were characterized by ATR-IR and NMR (Figure S3.1–S3.3). Their infrared spectra displayed a sharp peak at 744 cm^{-1} due to the $\nu_{C–S}$ and peaks at 1619 cm^{-1} (**L1H**) and 1614 cm^{-1} (**L2H**) may be attributed to C=N stretching of thiazole ring. The hydrazone (–HC=NNH–) formation was indicated by the presence of a $\nu_{C=N}$ peak at 1563 cm^{-1} and 1575 cm^{-1} in **L1H** and **L2H** respectively. In the ^{1}H NMR spectra, the proton resonated at 11.90 ppm and 12.50 ppm for **L1H** and **L2H** respectively, as a broad singlet was due to -NH proton. The ^{31}P NMR spectrum of **L1H** showed a singlet at δ= –15.40 ppm, which was appropriate for this type of phosphorus.

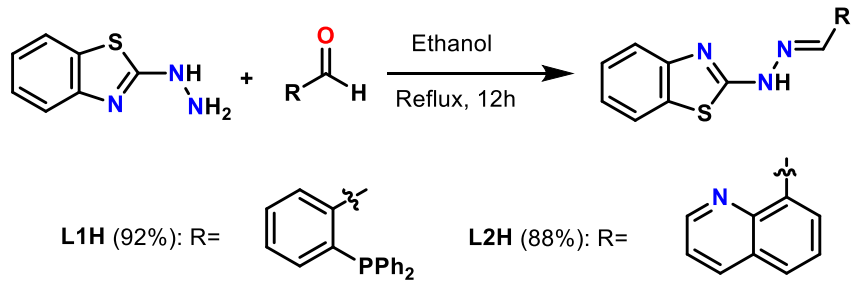

Scheme 3.3: Synthesis of ligands **L1H** and **L2H**

For the preparation of coumarin fused pyrrole ligand, 2-(pyridin-2-yl)chromen[4,3-*b*]pyrrol-4(1H)-one (**L3H**), the precursor 4-chloro-2-oxo-2H-chromene-3-carbaldehyde (**A**) was synthesized under Vilsmeier-Haack condition. The electrophilic substitution of chlorine in **A** with 2-picolylamine followed by the intramolecular aldol condensation reaction produced **L3H** in 72% yield (Scheme 3.4).

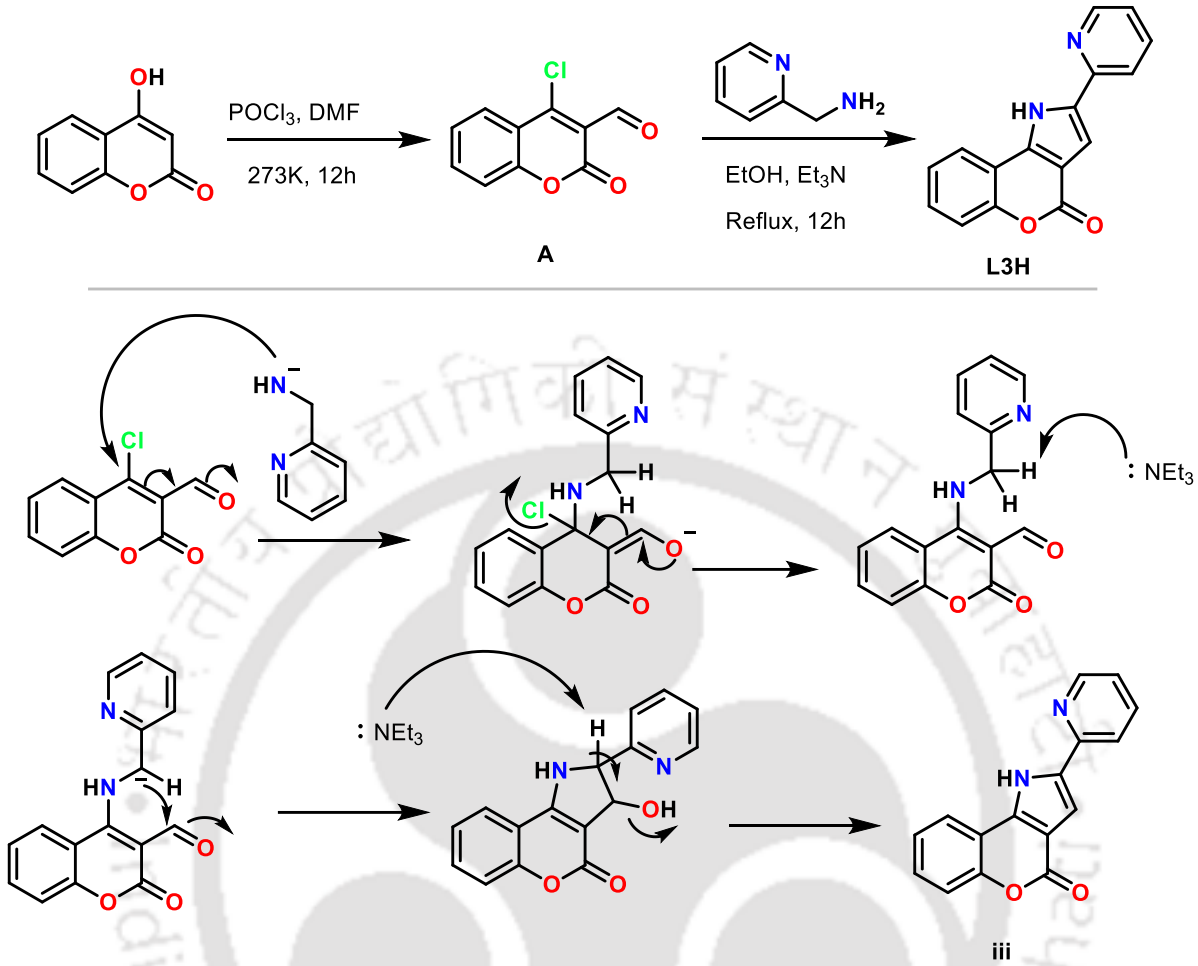

Scheme 3.4: Synthetic mechanism of **L3H**.

The presence of pyrrole–NH in **L3H** was confirmed from the peak at 10.92 ppm in ^{1}H NMR spectrum as well as presence of peak at 3283 cm^{-1} in the IR spectrum (Figure S3.1). Peaks due to lactone C=O and C–O–C stretching were observed at 1685 cm^{-1} and 1186 cm^{-1}, respectively.

Ligand, 3-(2-bromophenyl)-1-(pyridin-2-yl)imidazo[1,5-*a*]pyridine (**L4**) was obtained as light green solid from the reaction of 2,2′-dipyridyl ketone, 2-bromobenzaldehyde and NH_4OAc in hot acetic acid by a minor modification of reported procedure.[47] Following the same procedure, by taking 2,2′-dipyridyl ketone, 2-hydroxynaphthaldehyde and NH_4OAc, 1-(1-(pyridin-2-yl)imidazo[1,5-*a*]pyridin-3-yl)naphthalen-2-ol (**L5H**) was prepared in 68% yield as brown crystalline powder (Scheme 3.5). In the ^{1}H NMR spectrum, protons of the imidazo[1,5-*a*] nucleus in **L4** resonated at 8.73, 7.14, 6.97, 6.67 ppm, while that of in **L5H** resonated at 8.81, 7.15, 7.06, 6.64 ppm and their ^{13}C NMR spectrum

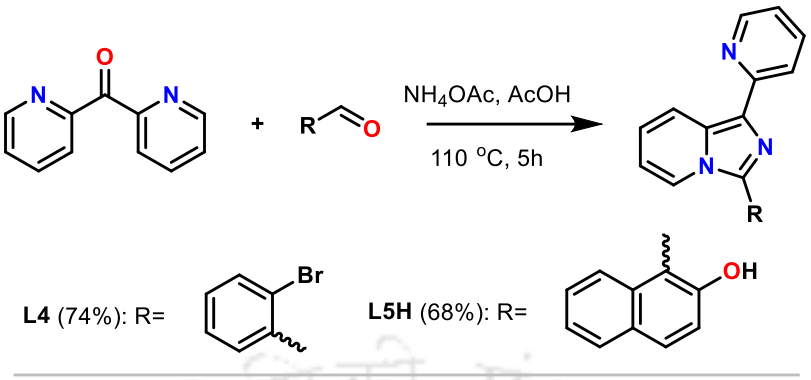

Scheme 3.5: Synthetic route for **L4** and **L5H**.

contained peaks matched with calculated number of carbons (Figure S3.4 and S3.5). The broad peak at 3066–2628 cm^{-1} in infrared spectrum of **L5H** was assigned to phenolic –OH group, the lowering in frequency may be due to intramolecular hydrogen bonding with imidazo[1,5-*a*]pyridine nitrogen. All ligands in their high-resolution mass spectrum rendered molecular ion peaks that matched well with calculated values (Figure S3.25).

3.2.2 Molecular structure of ligands

The molecular structure of all ligands was determined by single crystal X- ray diffraction analysis (Figure 3.1, S3.47 and Table S3.1–S3.11). The crystals of **L1H** and **L2H** were obtained by slow evaporation in DMF and crystallized in $P2_1/n$ and $P2_1/c$ space group respectively. The benzothiazole and phenylphosphene/quinoline groups were in opposite sides of C=N bond in **L1H** and **L2H** and thus in *E* configuration in their respective geometry. Both ligands displayed intermolecular discrete hydrogen bonded dimer through hydrazinyl-H and benzothiazole nitrogen having D···A distance 2.987(4) Å, 3.040(6) Å and D–H···A angle 167.3 ° and 175.0 ° in **L1H** and **L2H** respectively along 1-x, 1-y, 1-z (Figure S73–S74). Colorless crystals of **L3H** were obtained by slow evaporation of reaction mixture which crystallized in Pn space group. Pyrrole nitrogen and pyridine-N was seen in anti-conformation in a nearly planar structure. Presence of H-bonding between oxygen (O1) and pyrrole hydrogen (NH) in **L3H** with N1···O1 distance 2.866(5) Å and N1–H1···O2 angle 169.6° produced an infinite linear chain-like linkage (Figure S75) along -1+x, 1+y, z. Crystals of **L4** and **L5H** suitable for X-ray diffraction were obtained by slow evaporation their solution in methanol and dichloromethane (1:3) and crystallized in $P2_12_12_1$ and Pbca space group respectively. Phenolic group in **L5H** was involved in hydrogen bonding with pyridine

nitrogen resulting in a zig-zag 1D chain (Figure S76) where the O1···N1 distance, O1–H1···N1 angle and symmetry transformation were 2.771(2) Å, 158.0 ° and 1/2-x, -1/2+y, z respectively.

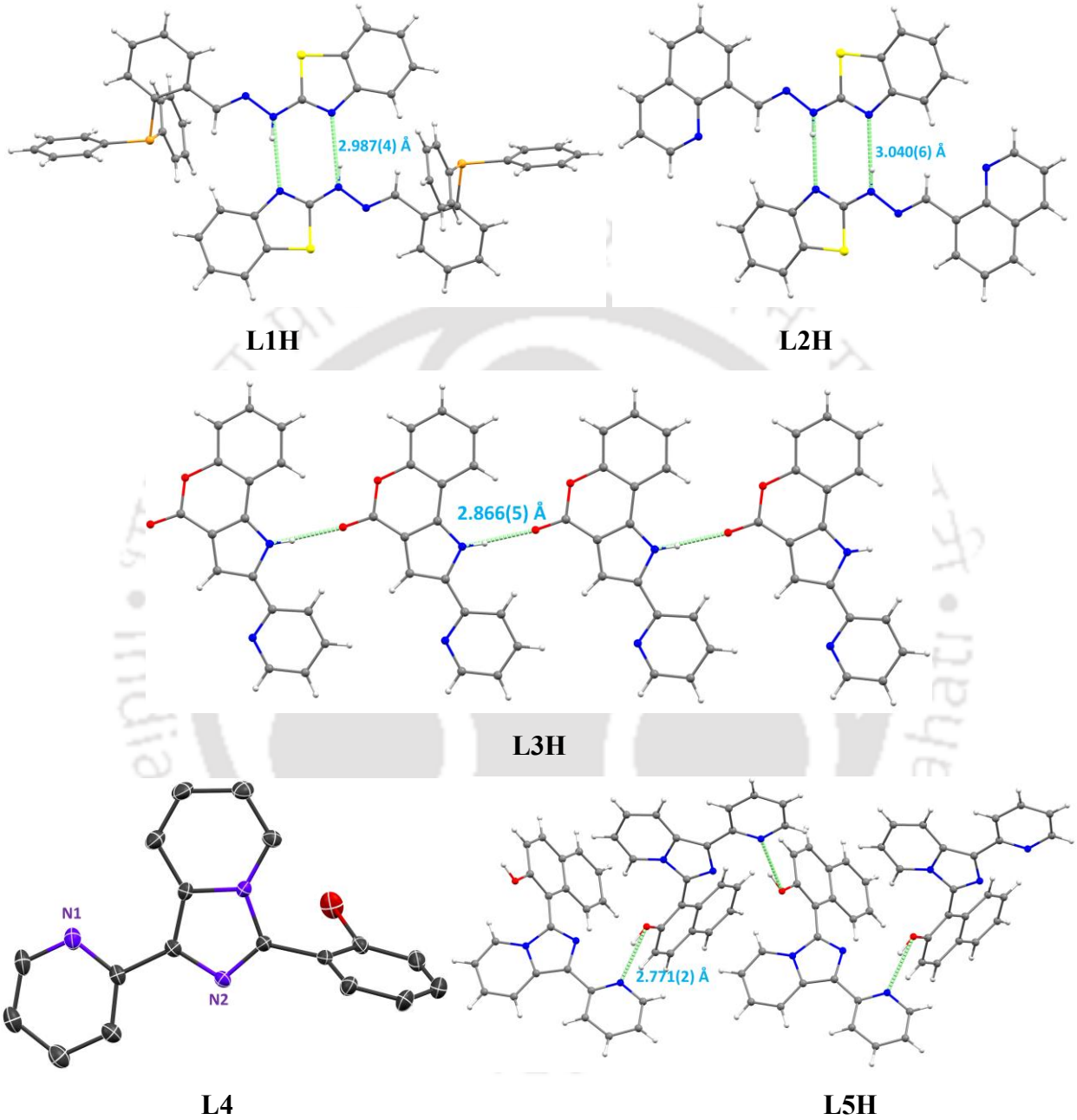

Figure 3.1: POV-Ray rendered ORTEP diagram (30% probability level) of all ligands and hydrogen bonding interaction in **L1H** – **L3H** and **L5H**.

3.2.3 Synthesis and characterization of complexes

Group 10 complexes with general composition [M(**L1**)Cl] {M = Ni (**1a**), Pd (**2a**), and Pt (**3a**)} were prepared from the reaction of $NiCl_2{\cdot}6H_2O$, $PdCl_2$ and $PtCl_2(CH_3CN)_2$ with ligand **L1H** in 1:1

molar ratio (Scheme 3.6). The peak corresponding to benzothiazole ring $\nu_{C=N}$ in **L1H** (1619 cm^{-1}) was absent in the respective IR spectra of **1a** – **3a** may be due to delocalization of double bond followed by metal coordination. The peak due to hydrazone imine $\nu_{C=N}$ in **L1H** (1563 cm^{-1}) was observed at a lower wavenumber in **1a** (1469 cm^{-1}), **2a** (1463 cm^{-1}), and **3a** (1478 cm^{-1}) indicating the coordination (Figure S3.1). The ^{1}H NMR peak for hydrazenyl nitrogen (-NH) which resonated at 11.90 ppm in **L1H** was absent in **1a** – **3a** confirmed its loss because of complexation (Figure S3.7, S3.11 and S3.14). Moreover, other protons were shifted to more up-field in **1a** as compared to **2a** and **3a** which indicating that Ni(II) center is more electron rich than Pd(II) and Pt(II) (Figure 3.2). From ^{31}P NMR, **1a** – **3a** displayed more deshielding effect and δ (ppm) values followed the trend **2a** (27.37) > **1a** (13.19) > **3a** (1.69) > **L1H** (–15.40). The stronger relativistic effect and high π-backdonation of platinum may be the cause for lesser deshielding making phosphorous to resonate at upfield along with appearance of Pt-satellites.

Attempts to isolate octahedral bis-complex of nickel(II) with **L1H** by using nickel chloride in 2:1 molar ratio also yielded only **1a**. Interestingly, when few drops of triethylamine were added to facilitate the deprotonation, a distorted square planar complex [Ni(**L1**)$_2$] (**1b**) was isolated and $PdCl_2$ also produced a similar complex [Pd(**L1**)$_2$] (**2b**) with two units of $\mathbf{L1}^-$. The ^{31}P NMR spectrum contained two peaks at 22.29, -14.49 ppm for **1b** and at 27.14, -13.30 ppm for **2b** indicating the presence of coordinated (+δ value) and uncoordinated (–δ value) phosphorous atoms (Figure 3.3). However, both complexes did not produce interpretable ^{1}H and ^{13}C NMR spectra.

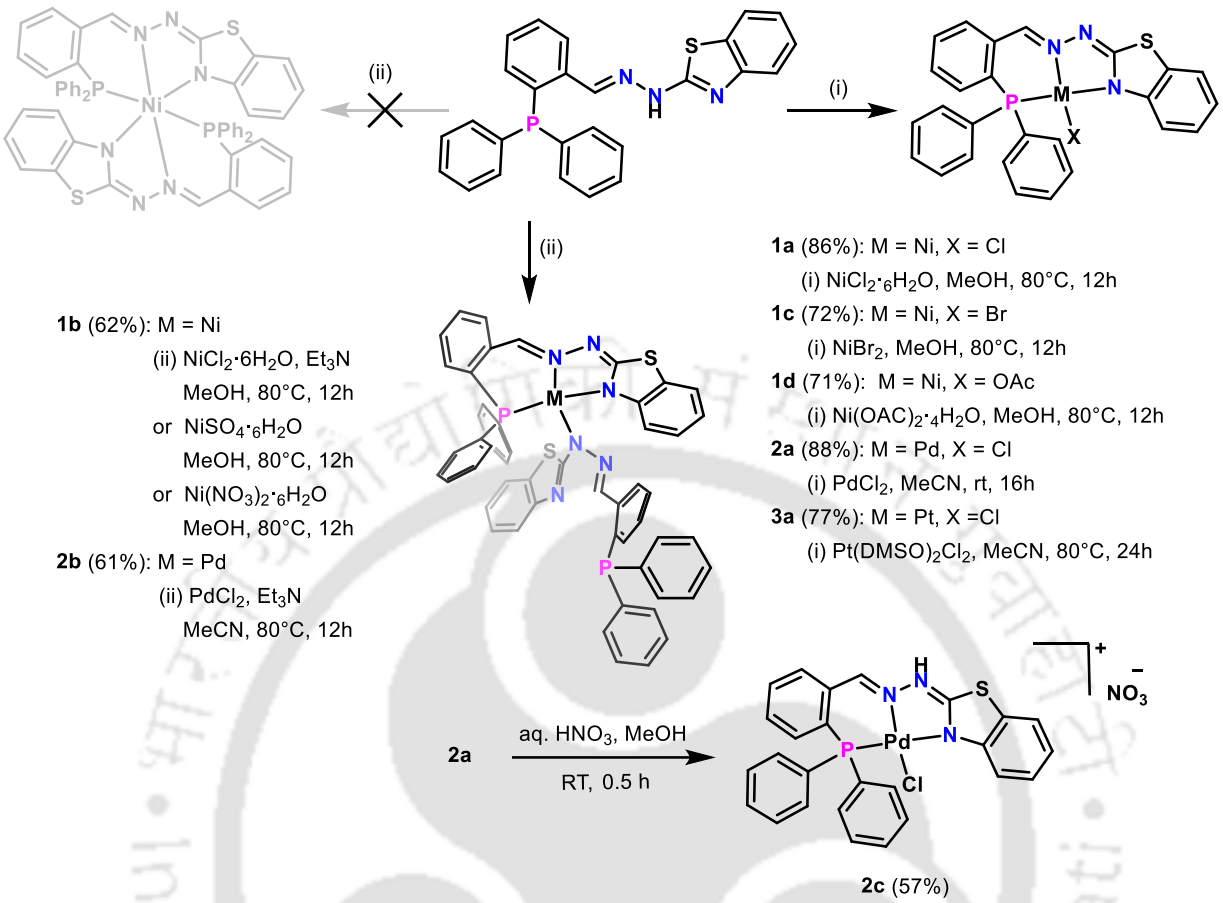

Scheme 3.6: Synthetic Scheme for **1a** – **1d**, **2a** – **2c** and **3a**.

The reaction of **L1H** with various nickel salts ($NiBr_2$, $Ni(OAc)_2{\cdot}4H_2O$, $Ni(NO_3)_2{\cdot}6H_2O$, and $NiSO_4{\cdot}4H_2O$) were also carried out by following the same procedure for **1a**. Nickel acetate and nickel bromide successfully produced [Ni(**L1**)X] {X = Br (**1c**), OAc (**1d**)} but, in case of nitrate and sulfate salts the complex [Ni(**L1**)$_2$] (**1b**) was isolated. ^{31}P NMR spectra **1c** and **1d** were comparable to that of **1a** (Figure 3.3). Presence of acetate co-ligand in **1d** was inferred from IR spectrum (1625 cm^{-1}) and ^1H NMR peak at δ = 1.28 ppm (-CH_3) (Figure S3.10).

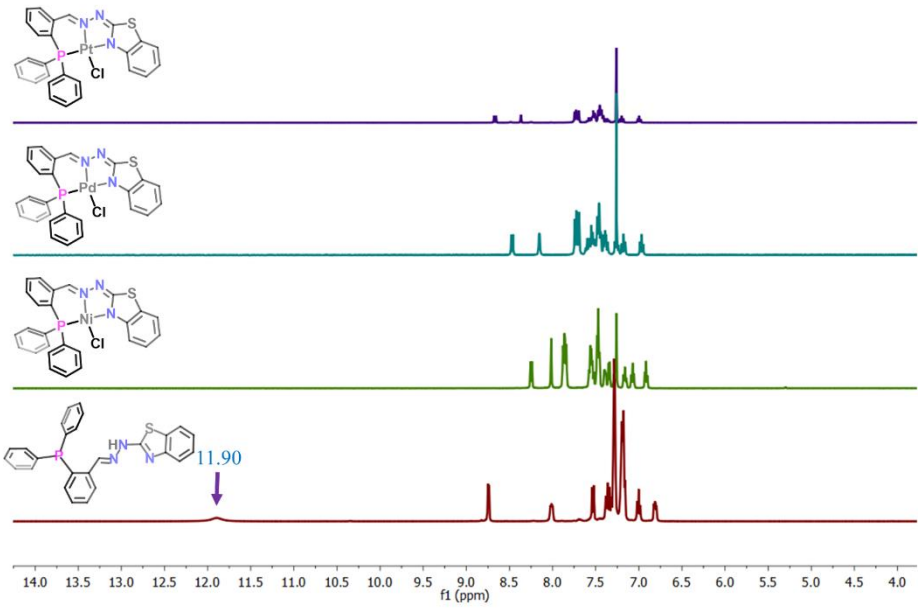

Figure 3.2: ^{1}H NMR (stacking view) of **L1H** and **1a – 3a**.

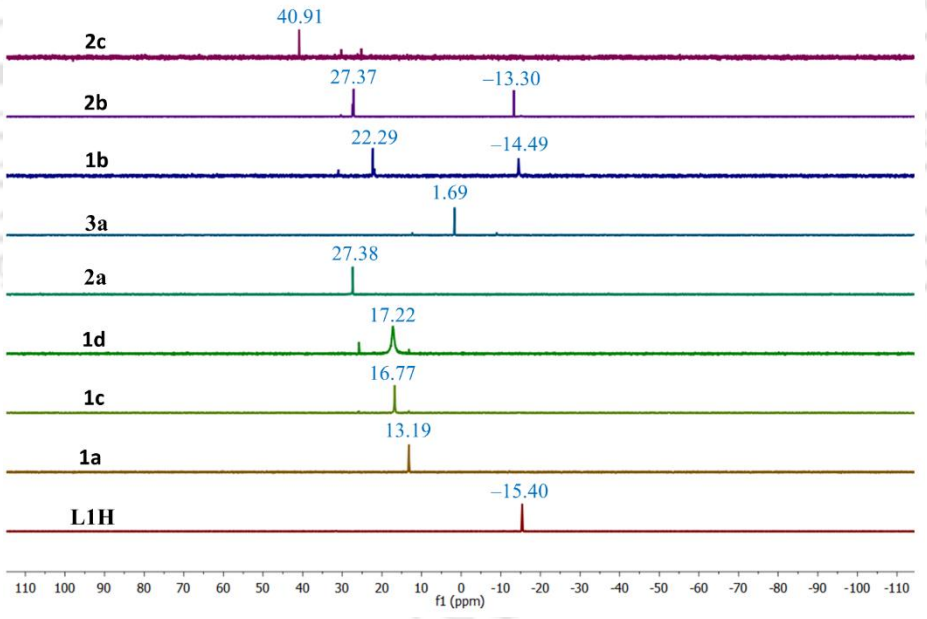

Figure 3.3: ^{31}P NMR (stacking view) of **L1H** and **1a – 3a**.

In an attempt to protonate the complexes of **L1**$^{-}$, methanolic solution of **1a**–**3a** (5.0 mL, 0.01M) were stirred with addition of 0.1 mL (0.5 M) aqueous HNO_3, for 0.5 h (Scheme 3.6). In case of **2a**, single crystal of protonated cationic complex [Pd(**L1H**)Cl]NO_3 (**2c**) was isolated after slow evaporation of the solution. Unfortunately, crystallization and isolation of similar protonated complex from the reaction mixture of **1a** and **3a** were not successful. In the ^{31}P NMR spectrum,

2c displayed peak at higher field (40.67 ppm) than that of in **2a** (27.37 ppm) may be due to cationic complex (Figure S3.13). HRMS molecular ion peak corresponding to the formula $[\mathbf{M}+H]^+$ for **1a**–**1d**, **2b** and **3a**, $[Pd_2(\mathbf{L1})_2Cl]^+$ for **2a**, $[M]^+$ for **2c** and $[M\text{-}X+MeCN]^+$ for **1c** (X = Br) and **1d** (X = OAc) matched well with calculated values (Figure S3.26–S3.33).

Under similar reaction condition of **1a**, **L2H** did not produce any pincer complex. When the stoichiometry was changed to 2:1 (**L2H**:$NiCl_2{\cdot}6H_2O$), $[Ni(\mathbf{L2})_2]$ (**1e**) was isolated as pure crystalline brown solid (Scheme 3.7). The complex **1e** was 2-electron paramagnet and the magnetic moment in solution was found to be 2.76 μ_B measured using Evan's NMR method. ^{1}H NMR spectrum of **1e** was recorded in far high field and resonances appeared as broad singlets at δ = 32.77, 25.47 and 14.94 ppm, due to the presence of paramagnetic Ni(II) center (Figure S3.18). The complex [Pd(**L2**)Cl] (**2d**) was isolated from the reaction of **L2H** with $PdCl_2$ in 1:1 ratio in acetonitrile, and by stirring **2d** with 1.2 equivalents of NaN_3 in acetone, produced [Pd(**L2**)N_3] (**2e**) at ambient temperature (Scheme 3.7).

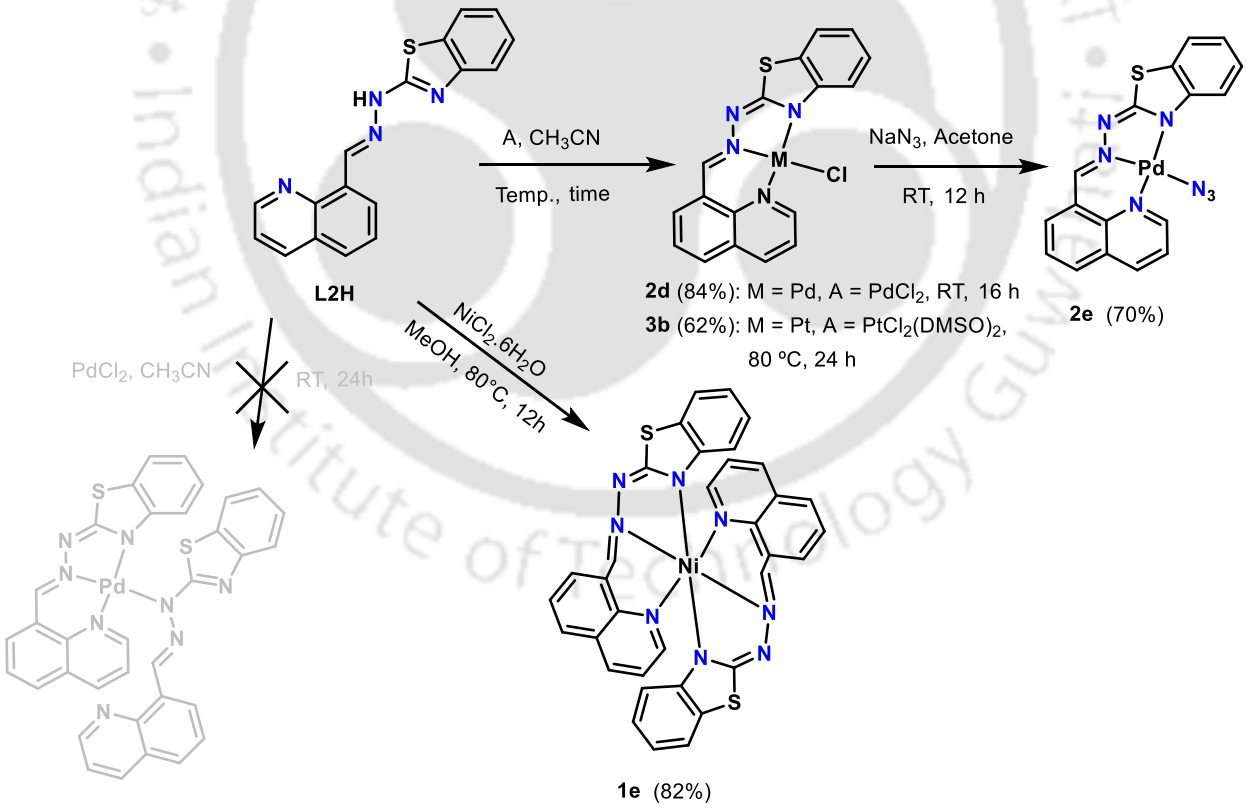

Scheme 3.7: Synthetic Scheme for **1e**, **2c**, **2d**, and **3b**

Presence of a sharp peak at 2038 cm^{-1} in ATR-IR spectrum of **2e** indicated the presence of coordinated azide ion (Figure S3.1). A platinum congener [Pt(**L2**)Cl] (**3b**) was also prepared by the reaction of **L2H** and $[PtCl_2(DMSO)_2]$ in acetonitrile. The ^1H NMR spectrum of **2d**, **2e** and **3b** lacked the signal due to -NH proton that was appeared at δ = 12.50 ppm in **L2H**, confirmed deprotonation (Figure S3.15–S3.17). Other protons except -CH=N were resonated at downfield while imine proton shifted to upfield as compared to ligand due to coordination to the metal ion. The HRMS spectrum of **1e**, **2d**, **2e**, and **3b** displayed peaks at *m/z* at 665.0833, 854.9197, 861.9499 and 539.0587 {calcd. 665.0833 for $[Ni(\mathbf{L2})_2+H]^+$, 854.9171 for $[Pd_2(\mathbf{L2})_2Cl]^+$, 861.9581 for $[Pd_2(\mathbf{L2})_2N_3]^+$ and 539.0613 for $[Pt(\mathbf{L2})MeCN]^+$} respectively (Figure S3.34–S3.37).

The complexes $[Ni(\mathbf{L3})_2(H_2O)_2]$ (**1f**), $[Pd(\mathbf{L3})_2]$ (**2f**) and $[Pt(\mathbf{L3})_2]$ (**3c**) were synthesized by refluxing **L3H**, $NiCl_2{\cdot}6H_2O$ / $PdCl_2$ / $[PtCl_2(DMSO)_2]$ in 2:1 molar ratio along with few drops of triethylamine (Scheme 3.8). The sharp peak in the ATR-IR spectrum of **L3H** at 3283 cm^{-1} due to pyrrole N-H stretching was absent in **1f**, **2f** and **3c** which indicated its deprotonation. This was also established by the ^1H NMR spectra where the broad peak for –NH proton at 10.92 ppm in **L3H** was absent in **1f** and **2f**. NMR spectra of **3c** was not recorded due to its poor solubility in common deuterated solvents.

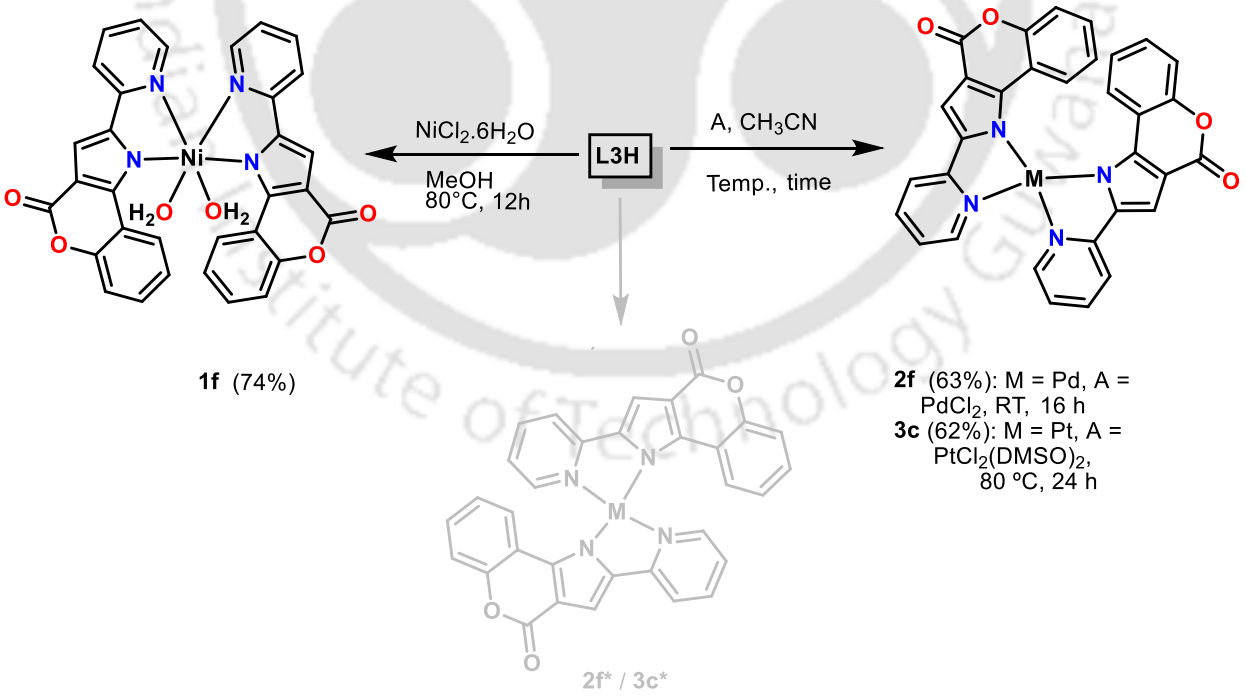

Scheme 3.8: Synthetic Scheme for **1f**, **2f** / **2f*** and **3c** / **3c***

In ATR-IR spectrum of **1f**, the broad peak at 3296 cm^{-1} may be due to water bound to nickel ion and at 1685, 1726 and 1701 cm^{-1} respectively in **L3H**, **1f** and **2f** were due to $\nu_{C=O}$. The high-resolution mass spectrum also established the presence of $[Ni(\mathbf{L3})_2–H_2O+H]^+$, and $[M+H]^+$ (M= **2f** and **3c**) ions (Figure S3.38–S3.38). The ^{1}H NMR spectrum of **1f** displayed broad peaks due to paramagnetic Ni(II) center and it showed magnetic moment 2.81 μB which was in congruent with two unpaired electrons. The possible geometry of **2f**/**2f*** and **3c**/**3c*** was confirmed from their X-ray structure and discussed in crystallographic section.

The reaction of **L4** with $NiCl_2{\cdot}6H_2O$ produced $[Ni(\mathbf{L4})_2(H_2O)_2]Cl_2$ (**1g**) which was a two-electron paramagnetic Ni(II) complex and the magnetic moment was 2.73 μ_B calculated using Evan's NMR method. A similar procedure was carried out with NNO- tridentate ligand **L5H** to synthesize a pincer Ni(II) complex, but a complex with two equivalents of ligand alike **1g** was identified as $[Ni(\mathbf{L5H})_2(H_2O)_2]Cl_2$ (**1h**) (Scheme 3.9). All the trials including alteration in stoichiometric ratio and reaction condition to isolate a pincer Ni(II) complex using **L5H** was not successful. The complex **1h** was paramagnetic (2.69 μ_B) and thus did not produce any interpretable NMR spectra. Presence of water molecule in the complex was detected in ATR-IR spectrum (3448 cm^{-1}) (Figure S3.1). Under the similar condition of **2b** and **3a**, $[M(\mathbf{L4})Cl_2]$ {M = Pd(**2g**), Pt (**3d**)} was precipitated and similarly, **L5H** yielded pincer Pd(II) and Pt(II) complexes of composition [M(**L5**)Cl] {M = Pd (**2h**), Pt (**3e**)} using the conditions of **2f** and **3c** (Scheme 3.9). Complexes **1g**, **1h, 2g**, **2h**, **3d**, and **3e** were also characterized by high resolution mass spectrometry and successfully rendered peaks that were in congruence with calculated values along with isotopic pattern (Figure S3.41–S3.45). The ^{1}H NMR spectrum of **L4** and **L5H** contained peaks respectively at δ = 8.73, 7.14–6.67 ppm and 8.81, 7.15–6.64 ppm corresponding to imidazo[1,5-*a*]pyridine nucleus. In Pd(II)/Pt(II) complexes **2g**, **2h**, **3d**, and **3e**, due to coordination, the peaks at 8.73 ppm (**L4**) and 8.81 ppm (**L5H**) were shifted to upfield, while the other peaks were observed at more downfield (Figure S3.21–S3.24).

Furthermore, field emission scanning electron microscope images were taken to understand the morphology of all compounds and the smooth surface images without any pores established existence of molecular packing in elevated order (Figure S3.46).

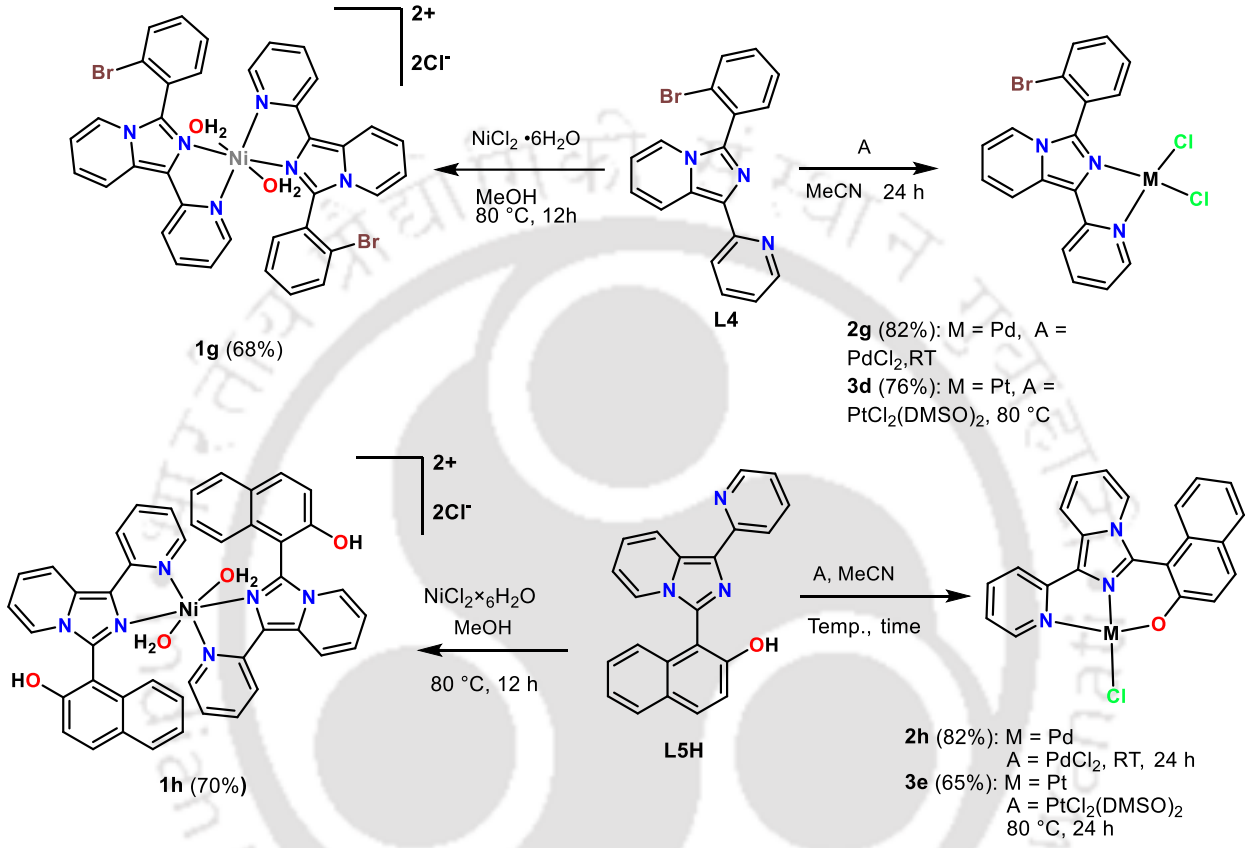

Scheme 3.9: Synthesis of **1g**, **2g**, **1h**, **2h**, **3d**, and **3e**.

3.2.4 Electronic spectra

The electronic absorption spectra of all ligands and complexes were recorded in acetonitrile in the range of 200–700 nm (Figure 3.4). The electronic spectrum of **L1H** and **L2H** showed a prominent peak at 345 nm (27400 $M^{-1}cm^{-1}$) and 365 nm (25000 M^{-1} cm^{-1}) mainly due to n → π* transition. Complexes of **L1H** and **L2H**, exhibited a new peak at around 490 nm which may be attributed to MLCT transition with decrease in the molar absorptivity of n → π* bands and appearance of band due to π → π* transition at around 290 nm. The trend in ε values of 490 nm band was **2b** < **1b** < **1c** < **2a** < **1a** < **1d** < **3a**. The Pt(II) complex displayed stronger absorption may be due to strong spin-orbit coupling which renders greater intensity to the d-d transition, thus absorption was more

intense than Ni(II) and Pd(II) congener. The major twin bands due to n → π* transition was observed at 340 nm (28490 $M^{-1}cm^{-1}$) and 325 nm (29930 $M^{-1}cm^{-1}$) in **L3H**. The Ni(II) complex **1f** exhibited red shift at 361 nm (14310 $M^{-1}cm^{-1}$) while **2f** and **3c** displayed comparatively less intense bands at 341 nm (9280 $M^{-1}cm^{-1}$) and 395 nm (15430 $M^{-1}cm^{-1}$) respectively possibly due to ILCT. Two major broad bands were observed for **L4** at 294 nm (9695 $M^{-1}cm^{-1}$) and 358 nm (5815 $M^{-1}cm^{-1}$) while its Ni(II) complex **1g**, displayed bands at 360 nm (31285 $M^{-1}cm^{-1}$) and 325 nm (22250 $M^{-1}cm^{-1}$) due to coordination. The **2g**, exhibited a peak at 378 nm (12330 $M^{-1}cm^{-1}$) while the **3d** displayed a band at 406 nm (8390 $M^{-1}cm^{-1}$), 365 nm (10500 $M^{-1}cm^{-1}$) and 383 nm (10470 $M^{-1}cm^{-1}$). Similarly, for **L5H**, two split broad bands were seen at 332 nm (21820 $M^{-1}cm^{-1}$) and 360 nm (19740 $M^{-1}cm^{-1}$) while in **1h**, **2h** and **3e**, major bands at 277 nm (17230 $M^{-1}cm^{-1}$), 341 nm (22260 $M^{-1}cm^{-1}$); 382 nm (9910 $M^{-1}cm^{-1}$), 400 nm (8650 $M^{-1}cm^{-1}$); and 395 nm (13650 $M^{-1}cm^{-1}$), 451 nm (12430 $M^{-1}cm^{-1}$) were observed possibly due to MLCT.

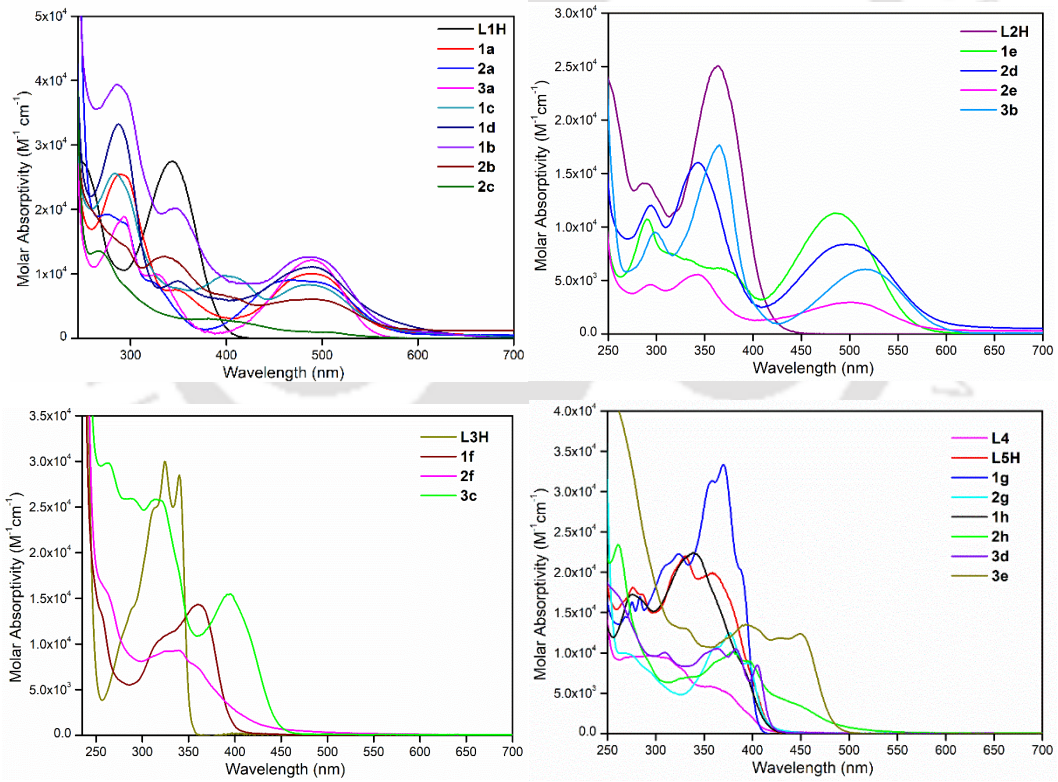

Figure 3.4: Electronic spectra of all ligand and complexes in acetonitrile.

3.2.5 Crystallography and coordination chemistry of complexes

The molecular structure of all complexes discussed here was established by single crystal X-ray diffraction. The crystals of **1a, 1c**, **1d**, **2a** were obtained by slow evaporation in DMF while **1b**,

2b, and **3a** from 1:3 mixture of methanol and dichloromethane and **2c** from the reaction mixture (Table S3.12–S3.31). In **1a** – **3a**, the ligand **L1**$^{-}$ coordinated in a tridentate NNP pincer mode by forming a five-membered chelate ring using benzothiazolate nitrogen (N_T) and imine nitrogen (N_I), a six-membered chelate using N_I and phosphorus donor (P) was also formed while the fourth position was occupied by a chloride ion. The delocalization of benzothiazole ring double bond at C2-carbon after deprotonation of proximal hydrazino nitrogen (N_H) was also confirmed from bond distances. In **L1H**, C2–N_H bond length was 1.334(3) Å and in **1a** – **3a** it was decreased by 0.023(3)–0.039(4) Å while lengthening of C2–N_T distance by 0.047(3)–0.060(4) Å was also seen in **1a** – **3a** respectively as compared to that of in **L1H** (1.292(3) Å. The fluctuation in imine (C8=N) bond distance was also observed in **1a** (1.299(3) Å), **2a** (1.287(8) Å), and **3a** (1.281(7) Å) as compared to that of in **L1H** (1.262(3) Å) due to the trans influence of chloride on N_I as well as π-back donation (Table 3.1).

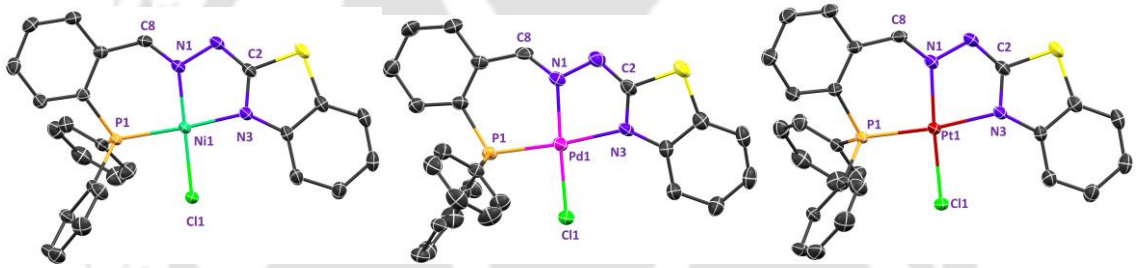

1a **2a** **3a**

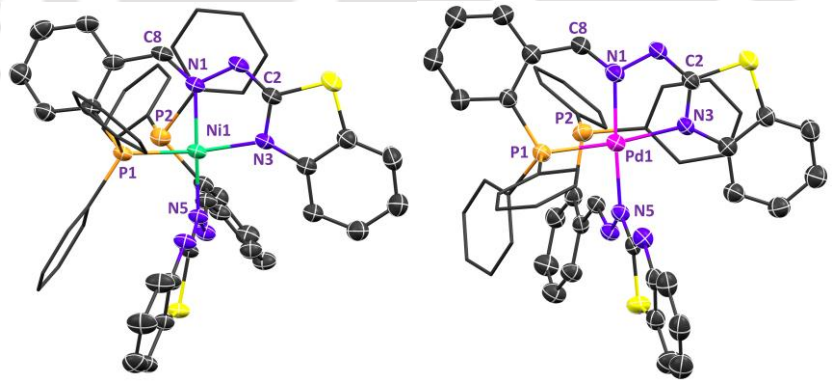

1b **2b**

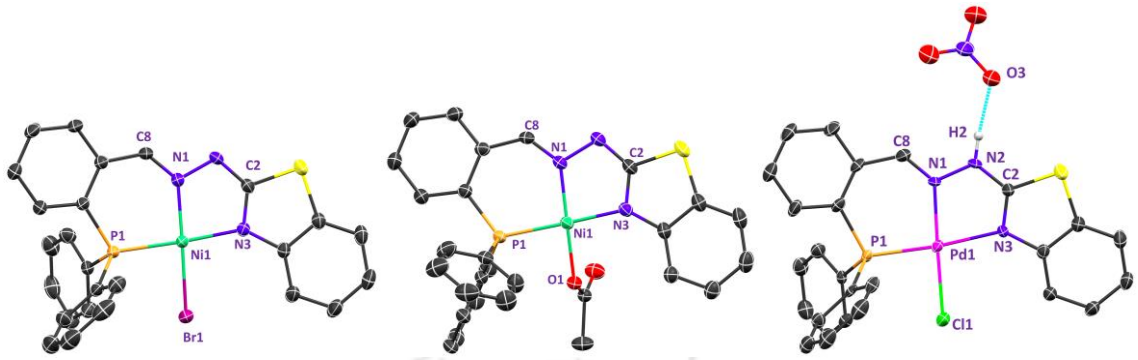

1c **1d** **2c**

Figure 3.5: POV-Ray rendered ORTEP diagrams (30% probability level) of **1a** – **1d**, **2a** – **2c**, and **3a**. Hydrogen atoms (except H2 in **2c**) are omitted for clarity.

As two equivalents of **L1H** was used to produce **1b** and **2b**, the 4th coordination site was occupied by hydrazenylate nitrogen (N_H) of another unit of anionic **L1**$^-$ in both complexes as confirmed by X-ray structure. The bond distances followed the trend Ni–N_H < Ni–N_I < Ni–N_T in **1b** and Pd–N_I < Pd–N_H < Pd–N_T in **2b** may be due to combined effect of better σ-donating ability of anionic N_H and increased π-donation into C=N_I group. The distance of Pd–N_I in **2a** was slightly shorter than that in **2b** while Ni–N_I was nearly same in both **1a** and **1b** due to the negligible trans influence (Table 3.1). Both **1b** and **2b** contained free phosphine group and the nonbonded M···P2 distance was 4.893(1) Å (**1b**) and 5.036 Å (**2b**). The 4th position, that was occupied by chloride ligand in **1a** has been replaced by bromide and acetate ions in **1c** and **1d** respectively. The imine (C8=N_I) bond distance in **1c** and **1d** was comparable but 0.032(1)-0.035(1) Å longer than that of free ligand because of π-back bonding due to coordination.

Table 3.1: Selected bond lengths (Å) in **L1H**, **1a** – **1d**, **2a** – **2c**, and **3a**.

	M – P1	M – N_I	M – N_T	M – X	C8 – N_I	C2 – N_H	C2 – N_T
L1H					1.262(3)	1.334(3)	1.292(3)
1a	2.165(1)	1.898(2)	1.937(2)	2.162(1)	1.299(3)	1.311(3)	1.339(3)
2a	2.212(2)	2.035(5)	2.086(5)	2.287(2)	1.287(8)	1.325(8)	1.333(8)
3a	2.212(1)	2.013(4)	2.077(4)	2.300(1)	1.281(7)	1.295(7)	1.352(7)
1b	2.161(1)	1.898(4)	1.934(4)	1.892(3)	1.299(6)	1.301(6)	1.349(6)
2b	2.227(3)	2.021(8)	2.085(7)	2.049(7)	1.285(11)	1.322(11)	1.336(11)
1c	2.1707(8)	1.904(2)	1.948(2)	2.3071(5)	1.294(4)	1.313(4)	1.341(4)

1d	2.154(5)	1.885(2)	1.907(2)	1.877(1)	1.297(2)	1.312(3)	1.340(2)
2c	2.223(3)	2.021(7)	2.096(8)	2.285(3)	1.275(13)	1.321(13)	1.307(13)

(**1a** – **1d**, M = Ni; **2a** – **2c**, M = Pd; **3a**, M = Pt; **1a**,**2a**, **3a** and **2c**, X = Cl; **1b** and **2b**, X = N_H; **1c**, X = Br; and **1d**, X = OAc)

Table 3.2: Selected bond angles (deg) in **1a** – **1d**, **2a** – **2c**, and **3a**.

	P1–M–X	N_I–M–P1	N_I–M–N_T	N_T–M–X	N_T–M–P1	N_I–M–X
1a	86.16(4)	93.51(6)	83.15(7)	97.14(6)	171.84(5)	179.57(5)
2a	88.09(6)	93.70(15)	80.3(2)	97.87(14)	172.20(14)	177.98(14)
3a	88.59(5)	94.45(13)	79.47(17)	97.52(12)	172.64(12)	176.96(13)
1b	93.44(12)	88.76(12)	82.73(16)	96.61(16)	164.83(12)	172.53(15)
2b	90.0(2)	93.5(3)	79.7(3)	96.9(3)	171.8(2)	176.1(3)
1c	84.85(2)	94.14(8)	83.24(10)	97.69(7)	176.62(8)	177.86(8)
1d	85.47(4	94.97(5)	83.62(7)	96.72(6)	168.63(5)	176.00(6)
2c	86.93(10)	94.6(2)	80.2(3)	98.3(2)	174.8(2)	177.4(3)

(**1a** – **1d**, M = Ni; **2a** – **2c**, M = Pd; **3a**, M = Pt; **1a**,**2a**, **3a** and **2c**, X = Cl; **1b** and **2b**, X = N_H; **1c**, X = Br; and **1d**, X = OAc)

In **2c**, nitrate ion was in hydrogen bonded with N_H–H with distance N2 ···O3 of 2.69(2) Å. The effect of added proton to N_H shifts the π-bond onto N_T, as a result compared to **2a** (i) C2–N_T length in **2c** decreased by 0.026(5) Å and (ii) Pd–N_I length lessened by 0.014(2) Å. Thus, the divalent Ni, Pd and Pt displayed distorted square planar geometry in **1a** – **1d**, **2a** – **2c**, and **3a** (Figure 3.5, Table 3.1 and 3.2).

Crystals of **1e**, **2d**, and **2e** were obtained from slow evaporation of DMF solution and **3b** was found from 3:1 mixture of methylene chloride and methanol. In **1e**, two **L2**$^-$ units were coordinated in $N_IN_QN_T$-tridentate fashion and the quinoline nitrogen (N_Q) and N_T were *trans* to each other. The N_I–Ni–N_Q chelate ring was six-membered while N_I–Ni–N_T was five-membered and displayed a distorted octahedral geometry around nickel(II) ion (Figure 3.6, Table S3.32–S3.34). Interestingly, **1e** was not a centrosymmetric molecule as one of the ligand units was not planar. From the trans angles N_T–Ni–N_Q (167.2(1)°) and N_I–Ni–N_I (166.1(1)°), a cis-cis-trans-(N_QN_Q)(N_TN_T)(N_IN_I) configuration was found around the metal center. In **2d**, **L2**$^-$ spanned three coordination sites and hold Pd(II) in NNN- pincer mode. Like **2a**, the fourth location was occupied by chloride ion and

N_Q lies trans to N_T as in **1e**. The chloride ligand in **2d** was replaced by azide group in **2e** and the azide group coordinated with one terminal nitrogen atom (N_A) in bent fashion (Figure 3.6). The coordination mode of ligand in **3b** and bond parameters were nearly like that of in **2d**. The divalent metal center in **2d**, **2e** and **3b** possessed a five membered N_I–Pd–N_Q and a six membered N_I–Pd–N_T chelate ring and thus displayed a distorted square planar geometry around the metal center (Figure S3.57–S3.59, Table S3.35–S3.41).

The complexes **1f**, **2f** and **3c** crystallized from DMF solution and found in I2/c (**1f**) and $P\bar{1}$ (**2f**, **3c**) space group. In **1f**, Ni(II) center embedded with two bidentate **L3**$^-$ ions bound by pyridine-N (N_P) (neutral) and pyrrole nitrogen (N_L) (anionic) atoms. The two N_L were in *trans* position while two N_P were in *cis*. Two water molecules were positioned at remaining two *cis* sites and thus surrounded in a distorted octahedral geometry around Ni(II) (Figure 3.7, table S3.43–SS3.44). The nickel-bound water molecules were involved in bifurcated hydrogen bonding interactions between

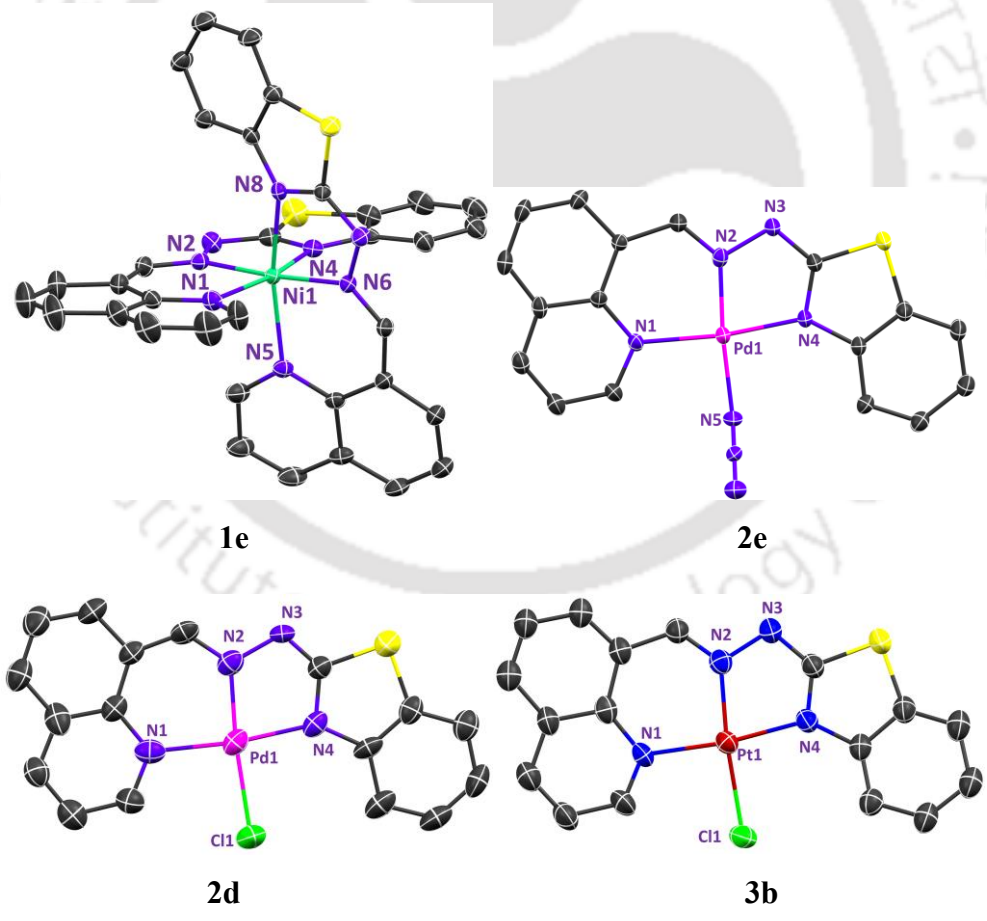

1e **2e**

2d **3b**

Figure 3.6: POV-Ray rendered ORTEP diagrams (30% probability level) of **1e**, **2d**, **2e**, and **3b**. Hydrogen atoms are omitted for clarity.

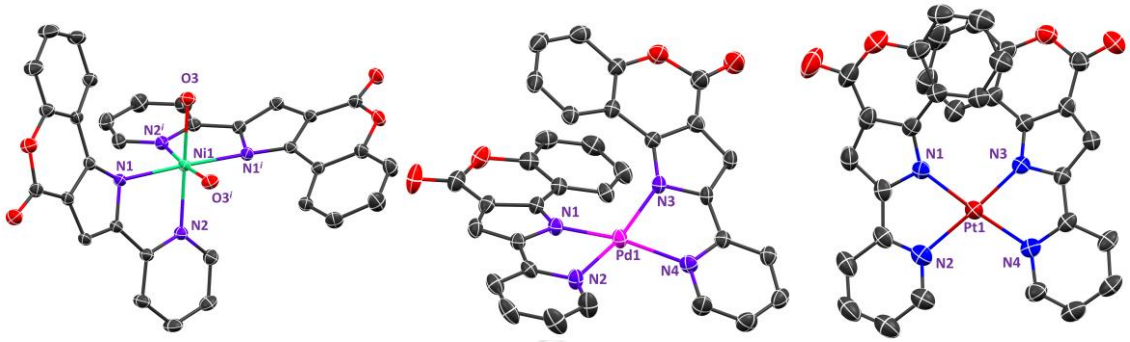

1f **2f** **3c**

Figure 3.7: Molecular structure of **1f**, **2f** and **3c**. Hydrogen atoms are omitted for clarity and thermal ellipsoids are shown at the 30% probability level.

oxygen of DMF (O3···O4, 2.658(4) Å, O3-H···O4: 166.4°) along 1-x, y, 1.5-z and carbonyl oxygen of coumarin moiety (O3···O2, 2.802(3) Å, O3-H···O2: 168.9°) along x, y, z (Figure 3.8). Both **2f** and **3c** also contained two **L3**$^{-}$ units but interestingly, N_P and N_L were oriented *trans* to each other.

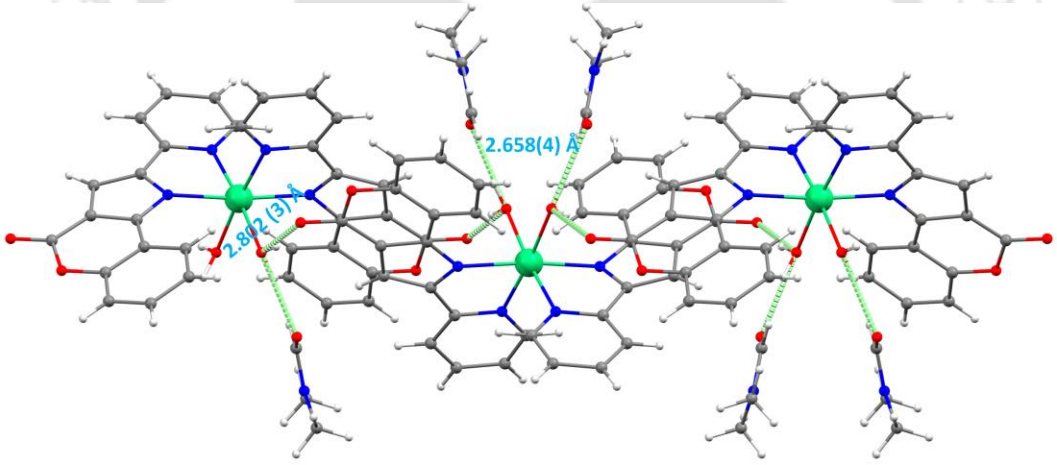

Figure 3.8: Hydrogen bonding interaction in **1f**.

This has brought two sterically bulky coumarin moieties in close vicinity. As a result, these two coumarin moieties got twisted with respect to each other and the angle calculated between the pyrrole rings was 37.4° (**2f**) and 33.22° (**3c**). Overall, the central metal ion had a severely distorted square planar geometry which was also evident from the bond angles around the metal center (Table 3.3, 3.4, S3.45–S3.48). The calculated geometry index (τ_4) was 0.256 (in **2f**) and 0.148 (in **3c**). This interesting geometry is due to the trans effect as **L3**$^{-}$ was a N, N^{-} donor and the anionic N_L being a strong sigma donor exerting a significant trans influence. Thus, to minimize electronic

repulsion, Pd(II)/Pt(II) forced N_P and N_L to occupy positions *trans* to each other thereby avoided two N_L facing each other in opposite.

To investigate theoretically, the **2f** and **2f*** (Scheme 3.8) were optimized using density functional theory. In **2f***, both HOMO and LUMO electron density were accumulated along the axis while in 2f, the electron clouds were seen in one side along the molecular axis. Thus, to minimize the tension from electronic repulsion, thus *trans* geometry (**2f**) was favored rather than *cis* (**2f***) (Figure 3.11). Also, in **2f***, the complex was facing intense distortion in geometry due to steric hindrance at both ends of ligands.

Table 3.3: Selected bond lengths (Å) in **1f**, **2f** and **3c**. (in **1f**, N3 = $N1^i$, N4 = $N2^i$)

	M – N1	M – N2	M – N3	M – N4	M – O1
1f (M = Ni)	2.134(2)	2.077(2)	2.134(2)	2.077(2)	2.092(2)
2f (M = Pd)	2.030(4)	2.100(5)	2.013(4)	2.108(5)	
3c (M = Pt)	2.034(9)	2.015(8)	2.041(8)	1.994(8)	

Table 3.4: Selected bond angles (deg) in **1f**, **2f** and **3c**

	N1–M–N2	N3–M–N1	N1–M–N4	N3–M–N2	N3–M–N4	N2–M–N4
1f (M = Ni)	80.32(7)	174.29(10)	95.84(7)	95.84(7)	80.32(7)	96.22(11)
2f (M = Pd)	79.57(18)	101.86(18)	162.34(18)	161.52(19)	79.38(18)	104.93(18)
3c (M = Pt)	78.7(3)	100.6(4)	173.7(3)	175.7(4)	78.8(3)	102.3(3)

Crystals of **1g** were obtained from 1:1 mixture of methanol and dichloromethane while **1h** was obtained from the slow evaporation of reaction mixture. Both were found in $P\bar{1}$ and C2/c space group, **1h** contained half of the molecule in asymmetric units. The 2-bromophenyl rings in **1g** and 2-hydroxy naphthyl rings in **1h** were highly disordered and thus modelled using partial occupancy factor. Ni(II) center in each molecule was coordinated by two ligand unit molecules using pyridine-N (N_{PY}) and imidazo[1,5-a]pyridine-N (N_{IM}) in which both N_{PY} were *trans* to each other while two N_{IM} were in *cis* fashion. Other two coordination sites were occupied by water molecule (O_W) and two chloride ions were present outside of the coordination sphere to balance the charge of the

complex. Thus, Ni(II) center possessed distorted octahedral geometry having *trans-cis-cis* configuration for N_{PY}-N_{IM}-O_W (Figure 3.9, Table S3.50, S3.51, S3.57 and S3.58).

From the slow evaporation of DMF solution, complexes **2g**, **2h**, **3d**, and **3e** produced crystals suitable for X-ray analysis. In the isostructural **2g** and **3d**, ligand **L4** coordinated in bidentate mode through N_{IM} and N_{PY} with Pd(II) and Pt(II) centers and other two sites were occupied by two chloride ions, possessed a distorted square planar geometry (Figure 4, Table S3.52–S3.55). In **3d**, the Pt(II) center was similar to cisplatin type of molecules which inspired us to investigate its interaction with CT-DNA and BSA along with other platinum(II) complexes described here. In both isostructural **2h** and **3e**, $\mathbf{L5}^-$ chelated three coordinate sites in tridentate NNO- pincer fashion. The fourth coordination site was engaged by a chloride ion situated trans to N_{IM} along with a five and six membered chelate ring (N_{PY}–M–N_{IM} and hydroxy-O–M– N_{IM}) and thus displayed distorted square planar geometry around metal center (Figure 3.9, Table S3.59–S3.62). The Pd–N_{IM} bond lengths in **2h** and **3e** were 0.11(2) Å and 0.095(4) Å shorter than that of in **2g** and **3d**. This shortening in bond distance may be due to geometrical demand of pincer mode coordination.

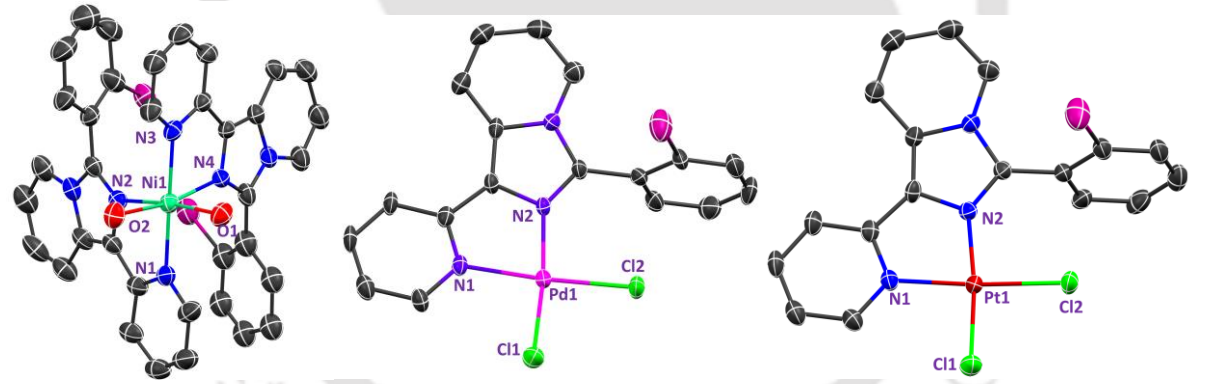

1g **2g** **3d**

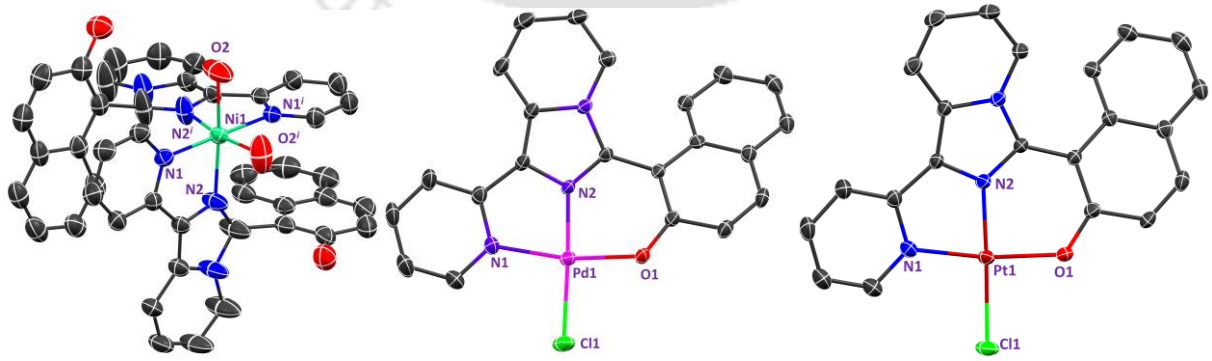

1f **2h** **3e**

Figure 3.9: Molecular structure of **1g**, **2g**, **1h**, **2h**, **3d** and **3e**. Hydrogen atoms and counter ions are omitted for clarity, and thermal ellipsoids are shown at the 30% probability level.

3.2.6 Computational study

In the HOMO of **L1H** electron density was spread all over the molecule while in **1a**–**3a** that was more concentrated on benzothiazole moiety. The LUMO of all four was similar and electron density accumulated around (i) imine group (ii) thiazole ring and (iii) phenyl ring that is linked imine group and phosphorus atom (Figure 3.10). With respect to **L1H**, HOMO-LUMO energy gap decreased by 1.291 (**1a**), 1.226 (**2a**) and 1.218 eV (**3a**) and similar decreasing trend was also observed in **1c**, **1d**, and **2c**. In bis-**L1**$^{-}$ complexes **1b** and **2b**, HOMO was concentrated on monodentate **L1**$^{-}$ and LUMO was similar to that was found in complexes of **L1H** but was localized on tridentate **L1**$^{-}$. The HOMO of **L2H**, **2d**, **2e** and **3c** had contribution from whole molecule while the LUMO was accumulated on quinoline and hydrazone moieties. In the octahedral Ni(II) complex **1e** held by two ligands, HOMO was spread on one **L2**$^{-}$ unit and LUMO was on the other unit (Table 3.65). The energy gap of **L2H** was higher than that of its complexes and followed the trend: **L2H** > **2e** > **2d** > **3b** > **1e**. Both HOMO and LUMO of **L3H** was distributed all over the molecule with ΔE = 4.028 eV while in **1f**, HOMO was centered around metal center and LUMO was escalated throughout the molecular framework and energy gap decreased to 1.924 eV. As mentioned earlier, HOMO as well as LUMO electron density of **2f** and **3c** was accumulated on two pyrrolide moiety and the energy gap decreased to 0.586 eV (**2f**) and 0.612 eV (**3c**). In disubstituted imidazo[1,5-*a*]pyridine ligand **L4**, HOMO was distributed over almost whole molecule while LUMO was over pyridiyl and imidazo[1,5-*a*]pyridiyl moieties. In **1g**, highest occupied molecular orbital was centered around metal center while LUMO was on pyridyl and imidazo[1,5-*a*]pyridyl moieties of one of the ligand units. In complexes **2g** and **3d** HOMO was located around metal center and chloride but their lowest unoccupied orbitals moved towards imidazo[1,5-*a*]pyridyl and pyridyl part of the ligand. The 2-bromophenyl ring did not contribute to both orbital of **L4** and its complexes. The HOMO-LUMO energy gap got lowered in complexes **1g** (1.794 eV), **2h** (3.078 eV) and **3d** (2.931 eV) than that of **L4** (3.993 eV). Similarly, both HOMO and LUMO were spread over whole molecular framework in **L5H** while in pincer Pd(II) (**2h**) and Pt(II) (**3e**) complexes, HOMO was localized around metal center and naphthalene moiety of the

molecule while to LUMO naphthalene moiety did not contribute. The order of HOMO-LUMO energy gap was found as: **L5H** (3.630 eV) > **2h** (2.730 eV) > **3e** (2.695 eV) (Table 3.65).

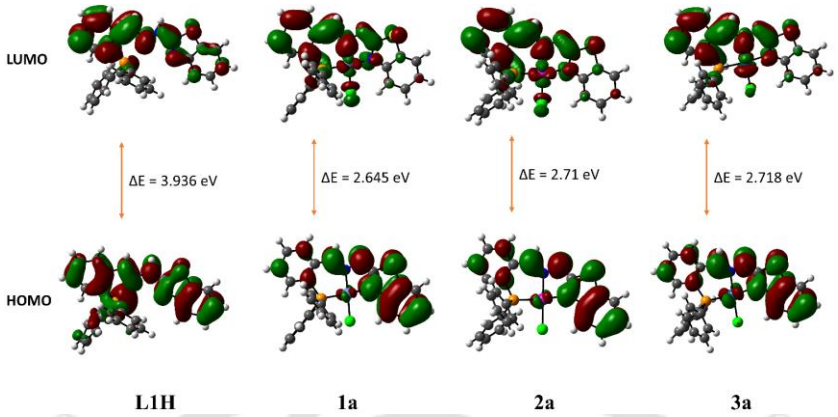

Figure 3.10: HOMO, LUMO orbitals, and energy gap in **L1H** and **1a**–**3a**.

Electrostatic potential map (MEP) was calculated to predict electrostatic region in the molecule in terms of color grading where red, blue and green represent negative, positive and neutral regions respectively. It was observed from MEP analysis that most of the negative charges accumulated near electronegative atoms and positive regions were at carbons and protons. The metal center was located near positive sites thus, can be susceptible to nucleophilic attack (Figure S3.87).

Time-dependent density functional theory (TD-DFT) calculation was also carried out using same basis sets and integral equation formalism polarizable continuum (IEFPCM) model was implemented using acetonitrile as solvent for all ligands and complexes (Table S3.66). It was observed that calculated wavelength of electronic transitions matched closely with experimental data for the ligands, but deviated slightly for complexes and matched with appropriate FMOs transitions.

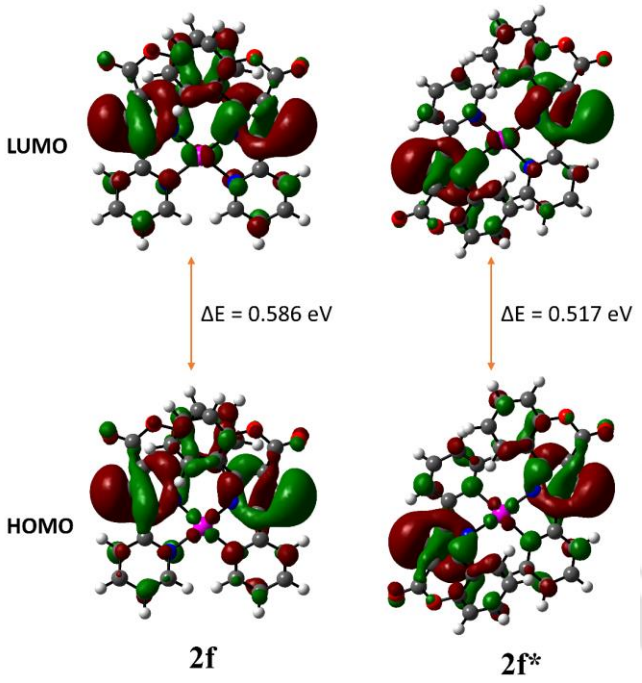

Figure 3.11: HOMO and LUMO molecular orbitals of **2f** and **2f***.

3.2.7 Assessment of catalytic activities of 1a–1h in imine synthesis from alcohol and amine:

The nickel complexes were employed as catalysts in the acceptorless dehydrogenative coupling (ADC) of alcohols and amines to produce imines along with green byproducts. The role of various solvents was screened using the reaction of benzyl alcohol and benzylamine catalyzed by **1a** (1.0 mol %) at 80 °C and 16 h. Among the tested solvents, toluene produced maximum yield which decreased in THF, DCM, DMF and chloroform. Then the effect of temperature was investigated at 50 °C, 80 °C, 110 °C and 140 °C and the best yield was obtained at 110 °C (Table 3.5, entry 5–8). A similar variation in time was also examined at several time interval and maximum product was isolated at 12 h. The use of different bases also affected the product yield in toluene at 110 °C for 12 hours. Triethylamine gave 51% yield and K_2CO_3 produced only 65% while the use of ^{t}BuOK amplified the product yield to 99%. When the catalyst loading was decreased to 0.5 mol% and 0.25 mol%, the product yield diminished to 72% and 45%. Thus, the reaction of benzyl alcohol and benzylamine catalyzed by 1.0 mol% of **1a** at 110 °C and 12 h in toluene and ^{t}BuOK was concluded as optimum condition (Table 3.5, entry 11). The role of catalysts **1a**–**1g** also affected the product yield at optimum condition and can be attributed to various factors including electronic nature of ligand and co-ligands as well as geometry of the complexes. The complex **1b**–**1d**

produced slightly less yield compared to that of **1a** which may be due to effect of co-ligand present in these isostructural complexes (Table 3.5, entry 16–18). Better activity of **1a** than **1c** may be due to electrophilicity of metal center which also supported by NBO analysis where Ni showed a charge of +0.32414 and +0.27123 in **1a** and **1c** respectively. But, **1d** that possessed more natural charge than **1a**–**1c** but produced less yield may due to chelation effect of acetate group. Similarly, **1b**, despite more electronegative Ni center, produced less yield which may be due to less nickel content present in the complex. Moreover, among octahedral Ni(II) complexes, **1e** and **1g** produced less product (65% and 68%) and **1f** generated comparatively more yield (77%) while **1h** produced comparatively more yield (78%). The use of 0.5 mol% of Pd(II) complex **2a** excellently produce 97% amine indicated high reactivity of palladium complex in ADC reaction. With the ideal conditions, the scope of amines with benzyl alcohol were explored. Hydrazide and aromatic amines containing -OH, -NO_2 and -CN substituents effectively produced imines in high yield using only 1.0 mol% of **1a** and aliphatic amines yielded 65–72% of product.

Table 3.5: Optimization table for imines synthesis

Entry	Catalyst (mol%)	Base	Solvent	T/°C	Time (h)	Yield[#] (%)
1.	**1a** (1)	KOH	THF	80	16	42
2.	**1a** (1)	KOH	$CHCl_3$	80	16	54
3.	**1a** (1)	KOH	DMF	80	16	63
4.	**1a** (1)	KOH	DCM	80	16	47
5.	**1a** (1)	KOH	Toluene	80	16	73
6.	**1a** (1)	KOH	Toluene	110	16	81
7.	**1a** (1)	KOH	Toluene	140	16	74
8.	**1a** (1)	KOH	Toluene	50	16	40
9.	**1a** (1)	KOH	Toluene	110	8	54
10.	**1a** (1)	KOH	Toluene	110	12	82
11.	**1a** (1)	^tBuOK	Toluene	110	12	99
12.	**1a** (1)	K_2CO_3	Toluene	110	12	65
13.	**1a** (1)	Et_3N	Toluene	110	12	51

14.	**1a** (0.5)	^{t}BuOK	Toluene	110	12	72
15.	**1a** (0.25)	^{t}BuOK	Toluene	110	12	45
16.	**1b** (1)	^{t}BuOK	Toluene	110	12	61
17.	**1c** (1)	^{t}BuOK	Toluene	110	12	92
18.	**1d** (1)	^{t}BuOK	Toluene	110	12	78
19.	**1e** (1)	^{t}BuOK	Toluene	110	12	65
20.	**1f** (1)	^{t}BuOK	Toluene	110	12	77
21.	**1g** (1)	^{t}BuOK	Toluene	110	12	68
22.	**1h** (1)	^{t}BuOK	Toluene	110	12	78
23.	**2a** (0.5)	^{t}BuOK	Toluene	110	12	92

Isolated Yields

Scheme 3.10: Substrate scope in imine synthesis from alcohol and amine catalyzed by **1a**.[a]

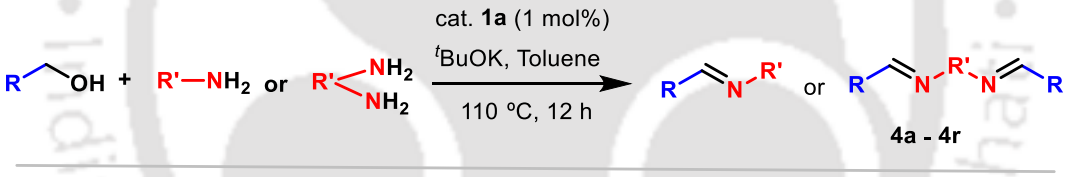

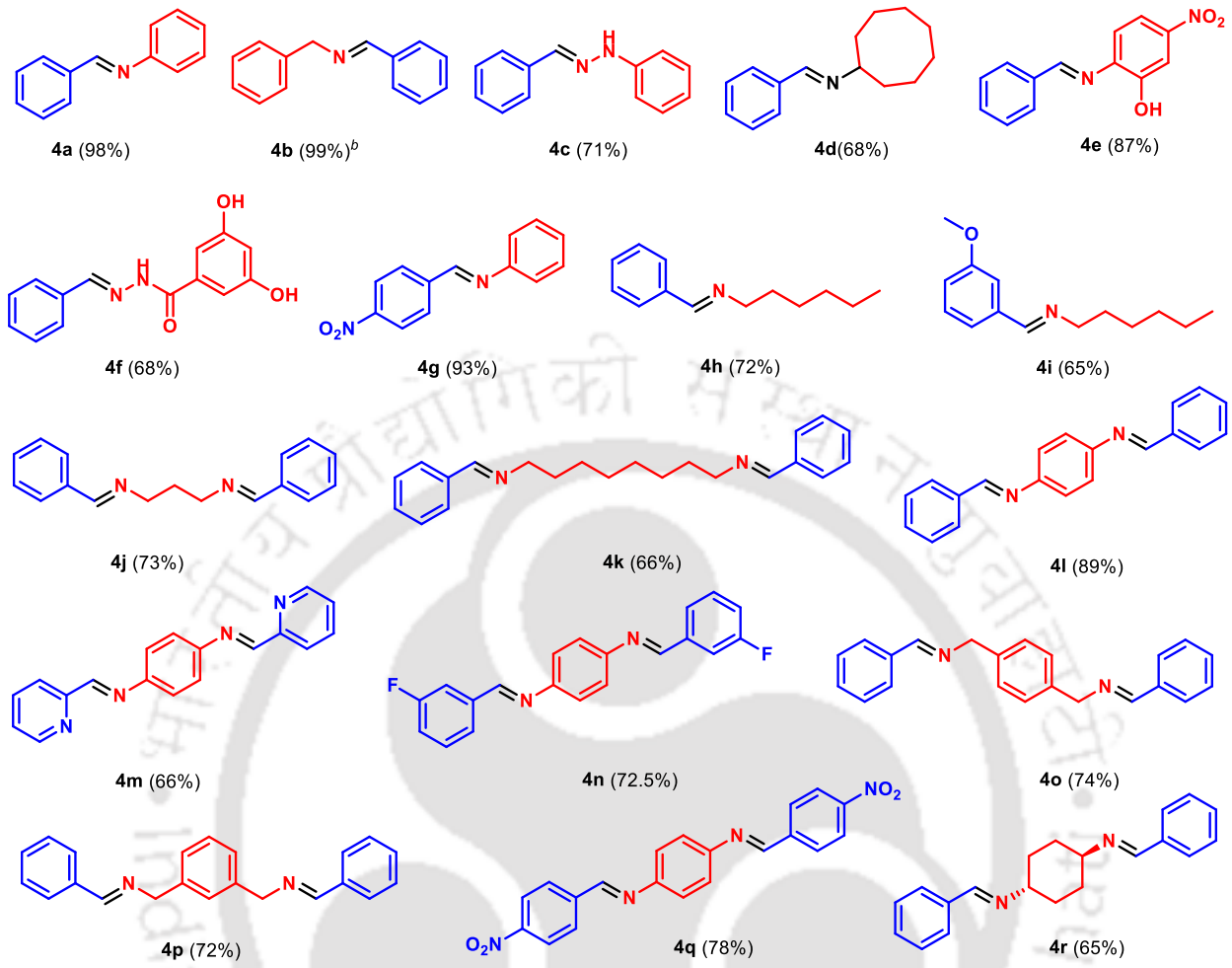

[a]Reaction condition: Aryl alcohol (0.6 mmol), amine (0.5 mmol) or diamine (0.25 mmol), catalyst **1a** (1.0 mol%) [t]BuOK (0.5 mmol), toluene (5 mL), 110 ºC and 12 h. Isolated yield. [b] NMR yield determined using mesitylene as internal standard.

The diimines are important precursors used to synthesize various ligands for synthesis of metal complexes. Thus, the substrate scope was adopted towards the synthesis of several diimines (**4j**–**4r**) using different alcohols and diamines, which afforded the products in good yield (Scheme 3.10). The reaction under optimized condition was carried out in presence of radical scavenger TEMPO, produced 92 % of product indicated the non-radical pathway in the catalytic conversion. The mechanistic pathway of the conversion based on previous reports,[27,28,48] and results of control experiments (Scheme 3.11), a plausible mechanism is presented in Scheme 3.12. The steps involved with the formation of Ni(II) alkoxide intermediate (A), that produce aldehyde (detected in HRMS analysis) and Ni–H species (C) after β–hydride elimination. The imine was formed by the reaction of amine with *in situ* generated aldehyde.

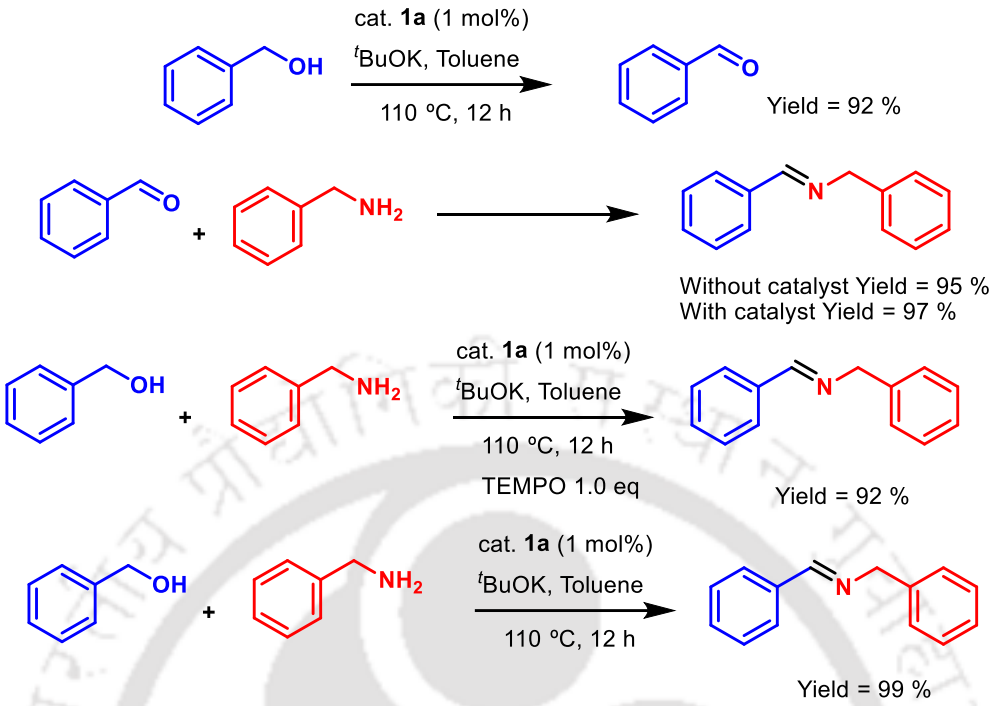

Scheme 3.11: Control Experiments

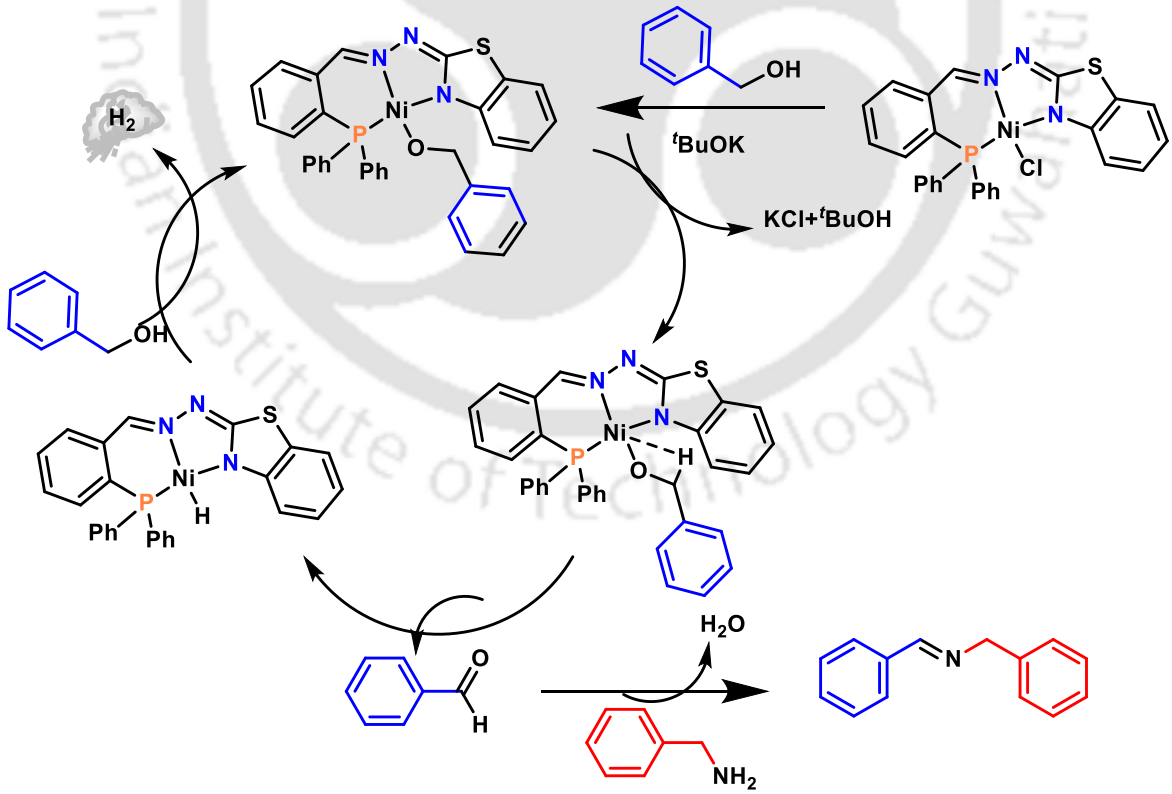

Scheme 3.12: Plausible mechanism for the synthesis of imine (**4b**) using catalyst **1a**.

3.2.8 Assessment of catalytic activities of 2a–2h in Mizoroki-Heck coupling reaction:

All eight palladium complexes were also employed as catalysts in the Mizoroki-Heck cross-coupling reaction. The optimization of reaction conditions was carried out with a model reaction between bromobenzene and 4-methylstyrene. Based on the literature, the model reaction catalyzed by **2a** was optimized with variation in solvent and base at 120 °C and 12 hours. Among several bases, K_2CO_3 was recognized as a superlative base while the yield was less in case of Et_3N, KOH, and ^{t}BuOK (Table 3.13, entry 1–4). In the solvent screening process, ethanol yielded 84% product using catalyst **2a** and without requirement of any additional additive. Remarkably, the application of alcohol-based solvents made from biomass are relatively uncommon in Heck coupling reaction.[49,50] The use of conventional solvents DMF, DMSO and 1,4-dioxane produced comparatively less yield (Table 3.8, entry 4–8). Time and temperature were also affected the product yield, as high temperature was not required for ethanol, decrease in temperature to 90 °C did not remarkably influence the product yield while lessening in yield was observed at lower temperature (Table 3.8, entry 8–11). The formation of 4-methylstilbene was also impacted with the variation in time and a maximum yield (88 %) was achieved in 8 hours. Lessening of the catalyst loading to 0.5% also dropped the yield to 58% but the use of iodobenzene under this loading produced 4-methylstilbene in 92%. The efficiency of all other Pd(II) complexes **2b** – **2h** were also examined with the model reaction in ethanol at 90 °C and 8 h without any additive (Table 3.6, entry 16–22). These catalysts were successfully produced the coupled product with some variations in yield which can be attributed to several factors including ligand framework and geometry of the complexes. In **2a**, Pd(II) center achieved hemi-lability being chelated by phosphorous and nitrogen, offered higher yield compared to that of **2d** and **2e**. Among **2a** and **2b**, the fluctuation in yield may be due to the co-ligand present in 4th coordination site as well as less Pd content, as a result only 61% product was formed with **2b**. The similar trend was also seen in **2d** and **2e**, the azide being better leaving group yielded more product than the chloride analogue **2d** and NBO analysis also supported this by envisaging higher charge on Pd in **2e** (+0.56227) than in **2d** (+0.49657). Monoanionic bidentate ligand containing **2f** offered a lesser yield may be due to alteration in ligand electronic properties as well as severe distortion in geometry.

Table 3.6: Optimization table for Heck coupling reaction.

Entry	Catalyst (mol%)	Base	Solvent	T/°C	Time (h)	Yield[#] (%)
1.	**2a** (1)	KOH	DMF	120	12	62
2.	**2a** (1)	^{t}BuOK	DMF	120	12	58
3.	**2a** (1)	K_2CO_3	DMF	120	12	65
4.	**2a** (1)	Et_3N	DMF	120	12	50
5.	**2a** (1)	K_2CO_3	Toluene	120	12	45
6.	**2a** (1)	K_2CO_3	DMSO	120	12	54
7.	**2a** (1)	K_2CO_3	dioxane	120	12	15
8.	**2a** (1)	K_2CO_3	Ethanol	120	12	84
9.	**2a** (1)	K_2CO_3	Ethanol	90	12	86
10.	**2a** (1)	K_2CO_3	Ethanol	50	12	41
11.	**2a** (1)	K_2CO_3	Ethanol	25	12	27
12.	**2a** (1)	K_2CO_3	Ethanol	90	16	87
13.	**2a** (1)	K_2CO_3	Ethanol	90	8	88
14.	**2a** (1)	K_2CO_3	Ethanol	90	5	62
15.	**2a** (0.5)	K_2CO_3	Ethanol	90	8	58 (92)[b]
16.	**2b** (1)	K_2CO_3	Ethanol	90	8	61
17.	**2c** (1)	K_2CO_3	Ethanol	90	8	72
18.	**2d** (1)	K_2CO_3	Ethanol	90	8	67
19.	**2e** (1)	K_2CO_3	Ethanol	90	8	70
20.	**2f** (1)	K_2CO_3	Ethanol	90	8	58
21.	**2g** (1)	K_2CO_3	Ethanol	90	8	91
22.	**2h** (1)	K_2CO_3	Ethanol	90	8	98

Isolated yields, [b] Iodobenzene was used.

Scheme 3.13: Substrate scope in the Heck coupling reaction catalyzed by **2h.**[a]

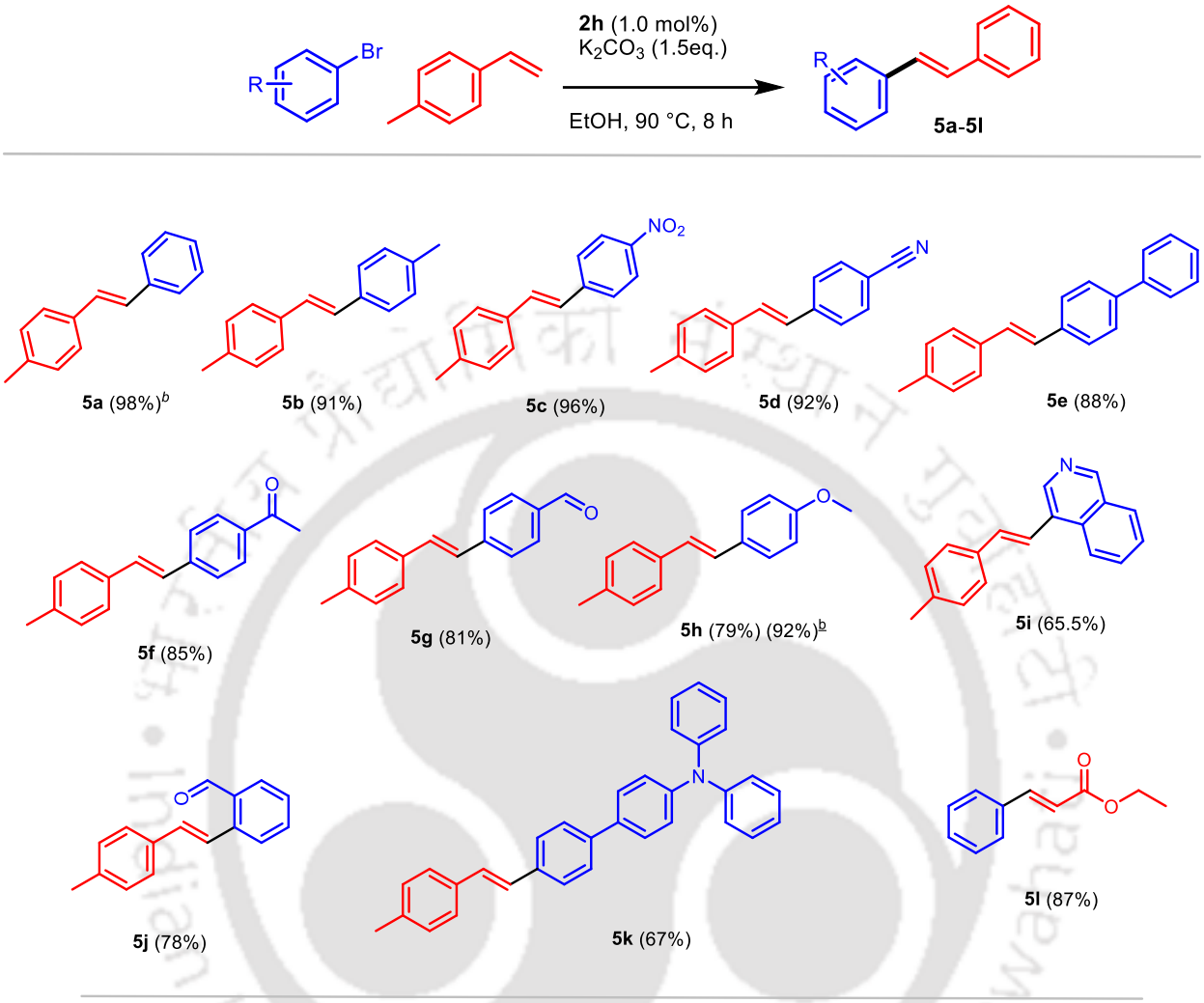

[a] Reaction condition: Aryl bromide/iodide (0.5 mmol), 4-methylstyrene (0.6 mmol), catalyst **2h** (1.0 mol%) K_2CO_3 (0.75 mmol), ethanol (5 mL), 90 ºC, and 8 h. Isolated yield. [b]4NMR yield, [c]4-iodoanisole was used.

But, **2g**, which contained neutral bidentate ligand produced 91% product indicated the role of imidazo[1,5-a]pyridine moiety in the ligand frame work. The NNO- pincer Pd(II) complex of disubstituted imidazo[1,5-a]pyridine (**2h**) that displayed +0.55281 charge on Pd calculated by NBO analysis produced highest yield (98%) and was recognized as superior catalyst among all eight Pd(II) complexes. This superior catalytic activity of **2h** may be attributed the presence of imidazo[1,5-*a*]pyridine ligand that enhance the catalytic efficiency as reported earlier[12,51] and NNO- mode of binding to form NNO- pincer Pd complexes.[52–56] The Ni(II) complex **1a** was unable

to produce the coupled product. With these optimal conditions, scope for Heck coupling was also examined for substrates bearing a wide variation in functional groups. Both electron-rich and electron-deficient aryl bromides, as well as heterocyclic derivative (**5i**) provided good yields using only 1 mol% of **2h** as catalyst. The use of ethyl acrylate was also succeeded with 87% of product formation.

The new molecule **5k** obtained from Heck coupling using **2h** as catalyst contained extended conjugation was favorable for strong photophysical properties and thus selected for electronic spectral investigation. The absorption spectrum of molecule exhibited two prominent bands at 350 nm and 217 nm. The molecule was strongly emissive and displayed dual fluorescence with emission bands in the range of 380–420 nm and 510–590 nm on excitation at 350 nm in hexane, ethylacetate, acetonitrile, chloroform, dichloromethane, methanol, ethanol, isopropanol, DMF, and DMSO. The higher energy band was less affected by the nature of solvents, but the lower energy band was greatly influenced by solvent polarity, which may due to intermolecular charge transfer (ICT) (Figure 3.12). Although solutions of **5k** were colorless to the naked eye but displayed different colors when observed under a UV lamp (365 nm), the distinct fluorescence response indicated positive fluorescence solvatochromism.[57–59] Thus, **5k** may serve as a sensitive probe in biological systems, aid in the design of smart fluorescent materials, and function as a component in molecular logic gates and optoelectronic devices.[60–63]

The homogeneity of the catalyst **1a** and **2h** was also tested using hot filtration test and no substantial changes in product yield was observed. To check Pd nano particle formation, ICP-MS analysis of reaction mixture was done after filtration. The quantity of Pd detected was 12.112 ppm (87.7% recovery), indicated absence of Pd nano particles.

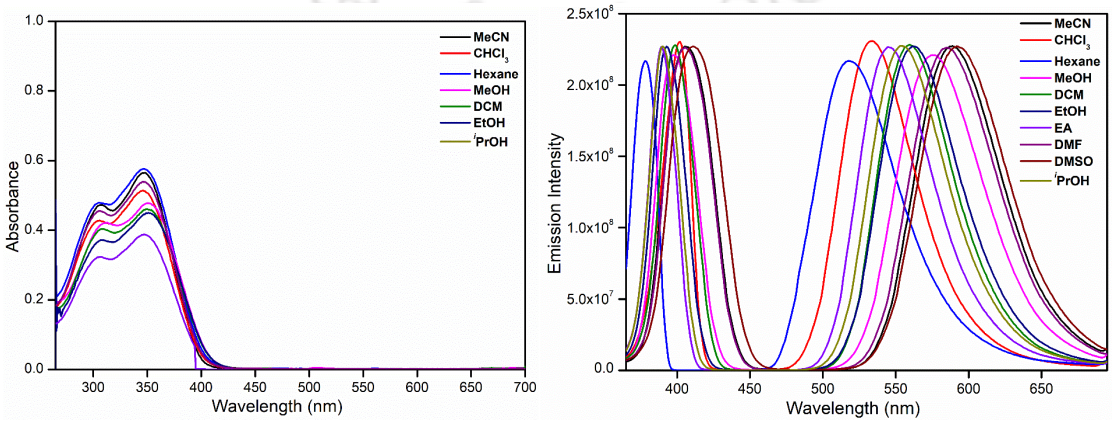

(a) (b)

(c)

Figure 3.12: (a) Absorption spectra, (b) emission spectra (λ_{ex} = 350 nm) of **5k and** (c) image of **5k** under 365 nm UV lamp in different solvents.

Further, the versatility of Pd(II) catalysts was tested in a model reaction and effectively produced [2,2'-bithiophene]-5,5'-dicarbaldehyde from thiophene-2-carbaldehyde (Scheme 3.14) via cross dehydrogenative coupling (Table 3.7).

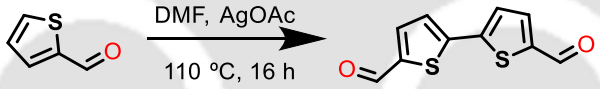

Scheme 3.14: Cross dehydrogenative coupling of thiophene-2-carbaldehyde

Tables 3.7: Cross-dehydrogenative coupling of thiophene-2carbaldehyde.

Catalyst	**2a**	**2b**	**2c**	**2d**	**2e**	**2f**	**2g**	**2h**
Yield (%)	72	45	70	64	68	42	51	84

3.2.9 Biomolecule interaction

3.2.9.1 DNA Binding Study

Given the critical role of platinum complexes in metallodrug development, we investigated the DNA-binding interactions of all platinum complexes described here by using electronic spectroscopy. The complexes **3a**–**3e** (15 μM) were titrated with gradual addition of CT-DNA (0–15 μM) resulted increase in intensity of peak at 260 nm (Figure 3.13, S3.69). The intrinsic binding constant (K_b) of **3a**–**3e** were calculated using the Benesi-Hilderbrand equation (Eq. 3.1) and Gibbs free energy (ΔG) was calculated using equation 3.2 (Table 3.8).

$$\frac{1}{A_{obs}-A_0} = \frac{1}{A_{max}-A_0} + \frac{1}{K_b(A_{max}-A_0)[Complex]} \qquad \text{(Eq. 3.1)}$$

$$\Delta G = -RT\ ln\ Kb \qquad \text{(Eq. 3.2)}$$

Where [DNA] is the concentration of DNA in base pairs, A_0, A_{obs}, and A_{obs} are the absorbances of free complex, complex in presence of DNA, and for the complex in the fully bound form respectively. The binding constant K_b can be obtained from the plot $1/(A_{obs} - A_0)$ *vs* [Complex].

Table 3.8: K_b and ΔG values from UV-Vis titration of CT–DNA with **3a**–**3e** individually.

Complexes	**3a**	**3b**	**3c**	**3d**	**3e**
K_b ($\times 10^4$ M^{-1})	0.31	0.96	1.19	1.34	1.31
ΔG (Kcal mol^{-1})	-4.76	-5.44	-5.57	-5.64	-5.62

The K_b values were found to lie in the range of 10^3–10^4 M^{-1}, the higher value indicated strong interaction of these Pt(II) complexes with CT-DNA. The complex **3e** (-5.62 Kcal mol^{-1}) had the lowest value of calculated Gibbs free energy (ΔG) (Table 3.9) and **3a** (-4.76 Kcal mol^{-1}) had the highest, which indicated spontaneity of the process.

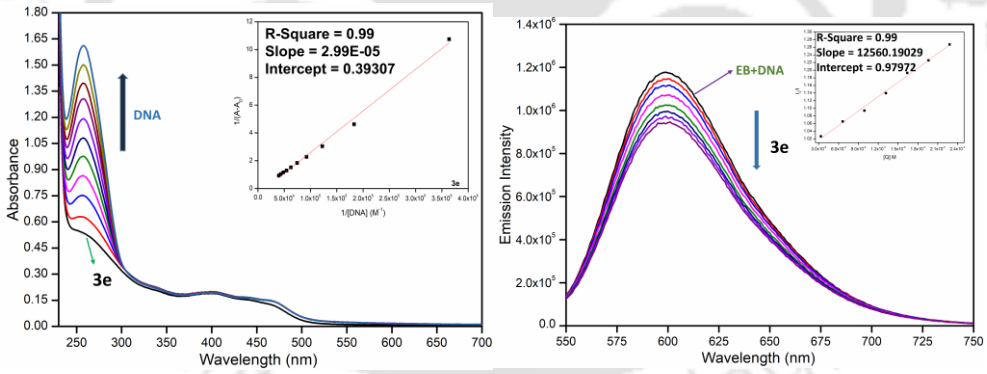

(a) (b

Figure 3.13: (a) UV titration curve of **3e** upon gradual addition of CT-DNA and the inset is Benesi-Hilderbrand plot. (b) EB-DNA emission spectra quenched by gradual addition of **3e** and the inset is Stern-Volmer plot.

The DNA-binding affinities were also assessed using the fluorescence method by titrating ethidium bromide (EB) intercalated CT-DNA with **3a**–**3e**. The fluorescence intensity of EB–DNA adduct quenched with increasing concentration of **3a**–**3e**. A substantial quenching in emission intensity was observed in case of pincer complexes **3a**, **3b** and **3e** while **3c** and **3d** displayed

minimal effect on intensity of EB-DNA adduct (Figure 3.13, S3.71). Quenching of fluorescence intensity indicated displacement of EB by the complexes through intercalative mode of binding. The Stern−Volmer equation (Eq. 3.3) and Scatchard equation (Eq. 3.4) was used to calculate the Stern−Volmer quenching constant (K_{SV}), bimolecular quenching constant (K_q), intrinsic binding constant (K_b) and number of binding sites (n) (Table 3.9).

$$\frac{I_0}{I} = 1 + K_{SV}[Q] = 1 + K_q\tau_0[Q] \qquad \text{(Eq. 3.3)}$$

$$log(\frac{I_0 - I}{I}) = logKb + nlog[Q] \qquad \text{(Eq. 3.4)}$$

where I_0 and I represent the fluorescence intensities in absence and presence of the quencher 'Q' (here Q is the studied complexes) respectively. [Q] is the quencher concentration, and K_{SV} denotes the Stern– Volmer quenching constant calculated from the plot of I_0/I *vs* [Q], K_q is the biomolecular quenching constant and τ_0 is the mean lifetime of the fluorophore=23ns. The binding constant K_b is the intercept of log (I_0 - I)/I *vs* log [Q] plot. The number of binding sites per nucleotide is n.

Table 3.9: K_{SV}, K_q, K_b, and n values from EB–DNA emission titration with **3a**–**3e**.

Complexes	K_{SV} (10^4 M^{-1})	K_q 10^{11} M^{-1} s^{-1})	K_b (10^4 M^{-1})	ΔG (kcal mol^{-1})	n
3a	0.80	3.47	0.86	5.37	1.01122
3b	0.90	3.91	1.61	5.74	1.05703
3c	0.23	1.02	0.03	3.34	0.79578
3d	0.44	1.91	0.10	4.06	0.85471
3e	1.26	5.46	10.26	6.83	1.20124

The lowest K_{SV} value was 2.3×10^3 M^{-1} (**3c**) and highest was 1.256×10^4 M^{-1} for **3e** which may be due to its NNO- pincer type planar structure and comparable with reported Pt(II) complexes[42,64–66]. In the context of anticancer drug design, binding affinities in terms of K_{SV} are critical as they reflect the potential to effectively interact with biomolecular targets. The observed binding constant values of **3b** (0.9×10^4 M^{-1}) and **3e** (1.26×10^4 M^{-1}) positioned within or above the range of cisplatin (0.948×10^4 M^{-1}) indicated promising pharmacokinetic potential. The Kq values followed the trend: **3e** > **3b** > **3a** > **3d** > **3c** which were higher than scattering collision quenching constant (2×10^{10} M^{-1}) for the biopolymer, indicating involvement of static quenching process. The values of 'n' were nearly 1 for **3a**–**3e** suggesting presence of single binding site. The K_b was

higher for two planar complex **3b** (1.61×10^4 M^{-1}) and **3e** (1.03×10^5 M^{-1}) than that of other three complexes. Thus, noticeable quenching of fluorescence intensity as well as high binding constant was a sign of displacement of EB from the EB–DNA adduct by these Pt(II) complexes.

3.2.9.2 BSA Binding Study

Human serum albumin (HSA) transports ions and drugs *via* the circulatory system to cells and tissues. Bovine serum albumins (BSA) due to its structural similarity with HSA, are commonly employed for examining the interactions of newly discovered drugs. BSA is composed of three α-helical domains (I–III) with each subdivided into A and B subdomains, and contains two tryptophan residues (Trp-134 in IA and Trp-213 in IIA) that fluoresces BSA. Thus, addition of bioactive molecules, quenching in the fluorescence intensity of BSA indicates conformational changes mainly at tryptophan sites. Electronic spectroscopy is a popular tool and highly potent in decoding the interactions of BSA with bioactive compounds. Hence, we used absorption spectroscopy as well as several fluorescence techniques such as emission, synchronous, and steady-state anisotropy measurements to examine the interaction of **3a**–**3e** with BSA.

Absorption study: A titration experiment was conducted with the gradual addition of **3a**–**3e** individually to a fixed concentration of BSA in HEPES buffer (10.0 mM, pH= 7.4). It was observed that intensity of band at 280 nm increased on addition of complex due to the interaction with BSA (Figure 3.14 and S3.74). The intrinsic binding constant (K_b) were calculated for **3a**–**3e** using equation 3.1 and the highest K_b value was observed for **3e** (2.96×10^4 M^{-1}). The high K_b values for all **3a**–**3e** indicated strong interaction of these Pt(II) complexes with BSA as well as the spontaneity of the process was confirmed from negative Gibbs free energy (Table 3.10).

Emission Study Like absorption spectral study, a similar titration was done using fluorescence spectroscopy and the intensity of BSA was effectively quenched by **3a** – **3e** which may have triggered conformational fluctuations within the protein structure (Figure 3.14 and S3.75). The values of K_{SV}, K_q, K_b and n were calculated using equation 3.3 and 3.4 and the value are given in Table 3.11. The variation in binding affinity for **3a**–**3e** with BSA may be attributed to ligand moieties, coordination mode and planarity of the complex. The K_{SV} followed the order: **3e** (4.56×10^4 M^{-1}) > **3c** (3.46×10^4 M^{-1}) > **3a** (2.37×10^4 M^{-1}) > **3b** (2.11×10^4 M^{-1}) > **3d** (1.80×10^4 M^{-1}). The Kq values ($1.02 – 5.46 \times 10^{11}$ M^{-1} s^{-1}) were found to be ~10 times higher than the collision

quenching constant (2.0×10^{10} M^{-1} s^{-1}) values known among various quenchers[67] indicating that **3a**–**3e** displayed static quenching through the interactions with BSA. The number of binding sites (n) was nearly 1 for all five complexes signifying the presence of single binding site in BSA for **3a** – **3e**. The K_b values were in the range 0.04 – 2.93 × 10^{11} M^{-1} and comparable with Pt(II) complexes reported in the literature.[40,68]

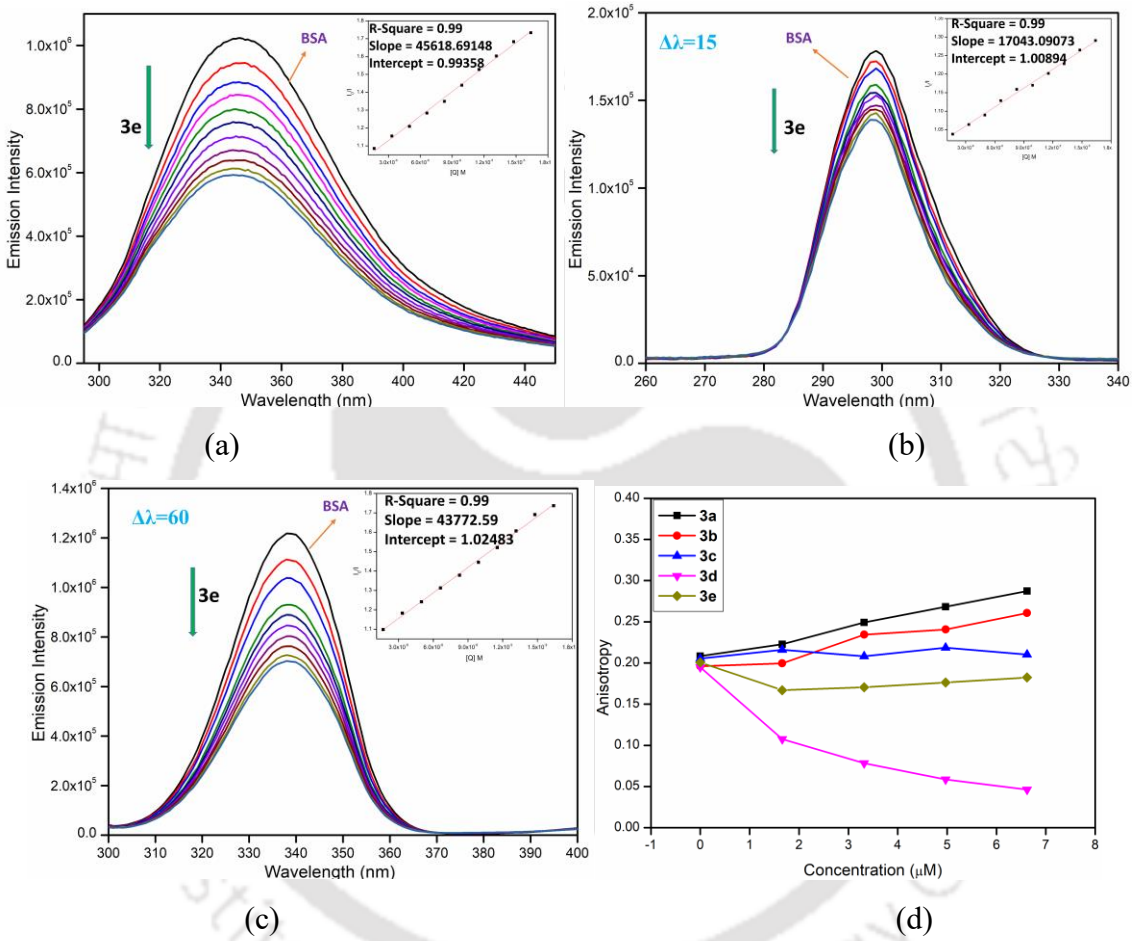

Figure 3.14: (a) Emission spectra of BSA in the absence and presence of **3e**, (b) Fluorescence anisotropy of BSA on addition of **3a**–**3e**. Synchronous spectra of BSA in the absence and presence of **3e** at Δλ = 60 nm (c) and 5 nm (d). The insets are Stern-Volmer plots.

Table 3.10: K_b and ΔG values from UV-Vis titration of BSA with **3a**–**3e** individually.

Complexes	**3a**	**3b**	**3c**	**3d**	**3e**
K_b ($\times 10^4$ M^{-1})	0.98	0.086	0.66	0.49	2.96
ΔG (Kcal mol^{-1})	-5.45	-4.00	-5.21	-5.04	-6.11

Table 3.11: K_{SV}, K_q, K_b, and n values of BSA for complexes **3a**–**3e**.

Complexes	K_{SV} (10^4 M^{-1})	K_q (10^{12} M^{-1} s^{-1})	K_b (10^4 M^{-1})	ΔG (kcal mol^{-1})	n
3a	2.37	1.03	0.13	4.23	0.73
3b	2.11	0.92	0.25	4.64	0.81
3c	1.80	0.78	0.04	3.62	0.66
3d	3.46	1.50	0.29	4.72	0.77
3e	4.56	1.98	2.93	6.09	0.96

Synchronous fluorescence experiment A synchronous fluorescence study was employed to explore the conformational shifts in the microenvironment of tryptophan (Trp) and tyrosine (Tyr) residues within BSA on addition of complexes **3a**–**3e**. Fixed excitation–emission wavelength intervals of Δλ = 60 nm and 15 nm were used for selective monitoring of tryptophan and tyrosine microenvironment. Increasing the concentration of **3a**–**3e** gradually diminished fluorescence intensity accompanied by a red shift in the tryptophan residue. In the tyrosine microenvironment, only **3c** and **3d** showed a reduction in fluorescence intensity (Figure 3.14, S3.78). All synchronous fluorescence spectra were used to calculate K_{SV}, K_q, K_b and n (Table 3.12). The highest K_{SV} was found for **3e** (4.38×10^4 M^{-1}) at Δλ = 60 nm while that was for **3d** (1.98×10^4 M^{-1}) at Δλ = 15 nm.

Table 3.12: K_{SV}, K_q, K_b, and n values of BSA (synchronous fluorescence data) for **3a**–**3e**.

Complexes	Δλ (nm)	K_{SV} ($\times 10^4$ M^{-1})	K_q (10^{11} M^{-1} s^{-1})	K_b (M^{-1})	ΔG (kcal mol^{-1})	n
3a	15	0.54	2.33669	1.08×10^2	-2.77	0.63
	60	1.74	7.56141	2.06×10^3	-4.52	0.79
3b	15	0.64	2.79904	9.59×10^2	-4.07	0.80
	60	1.86	8.09819	1.07×10^3	-4.13	0.74
3c	15	1.32	5.72494	1.75×10^6	-8.51	1.43
	60	1.82	7.93	1.25×10^5	-6.95	1.17
3d	15	1.98	8.6269	9.16×10^4	-6.77	1.14
	60	3.29	14.2938	8.14×10^3	-5.33	0.87
3e	15	1.70	7.41004	5.67×10^3	-5.12	0.90
	60	4.38	19.0316	1.19×10^4	-5.56	0.88

Steady-state fluorescence anisotropy: The steady-state fluorescence anisotropy of BSA was recorded with gradual addition of **3a**–**3e** separately to observe their interactions with the protein. As the rotational motion depends on structural rigidity, the addition of Pt(II) complexes to BSA solution led to the formation of BSA– Pt(II)complex adducts which alter the Brownian motion of protein, resulting change in anisotropy. The equation 3.5 was used to determine the steady-state anisotropy (r).

$$r = (I_{VV} - GI_{VH})/(I_{VV} + 2GI_{VH}) \qquad \text{(Eq. 3.5)}$$

$$G = I_{VH}/I_{HH}$$

Where G is the instrumental grating factor, I_{VV} and I_{VH} denotes the intensities obtained with the excitation polarizer in the vertical position and the emission polarizer in both the horizontal and vertical positions, respectively.

Figure 3.14d represents the plot of anisotropy (r) *vs* concentration of **3a**–**3e** which indicated that all Pt(II) complexes interacted with the BSA and alter the rotational motion.[69,70]

As **3e** showed highest binding constant, molecular docking study was performed to visualize its interaction with CT-DNA and BSA using Autodock 4.2.6 software.[71] The complex **3e** displayed intercalative mode of binding with CT-DNA (pdb id- 1bna)[72] (Figure 3.15) as established from electronic spectral study. The high binding energy (–10.54) and nanomolar inhibition constant (18.89 nM) (Table 3.13) was an indication of strong binding affinity and also comparable with some reported Pt(II) complexes.[73]

Table 3.13: Binding energy of **3e** DNA and BSA calculated from docking.

Biomolecules	Binding energy	Inhibition constant	Temperature
DNA	-10.54 kcal/mol	18.89 nM	298.15 K
BSA	-10.48 kcal/mol	20.81 nM	298.15 K

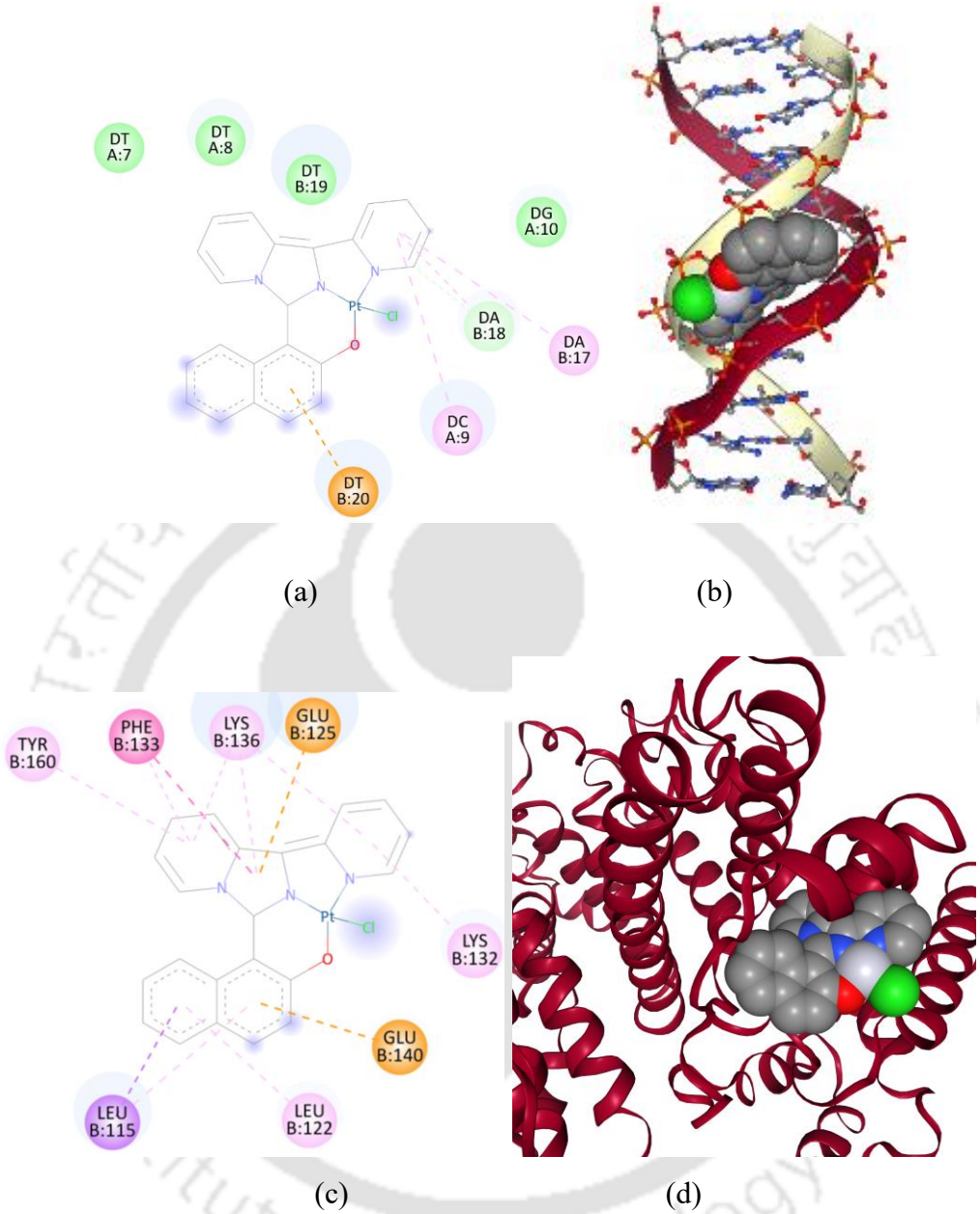

Figure 3.15: 2D and 3D Docking pose of **3e** with (a, b) CT-DNA (pdb id- 1bna) and (c, d) BSA (pdb id- 3v03)

After getting docked with BSA (pdb id- 3vo3),[74] **3e** exhibited –10.48 kcal/mol binding energy and 20.81 nM inhibition constant. Also, the complex displayed several interactions (Table 3.14) indicated the interaction at IB subdomain near to tryptophan134 (Figure 3.15)

Table 3.14: List of non-bonding interactions between **3e** and BSA (pdb id- 3v03).

Residue	Amino acid	Distance (Å)	Residue	Amino acid	Distance (Å)	Residue	Amino acid	Distance (Å)
115B	LEU	3.14	132B	LYS	3.23	136B	LYS	2.07*
115B	LEU	3.36	132B	LYS	3.44	137B	TYR	3.29
117B	PRO	3.99	133B	PHE	3.98	160B	TYR	3.30
122B	LEU	3.15	136B	LYS	3.61	125B	GLU	3.92

(* H-bonding, others are hydrophobic interaction)

3.3 Conclusion

In conclusion, we present the synthetic procedure of a series of Ni(II), Pd(II) and Pt(II) complexes of various ligands bearing benzothiazole, coumarin fused pyrrole and imidazo[1,5-a]pyridine moieties. The ligands were structurally and electronically diverse by containing a wide range of P-, N- and O- donor sites. All the ligands and complexes were characterized thoroughly using various spectroscopic techniques, and their molecular structures were confirmed by single crystal X-ray diffraction method. Computational investigation was also performed to optimize the geometry and the calculated energies of all compounds were in accordance with experimental findings and most importantly, the severely distorted square planar geometry of **2f** and **3c** were also supported by FMOs. The nickel(II) complexes were employed as catalysts in synthesis of imines/diimines via acceptorless dehydrogenative coupling of alcohols and amines/diamine. Among all Ni(II) complexes, **1a** gave maximum yield of 99% in 12 h using only 1.0 mol% catalyst loading offered a cost-effective and sustainable alternative to existed noble metal catalysts. The catalytic activity of Pd(II) complexes was assessed in Heck coupling reaction, and all the palladium(II) complexes **2a**–**2h** effectively produced 1-methylstilbene in good to excellent yields in ethanol at 90 ºC and 8 hours, surpassing many existing conventional systems relying on DMF or DMSO solvent at high temperature. The pincer Pd(II) complex **2h** was superior catalyst among all, with a yield of 98% using only 1.0 mol% catalyst loading. Among the Heck products, photophysical study of **5k** was examined and it displayed positive fluorescence solvatochromism which can be used as sensing probe and in the design of optoelectronic devices. Furthermore, the versatility of Pd(II) catalysts was tested in cross-dehydrogenative coupling of thiophene-2-carboxaldehyde and formed the product in good yield. The variation in catalytic activity was mainly due to ligand environment which played a pivotal role in creating a tunable electronic

environment around the metal center and thus enhanced their catalytic activity. The platinum complexes of all ligands were inspected for their interaction with biomolecules such as CT-DNA and BSA and among all Pt(II) complexes, **3e** displayed the highest binding constants with these two biomolecules. Molecular docking study was also carried out to visualize the interaction of **3e** with CT-DNA and BSA, showed high binding free energy and intercalative binding mode with CT-DNA which was in congruence with experimental findings. Hence, the study highlighted the effect of ligand framework on the geometry of complexes as well as the catalytic and bio activity of the resulting complexes. Thus, the combined catalytic and biological evaluation of group 10 complexes within a unified ligand framework, underscored a versatile platform for the development of multifunctional catalysts that could facilitate a range of organic transformations and further investigations on *in vitro* anticancer activities.

3.4 Experimental section

3.4.1 Synthesis of Ligands

[N-(2-diphenylphosphanyl-phenyl)methylideneamino]-1,3-benzothiazol-2-amine (**L1H**):

2-(diphenylphosphaneyl)benzaldehyde (1.451 g, 5 mmol) and 2-hydrazineylbenzo[d]thiazole (0.826 g, 5 mmol) were taken in 10 mL of absolute ethanol and the mixture was refluxed for 12 h. Then, it was cooled at room temperature, precipitate was filtered, washed with cold ethanol (50 mL), and dried over fused $CaCl_2$ to produce analytical pure compound **L1H** as ivory colored solid. Yield: (2.012 g) 92%. Anal. calcd for $C_{26}H_{20}N_3PS$: C, 71.38%; H, 4.61%; N, 9.61; found: C, 71.52%; H, 4.64%; N, 9.50. ATR-IR (neat, cm^{-1}): 1618, 1563, 1467, 1432, 1263, 1021, 744, 693, 487, 427. ^{1}H NMR (400 MHz, DMSO-d_6) δ 11.90 (s, 1H), 8.74 (d, J = 4.9 Hz, 1H), 8.01 (dd, J = 6.6, 4.0 Hz, 1H), 7.53 (d, J = 7.4 Hz, 1H), 7.39 – 7.32 (m, 2H), 7.31 – 7.25 (m, 6H), 7.19 (ddt, J = 10.4, 6.9, 2.9 Hz, 6H), 7.00 (t, J = 7.6 Hz, 1H), 6.81 (dd, J = 6.9, 4.6 Hz, 1H). ^{13}C NMR (126 MHz, DMSO-d_6) δ 168.0, 150.3, 142.1, 141.9, 138.0, 137.8, 136.1, 136.1, 134.2, 134.0, 133.8, 132.3, 132.1, 132.1, 130.4, 129.6, 129.1, 128.9, 128.7, 128.6, 126.5, 126.4, 126.1, 122.2, 121.2, 119.0. ^{31}P NMR (243 MHz, DMSO-d_6) δ -15.40. UV- Vis: nm (M^{-1} cm^{-1}) 345 (27400). HRMS (ESI) *m/z* calculated for (**L1H**+H)$^+$: 438.1188; found 438.1198.

[N-quinolin-8-ylmethylideneamino]-1,3-benzothiazol-2-amine (**L2H**):

The ligand **L2H** was prepared following the similar procedure for **L1H** by taking quinoline-8-carbaldehyde (0.785 g, 5.0 mmol) and 2-hydrazineylbenzo[d]thiazole (0.826 g, 5.0 mmol) to

produce **L2H** as vanilla colored solid. Yield: (1.34 g) 88%. Anal. calcd for $C_{17}H_{12}N_4S$: C, 67.08%; H, 3.97%; N, 18.41; found: C, C, 67.12%; H, 4.01%; N, 18.35. ATR-IR (neat, cm^{-1}): 1614, 1575, 1439, 1266, 1123, 899, 827, 791, 745, 625, 428. ^{1}H NMR (400 MHz, DMSO-d_6) δ 12.50 (s, 1H), 9.39 (s, 1H), 8.99 (dd, *J* = 4.1, 1.7 Hz, 1H), 8.43 (dd, *J* = 8.3, 1.6 Hz, 1H), 8.37 – 8.27 (m, 1H), 8.11 – 8.00 (m, 1H), 7.80 (d, *J* = 7.7 Hz, 1H), 7.73 (t, *J* = 7.7 Hz, 1H), 7.62 (dd, *J* = 8.3, 4.2 Hz, 1H), 7.49 (d, *J* = 7.8 Hz, 1H), 7.31 (t, *J* = 8.2 Hz, 1H), 7.13 (t, *J* = 7.5 Hz, 1H). ^{13}C NMR (151 MHz, DMSO-d_6) δ 167.2, 150.5, 145.1, 136.7, 131.2, 129.6, 128.2, 126.7, 126.1, 125.0, 122.0, 121.8, 121.6. UV- Vis: nm (M^{-1} cm^{-1}) 365 (25000), 289 (14070). HRMS (ESI) *m/z* calculated for [**L2H**+H]$^+$: 305.0855, found 305.0855.

2-(pyridin-2-yl)chromeno[4,3-b]pyrrol-4(1H)-one (**L3H**):

4-chloro-2-oxo-2H-chromene-3-carbaldehyde (**A**) was synthesized by some modification of reported procedure. 4-hydroxy-2-oxo-2H-chromene was taken in dimethylformamide (10 mL) and kept at 273K. In a closed container, $POCl_3$ (2.0 mL) was taken in 5.0 mL DMF and kept at 273K. After few hours, $POCL_3$ solution was added to 4-hydroxy-2-oxo-2H-chromene solution at 273K with constant stirring. After 2 hours of stirring, the reaction mixture was kept at 273K for overnight. Next day, water was added carefully portion wise to the mixture with vigorous stirring at same temperature. Precipitates of **A** were collected by filtration followed by washing with water, dried over fused $CaCl_2$. 2.0 mmol (0.417 mg) of **A** was taken in 10mL absolute ethanol and 2.0 mmol of 2-picolylamine (0.216 g) was added to it followed by few drops of triethylamine. The mixture was stirred at reflux for 12 hours, cooled at room temperature and left undisturbed for few days. Colorless crystals of **L3H** were collected and washed with cold ethanol (20 mL). Yield: (0.377 g) 72%. Anal. calcd for $C_{16}H_{10}N_2O_2$: C, 73.27%; H, 3.84%; N, 10.68; found: C, 73.42%; H, 3.91%; N, 10.51. ATR-IR (neat, cm^{-1}): 3283, 1686, 1450, 1186, 1088, 969, 744, 473. ^{1}H NMR (400 MHz, Chloroform-d) δ 10.92 (s, 1H), 8.49 (d, J = 4.4 Hz, 1H), 7.77 – 7.66 (m, 3H), 7.39 (dd, J = 6.0, 1.3 Hz, 2H), 7.26 – 7.22 (m, 2H), 7.21 – 7.15 (m, 1H). ^{13}C NMR (126 MHz, Chloroform-d) δ 159.3, 152.4, 148.9, 148.9, 137.4, 136.7, 135.8, 129.4, 124.3, 122.6, 120.8, 119.7, 117.8, 113.5, 111.1, 106.2. UV- Vis: nm (M^{-1} cm^{-1}) 340 (28496), 325 (29934), 313 (24877), 290 (14047). HRMS (ESI) *m/z* calculated for [**L3H**+H]$^+$: 263.0815, found 263.0825.

3-(2-bromophenyl)-1-(pyridin-2-yl)imidazo[1,5-a]pyridine (**L4**):

Ligand **L4** was synthesized by following a reported procedure.[3] A mixture consisting of 2,2′-dipyridyl ketone (0.460 g, 2.5 mmol), 2-bromobenzaldehyde (0.925 g, 5 mmol), NH_4OAc (0.965 g, 10 mmol) in 20 mL of glacial acetic acid was stirred at 110 °C for 5 h. Then reaction mixture was cooled to room temperature and poured into 100 mL of ice water. The formed solid was then filtered, dried, and recrystallized from ethanol. Yield: (0.648 g) 74%. Anal. calcd for $C_{18}H_{12}N_3Br$: C, 61.73%; H, 3.45%; N, 12.00; found: C, 61.58%; H, 3.50%; N, 11.88. ATR-IR (ν, cm^{-1}): 1585, 1523, 1474, 1140, 1006, 790, 776, 743, 706, 618, 422, 438, 403. ^{1}H NMR (400 MHz, Chloroform-*d*) δ 8.73 (d, *J* = 9.2 Hz, 1H), 8.66 – 8.61 (m, 1H), 8.22 (d, *J* = 8.1 Hz, 1H), 7.79 – 7.68 (m, 2H), 7.66 – 7.59 (m, 2H), 7.49 (t, *J* = 7.5 Hz, 1H), 7.39 (td, *J* = 7.7, 1.6 Hz, 1H), 7.14 – 7.06 (m, 1H), 6.97 (dd, *J* = 9.2, 6.4 Hz, 1H), 6.67 (t, *J* = 6.8 Hz, 1H). ^{13}C NMR (126 MHz, Chloroform-*d*) δ 155.1, 149.2, 136.9, 136.4, 133.7, 133.3, 131.5, 131.3, 130.3, 129.7, 128.0, 124.6, 122.5, 121.7, 121.4, 120.6, 120.1, 113. UV- Vis: nm (M^{-1} cm^{-1}) 264 (9150), 294 (9700), 328 (7930), 358 (5810). HRMS (ESI) m/z calcd for [**L4**+H]$^+$: 350.0287, found: 350.0292.

1-(1-(pyridin-2-yl)imidazo[1,5-a]pyridin-3-yl)naphthalen-2-ol (**L5H**):

A mixture consisting of 2,2′-dipyridyl ketone (0.460 g, 2.5 mmol), 2-hydroxynaphthaldehyde (5 mmol), NH_4OAc (0.965 g, 10 mmol) in 20 mL of glacial acetic acid was stirred at 110 °C for 5 h. Then reaction mixture was cooled to room temperature and poured into 100 mL of ice water. The formed solid was then filtered, dried, and recrystallized from ethanol. Yield: (0.573 g) 68%. Anal. calcd for $C_{22}H_{15}N_3O$: C, 78.32%; H, 4.48%; N, 12.46; found: C, 78.41%; H, 4.52%; N, 12.31. ATR-IR (ν, cm^{-1}): 2588, 1625, 1591, 1508, 1435, 1347, 1275, 1245, 1143, 1073, 970, 820, 739, 706, 625, 599. ^{1}H NMR (400 MHz, Chloroform-*d*) δ 8.81 (d, *J* = 9.2 Hz, 1H), 8.67 (d, *J* = 5.6 Hz, 1H), 8.21 (d, *J* = 8.0 Hz, 1H), 7.90 (dd, *J* = 8.1, 5.4 Hz, 2H), 7.75 (td, *J* = 7.8, 1.8 Hz, 1H), 7.54 (d, *J* = 7.2 Hz, 1H), 7.48 – 7.38 (m, 2H), 7.36 (d, *J* = 8.9 Hz, 1H), 7.29 (s, 1H), 7.15 (dd, *J* = 7.9, 4.4 Hz, 1H), 7.06 – 6.99 (m, 1H), 6.64 (t, *J* = 7.4 Hz, 1H). ^{13}C NMR (151 MHz, Chloroform-*d*) δ 155.1, 154.5, 149.3, 136.6, 134.1, 132.0, 130.8, 130.3, 129.2, 129.1, 127.4, 124.6, 123.7, 123.5, 122.0, 121.9, 121.0, 120.0, 118.9, 113.9, 107.5. UV- Vis: nm (M^{-1} cm^{-1}) 332 (21830), 287 (17220), 278 (17980), 360 (19750). HRMS (ESI) m/z calcd for [**L5H**+H]$^+$: 338.1288, found: 338.1295.

3.4.2 Synthesis of complexes

[Ni(**L1**)Cl] (**1a**)

Nickel chloride hexahydrate (119 mg, 0.5 mmol) in 10 mL methanol was added to a methanolic solution of **L1H** (218.5 mg, 0.5 mmol) and the mixture was refluxed at 80 °C with continuous stirring for 12 h. The resulting shiny denim blue precipitates were separated by filtration, washed with cold ethanol (20 mL), diethyl ether (10 mL), and dried in vacuo to afford the pincer nickel complex [Ni(**L1**)Cl] (**1a**). Yield: (228 mg), 86%. Anal. calcd for $C_{26}H_{19}ClN_3NiPS$: C, 58.85%; H, 3.61%; N, 11.06; found: C, 59.02%; H, 3.65%; N, 10.98. ATR-IR (neat, cm^{-1}): 1493, 1469, 1238, 998, 745, 688, 515, 480, 437, 422. ^{1}H NMR (500 MHz, Chloroform-*d*) δ 8.25 (d, *J* = 8.3 Hz, 1H), 8.02 (s, 1H), 7.86 (dd, *J* = 11.3, 8.0 Hz, 4H), 7.55 (dt, *J* = 13.9, 7.5 Hz, 3H), 7.47 (t, *J* = 7.2 Hz, 4H), 7.42 – 7.37 (m, 1H), 7.35 (d, *J* = 7.7 Hz, 1H), 7.28 (d, *J* = 7.6 Hz, 1H), 7.16 (t, *J* = 8.2 Hz, 1H), 7.07 (t, *J* = 7.8 Hz, 1H), 6.92 (t, *J* = 7.5 Hz, 1H). ^{13}C NMR (151 MHz, Chloroform-*d*) δ 176.8, 149.6, 148.6, 136.5, 136.4, 134.4, 134.0, 133.9, 132.6, 131.5, 130.6, 130.1, 129.0, 128.9, 128.3, 128.0, 125.8, 121.3, 120.8, 120.7, 120.4, 116.7. ^{31}P NMR (202 MHz, Chloroform-*d*) δ 13.19. UV-Vis: nm (M^{-1} cm^{-1}) 490(10020), 351 (77440), 288 (25200). 490(10020), 351 (77440), 288 (25200). HRMS (ESI) *m/z* calculated for [**1a**+H]$^+$: 530.0156, found 530.0155.

[Ni(**L1**)$_2$] (**1b**)

The complex **1b** was synthesized by the reaction of 1.0 mmol of **L1H** with Nickel Chloride hexahydrate (0.5 mmol) in 10 mL methanol with few drops of triethylamine and was refluxed with continuous stirring for 12h. The resulting a shiny black color precipitates formed were separated by filtration, washed with diethyl ether, and dried in vacuo to afford the nickel complex [Ni(**L1**)$_2$] (**1b**). Yield: (289 mg), 62%. Anal. calcd for $C_{52}H_{38}N_6NiP_2S_2$: C, 67.04%; H, 4.11%; N, 9.02; found: found: C, 67.12%; H, 4.12%; N, 8.93. ATR-IR (neat, cm^{-1}): 1551, 1461, 1433, 1259, 1102, 999, 742, 690, 489, 425. ^{31}P NMR (243 MHz, Chloroform-*d*) δ 22.29, -14.49. UV- Vis: nm (M^{-1} cm^{-1}) 490 (6950), 400, (20260), 348, (23070). HRMS (ESI) *m/z* calcd for (**1b**+H)$^+$ 931.1501; found 931.1484.

[Ni(**L1**)Br] (**1c**)

Nickel bromide (109 mg, 0.5 mmol) in 10 mL methanol was added to a methanolic solution of **L1H** (219 mg, 0.5 mmol) and the mixture was refluxed with continuous stirring for 12h. The resulting shiny denim blue precipitates were separated by filtration, washed with cold ethanol (20 mL), diethyl ether (10 mL), and dried in vacuo to afford the pincer nickel complex [Ni(**L1**)Br] (**1c**). Yield (207 mg), 72%. Anal. calcd for $C_{26}H_{19}BrN_3NiPS$: C, 54.30%; H, 3.33%; N, 7.31;

found: C, 54.38%; H, 3.29%; N, 7.25. ATR-IR (neat, cm^{-1}): 1569, 1483, 1252, 1003, 972, 742, 689, 481, 453, 420. ^{1}H NMR (400 MHz, Chloroform-*d*) δ 8.32 (d, *J* = 8.3 Hz, 1H), 8.02 (s, 1H), 7.87 (t, *J* = 9.0 Hz, 4H), 7.54 (q, *J* = 6.6, 6.0 Hz, 3H), 7.48 (d, *J* = 7.5 Hz, 4H), 7.37 (d, *J* = 7.6 Hz, 1H), 7.33 (d, *J* = 7.7 Hz, 1H), 7.28 (s, 1H, merged with Chloroform-*d*), 7.09 (q, *J* = 8.6, 8.0 Hz, 2H), 6.92 (t, *J* = 7.5 Hz, 1H). ^{13}C NMR (101 MHz, Chloroform-*d*) δ 177.5, 149.7, 148.4, 136.3, 136.2, 134.5, 134.2, 134.1, 133.9, 133.9, 132.6, 131.6, 131.0, 130.2, 129.3, 129.0, 128.9, 128.7, 125.7, 121.5, 121.0, 118.2. ^{31}P NMR (162 MHz, Chloroform-*d*) δ 16.77. UV- Vis: nm (M^{-1} cm^{-1}) 490 (8310), 400 (9750), 284 (25550). HRMS (ESI) *m/z* calculated for [**1c**+H]$^{+}$: 575.9622, found 575.9585.

[Ni(**L1**)OAc] (**1d**)

Nickel acetate tetrahydrate (124 mg, 0.5 mmol) in 10 mL methanol was added to a methanolic solution of **L1H** (219 mg, 0.5 mmol) and the mixture was refluxed with continuous stirring for 12 h. The resulting shiny denim blue precipitates were separated by filtration, washed with cold ethanol (20 mL), diethyl ether (10 mL), and dried in vacuo to afford the pincer nickel complex [Ni(**L1**)OAc] (**1d**). Yield (197 mg), 71%. Anal. calcd for $C_{28}H_{22}N_3NiO_2PS$: C, 60.68%; H, 4.00%; N, 7.58; found: C, 60.82%; H, 3.95%; N, 7.51. ATR-IR (neat, cm^{-1}): 1625, 1471, 1313, 1279, 992, 750, 689, 545, 488, 442, 426. ^{1}H NMR (400 MHz, Chloroform-*d*) δ 7.93 (d, *J* = 7.2 Hz, 4H), 7.89 (s, 1H), 7.57 (t, *J* = 7.4 Hz, 2H), 7.50 (q, *J* = 7.7 Hz, 5H), 7.36 (d, *J* = 7.7 Hz, 2H), 7.31 (t, *J* = 7.5 Hz, 1H), 7.23 (d, *J* = 7.4 Hz, 1H), 7.11 (d, *J* = 7.4 Hz, 1H), 7.08 – 7.02 (m, 1H), 6.94 – 6.88 (m, 1H), 1.28 (s, 3H). ^{13}C NMR (101 MHz, Chloroform-*d*) δ 177.7, 176.9, 150.0, 148.8, 137.1, 133.6, 132.8, 131.8, 130.6, 130.0, 129.1, 126.1, 121.7, 120.7, 114.4, 22.8. ^{31}P NMR (162 MHz, Chloroform-*d*) δ 17.22. UV- Vis: nm (M^{-1} cm^{-1}) 578 (2600), 490 (11060), 351 (8870), 288 (33200). HRMS (ESI) *m/z* calculated for [**1c**+H]$^{+}$: 535.0651, found 535.0628.

[Pd(**L1**)Cl] (**2a**)

Solid palladium dichloride (71 mg, 0.4 mmol) was taken in 10 mL acetonitrile and was refluxed till all palladium dissolved. To the light-yellow color hot solution, Solid **L1H** (175 mg, 0.4 mmol) was added resulting a deep red color solution. The reactants were left with continuous stirring for 16 h at ambient temperature. The precipitates formed were separated by filtration, washed with diethyl ether, and dried in vacuo to afford the pincer palladium complex [Pd(**L1**)Cl] (**2a**). Yield: (203 mg), 88%. Anal. calcd for $C_{26}H_{19}ClN_3PdPS$: C, 53.99%; H, 3.31%; N, 7.27; found: C, C,

54.12%; H, 3.38%; N, 7.20. ATR-IR (neat, cm^{-1}): 1463, 1370, 1232, 1005, 919, 747, 691, 543, 518, 493, 422. ^{1}H NMR (400 MHz, Chloroform-*d*) δ 8.47 (d, *J* = 8.2 Hz, 1H), 8.15 (d, *J* = 3.9 Hz, 1H), 7.78 – 7.67 (m, 4H), 7.61 – 7.51 (m, 3H), 7.49 – 7.43 (m, 4H), 7.39 (dd, *J* = 12.5, 7.7 Hz, 2H), 7.26 (s, 2H), 7.20 – 7.15 (m, 1H), 7.01 – 6.93 (m, 1H). ^{13}C NMR (151 MHz, Chloroform-*d*) δ 150.4, 144.2, 137.8, 137.7, 135.2, 135.1, 134.3, 134.2, 133.0, 132.0, 131.0, 131.0, 130.0, 129.1, 129.1, 128.3, 127.9, 126.4, 121.3, 118.3, 117.9, 116.9. ^{31}P NMR (162 MHz, Chloroform-d) δ 27.37. UV- Vis: nm (M^{-1} cm^{-1}) 490 (8810), 324
(8740), 295 (17790), 278 (19210). HRMS (ESI) *m/z* calculated for (2(**2a**)-Cl)$^{+}$ 1120.9844; found 1120.9838.

[Pd(**L1**)$_2$] (**2b**)

Palladium dichloride (35.6 mg, 0.2 mmol) was taken in 10 mL acetonitrile and was refluxed till all palladium dissolved. To the light-yellow color solution, 175 mg (0.4 mmol) of **L1H** in acetonitrile was added followed by few drops of triethylamine. The resultant deep orange color solution was refluxed with continuous stirring for 12 h at 80 ºC. The precipitates formed were separated by filtration, washed with diethyl ether, and dried in vacuo to afford the pincer palladium complex [Pd(**L1**)$_2$] (**2b**). Yield: (100 mg) 51%. Anal. calcd for $C_{52}H_{38}N_6PdP_2S_2$: C, 63.77%; H, 3.91%; N, 8.58; found: C, 63.81%; H, 3.95%; N, 8.47. ATR-IR (neat, cm^{-1}): 1486, 1464, 1233, 1131, 1009, 747, 696, 543, 504, 421. ^{31}P NMR (243 MHz, Chloroform-*d*) δ 27.14, -13.30. UV-Vis: nm (M^{-1} cm^{-1}) 490 (6060), 338 (1260), 294 (14380). HRMS (ESI) *m/z* calcd for (**2b**+H)$^{+}$ 979.1199; found 979.1221.

[Pd(**L1H**)Cl]NO_3 (**2c**)

Complex **2a** (58 mg, 0.1 mmol) was taken in 10 mL methanol. To this solution, 100µL of aqueous HNO_3 from a 1M stock solution was added dropwise with continuous stirring. The solution was left for few days, crystals were collected, washed with diethyl ether, and dried in vacuo to afford the cationic palladium complex [Pd(**L1H**)Cl]NO_3 (**2c**). Yield: (33 mg), 57%. Anal. calcd for $C_{26}H_{20}ClN_4O_3PPdS$: C, 48.69%; H, 3.14%; N, 8.74; found: C, 48.79%; H, 3.10%; N, 8.67. ATR-IR (neat, cm^{-1}): 3448, 1712, 1437, 1274, 1120, 996, 754, 693, 539. ^{1}H NMR (600 MHz, Chloroform-*d*) δ 8.34 (dd, *J* = 7.7, 4.1 Hz, 1H), 7.71 – 7.67 (m, 2H), 7.61 (dd, *J* = 12.2, 7.5 Hz, 7H), 7.54 – 7.46 (m, 8H), 7.09 (dd, *J* = 14.7, 7.7 Hz, 1H). ^{13}C NMR (101 MHz, Chloroform-*d*) δ 134.85, 134.76, 134.29, 134.18, 133.64, 133.52, 133.19, 133.16, 132.96, 132.93, 132.45, 132.35,

131.16, 131.03, 130.31, 130.26, 129.19, 129.06. ^{31}P NMR (243 MHz, Chloroform-*d*) δ 40.09. UV-Vis: nm (M^{-1} cm^{-1}) 510 (970), 387, (2940) 270 (13400). HRMS (ESI) *m/z* calculated for (**2c**)$^+$ 579.9831; found 579.9792.

[Pt(**L1**)Cl] (**3a**)

Cis-dichlorobis(dimethylsulfoxide)platinum(II) (84.5 mg, 0.2 mmol) was taken in 10 mL acetonitrile and was refluxed till all dissolved. To this solution, **L1H** (87.5 mg, 0.2 mmol) was added resulting ruby red solution and refluxed with continuous stirring for 24 h. The solvent was reduced to 5 mL, precipitates formed were separated by filtration, washed with diethyl ether, and dried in vacuo to afford the pincer platinum complex [Pt(**L1**)Cl] (**3a**). Yield: (102.5 mg), 77%. Anal. calcd. for $C_{26}H_{19}ClN_3PtPS$: C, 46.82%; H, 2.87%; N, 6.30; found: C, 46.74%; H, 2.80%; N, 6.18. ATR-IR (neat, cm^{-1}): 1478, 1237, 1004, 742, 691, 493, 548, 520, 493, 460, 433. ^{1}H NMR (400 MHz, Chloroform-*d*) δ 8.67 (d, *J* = 8.1 Hz, 1H), 8.37 (s, 1H), 7.76 – 7.69 (m, 4H), 7.60 – 7.56 (m, 1H), 7.55 – 7.50 (m, 3H), 7.44 (ddd, *J* = 9.9, 8.1, 5.1 Hz, 6H), 7.40 – 7.34 (m, 1H), 7.20 (t, *J* = 8.4 Hz, 1H), 6.99 (t, *J* = 7.6 Hz, 1H). ^{13}C NMR (101 MHz, Chloroform-*d*) δ 150.5, 145.2, 138.1, 137.9, 135.2, 135.0, 134.8, 134.3, 134.2, 132.8, 131.8, 131.3, 131.2, 129.0, 128.9, 128.3, 126.4, 121.5, 121.3, 118.5, 117.9, 116.2. ^{31}P NMR (162 MHz, Chloroform-*d*) δ 1.69. UV- Vis: nm (M^{-1} cm^{-1}) 552 (1220), 490 (12180), 330 (980), 295. (18690). HRMS (ESI) *m/z* calculated for (**3a**+H)$^+$ 668.0442; found 668.0402.

[Ni(**L2**)$_2$] (**1e**)

Nickel chloride hexahydrate (60 mg, 0.25 mmol) in 10 mL methanol was added to a methanolic solution of **L2H** (0.5 mmol) under reflux. The dark red solution was stirred for overnight, solvent was removed, washed with diethyl ether, and dried in *vacuo* to produce complex **1e**. Yield: (136 mg), 82%. Anal. calcd. for $C_{34}H_{22}N_8NiS_2$: C, 46.82%; H, 2.87%; N, 6.30; found: C, 47.01%; H, 2.92%; N, 6.35. ATR-IR (neat, cm^{-1}): 1669, 1444, 1382, 1258, 1028, 832, 756, 670, 556, 458. UV- Vis: nm (M^{-1} cm^{-1}) 490 (11260), 370 (5590), 292 (10650). HRMS (ESI) *m/z* calcd for, (**1e**+H)$^+$ 665.0835; found 665.0833.

[Pd(**L2**)Cl] (**2d**)

For the synthesis of complex **2d**, the method of synthesis of **1a** was followed by taking 0.5 mmol of ligand **L2H** and 0.5 mmol of $PdCl_2$. The resulting deep red precipitates were washed with ether

and dried to produce pure complex **2d**. Yield: (187 mg), 84%. Anal. calcd. for $C_{17}H_{11}ClN_4PdS$: C, 45.86%; H, 2.49%; N, 12.58; found: C, 45.92%; H, 2.51%; N, 12.48. ATR-IR (neat, cm^{-1}): 1497, 1451, 1265, 1046, 833, 748, 681, 420. ^{1}H NMR (600 MHz, Chloroform-*d*) δ 10.53 (d, *J* = 5.5 Hz, 1H), 8.68 (d, *J* = 8.1 Hz, 1H), 8.48 (d, *J* = 8.0 Hz, 1H), 8.14 (s, 1H), 8.01 (d, *J* = 7.3 Hz, 1H), 7.96 (d, *J* = 7.9 Hz, 1H), 7.74 – 7.70 (m, 2H), 7.38 (d, *J* = 7.7 Hz, 1H), 7.23 (d, *J* = 8.3 Hz, 1H), 7.03 (t, *J* = 7.5 Hz, 1H). ^{13}C NMR (101 MHz, Chloroform-*d*) δ 158.5, 149.3, 141.8, 139.7, 138.2, 133.0, 129.7, 128.6, 128.5, 127.5, 126.3, 122.5, 121.8, 121.5, 121.5, 117.7, 116.9. UV- Vis: nm (M^{-1} cm^{-1}) 490 (8330), 345 (15950), 296 (11940). HRMS (ESI) *m/z* calcd for (2(**2d**)-Cl)$^+$ 854.9171; found 854.9196.

[Pd(**L2**)N_3] (**2e**)

The complex **2d** (111.3 mg, 0.25 mmol) was taken in 10 mL acetone and solid sodium azide (0.3 mmol) was added to it. The reaction mixture was stirred for 12 h at ambient temperature. The deep pink fiber like precipitated was filtered and the residue was soluble in excess chloroform and again filtered. The filtrates were removed and solids were collected, washed with ether, and dried over fused calcium chloride to produce **2e**. Yield: (79 mg), 70%. Anal. calcd. for $C_{17}H_{11}N_7PdS$: C, 45.19%; H, 2.45%; N, 21.70; found: C, C, 45.26%; H, 2.41%; N, 21.81. ATR-IR (neat, cm^{-1}): 2038, 1491, 1274, 1037, 773, 753, 682, 471, 418. ^{1}H NMR (600 MHz, Chloroform-*d*) δ 10.02 (m, 1H), 8.60 (d, *J* = 8.1 Hz, 1H), 8.25 (s, 1H), 8.09 – 8.04 (m, 2H), 7.99 (d, *J* = 8.2 Hz, 1H), 7.83 (dt, *J* = 15.8, 7.3 Hz, 2H), 7.46 (d, *J* = 7.7 Hz, 1H), 7.38 (t, *J* = 7.8 Hz, 1H), 7.09 (t, *J* = 7.5 Hz, 1H). ^{13}C NMR (101 MHz, Chloroform-*d*) δ 157.1, 143.7 (d, *J* = 12.7 Hz), 142.4, 138.9, 137.56, 135.5, 133.6, 133.2, 127.9, 127.6, 127.2, 123.0, 115.7, 115.1. UV- Vis: nm (M^{-1} cm^{-1}) 500 (2960), 345 (5510), 295 (4600). HRMS (ESI) *m/z* calcd for (2(**2e**)-N_3)$^+$ 861.9581; found 861.9499.

[Pt(**L2**)Cl] (**3b**)

84.5 mg (0.2 mmol) of Cis-dichlorobis(dimethylsulfoxide)platinum(II) was taken in 10 mL acetonitrile and was refluxed till all solid dissolved. To this solution, **L2H** (61 mg, 0.2 mmol) was added and the resulting violet solution was refluxed with continuous stirring for 24 h. The mixture was cooled, solvent evaporated to 2 mL and the precipitates formed were separated by filtration, washed with diethyl ether, and dried in vacuo to afford the pincer platinum complex **3b**. Yield: (66 mg), 62%. Anal. calcd. for $C_{17}H_{11}ClN_4PtS$: C, 38.24%; H, 2.08%; N, 10.49; found: found: C, 38.42%; H, 2.04%; N, 10.53. ATR-IR (neat, cm^{-1}): 1500, 1453, 1234, 1036, 827, 747, 685, 445,

422. ^{1}H NMR (400 MHz, Chloroform-*d*) δ 10.81 (d, *J* = 5.8 Hz, 1H), 8.81 (d, *J* = 8.3 Hz, 1H), 8.58 – 8.44 (m, 2H), 8.03 – 7.94 (m, 2H), 7.77 – 7.68 (m, 2H), 7.41 (d, *J* = 8.2 Hz, 1H), 7.29 (d, *J* = 7.3 Hz, 1H), 7.06 (t, *J* = 7.6 Hz, 1H). ^{13}C NMR (101 MHz, Chloroform-*d*) δ 158.1, 142.2, 139.6, 139.4, 134.4, 134.2, 127.1, 126.3, 123.0, 122.6, 122.4, 122.4, 121.7, 121.5, 117.2. UV- Vis: nm (M^{-1} cm^{-1}) 301 (9390), 367 (17420), 516 (6040). HRMS (ESI) *m/z* calculated for (**3b**-Cl+CH_3CN)$^{+}$ 539.0613; found 539.0587.

[Ni(**L3**)$_2$(H_2O)$_2$] (**1f**)

Ligand **L3H** (131 mg, 0.5 mmol) was taken in 5.0 mL methanol and stirred under reflux. Nickel chloride hexahydrate (60 mg, 0.25 mmol) in 5.0 mL methanol was added to it followed by few drops of triethylamine. The mixture and was refluxed for 12h, cooled to produce brown precipitate which was then filtered, washed with ether, and dried over fused $CaCl_2$ to produce pure nickel complex **1f**. Yield: (114 mg), 74%. Anal. calcd. for $C_{32}H_{22}N_4NiO_6$: C, 62.27%; H, 3.59%; N, 9.08; found: C, 62.34%; H, 3.61%; N, 8.90. ATR-IR (neat, cm^{-1}): 3281, 1658, 1602, 1446, 1189, 1089, 972, 739, 471, 451. ^{1}H NMR (600 MHz, DMSO-d_6) δ 14.65 (s, 2H), 8.28 (d, *J* = 6.0 Hz, 3H), 7.65 (s, 4H), 7.47 (s, 4H), 7.43 – 7.34 (m, 4H), 7.27 (s, 2H), 6.97 (s, 3H), 5.22 (s, 2H). ^{13}C NMR (151 MHz, DMSO-d_6) δ 153.2, 151.6, 131.9, 129.6, 124.3, 122.7, 121.3, 116.1, 113.5, 104.2. UV- Vis: nm (M^{-1} cm^{-1}) 318 (10385), 335 (11425), 361 (14310), 507 (256). HRMS (ESI) *m/z* calcd for (**1f**-2H_2O+H)$^{+}$ 581.0754; found 581.0754.

[Pd(**L3**)$_2$] (**2f**)

Solid palladium dichloride (44.5 mg, 0.25 mmol) was taken in 10 mL acetonitrile and was refluxed till all palladium dissolved. To the light-yellow color hot solution, Solid **L3H** (131 mg, 0.5 mmol) was added followed by few drops of triethylamine. The resulting deep red color solution were left with continuous stirring for 16 h at ambient temperature. The precipitates formed were separated by filtration, washed with diethyl ether, and dried in vacuo to afford the complex **2f**. Yield: (99 mg), 63%. Anal. calcd. for $C_{32}H_{18}N_4PdO_4$: C, 61.11%; H, 2.88%; N, 8.91; found: C, 61.20%; H, 2.91%; N, 8.82. ATR-IR (neat, cm^{-1}): 1702, 1605, 1539, 1450, 1189, 1085, 955, 743, 447, 422. ^{1}H NMR (400 MHz, DMSO-d_6) δ 8.66 (d, *J* = 6.3 Hz, 2H), 8.54 – 8.49 (m, 2H), 8.04 (d, *J* = 8.2 Hz, 2H), 7.89 (td, *J* = 7.8, 1.8 Hz, 2H), 7.64 (s, 2H), 7.46 (dd, *J* = 11.7, 1.3 Hz, 4H), 7.39 – 7.33 (m, 4H). ^{13}C NMR (151 MHz, DMSO-d_6) δ 158.22, 151.65, 149.25, 149.15, 137.40, 136.76, 136.67, 129.30, 124.34, 122.65, 120.01, 116.98, 113.71, 113.51, 109.72, 106.43. UV- Vis: nm (M-

[1] cm^{-1}) 294 (8212), 325 (9240), 341 (9282), 352 (7945), 440 (826). HRMS (ESI) *m/z* calcd for (**2f**+H)$^+$ 629.0448; found 629.0405.

[Pt(**L3**)$_2$] (**3c**)

Cis-dichlorobis(dimethylsulfoxide)platinum(II) (21 mg, 0.05 mmol) and **L3H** (26.4 mg, 0.1 mmol) was mixed in 10 mL acetonitrile along with few drops of triethylamine. The mixture was refluxed with continuous stirring for 24 h. The yellow precipitates formed were separated by filtration, washed with diethyl ether, and dried in vacuo to produce the platinum complex **3c**. Yield: (25.5 mg), 71%. Anal. calcd. for $C_{32}H_{18}N_4PtO_4$: C, 53.56%; H, 2.53%; N, 7.81; found: C, 53.62%; H, 2.50%; N, 7.72. ATR-IR (neat, cm^{-1}): 1702, 1611, 1546, 1454, 1191, 1089, 958, 746, 733, 449, 430. UV- Vis: nm (M^{-1} cm^{-1}) 265 (29804), 292 (25854), 319 (25751), 395 (15429). HRMS (ESI) *m/z* calculated for (**3c**+H)$^+$ 718.1051; found 718.1022.

[Ni(**L4**)$_2$(H_2O)$_2$]Cl_2 (**1g**)

Nickel chloride hexahydrate (60 mg, 0.25 mmol) and **L5** (175 mg, 0.5 mmol) were taken in 10 mL methanol and refluxed for overnight. The solution was left undisturbed for few days to produce cloud green crystals of **1g**. Yield: (147 mg), 68%. %. Anal. calcd. for [$C_{36}H_{28}N_6Br_2NiO_2$]Cl_2: C, 49.93%; H, 3.26%; N, 9.70; found: C, 50.14%; H, 3.28%; N, 9.64%. ATR-IR (neat, cm^{-1}): 3324 (broad), 1608, 1479, 1369, 1150, 1057, 781, 743, 706, 418. UV- Vis: nm (M^{-1} cm^{-1}) 277 (15860), 285 (16405), 325(22248), 360 (31285), 371 (33242) 447 (27), 682 (18). HRMS (ESI) *m/z* calcd for [**1g**-2H_2O]$^{2+}$ 378.9875; found 378.9877.

[Pd(**L4**)Cl_2] (**2g**)

Solid palladium dichloride (44.5 mg, 0.25 mmol) was taken in 10 mL acetonitrile and was heated till all $PdCl_2$ dissolved. To this solution, 87.5 mg (0.25 mmol) of **L4** was added and the yellow solution was stirred for 24 h at ambient temperature. The precipitates formed were separated by filtration, washed with diethyl ether, and dried in to afford palladium complex **2g**. Yield: (108 mg), 82%. Anal. calcd. for $C_{18}H_{12}BrCl_2N_3Pd$: C, 40.98%; H, 2.29%; N, 7.97; found: C, 41.14%; H, 2.35%; N, 7.93%. ATR-IR (neat, cm^{-1}): 1604, 1557, 1512, 1335, 1244, 1150, 1050, 1022, 1009, 772, 739, 703, 633, 591, 416. ^{1}H NMR (400 MHz, DMSO-d_6) δ 9.01 – 8.96 (m, 1H), 8.44 (d, *J* = 9.4 Hz, 1H), 8.32 (d, *J* = 8.1 Hz, 1H), 8.27 ($CHCl_3$), 8.19 (t, *J* = 8.4 Hz, 1H), 7.79 (dd, *J* = 5.8, 3.4 Hz, 1H), 7.75 (d, *J* = 7.2 Hz, 1H), 7.63 (dd, *J* = 6.0, 3.3 Hz, 1H), 7.59 – 7.54 (m, 2H), 7.49 (q, *J* =

7.1, 6.0 Hz, 2H), 7.11 (s, 1H), 5.72 (CH_2Cl_2). ^{13}C NMR (151 MHz, DMSO-d_6) δ 152.6, 149.2, 140.7, 138.9, 134.1, 133.0, 132.3, 128.3, 128.0, 127.8, 127.2, 127.2, 124.9, 123.7, 122.6, 120.3, 117.2, 116.8, 79.2 ($CHCl_3$), 54.9 (CH_2Cl_2). UV- Vis: nm (M^{-1} cm^{-1}) 268 (9973), 361 (10597), 378 (12333), 396 (8703). HRMS(ESI) *m/z* calcd for [**2g**-Cl]$^+$ 491.8923; found 491.8925.

[Pt(**L4**)Cl_2] (**3d**)

Following the procedure of **3a**, complex [Pt(**L4**)Cl_2] (**3d**) was prepared using ligand **L4** (35 mg, 0.1 mmol) and $PtCl_2(DMSO)_2$ (42 mg, 0.1 mmol) in acetonitrile. Yield: (46.5 mg), 76%. Anal. calcd. for $C_{18}H_{12}BrCl_2N_3Pt$: C, 35.09%; H, 1.96%; N, 6.82; found: C, 35.20%; H, 2.04%; N, 6.78%. ATR-IR (neat, cm^{-1}): 1642, 1608, 1561, 1513, 1485, 1428, 1338, 1150, 1024, 957, 769, 739, 704, 694, 638, 430, 416. ^1H NMR (400 MHz, DMSO-d_6) δ 9.42 – 9.30 (m, 1H), 8.47 (d, J = 9.4 Hz, 1H), 8.34 (d, J = 7.9 Hz, 1H), 8.26 – 8.20 (m, 1H), 7.83 – 7.79 (m, 1H), 7.74 (d, J = 7.2 Hz, 1H), 7.67 (dd, J = 5.8, 3.5 Hz, 1H), 7.61 – 7.56 (m, 2H), 7.55 – 7.47 (m, 2H), 7.13 (t, J = 7.2 Hz, 1H), 5.72 (CH_2Cl_2). ^{13}C NMR (101 MHz, Chloroform-*d*) δ 153.46, 148.16, 140.22, 139.62, 134.34, 133.40, 132.60, 129.67, 128.74, 128.18, 128.09, 127.28, 125.06, 124.13, 122.96, 120.28, 116.91, 116.84, 55.08 (CH_2Cl_2), 48.87 (MeOH). UV- Vis: nm (M^{-1} cm^{-1}) 310 (10042), 365 (10498), 383 (10466), 406 (8391). HRMS (ESI): *m/z* calcd for [**3d**+H]$^+$ 579.9524; found 579.9492.

[Ni(**L5H**)$_2$(H_2O)$_2$]Cl_2 (**1h**)

Nickel chloride hexahydrate (60 mg, 0.25 mmol) in 10 mL methanol was added to a methanolic solution of **L5H** (0.5 mmol) under reflux. The light brown solution was stirred for overnight, solvent was removed, washed with diethyl ether, and dried in *vacuo* to produce light green crystalline powder of complex **1h**. Yield: (147 mg), 70%. Anal. calcd. for [$C_{44}H_{34}N_6NiO_4$]Cl_2: C, 62.89%; H, 4.08%; N, 10.00 %; found: C, 63.00%; H, 4.15%; N, 9.86%. ATR-IR (neat, cm^{-1}): 3048, 1602, 1515, 1477, 1735, 1279, 1242, 1146, 1080, 823, 776, 739, 703, 512, 419. UV- Vis: nm (M^{-1} cm^{-1}) 277 (17230), 341 (22260). HRMS (ESI) *m/z* calcd for (**1h**–2H_2O)$^{2+}$ 366.0886; found 366.0863.

[Pd(**L5H**)Cl] (**2h**)

$PdCl_2$ (89 mg, 0.5 mmol) was taken in 10 mL acetonitrile and was heated till all palladium dichloride dissolved. To this, 168.5 mg (0.5 mmol) of **L5H** was added followed by few drops of Et_3N resulting a brown solution. After stirring for 24 h at room temperature, the solvent was

reduced to half. The complex **2h** precipitated and separated by filtration, washed with diethyl ether and dried. Yield: (196 mg), 82%. Anal. calcd. for $C_{22}H_{14}ClN_3OPd$: C, 55.25%; H, 2.95%; N, 8.79; found: C, 55.41%; H, 3.04%; N, 8.72%. ATR-IR (neat, cm^{-1}): 2583, 1639, 1605, 1519, 1385, 1240, 1106, 820, 750, 667, 515, 420. ^{1}H NMR (400 MHz, DMSO-d_6) δ 8.78 (d, J = 6.1 Hz, 1H), 8.51 (d, J = 9.6 Hz, 1H), 8.40 (d, J = 8.3 Hz, 1H), 8.23 (t, J = 8.6 Hz, 1H), 7.96 (d, J = 7.2 Hz, 1H), 7.89 (d, J = 8.1 Hz, 1H), 7.83 (d, J = 9.1 Hz, 1H), 7.55 – 7.48 (m, 2H), 7.45 (d, J = 7.0 Hz, 1H), 7.34 (d, J = 7.2 Hz, 1H), 7.26 (dd, J = 18.8, 8.7 Hz, 2H), 7.15 – 7.10 (m, 1H). ^{13}C NMR (101 MHz, DMSO-d_6) δ 166.55, 152.43, 151.25, 140.14, 133.73, 131.73, 130.11, 128.75, 128.73, 127.22, 126.82, 126.73, 126.56, 125.13, 124.82, 122.95, 122.44, 120.55, 117.96, 114.73, 102.33. UV- Vis: nm (M^{-1} cm^{-1}) 262 (23360), 382 (9910), 400 (8650), 420 (4890), 458 (2920). HRMS (ESI) *m/z* calcd for [**2h**-Cl]$^+$ 442.0175; found 442.0151.

[Pt(**L5H**)Cl] (**3e**)

Cis-dichlorobis(dimethylsulfoxide)platinum(II) (42 mg, 0.1 mmol) was taken in 10 mL acetonitrile and was refluxed till all salt dissolved. To this solution, **L5H** (34 mg, 0.1 mmol) was added followed by few drops of triethylamine. The resulting deep brown solution was refluxed with continuous stirring for 24 h. The precipitates formed were separated by filtration, washed with diethyl ether, and dried in *vacuo* to afford the pincer platinum complex [Pt(**L5**)Cl] (**3e**). Yield: (37 mg), 65%. Anal. calcd. for $C_{22}H_{14}ClN_3OPt$: C, 46.61%; H, 2.49%; N, 7.41; found: C, 46.72%; H, 2.53%; N, 7.30%. ATR-IR (neat, cm^{-1}): 1740, 1610, 1511, 1482, 1362, 1240, 1203, 989, 829, 756, 730, 662, 536, 417.^{1}H NMR (400 MHz, DMSO-d_6) δ 9.16 (d, J = 5.9 Hz, 1H), 8.58 (d, J = 9.3 Hz, 1H), 8.45 (d, J = 8.2 Hz, 1H), 8.29 – 8.24 (m, 1H), 7.97 (d, J = 7.4 Hz, 1H), 7.90 (dd, J = 15.4, 8.5 Hz, 2H), 7.51 (dt, J = 10.3, 6.3 Hz, 3H), 7.35 (d, J = 9.1 Hz, 2H), 7.28 (d, J = 8.4 Hz, 1H), 7.16 (t, J = 6.5 Hz, 1H). ^{13}C NMR (101 MHz, DMSO-d_6) δ 164.70, 152.73, 150.65, 138.99, 130.90, 130.82, 130.48, 129.27, 128.55, 127.61, 127.27, 126.23, 125.61, 125.45, 122.70, 122.63, 120.46, 117.34, 114.28, 101.84, 79.28($CHCl_3$). UV- Vis: nm (M^{-1} cm^{-1}) 332 (13350), 395 (13650), 431 (11960), 451 (12430). HRMS (ESI) *m/z* calcd for [**3e**+H]$^+$ 568.0542; found 568.0515

3.4.3 Computational study

For computational study, all calculations were performed by using Gaussian16 (G16) program and GaussView 5.0 was used for picturization.[75,76] The geometry of all ligands and complexes was optimized using B3LYP hybrid functional and 6-311g(d,p)/LanL2DZ basis set that matched well with

single crystal X-ray structure. Density functional theory (DFT) was used to model the frontier molecular orbitals to predict the kinetic stability and chemical reactivity (Appendix II).

3.4.4 Crystallographic data collection

For the single crystal XRD data collection of the appropriate single crystals of **L2H**, **1a**, **2a**, **1e**; a single source Super Nova CCD System instrument from Agilent Technologies equipped with a fine focus 1.75 kW sealed tube with Mo-Kα radiation was used at room temperature. The data were reduced using CrysAlisPro and Autochem2.1 software.[77] For rest of the ligands and complexes, data was collected at room temperature using a Bruker SMART APEX CCD diffractometer equipped with fine focus 1.75 kW sealed tube of Mo-Kα (λ = 0.71073 Å) X-ray source, with increasing ω (width of 0.3° per frame) at a scan speed of either 3 or 5 s per frame.[78] The SMART software was used for data acquisition and the SAINT software for data extraction. The structure solution was performed by direct methods using APEX4, SHELXT, CrysAlispro, Autochem and refined with Olex2-1.5 using SHELXL program.[79,80] All atoms except hydrogen atoms are tuned using anisotropic displacement parameters, whereas hydrogen atoms are tuned using relative isotropic parameters. The disorder in molecular structure of **1g** and **1h** was fixed using partial occupancies factor, unidentified electron densities were masked using OLEX2 utility.[81] PLATON was used for structure validation and for pictorial depiction linked to X-ray single crystal data, Mercury and ORTEP software was used.[82–84]

3.4.5 Optimization of imines synthesis from alcohols and amines.

Benzylamine (0.5 mmol), benzyl alcohol (0.6 mmol), base (0.75 mmol), and catalyst (x mol%) were mixed in a solvent (5.0 mL) and was stirred at specified temperature for a given time. After the completion of the reaction, the mixture was cooled, diluted with ethyl acetate (10.0 mL). Then it was filtered through a short pad of celite and filtrate was washed with copious amount of ethylacetate. The solvent was removed under reduced pressure, and the crude product was purified by preparative thin layer chromatography to produce isolated yields.

3.4.6 General procedure for imines synthesis.

Aryl/alkyl amine (0.5 mmol) or diamine (0.25 mmol), aryl alcohol (0.6 mmol), ^{t}BuOK (0.5 mmol), catalyst **1a** (1.0 mol%), and toluene (5.0 mL) was stirred at 110 ºC for 12 h. After the completion of the reaction, the mixture was cooled, diluted with ethylacetate. Then it was filtered through a

short pad of celite and washed with ethyl acetate (2×10.0 mL). The solvent was removed under reduced pressure, and the crude product was purified by preparative thin layer chromatography.

3.4.7 Specific procedures and characterization data for imines 4a-4r

(E)-N,1-diphenylmethanimine (4a)[85]

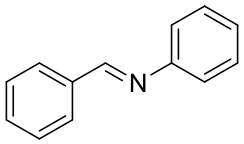

^{1}H NMR (400 MHz, Chloroform-*d*) δ 8.41 (s, 1H), 7.92 – 7.85 (m, 2H), 7.43 (dd, *J* = 5.0, 1.8 Hz, 3H), 7.36 (td, *J* = 7.1, 2.0 Hz, 2H), 7.23 – 7.17 (m, 3H). ^{13}C NMR (151 MHz, Chloroform-d) δ 152.2, 136.3, 131.5, 129.3, 129.0, 128.9, 126.1, 121.1.

(E)-N-benzyl-1-phenylmethanimine (4b) [86]

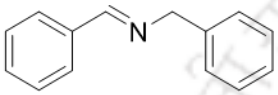

^{1}H NMR (600 MHz, Chloroform-*d*) δ 8.45 (s, 1H), 7.85 (d, *J* = 7.5 Hz, 2H), 7.47 (d, *J* = 5.6 Hz, 3H), 7.41 (d, *J* = 4.1 Hz, 4H), 7.34 – 7.32 (m, 1H), 4.89 (s, 2H). ^{13}C NMR (151 MHz, Chloroform-*d*) δ 162.1, 139.4, 136.2, 130.8, 128.7, 128.6, 128.4, 128.0, 127.1, 65.1.

(E)-1-benzylidene-2-phenylhydrazine (4c) [87]

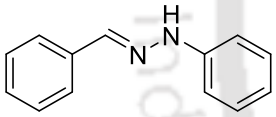

^{1}H NMR (600 MHz, Chloroform-d) δ 7.67 (d, J = 7.4 Hz, 3H), 7.60 (s, 1H), 7.38 (t, J = 7.5 Hz, 2H), 7.33 – 7.27 (m, 3H), 7.13 (d, J = 7.9 Hz, 2H), 6.89 (t, J = 7.2 Hz, 1H). ^{13}C NMR (151 MHz, Chloroform-d) δ 144.8, 137.4, 135.5, 129.5, 128.8, 128.6, 126.3, 120.3, 112.9.

(E)-N-cyclooctyl-1-phenylmethanimine (4d) [88]

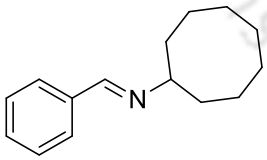

^{1}H NMR (600 MHz, Chloroform-*d*) δ 8.26 (s, 1H), 7.72 (dd, *J* = 6.5, 2.9 Hz, 2H), 7.41 – 7.37 (m, 3H), 3.39 (tt, *J* = 8.7, 3.7 Hz, 1H), 1.89 – 1.81 (m, 4H), 1.70 (m, *J* = 13.1, 3.5 Hz, 2H), 1.65 – 1.47 (m, 8H). ^{13}C NMR (151 MHz, Chloroform-*d*) δ 157.75, 136.79, 130.32, 128.60, 128.13, 71.75, 34.21, 27.41, 25.86, 24.28.

(E)-2-(benzylideneamino)-5-nitrophenol (4e) [89]

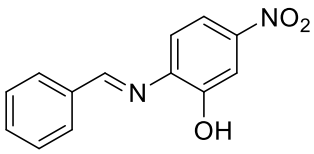

^{1}H NMR (600 MHz, Chloroform-*d*) δ 8.82 (s, 1H), 8.26 (s, 1H), 8.15 (d, *J* = 8.2 Hz, 1H), 7.96 (d, *J* = 7.3 Hz, 2H), 7.78 (s, 1H), 7.56 (dt, *J* = 27.0, 6.8 Hz, 3H), 7.10 (d, *J* = 8.8 Hz, 1H). ^{13}C NMR (151 MHz, Chloroform-d) δ 160.6, 157.9, 135.6, 135.1, 129.5, 129.3, 124.8, 115.2, 112.2.

(E)-N'-benzylidene-3,5-dihydroxybenzohydrazide (4f) [90]

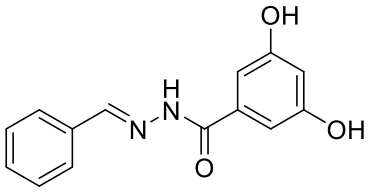

^{1}H NMR (600 MHz, DMSO-d6) δ 11.71 (s, 1H), 9.66 (s, 2H), 8.43 (s, 1H), 7.71 (d, J = 5.9 Hz, 2H), 7.43 (d, J = 7.3 Hz, 3H), 6.78 (s, 2H), 6.45 (s, 1H). ^{13}C NMR (151 MHz, DMSO-d6) δ 163.7, 158.6, 147.9, 135.6, 134.5, 130.2, 129.0, 127.2, 106.0, 105.9.

(E)-1-(4-nitrophenyl)-N-phenylmethanimine (4g) [91]

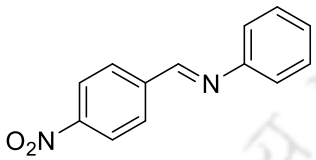

^{1}H NMR (600 MHz, Chloroform-*d*) δ 8.59 (s, 1H), 8.39 – 8.31 (m, 2H), 8.11 (d, *J* = 8.7 Hz, 2H), 7.46 (t, *J* = 7.7 Hz, 2H), 7.33 (t, *J* = 7.4 Hz, 1H), 7.29 (d, *J* = 7.3 Hz, 2H). ^{13}C NMR (151 MHz, Chloroform-d) δ 157.5, 151.1, 149.5, 141.7, 129.5, 129.5, 127.2, 124.1, 121.1.

(E)-N-hexyl-1-phenylmethanimine (4h) [92]

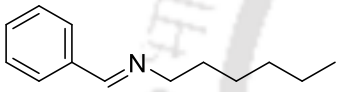

^{1}H NMR (600 MHz, Chloroform-*d*) δ 8.23 (s, 1H), 7.81 – 7.70 (m, 2H), 7.36 (s, 3H), 3.60 (t, *J* = 7.1 Hz, 2H), 1.79 – 1.67 (m, 2H), 1.47 – 1.28 (m, 6H), 0.92 (t, *J* = 6.8 Hz, 3H). ^{13}C NMR (151 MHz, Chloroform-*d*) δ 160.3, 136.3, 130.1, 128.3, 127.8, 61.6, 31.5, 30.8, 26.9, 22.5, 13.9.

(E)-N-hexyl-1-(3-methoxyphenyl)methanimine (4i) [92]

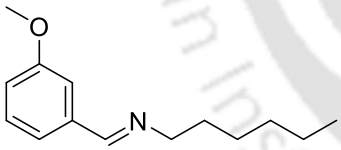

^{1}H NMR (600 MHz, Chloroform-*d*) δ 8.14 (s, 1H), 7.30 (s, 1H), 7.20 (dt, *J* = 16.1, 7.5 Hz, 2H), 6.90 – 6.86 (m, 1H), 3.72 (s, 3H), 3.52 (s, 1H), 1.64 (p, *J* = 7.1 Hz, 2H), 1.35 – 1.23 (m, 7H), 0.85 (t, *J* = 6.7 Hz, 3H). ^{13}C NMR (151 MHz, Chloroform-*d*) δ 160.2, 159.7, 137.6, 129.2, 121.0, 116.8, 111.4, 61.4, 54.8, 31.5, 30.7, 26.8, 22.4, 13.8.

(1E,1'E)-N,N'-(propane-1,3-diyl)bis(1-phenylmethanimine) (4j) [93]

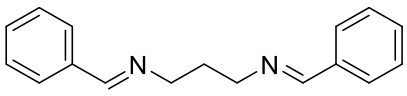

^{1}H NMR (600 MHz, Chloroform-*d*) δ 8.30 (s, 2H), 7.77 (s, 4H), 7.42 (s, 6H), 3.76 (t, *J* = 6.8 Hz, 4H), 2.18 (p, *J* = 6.8 Hz, 2H). ^{13}C NMR (151 MHz, Chloroform-*d*) 161.1, 136.2, 130.4, 128.4, 127.9, 59.0, 31.8.

(1E,1'E)-N,N'-(octane-1,8-diyl)bis(1-phenylmethanimine) (4k) [86]

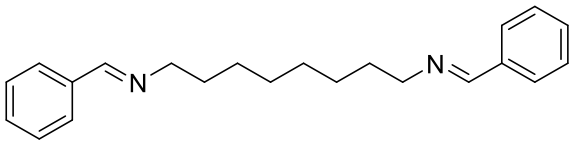

^{1}H NMR (600 MHz, Chloroform-*d*) δ 8.24 (s, 2H), 7.73 (dd, *J* = 6.5, 3.0 Hz, 4H), 7.43 – 7.33 (m, 6H), 3.59 (t, *J* = 7.0 Hz, 4H), 1.77 – 1.67 (m, 4H), 1.36 (s, 8H). ^{13}C NMR (151 MHz, Chloroform-*d*) δ 160.6, 136.2, 130.3, 128.4, 127.9, 61.6, 30.80, 29.3, 27.2.

(1E,1'E)-N,N'-(1,4-phenylene)bis(1-phenylmethanimine) (4l) [94]

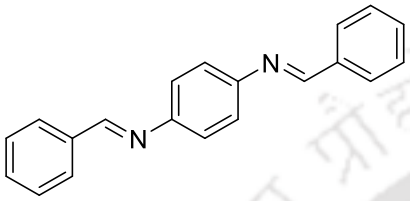

^{1}H NMR (600 MHz, Chloroform-*d*) δ 8.55 (s, 2H), 7.96 (s, 4H), 7.52 (s, 6H), 7.33 (s, 4H). ^{13}C NMR (151 MHz, Chloroform-*d*) δ 159.8, 150.1, 136.4, 131.4, 128.9, 128.9, 121.9.

(1E,1'E)-N,N'-(1,4-phenylene)bis(1-(pyridin-2-yl)methanimine) (4m) [95]

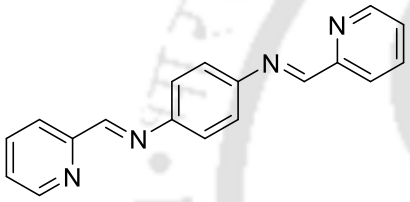

^{1}H NMR (600 MHz, Chloroform-*d*) δ 8.68 (d, *J* = 4.1 Hz, 2H), 8.62 (s, 2H), 8.17 (d, *J* = 7.9 Hz, 2H), 7.79 – 7.75 (m, 2H), 7.34 (s, 4H), 7.32 (dd, *J* = 7.0, 4.5 Hz, 2H). ^{13}C NMR (151 MHz, Chloroform-*d*) δ 160.2, 154.6, 149.8, 149.6, 136.7, 125.2, 122.3, 122.0.

(1E,1'E)-N,N'-(1,4-phenylene)bis(1-(3-fluorophenyl)methanimine) (4n) [96]

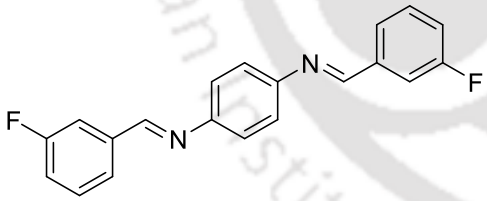

^{1}H NMR (400 MHz, Chloroform-*d*) δ 8.48 (s, 2H), 7.71 – 7.62 (m, 4H), 7.44 (td, *J* = 7.9, 5.7 Hz, 2H), 7.29 (s, 4H), 7.18 (td, *J* = 8.3, 2.6 Hz, 2H). ^{13}C NMR (151 MHz, Chloroform-*d*) δ 164.1, 162.4, 158.3, 149.8, 138.7, 130.4, 125.1, 122.1, 118.5, 114.7.

(1E,1'E)-N,N'-(1,4-phenylenebis(methylene))bis(1-phenylmethanimine) (4o) [85]

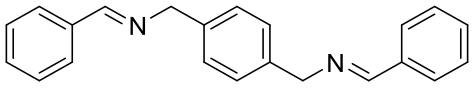

^{1}H NMR (600 MHz, Chloroform-*d*) δ 8.41 (s, 2H), 7.84 (s, 4H), 7.42 (d, *J* = 35.3 Hz, 10H), 4.86 (s, 4H). ^{13}C NMR (151 MHz, Chloroform-*d*) δ 161.8, 138.0, 136.2, 130.7, 128.6, 128.3, 128.2, 64.7.

(1E,1'E)-N,N'-(1,3-phenylenebis(methylene))bis(1-phenylmethanimine) (4p) [85]

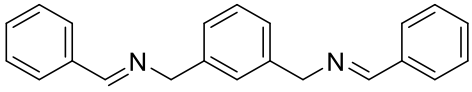

^{1}H NMR (600 MHz, Chloroform-*d*) δ 8.44 (s, 2H), 7.86 (s, 4H), 7.47 (d, *J* = 6.9 Hz, 6H), 7.44 – 7.40 (m, 2H), 7.34 (d,

J = 7.5 Hz, 2H), 4.90 (s, 4H). ^{13}C NMR (151 MHz, Chloroform-*d*) δ 162.2, 139.7, 136.3, 130.9, 128.8, 128.7, 128.5, 128.4, 126.9, 65.2.

(1E,1'E)-N,N'-(1,4-phenylene)bis(1-(4-nitrophenyl)methanimine) (4q) [97]

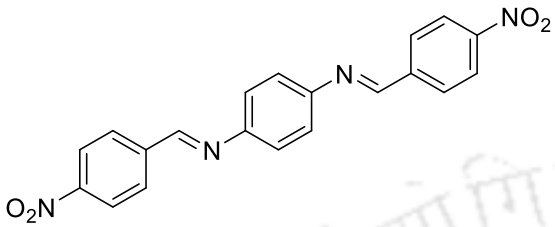

^{1}H NMR (600 MHz, Chloroform-*d*) δ 8.62 (s, 2H), 8.35 (d, *J* = 8.2 Hz, 4H), 8.10 (d, *J* = 8.2 Hz, 4H), 7.37 (s, 4H). ^{13}C NMR (151 MHz, Chloroform-*d*) δ 157.2, 149.9, 149.5, 141.6, 129.6, 124.2, 122.3.

(1E,1'E)-N,N'-((1r,4r)-cyclohexane-1,4-diyl)bis(1-phenylmethanimine) (6r) [98]

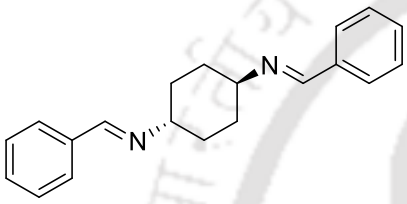

^{1}H NMR (600 MHz, Chloroform-*d*) δ 8.38 (s, 2H), 7.76 (s, 4H), 7.46 – 7.38 (m, 6H), 3.30 (s, 2H), 1.91 – 1.80 (m, 8H). ^{13}C NMR (151 MHz, Chloroform-d) δ 159.4, 136.6, 130.5, 128.6, 128.2, 69.3, 32.7.

3.4.8 Optimization of Heck coupling reaction.

Bromobenzene (0.5 mmol), 4-methylstyrene (0.6 mmol), base (0.75 mmol), and catalyst (x mol%) were mixed in solvent (5.0 mL) and was stirred at specified temperature for a given time. After the completion of the reaction, the mixture was cooled, diluted with ethyl acetate (20.0 mL). Then it was filtered through a short pad of celite and filtrate was removed under reduced pressure; the crude product was purified by preparative thin layer chromatography to produce isolated yields.

3.4.9 General procedure for Heck coupling reaction.

Aryl bromide/iodide (0.5 mmol), 4-methylstyrene/ethylacrylate (0.6 mmol), K_2CO_3 (0.75 mmol), catalyst **2h** (1.0 mol%), and ethanol (5.0 mL) was stirred at 90 ºC for 8 h. After the completion of the reaction, the mixture was cooled, diluted with ethyl acetate (30.0 mL). Then it was filtered through a short pad of celite and filtrate was removed under reduced pressure, and the crude product was purified by preparative thin layer chromatography.

3.4.10 Specific procedures and characterization data for Heck coupling products 5a-5l

(E)-1-methyl-4-styrylbenzene(5a) [99]

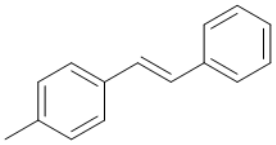

^{1}H NMR (400 MHz, Chloroform-*d*) δ 7.50 (d, *J* = 7.2 Hz, 2H), 7.41 (d, *J* = 8.0 Hz, 2H), 7.35 (t, *J* = 7.6 Hz, 2H), 7.25 (t, *J* = 3.6 Hz, 1H), 7.17 (d, *J* = 8.0 Hz, 2H), 7.07 (d, *J* = 2.3 Hz, 2H), 2.36 (s, 3H). ^{13}C NMR (126 MHz, Chloroform-*d*) δ 137.7, 134.7, 129.5, 128.8, 127.9, 127.5, 126.6, 126.5, 21.4.

(E)-1,2-di-p-tolylethene (5b) [100]

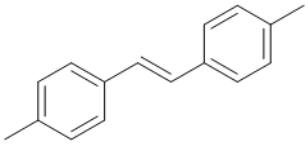

^{1}H NMR (400 MHz, Chloroform-*d*) δ 7.40 (d, *J* = 8.0 Hz, 4H), 7.16 (d, *J* = 7.9 Hz, 4H), 7.04 (s, 2H), 2.36 (s, 6H). ^{13}C NMR (126 MHz, Chloroform-*d*) δ 137.4, 134.9, 129.5, 127.8, 126.4, 21.4.

(E)-1-methyl-4-(4-nitrostyryl)benzene (5c) [101]

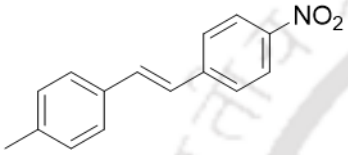

^{1}H NMR (400 MHz, Chloroform-*d*) δ 8.21 (d, *J* = 8.8 Hz, 2H), 7.62 (d, *J* = 8.7 Hz, 2H), 7.45 (d, *J* = 8.1 Hz, 2H), 7.24 – 7.18 (m, 3H), 7.10 (d, *J* = 16.3 Hz, 1H), 2.38 (s, 3H). ^{13}C NMR (126 MHz, Chloroform-*d*) δ 146.8, 144.3, 139.2, 133.6, 133.5, 129.8, 127.1, 126.8, 125.4, 124.3, 21.5.

(E)-4-(4-methylstyryl)benzonitrile (5d) [102]

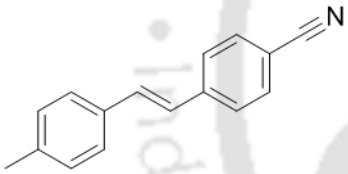

^{1}H NMR (400 MHz, Chloroform-*d*) δ 7.65 – 7.54 (m, 4H), 7.43 (d, *J* = 8.0 Hz, 2H), 7.22 – 7.16 (m, 3H), 7.04 (d, *J* = 16.3 Hz, 1H), 2.38 (s, 3H). ^{13}C NMR (126 MHz, Chloroform-*d*) δ 142.2, 138.9, 133.7, 132.6, 129.7, 127.0, 119.2, 110.5, 21.5.

(E)-4-(4-methylstyryl)-1,1'-biphenyl (5e) [103]

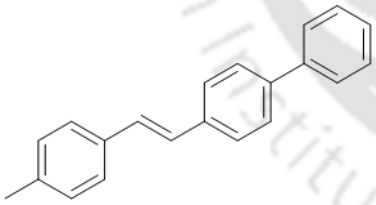

^{1}H NMR (500 MHz, Chloroform-*d*) δ 7.65 – 7.56 (m, 6H), 7.45 (t, *J* = 7.9 Hz, 4H), 7.35 (t, *J* = 7.4 Hz, 1H), 7.19 (d, *J* = 7.8 Hz, 2H), 7.14 (d, *J* = 16.5 Hz, 1H), 7.10 (d, *J* = 16.3 Hz, 1H), 2.37 (s, 3H). ^{13}C NMR (126 MHz, Chloroform-*d*) δ 140.9, 140.3, 137.7, 136.7, 134.7, 129.6, 128.9, 128.8, 127.5, 127.4, 127.3, 27.0, 126.9, 126.6, 21.4.

(E)-1-(4-(4-methylstyryl)phenyl)ethan-1-one (5f) [104]

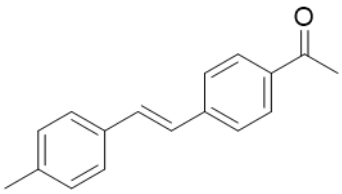

^{1}H NMR (400 MHz, Chloroform-*d*) δ 7.95 (d, *J* = 8.3 Hz, 2H), 7.57 (d, *J* = 8.3 Hz, 2H), 7.44 (d, *J* = 8.0 Hz, 2H), 7.24 – 7.16 (m, 3H), 7.08 (d, *J* = 16.3 Hz, 1H), 2.61 (s, 3H), 2.37 (s, 3H). ^{13}C NMR (126 MHz, Chloroform-*d*) δ 197.7, 142.4, 138.5, 135.9, 134.1, 131.6, 129.7, 129.0, 126.9, 126.6, 126.5, 26.7, 21.5.

(E)-4-(4-methylstyryl)benzaldehyde (5g) [105]

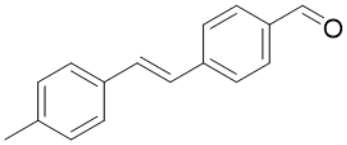

^{1}H NMR (400 MHz, Chloroform-*d*) δ 9.99 (s, 1H), 7.86 (d, *J* = 8.2 Hz, 2H), 7.64 (d, *J* = 8.1 Hz, 2H), 7.45 (d, *J* = 8.0 Hz, 2H), 7.25 – 7.17 (m, 3H), 7.10 (d, *J* = 16.3 Hz, 1H), 2.38 (s, 3H). ^{13}C NMR (126 MHz, Chloroform-*d*) δ 191.8, 143.883, 138.787, 135.3, 133.9, 132.3, 130.4, 129.7, 127.0, 126.9, 126.5, 21.5.

(E)-1-methoxy-4-(4-methylstyryl)benzene (5h) [100]

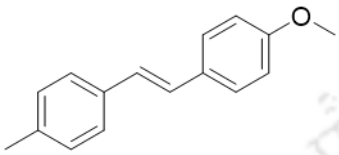

^{1}H NMR (400 MHz, Chloroform-*d*) δ 7.45 (d, *J* = 8.7 Hz, 2H), 7.40 (d, *J* = 8.0 Hz, 2H), 7.16 (d, *J* = 7.9 Hz, 2H), 7.03 (d, *J* = 16.3 Hz, 1H), 6.96 (d, *J* = 16.4 Hz, 1H), 6.90 (d, *J* = 8.7 Hz, 1H), 3.83 (s, 3H), 2.36 (s, 3H). ^{13}C NMR (126 MHz, Chloroform-*d*) δ 159.3, 137.2, 135.0, 130.5, 129.5, 127.7, 127.4, 126.7, 126.3, 114.2, 55.5, 21.5.

(E)-4-(4-methylstyryl)isoquinoline (5i) [106]

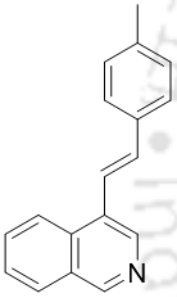

^{1}H NMR (400 MHz, Chloroform-*d*) δ 9.22 (s, 1H), 8.80 (s, 1H), 8.22 (d, *J* = 8.5 Hz, 1H), 8.05 (d, *J* = 8.1 Hz, 1H), 7.80 (t, *J* = 7.7 Hz, 1H), 7.73 – 7.66 (m, 2H), 7.56 (d, *J* = 8.0 Hz, 2H), 7.29 (d, *J* = 9.3 Hz, 2H), 7.24 (d, *J* = 16.6 Hz, 1H), 2.44 (s, 3H). ^{13}C NMR (126 MHz, Chloroform-*d*) δ 151.8, 140.4, 138.4, 134.5, 134.0, 133.3, 130.6, 129.7, 129.0, 128.3, 127.3, 126.9, 123.1, 121.5, 21.5.

(E)-2-(4-methylstyryl)benzaldehyde (5j) [107]

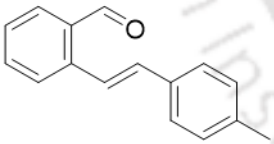

^{1}H NMR (400 MHz, Chloroform-*d*) δ 10.34 (s, 1H), 7.99 (d, *J* = 16.2 Hz, 1H), 7.84 (d, *J* = 7.0 Hz, 1H), 7.72 (d, *J* = 7.8 Hz, 1H), 7.58 (t, *J* = 7.6 Hz, 1H), 7.45 (dd, *J* = 13.6, 7.9 Hz, 3H), 7.20 (d, *J* = 7.9 Hz, 2H), 7.04 (d, *J* = 16.2 Hz, 1H), 2.38 (s, 3H). ^{13}C NMR (126 MHz, Chloroform-*d*) δ 192.8, 140.4, 138.5, 134.2, 133.8, 132.3, 129.6, 127.6, 127.3, 127.1, 123.8, 21.5.

(E)-4'-(4-methylstyryl)-N,N-diphenyl-[1,1'-biphenyl]-4-amine (5k)

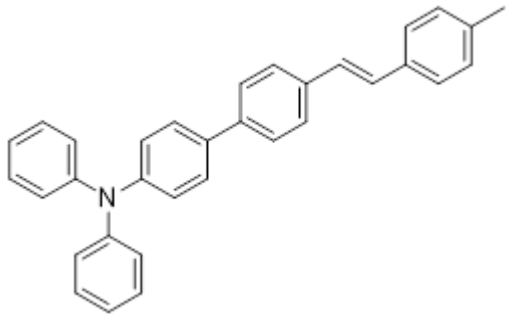

According to the general procedure, the reaction of 4'-bromo-N,N-diphenyl-[1,1'-biphenyl]-4-amine (0.5 mmol), 4-methylstyrene (0.6 mmol), K_2CO_3 (0.75 mmol), and catalyst **2h** (1.0 mol%) in ethanol for 16 h at 90 °C, affording the title compound as light-yellow solid after work-up and chromatography. ATR-IR

(neat, cm^{-1}): 1733, 1459, 1261, 1081, 1021, 802, 996. ^{1}H NMR (600 MHz, Chloroform-*d*) δ 7.56 (d, *J* = 3.0 Hz, 4H), 7.50 (d, *J* = 8.5 Hz, 2H), 7.43 (d, *J* = 7.9 Hz, 2H), 7.28 (d, *J* = 7.9 Hz, 4H), 7.18 (d, *J* = 7.8 Hz, 2H), 7.14 (d, *J* = 7.8 Hz, 6H), 7.10 (d, *J* = 6.2 Hz, 2H), 7.04 (t, *J* = 7.2 Hz, 2H), 2.37 (s, 3H). ^{13}C NMR (101 MHz, Chloroform-*d*) δ 147.7, 147.3, 129.6, 129.4, 128.5, 127.64, 127.4, 127.0, 126.90, 126.5, 124.6, 124.0, 123.1, 29.8. HRMS (ESI) m/z calculated for $[C_{33}H_{27}N+H]^+$: 438.2217, found: 438.2163.

ethyl (2E)-3-phenylprop-2-enoate (5k) [108]

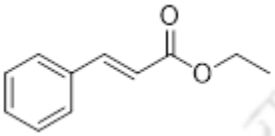

^{1}H NMR (600 MHz, Chloroform-*d*) δ 7.69 (d, *J* = 16.0 Hz, 1H), 7.54 – 7.49 (m, 2H), 7.42 – 7.34 (m, 3H), 6.44 (d, *J* = 16.0 Hz, 1H), 4.26 (q, *J* = 7.1 Hz, 2H), 1.33 (t, *J* = 7.1 Hz, 3H). ^{13}C NMR (151 MHz, Chloroform-*d*) δ 167.0, 144.65, 134.5, 130.3, 128.9, 128.1, 118.3, 60.6, 14.4.

3.4.11 Hot filtration test

Benzylamine (0.5 mmol), benzyl alcohol (0.6 mmol), ^{t}BuOK (0.75 mmol), and **1a** (1.0 mol%) were mixed in toluene (5.0 mL) and was stirred at 110 ºC. After 4 hours, the reaction mixture was filtered through a short pad of celite in hot condition and again stirred for next 8 h. After the completion of the reaction, the mixture was cooled, diluted with ethyl acetate (10.0 mL). Then it was filtered through a short pad of celite and filtrate was washed with copious amount of ethylacetate. The solvent was removed under reduced pressure, and the give 97% of **4b** after preparative thin layer chromatography.

Bromobenzene (0.5 mmol), 4-methylstyrene (0.6 mmol), K_2CO_3 (0.75 mmol), catalyst **2h** (1.0 mol%), and ethanol (5.0 mL) was stirred at 90 ºC. After 2 hours, the reaction mixture was filtered through a short pad of celite in hot condition and again stirred for next 6 h. After completion of the reaction, the mixture was cooled, diluted with ethyl acetate (30.0 mL). Then it was filtered through a short pad of celite and filtrate was removed under reduced pressure. The crude product was purified by preparative thin layer chromatography and the yield of product (**5a**) was 95%.

3.4.12 ICP-MS analysis

Bromobenzene (0.25 mmol), 4-methylstyrene (0.3 mmol), K_2CO_3 (0.35 mmol), catalyst **2h** (1.5 mg, 1.0 mol%), and ethanol (5.0 mL) was stirred at 90 ºC. After completion of reaction, it was filtered through a short pad of celite and filtrate was removed. The crude product was digested and

diluted to 20 mL volume. ICP-MS analysis showed 12117.364 ppb of Pd (87.7% recovered) that rule out the Pd nano particle formation.

3.4.13 Cross-dehydrogenative coupling of thiophene-2carbaldehyde

Thiophene-2-carbaldehyde (1.0 mmol), silver acetate (1.0 mmol), and catalyst (1.0 mol%) were mixed in dimethylformamide (5.0 mL) and were stirred at 110 °C for 16 h. After the completion of reaction, the mixture was cooled, diluted with ethyl acetate, and filtered through a short pad of celite. It was washed with sufficient water and organic phase was dried over anhydrous sodium sulphate. Then, solvent was removed under reduced pressure, and the crude product was purified by preparative thin layer chromatography to produce isolated yield of [2,2'-bithiophene]-5,5'-dicarbaldehyde. ^{1}H NMR (400 MHz, Chloroform-*d*) δ 9.91 (s, 1H), 7.72 (d, *J* = 4.0 Hz, 1H), 7.42 (d, *J* = 4.0 Hz, 1H). ^{13}C NMR (126 MHz, Chloroform-*d*) δ 182.71, 145.00, 144.04, 137.05, 126.64. NMR spectroscopic data were in accordance with literature values.[109]

3.4.14 Biomolecule interaction studies

3.4.14.1 DNA Binding Study:

The interaction of CT-DNA with complexes **3a**–**3e** was screened by utilizing analytical methods such as UV−Vis and fluorescence spectroscopy. The experiments were performed at room temperature in Tris-HCl buffer (5 mM tris-HCl and 50 mM NaCl, pH = 7.2). The DNA stock solution was prepared in tris-HCl buffer and concentration was determined spectrophotometrically from the absorbance at 260 nm (molar extinction coefficient is 6600 M^{-1} cm^{-1}) and stored at 4 °C in dark. Further, the absorbance of DNA stock solution at 260 and 280 nm gave a ratio of 1.8, signifying that the DNA was adequately protein free.[110] The titration experiment was carried out with fixed complex concentration (15 μM) to which DNA (0−15 μM) was gradually added for absorption measurement. For emission experiments, stock solution of ethidium bromide (EB) was prepared in deionized water. 10.0 μM of EB solution was mixed with 10.0 μM DNA solution and was titrated with variation of complex concentration (0–15 μM).

3.4.14.2 BSA Binding Study:

The binding study of **3a**–**3e** with BSA was performed using fluorescence spectroscopy. BSA stock solution was prepared by dissolving in HEPES buffer (10.0 mM, pH= 7.4) and concentration was determined from the absorbance at 278 nm (molar extinction coefficient 4.4×10^4 M^{-1} cm^{-1}). Stock

solutions of complexes **3a**–**3e** were prepared in DMSO and diluted in HEPES buffer for analysis. Titration study was carried out with a constant BSA concentration (15 μM) and gradually increasing concentration of complexes (0–16 μM). The excitation was set at 285 nm and emission spectra were collected in the range of 280–500 nm at 25 °C.

3.4.14.3 Steady-state fluorescence anisotropy

In HEPES buffer solution at pH 7.4, the fluorescence anisotropy of BSA in the absence and presence of the complexes **3a**–**3e** were recorded at 25 °C. The excitation slit (5 nm) and emission slit (10 nm) were set for the anisotropy study. The system was excited at 350 nm and emission wavelength was fixed at 533 nm.

3.4.15 Molecular docking of 3e with CT-DNA and BSA

Autoock4.2.6 and MGL Tools 1.5.6 programs were used to perform molecular docking study of **3e** with DNA and BSA.[71] The docking results were visualized by using BIOVIA Discovery Studio Visualizer. The crystal structure of DNA and BSA was obtained from Protein Data Bank (PDB ID: 1BNA, 3V03).[72] Then, the water molecules and co-crystal molecules were deleted from the crystal structure, followed by the addition of polar hydrogens and atomic Kollman charges. A blind docking was carried out with grid box dimensions 78 × 70 × 124 for DNA and 260 × 164 × 244 for BSA, grid points spaced 0.375 Å, and the receptor was kept inflexible during the study. Lamarckian Genetic Algorithm (GA) with a population size of 140 was used to generate the docked conformations with **3e**.

3.4.16 Solution state magnetic moment by Evans′ NMR method

Complex **1e**, **1f**, **1g** and **1h** were separately taken in 0.500 mL mixture of DMSO-D6/toluene (95:5 *v/v*) and loaded into a standard NMR tube. Then, a one-end sealed capillary tube filled with same solvent mixture up to the same height as sample and the capillary was carefully inserted into the NMR tube. Evans NMR spectrum was recorded using a 600 MHz operated spectrometer at 296 K as a normal ^{1}H NMR.

From the chemical shift difference, effective magnetic moment (μ_{eff}) was calculated by using the equation 3.6 and 3.7.

$$\mu_{eff} = 2.828\sqrt{T \cdot \chi_M} \qquad \text{(Eq. 3.6)}$$

$$\chi_M = \frac{3 \cdot \Delta f}{1000 \cdot f \cdot c} \quad \text{(Eq. 3.7)}$$

Where, *T* is the temperature in Kelvin and χ_M is the molar magnetic susceptibility of the sample in mL per mole. Δf is the chemical shift difference observed in Hz, f is the spectrometer frequency in Hz, c is the sample concentration in mM.

CCDC No. 2453369–2453373, 2453397–2453399, 2453417–2453421, 2453654–2453657, 2454026–2454029, 2453768-2453771 and 2482884 contain the crystallographic data for all ligands and complexes studied in this Chapter.

The ATR-IR, NMR and HRMS spectra of complexes, NMR spectra of catalytic products, electronic spectra of DNA/BSA interaction, and optimized structures, HOMO-LUMO orbitals, NBO analysis data and cartesian coordinates of all complexes can be found in Appendix II by using the following link:

https://drive.google.com/file/d/1HCKuPwApZm-TKF0FgofKGTrg8v1P2JdD/view?usp=sharing

3.5 References

1. Biffis, P. Centomo, A. Del Zotto and M. Zecca, *Chem. Rev.*, 2018, **118**, 2249–2295.
2. P. Devendar, R.-Y. Qu, W.-M. Kang, B. He and G.-F. Yang, *J. Agric. Food Chem.*, 2018, **66**, 8914–8934.
3. Torborg and M. Beller, *Adv. Synth. Catal*, 2009, **351**, 3027–3043.
4. K. Cooper, P. M. Burton and D. J. Nelson, *Synthesis (Germany)*, 2020, **52**, 565–573.
5. Zapf and M. Beller, *Top. Catal.*, 2002, **19**, 101–109.
6. S. E. Hooshmand, B. Heidari, R. Sedghi and R. S. Varma, *Green Chem*., 2019, **21**, 381-405.
7. H. J. Xu, Y. Q. Zhao and X. F. Zhou, *J. Org. Chem.*, 2011, **76**, 8036–8041.
8. M. J. West and A. J. B. Watson, *Org. Biomol. Chem.*, 2019, **17**, 5055–5059.
9. T. B. Boit, A. S. Bulger, J. E. Dander and N. K. Garg, *ACS Catal.*, 2020, **10**, 12109–12126.
10. V. Ritleng, M. Henrion and M. J. Chetcuti, *ACS Catal.*, 2016, **6**, 890–906.

11. S. Gonell, M. Poyatos, J. A. Mata and E. Peris, *Organometallics*, 2012, **31**, 5606–5614.
12. R. Rayasingh and V. Manivannan, *Dalton Trans.*, 2025, **54**, 7741–7752.
13. V. M. Chernyshev and V. P. Ananikov, *ACS Catal.*, 2022, **12**(2), 1180-1200
14. K. M. Morrison and M. Stradiotto, *Chem. Sci*., **2024**, 15, 7394-7407.
15. N. Hazari, P. R. Melvin and M. M. Beromi, *Nat. Rev. Chem., 2017*, 2017, **1**, 1–16.
16. J. E. Borowski, S. H. Newman-Stonebraker and A. G. Doyle, *ACS Catal.*, 2023, **13**, 7966–7977.
17. M. J. West and A. J. B. Watson, *Org. Biomol. Chem.*, 2019, **17**, 5055–5059.
18. E. Peris and R. H. Crabtree, *Chem. Soc. Rev.,* 2018, **47**, 1959-196.
19. E. B. Patricio-Rangel, K. González-Silva and D. Mendoza-Espinosa, *Organometallics*, 2023, **42**, 2893–2901.
20. M. L. Scheuermann, K. A. Grice, M. J. Ruppel, M. Roselló-Merino, W. Kaminsky and K. I. Goldberg, *Dalton Trans.*, 2014, **43**, 12018–12025.
21. K. Azizi and R. Madsen, *ChemCatChem.*, 2018, **10**, 3703–3708.
22. X. N. Fan, H. D. Ou, W. Deng and Z. J. Yao, *Inorg. Chem.*, 2020, **59**, 4800–4809.
23. R. Lima Oliveira, K. A. Ledwa, O. Chernyayeva, S. Praetz, C. Schlesiger and L. Kepinski, *Inorg. Chem.*, 2023, **62**, 13554–13565.
24. W. Cui, B. Zhaorigetu, M. Jia, W. Ao and H. Zhu, *RSC Adv.*, 2014, **4**, 2601–2604.
25. H. Chai, K. Yu, B. Liu, W. Tan and G. Zhang, *Organometallics*, 2020, **39**, 217–226.
26. Saha, S. M. Wahidurrahaman, P. Daw, G. Sengupta and J. K. Bera, *Chemistry - A European Journal*, 2014, **20**, 6542–6551.
27. Eizawa, S. Nishimura, K. Arashiba, K. Nakajima and Y. Nishibayashi, *Organometallics*, 2018, **37**, 3086–3092.
28. T. Higuchi, R. Tagawa, A. Iimuro, S. Akiyama, H. Nagae and K. Mashima, *Chem. Euro. J.*, 2017, **23**, 12795–12804.
29. R. J. Li, C. Ling, W. R. Lv, W. Deng and Z. J. Yao, *Inorg. Chem.*, 2021, **60**, 5153–5162.
30. M. Khatua, B. Goswami, A. Devi, N. Kamal, S. Hans and S. Samanta, *Inorg. Chem.*, 2024, **63**, 9786–9800.
31. R. Liu, Y. Hou, M. Bai, Z. Han, Z. Hao and J. Lin, *J. Catal.*, 2025, **442**, 115895.
32. R. A. Haque, P. O. Asekunowo, S. Budagumpi and L. Shao, *Eur. J. Inorg. Chem.*, 2015, **2015**, 3169–3181.

33. S. Chakrabortty, M. Kaur, M. Adhikari, K. K. Manar and S. Singh, *Inorg. Chem.*, 2021, **60**, 6209–6217.
34. M. M. Rahman, J. Zhang, Q. Zhao, J. Feliciano, E. Bisz, B. Dziuk, R. Lalancette, R. Szostak and M. Szostak, *Organometallics*, 2022, **41**, 2281–2290.
35. R. O. Pankov, D. O. Prima, A. Y. Kostyukovich, M. E. Minyaev and V. P. Ananikov, *Dalton Trans.*, 2023, **52**, 4122–4135.
36. R. K. Gupta, G. Sharma, R. Pandey, A. Kumar, B. Koch, P. Z. Li, Q. Xu and D. S. Pandey, *Inorg. Chem.*, 2013, **52**, 13984–13996.
37. S. Mandal, S. K. Tarai, P. Patra, P. Nandi, S. Sing, B. Rajak and S. C. Moi, *Langmuir*, 2022, **38**, 44, 13613–13625.
38. Pan, I. Mitra, S. Mukherjee, S. Ghosh, U. Chatterji and S. C. Moi, *Cite This: ACS Appl. Bio Mater.*, 2021, **2021**, 868.
39. Das, M. Saha, S. Mandal, S. Das, K. Das Saha and T. K. Mondal, *New J. Chem.*, 2023, **47**, 4931–4943.
40. Cócíć, S. Jovanović-Stević, R. Jelić, S. Matić, S. Popović, P. Djurdjević, D. Baskić and B. Petrović, *Dalton Trans.*, 2020, **49**, 14411–14431.
41. Tisoco, M. C. Donatoni, H. F. V. Victória, J. R. de Toledo, K. Krambrock, O. A. Chaves, K. T. de Oliveira and B. A. Iglesias, *Dalton Trans.*, 2022, **51**, 1646–1657.
42. S. Jovanović, K. Obrenčević, Ž. D. Bugarčić, I. Popović, J. Žakula and B. Petrović, *Dalton Trans.*, 2016, **45**, 12444–12457.
43. Cócíć, S. Jovanović-Stević, R. Jelić, S. Matić, S. Popović, P. Djurdjević, D. Baskić and B. Petrović, *Dalton Trans.*, 2020, **49**, 14411–14431.
44. N. Mirzadeh, T. S. Reddy, S. H. Privér and S. K. Bhargava, *Dalton Trans.*, 2019, **48**, 5183–5192.
45. S. Pavlović, B. Petrović, D. Ćoćić, A. Schreurer, S. Sretenović, M. D. Nešić, M. Nišavić, Z. Maric, I. Stanisavljević, I. Ćorović, B. Simović Marković, V. Maric, I. Jovanović, G. Radić, S. Radisavljević and S. Jovanović Stević, *Dalton Trans.*, 2024, *53*, 18560-18574.
46. Z. Yekke-Ghasemi, M. Ramezani, J. T. Mague and R. Takjoo, *New J. Chem.*, 2020, **44**, 8878–8889.
47. J. Wang, L. Dyers, R. Mason, P. Amoyaw and X. R. Bu, *J. Org. Chem.*, 2005, **70**, 2353–2356.

48. X. Zhang, J. Zhang, Z. Hao, Z. Han, J. Lin and G. L. Lu, *Organometallics*, 2021, **40**, 3843–3853.
49. S. Santoro, F. Ferlin, L. Luciani, L. Ackermann and L. Vaccaro, *Green Chem.*, 2017, **19**, 1601-1612.
50. G. Strappaveccia, E. Ismalaj, C. Petrucci, D. Lanari, A. Marrocchi, M. Drees, A. Facchetti and L. Vaccaro, *Green Chem.*, 2015, **17**, 365–372.
51. G. A. Ardizzoia, D. Ghiotti, B. Therrien and S. Brenna, *Inorganica Chim. Acta.*, 2018, **471**, 384–390.
52. V. Arumugam, W. Kaminsky and D. Nallasamy, *Green Chem.*, 2016, **18**, 3295–3301.
53. Sundarraman, R. Rengan and D. Semeril, *Organometallics*, 2022, **41**, 1314–1324.
54. L. J. Broere, N. P. Van Leest, B. De Bruin, M. A. Siegler and J. I. Van Der Vlugt, *Inorg. Chem.*, 2016, **55**, 8603–8611.
55. P. K. Sekar, R. Rengan and B. Sundarraman, *J. Org. Chem.*, 2024, **89**, 11161–11172.
56. S. Keesara, G. Narendra Babu and S. Pal, *App.l Organomet. Chem.*, 2017, **31**(11), e3778
57. R. Nagpal, S. Arora, K. Rawat, P. Ponnan and S. M. S. Chauhan, *Dyes and Pigments*, 2017, **142**, 262-271.
58. X. Jia, D. Zhao, J. You, T. Hao, X. Li, J. Nie and T. Wang, *Dyes and Pigments*, 2021, **184**, 108583.
59. K. Pauk, M. Hejdová, A. Imramovský, D. Zych, S. Zimosz, K. Malarz, R. Musioł and A. Slodek, *Dyes and Pigments*, 2025, **238**, 112700.
60. P. Debata, S. Patel and S. Vaidyanathan, *J Mater Chem C Mater*, 2025, **13**, 10413-10433.
61. Q. Wu, Y. Ya, Y. Song, Z. Wang, C. Jin, J. Liao, J. Yan, K. J. Huang, F. Yan and X. Tan, *Sens. Actuators B: Chem.*, 2025, **428**, 137257.
62. N. Li, W. Qin, Y. Chen, K. Liu, S. Wang and F. Kong, *Sens. Actuators B Chem.*, 2021, **346**, 130491.
63. J. Zhang, H. Huang, G. Song, K. Huang, Y. Luo, Q. Liu, X. He and N. Cheng, *Biosens. Bioelectron.*, 2022, **202**, 114003.
64. N. F. Romashev, P. A. Abramov, I. V Bakaev, I. S. Fomenko, D. G. Samsonenko, A. S. Novikov, K. K. H. Tong, D. Ahn, P. V Dorovatovskii, Y. V Zubavichus, A. A. Ryadun, O. A. Patutina, M. N. Sokolov, M. V Babak and A. L. Gushchin, *Inorg. Chem.,* 2022, **61**, 4, 2105–2118.

65. Icsel, V. T. Yilmaz, M. Aygun, B. Cevatemre, P. Alper and E. Ulukaya, *Dalton Trans.*, 2018, **47**, 11397.
66. R. O. Omondi, N. R. S. Sibuyi, A. O. Fadaka, M. Meyer, D. Jaganyi and S. O. Ojwach, *Dalton Trans.*, 2021, **50**, 8127–8143.
67. M. Poloni, O. Dangles and J. A. Vinson, *J. Agric. Food Chem.*, 2019, **67**, 9139–9147.
68. Ćoćić, S. Jovanović, S. Radisavljević, J. Korzekwa, A. Scheurer, R. Puchta, D. Baskić, D. Todorović, S. Popović, S. Matić and B. Petrović, *J. Inorg. Biochem.*, 2018, **189**, 91–102.
69. L. G. Flecha and V. Levi, *Biochem. Mol. Bio. Educ.*, 2003, **31**, 319–322.
70. S. Behera, R. Behura, M. Mohanty, R. Dinda, P. Mohanty, A. K. Verma, S. K. Sahoo and B. R. Jali, *Sensors Int.*, 2020, **1**, 100048.
71. M. Morris, H. Ruth, W. Lindstrom, M. F. Sanner, R. K. Belew, D. S. Goodsell and A. J. Olson, *J. Comput. Chem.*, 2009, **30**, 2785–2791.
72. R. Drew, R. M. Wing, T. Takano, C. Broka, S. Tanaka, K. Itakura and R. E. Dickerson, *Proc. Natl. Acad. Sci.*, 1981, **78**, 2179–2183.
73. B. Konovalov, M. D. Živković, J. Z. Milovanović, D. B. Djordjević, A. N. Arsenijević, I. R. Vasić, G. V Janjić, A. Franich, D. Manojlović, S. Skrivanj, M. Z. Milovanović, M. I. Djuran and S. Rajković, *Dalton Trans.*, 2018, **47**, 15091-15102.
74. K. A. Majorek, P. J. Porebski, A. Dayal, M. D. Zimmerman, K. Jablonska, A. J. Stewart, M. Chruszcz and W. Minor, *Mol. Immunol.*, 2012, **52**, 174–182.
75. M. J. ea Frisch, G. W. Trucks, H. B. Schlegel, G. E. Scuseria, Ma. Robb, J. R. Cheeseman, G. Scalmani, V. Barone, G. A. Petersson and H. Nakatsuji, *Gaussian, Inc. Wallingford, CT*, 2016, preprint.
76. R. Dennington, T. A. Keith and J. M. Millam, *Semichem Inc Shawnee Mission KS*.
77. C. P. R. O. Agilent and P. R. O. CrysAlis, *Yarnton, Oxfordshire, England*.
78. S. Bruker and S. SAINT, *Madison, Wisconsin, USA*.
79. M. Sheldrick, *Foundations of Crystallography*, 2015, **71**, 3–8.
80. M. Sheldrick, *Crystal Structure Communications*, 2015, **71**, 3–8.
81. O. V. Dolomanov, L. J. Bourhis, R. J. Gildea, J. A. K. Howard and H. Puschmann, *J. Appl. Cryst.*, 2009, **42**, 339–341.
82. M. N. Burnett and C. K. Johnson, *Oak ridge national laboratory report ORNL-6895, Oak Ridge, Tennessee*, 1996, preprint.

83. C. F. Macrae, I. J. Bruno, J. A. Chisholm, P. R. Edgington, P. McCabe, E. Pidcock, L. Rodriguez-Monge, R. Taylor, J. V. D. Streek and P. A. Wood, *Applied Crystallography*, 2008, **41**, 466–470.
84. L. Spek, *Acta Crystallogr., Sect. D: Biol. Crystallogr.*, 2009, **65**, 148–155.
85. S. Kasemthaveechok, P. Gérardo and N. von Wolff, *Chem. Sci.*, 2023, **14**, 13437–13445.
86. S. K. Schoustra, T. Groeneveld and M. M. J. Smulders, *Polym. Chem.*, 2021, **12**, 1635–1642.
87. Wang, J. Yang, Z. Luo, Z. Yao, J. Yang, H. Li and L. Xu, *Adv. Synth. Catal.*, 2024, **366**, 309–315.
88. M. Okimoto, Y. Takahashi, K. Numata, Y. Nagata and G. Sasaki, *Synth. Commun.*, 2005, **35**, 1989–1995.
89. O. Koleda, T. Broese, J. Noetzel, M. Roemelt, E. Suna and R. Francke, *J. O. Chem.*, 2017, **82**, 11669–11681.
90. Y. Sıcak, E. Başaran, B. Türkmenoğlu and M. Öztürk, *J. Mol. Struct.*, 2025, **1322**, 2, 140417.
91. R. J. Li, C. Ling, W. R. Lv, W. Deng and Z. J. Yao, *Inorg. Chem.*, 2021, **60**, 5153–5162.
92. T. Higuchi, R. Tagawa, A. Iimuro, S. Akiyama, H. Nagae and K. Mashima, *Chem. Euro. J.*, 2017, **23**, 12795–12804.
93. j. Simion, C. Simion, T. Kanda, S. Nagashima, Y. Mitoma, T. Yamada, K. Mimura and M. Tashiro, *J. Chem. Soc., Perkin Trans.*, 2001, 1, 2071-2078.
94. Chai, K. Yu, B. Liu, W. Tan and G. Zhang, *Organometallics*, 2020, **39**, 217–226.
95. G. Li, Y. Wu, G. Shan, W. Che, D. Zhu, B. Song, L. Yan, Z. Su and M. R. Bryce, *Chem. Commun.*, 2014, **50**, 6977–6980.
96. W. H. Ojala, B. Balidemaj, J. A. Johnson, S. N. Larson and C. R. Ojala, *CrystEngComm.*, 2014, **16**, 7226–7235.
97. B. Bag and J. M. Lehn, *Chem. Euro. J.*, 2025, **31**, e202500152.
98. W. Imhof, A. Göbel, L. Schweda, D. Dönnecke and K. Halbauer, *J. Organomet. Chem.*, 2005, **690**, 3886–3897.
99. X. Cui, Z. Li, C. Z. Tao, Y. Xu, J. Li, L. Liu and Q. X. Guo, *Org. Lett.*, 2006, **8**, 2467–2470.
100. Mendoza-Espinosa, R. González-Olvera, G. E. Negrón-Silva, D. Angeles-Beltrán, O. R. Suárez-Castillo, A. Álvarez-Hernández and R. Santillan, *Organometallics*, 2015, **34**, 4529–4542.

101. M. L. Kantam, M. Annapurna, P. R. Likhar, P. Srinivas, N. Mirzadeh and S. K. Bhargava, *J. Organomet. Chem.*, 2013, **723**, 129–136.
102. S. H. Huang, C. H. Liu and C. M. Yang, *Green Chem.*, 2014, **16**, 2706–2712.
103. Etemadi-Davan and N. Iranpoor, *Chem. Commun.*, 2017, **53**, 12794–12797.
104. K. N. Sharma, N. Satrawala, A. K. Srivastava, M. Ali and R. K. Joshi, *Org. Biomol. Chem.*, 2019, **17**, 8969–8976.
105. J. Xu, Y. Q. Zhao and X. F. Zhou, *J. Org. Chem*, 2011, **76**, 8036–8041.
106. T. Okita, K. K. Asahara, K. Muto and J. Yamaguchi, *Org. Lett.*, 2020, **22**, 3205–3208.
107. D. Goubet, P. Meric, J. R. Dormoy and P. Moreau, *J. Org. Chem.*, 1999, **64**, 4516–4518.
108. Z.Y. Wang, T. Yang, K.-K. Wang, D.-F. Liu, X. Ma, N. Wang, H. Liu, A. Sun and H. Liu, *Green Chem.,* 2023, **25**, 3040-3045.
109. V. N. Shinde, N. Bhuvanesh, A. Kumar, H. Joshi, *Organometallics* 2020, **39** (2), 324–333.
110. W. W. Wilfinger, K. Mackey and P. Chomczynski, *BioTechniques,* 1997, **22**, 474–481.

Chapter-4

Dinuclear Palladium(II) Complexes of N-(imidazo[1,5-*a*]pyridin-1-yl)picolinimidamides: Effect of Pd···Pd distance in C–C/P bond Formation

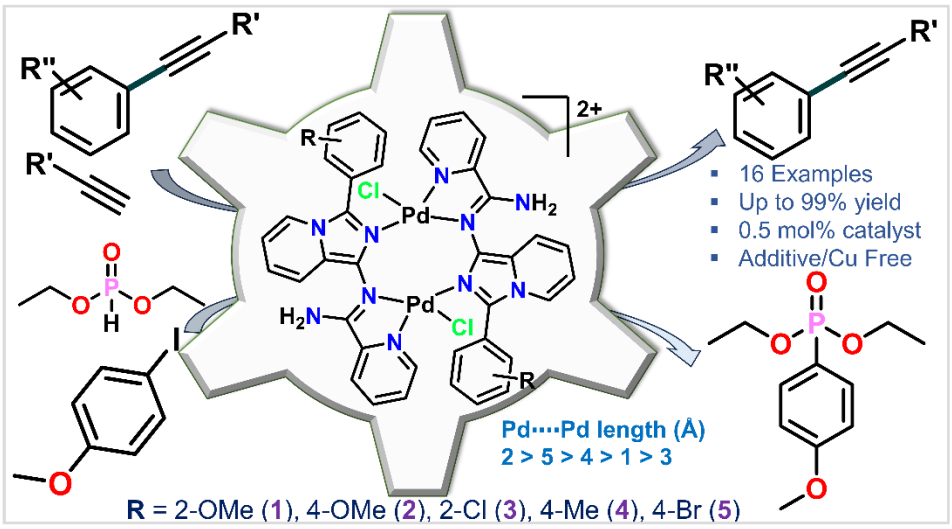

Abstract

This work describes the facile synthesis and characterization of three dinuclear palldium(II) complexes of substituted imidazo[1,5-a]pyridinylpicolinimidamides. Molecular structure of ligands and complexes was established using single crystal X-ray diffraction. All ligands coordinated with palladium center through pseudo-pincer type mode, Pd(II) possessed distorted square planar geometry and an eight-membered metallic cavity was observed. The complexes effectively catalyzed copper-free Sonogashira coupling reactions under mild reaction conditions with excellent functional group tolerance. Also, complexes were employed as catalyst in C–P bond formation reaction. High catalytic activity of these complexes was accredited to cooperativity and synergic effect of two Pd(II) center present with in optimum proximity.

4.1 Introduction

Transition metal complex, especially palladium catalyzed organic transformations have gained significant importance in both scientific research and industrial production valuable chemicals.[1,2] Abundant progress has been developed in terms of ligand framework, catalysis condition, catalyst loading, functional group tolerance. Designing of a robust, highly active catalyst using stable and tunable ligand system for the large-scale production of useful chemicals is still challenging.[3–6] In the history of homogenous palladium catalyst, mononuclear complexes dominated due to their ease of synthesis using structurally predictable ligands while dinuclear complexes delivered excellent catalytic activity compared to mononuclear due to the presence of two metal centers in proximal distance providing cooperativity and synergic effect between the reaction location.[7–11] Thus, designing of such ligand systems for dinuclear complexes with variation in metal-metal distance are basically critical. Also, there has been continuous demand to replace the prevailing toxic, expensive and/or unstable phosphene and carbene based ligands those were widely used for synthesis of palladium catalysts. Regarding this, nitrogen rich imidazo[1,5-*a*]pyridine based multidentate ligands turns to be an upright option as the use of these ligand system in Pd(II) catalyst synthesis is relatively rare.[12–15] Imidazo[1,5-a]pyridine-based heterocycles have attracted considerable attention due to their remarkable biological activity and photophysical properties.[16–18] When incorporated into palladium complexes, this unique ligand framework imparts distinct electronic and structural characteristics, enhancing their potential reactivity leading to efficient catalytic transformations.[19]

At this point, design of dinuclear Pd(II) catalysts using substituted imidazo[1,5-*a*]pyridin-1-yl-picolinimidamides and their utilization in catalysis is relatively rare and important. In the spectrum of Pd catalyzed organic transformation, C–C bond formation is vital which can be done *via* various coupling reactions. Among them, copper-free Sonogashira coupling is well known that offer a more sustainable and less toxic alternative for constructing aryl–alkyne linkages, which are vital in the synthesis of natural products and organic electronic materials.[20–23]

The Patra group reported some dinuclear palladium (**4.1**–**4.3**) complexes with varying intramolecular Pd···Pd distance using heteroscorpionate ligands and employed them as catalyst in tandem conversion of organofluoro molecules.[24] A dinuclear palladium complex (**4.4**) based on benzimidazolyl ligand was used as catalyst by Lindsay group in various cross-coupling reaction. The complex catalyzed Cu-free Sonogashira coupling in ethanol at 80 °C using TBAI as an additive in 8 h.[25]

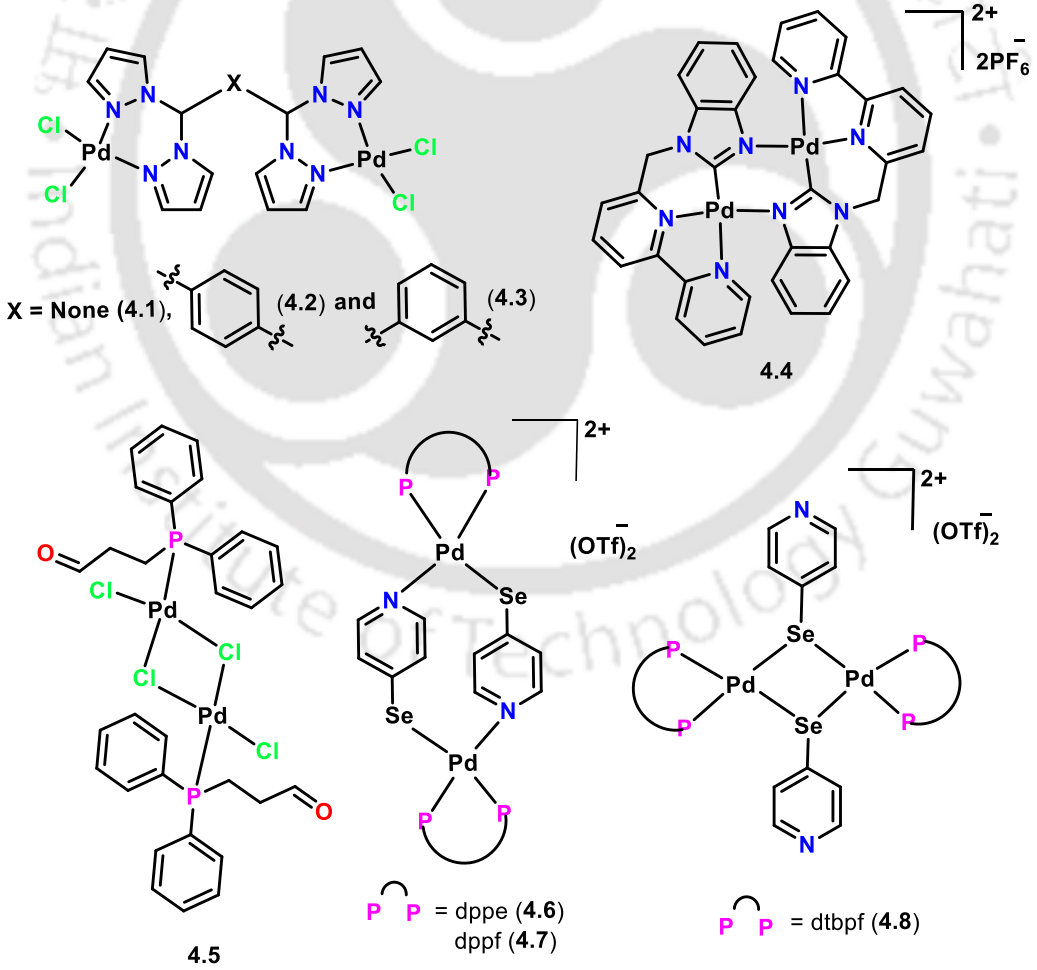

Scheme 1. Some reported dinuclear palladium catalysts used in coupling reactions.

In 2023, Hey-Hawkins group synthesized a dinuclear Pd(II) complex (**4.5**) of 3-(diphenylphosphino)propanal ligand and applied as catalyst (5 mol%) in Sonogashira coupling effectively produced alkynes in MeCN at 100 °C using DBU as base in 4 h (Scheme 1).[21] Recently, Dey and coworker reported some diphosphine chelated dinuclear Pd(II) complexes of 4-pyridylselenolate (**4.6** – **4.8**).[26] Among these complexes, 1,10-bis(di-tertbutylphosphino)ferrocene (dtbpf) chelate containg complex **4.8** existed as dinuclear while (1,2-bis (diphenylphosphino)ethane) dppe and 1,1'-Bis(diphenylphosphino)ferrocene (dppf) containg complexes **4.6** and **4.7** were present as di- and tetramer. They catalyzed Sonogashira coupling, produced diphenyl acetylene in DMA at 120 °C for 15 hours in presence CuI and potassium carbonate where complex **4.7** yielded maximum product (95%).

Rather than C–C coupling reaction, Pd catalyzed C–hetero bond formation especially C–P bond making strategies to synthesize phosphorylated compounds has gained popularity as these compounds are very useful in medicinal chemistry, agrochemical synthesis, materials chemistry and as ligands in metal complex design.[27–36] The C(sp^2)–P bonds are basically constructed by the metal catalyzed coupling of (hetero)aryl and alkenyl (pseudo)halides with H–P containing phosphorous compounds such as phosphonates, phosphene oxides and diarylphosphines.[37–40] However, many palladium catalyzed C–P bond formation protocols were relying on high catalyst loading, elevated temperature, toxic solvents, and long reaction time as well as the use of palladium salts along with supported ligands.[41–44] Thus, it is vital for the development of sustainable and efficient catalyst for the C(sp^2)–P coupling under mild reaction conditions.

This chapter explored the convenient synthesis and characterization of five novel dinuclear palladium complexes bearing substituted imidazo[1,5-a]pyridinylpicolinimidamide ligands. These complexes were employed as catalysts in Cu-free Sonogashira coupling and C–P bond formation and displayed high catalytic activity.

4.2 Results and discussion

4.2.1 Synthesis and Characterization.

Ligands *N*-(3-(2-methoxy/4-methoxy/2-chloro/4-methyl/4-bromophenyl)imidazo[1,5-*a*]pyridin-1-yl)picolinimidamide (**L1H/L2H/L3H/L4H/L5H**) were prepared from the reaction of 2-methoxy/4-methoxy/2-chloro/4-methyl/4-bromo benzaldehyde with 2-cynaopyridine respectively following a reported procedure with some modifications.[45] All ligands were isolated as yellow

fiber like solid in good yield, **L1H**, **L3H** and **L5H** were explicitly categorized by ATR-IR, UV-Vis, NMR, and High-Resolution Mass Spectrometry (HRMS) (Figure S4.1–S4.4 and S4.10) while spectroscopic data for **L2H** and **L4H** were well matched with the reported values.[45] The ^{1}H NMR spectrum of ligands displayed a broad peak at 9.28 ppm (**L1H**) and 9.17 ppm (**L3H**) corresponding to one proton of -NH_2 while the other proton may involve in H-bonding with imidazo[1,5-*a*]pyridine-N and thus was not resonated. The methoxy protons of **L1H** were detected at 3.83 ppm and the protons of imidazo[1,5-*a*]pyridine nucleus was observed at around 7-6 ppm. The HRMS spectrum of **L1H**, **L3H** and **L5H** displayed the peaks corresponding to $[C_{20}H_{17}N_5O+H]^+$ (344.1510), $[C_{19}H_{14}ClN+H]^+$ (348.1026) and $[C_{19}H_{14}BrN+H]^+$ (392.0514) were matched well with the calculated values.

The dinuclear palladium complexes $[Pd_2(\mathbf{X})_2Cl_2]Cl_2$ {**X** = **L1H** – **L3H** (**1** – **3**)} were synthesized using 1:1 molar equivalent of palladium chloride and respective ligand in acetonitrile at ambient temperature (Scheme 2). The orange/red colored Pd(II) complexes (**1** – **3**) were obtained as crystalline solids after removal of solvent followed by washed with diethylether. The similar method was followed for **L4H** and **L5H** with $PdCl_2$ and their methanolic solution was stirred with 1.2 equivalents of KPF_6 to produce orange solids of **4** and **5** having general formula $[Pd_2(\mathbf{X})_2Cl_2](PF_6)_2$ {**X** = **L4H** (**4**) and **L5H (5)**}. The binding of Pd(II) with ligands was confirmed by various spectroscopic techniques. In the ^{1}H NMR of ligands one hydrogen was not observable due to hydrogen bonding while there was no H-bonding in **1**–**5** as all their protons resonated (Figure S4.5–S4.9). The complex **1** contained two broad singlets at 9.56 ppm and 8.61 ppm due to protons of amine group and a similar trend was observed in other complexes which indicated binding of ligand in the neutral form. Also, the methoxy protons (-OCH_3) in **1** shifted to upfield (3.34 ppm) as compared to those in **L1H** (3.83 ppm) after palladium incorporation. The presence of PF_6 anion in **4** and **5** was confirmed from the peak at –144.2 ppm as septet in their respective ^{31}P NMR spectrum. In HRMS(ESI) spectrum, peaks observed for **1** – **5** corresponding to $[Pd_2(\mathbf{X})_2Cl_2]^{2+}$ (**X** = **L1H** – **L5H**) {*m/z* = 485.0174 (**1**), 485.0130 (**2**), 489.9632 (**3**), 469.0203 (**4**), 531.8982 (**5**)} and $[Pd_2(\mathbf{X})_2Cl_2–H]^+$ {*m/z* = 969.0270 (**1**), 969.0182 (**2**), 978.9184 (**3**), 937.0323(**4**), 1066.8212 (**5**)} matched well with calculated values along with isotopic pattern (Figure S4.11A–S4.15C).

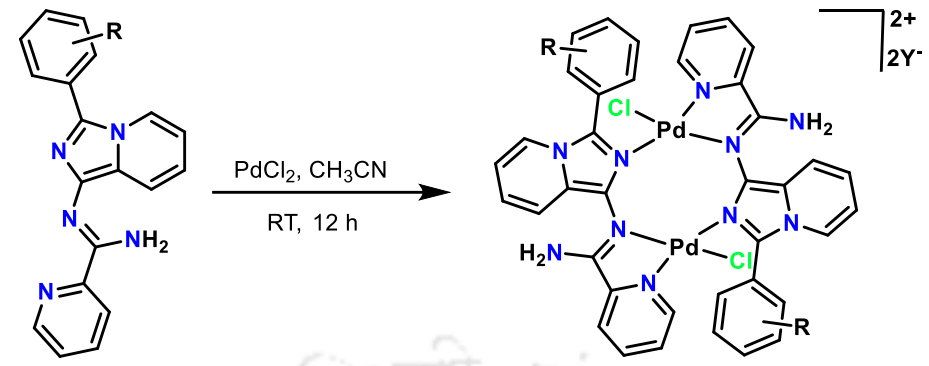

R = 2-OMe (**L1H**), 70%
R = 4-OMe (**L2H**), 63%
R = 2-Cl (**L3H**), 78%
R = 4-Me (**L4H**), 77%
R = 4-Br (**L5H**), 68%

Y = Cl, R = 2-OMe (**1**), 74%
Y = Cl, R = 4-OMe (**2**), 72%
Y = Cl, R = 2-Cl (**3**), 85%
Y = PF_6, R = 4-Me (**4**), 81%
Y = PF_6, R = 4-Br (**5**), 76%

Scheme 2. Synthesis of dinuclear palladium(II) complexes **1** – **5**.

Field Emission Scanning Electron Microscope (FESEM) was used to examine the surface morphology of ligands and palladium complexes (Figure S4.17). Obtained images revealed relatively smooth, densely packed surfaces lacking visible porosity, suggesting a high degree of molecular packing.

4.2.2 X-ray crystallography

The molecular structure of all ligands and Pd(II) complexes were confirmed using single crystal X-ray diffraction technique. The single crystals of **L1H**, **L3H** and **L5H** were obtained from dichloromethane solution and crystallized in $P\bar{1}$ space group while similar method produced crystal of **L2H** and **L4H** having $P2_1/c$ and $P2_1/n$ space group respectively (Table S4.1–S4.2). The X-ray structure of **L1H** – **L5H** showed the presence of N3 as imine nitrogen and N2 as amine (-NH_2) as evident from longer C6–N2 bond length by 0.052(2), 0.066(4), 0.056(3) and 0.038(1) Å compared to that of C6–N3 in **L1H** – **L5H** respectively (Table S4.3–S4.12). Also, the ligands were engaged in intramolecular hydrogen bonding between N2 and N4 with a distance of 2.694(5) Å (**L1H**), 2.753(3) Å (**L2H**), 2.733(3) Å (**L3H**), 2.734(2) Å (**L4H**) and 2.686 (6) Å (**L5H**) (Figure 1).

The single crystals of **1** – **5** were obtained from their solution in dimethylformamide. Complex **2** crystalized in $I4_1/a$ space group while others crystalized in $P\bar{1}$ space group (Table S4.13–S4.14). Crystals of **1** – **3** diffracted moderately due to which the chloride counter ions along with lattice

solvent molecules were not assignable properly from the Fourier map and thus were masked using solvent masking utility while **4** and **5** contained two PF_6 entities in the lattice Figure S4.26 and S4.27). Complexes **1** – **5** contained two ligand units in neutral form that coordinated with two palladium ions in a tridentate pseudo-pincer type binding mode. One ligand formed a five membered chelate ring with a Pd(II) ion by coordinating through pyridine nitrogen (N_{PY}) and imine nitrogen (N_{IM}), while the imidazo[1,5-*a*]pyridine nitrogen (N_{IP}) bridged with another Pd(II) center.

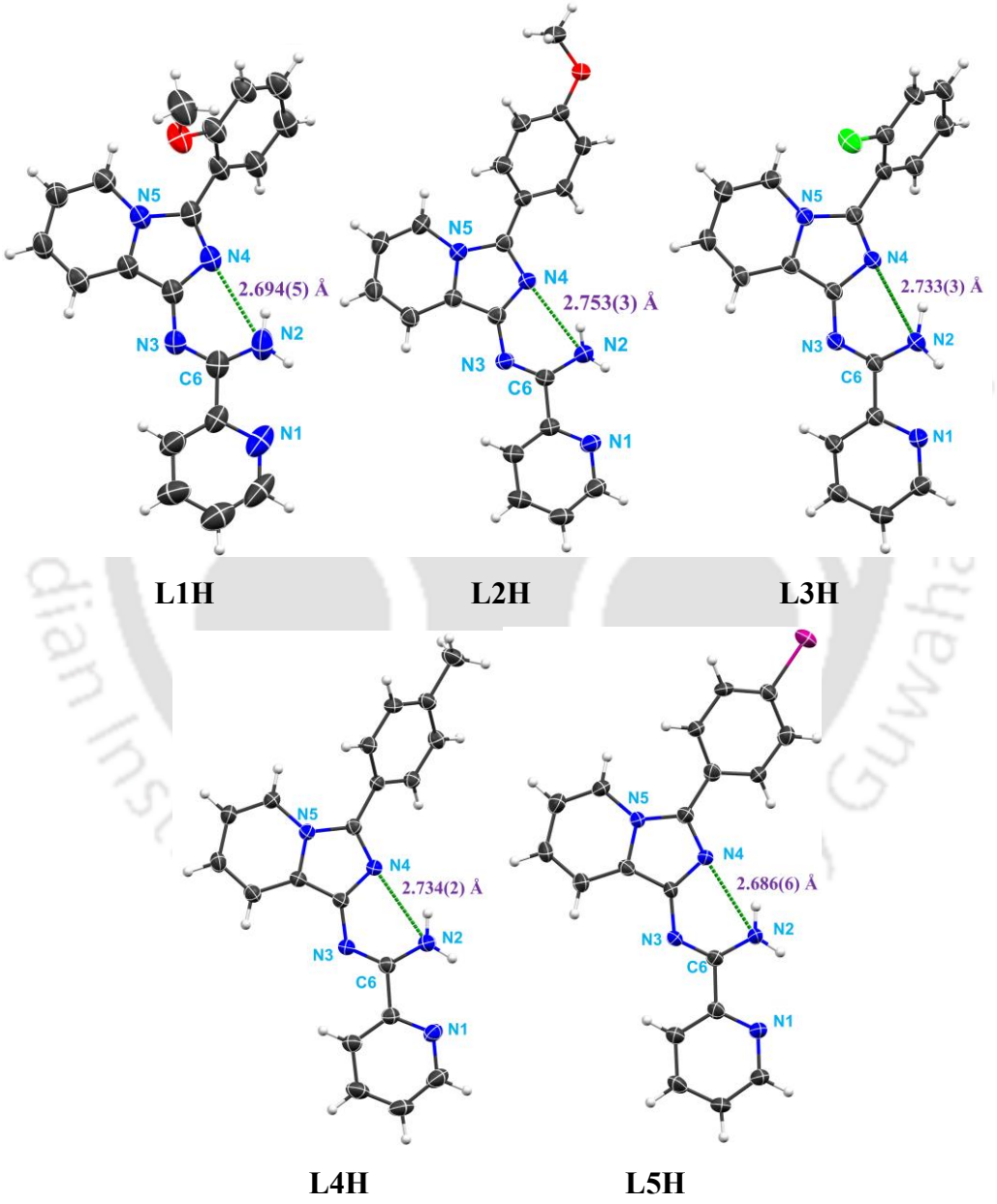

Figure 1: Molecular structures of **L1H** – **L5H** showing intramolecular hydrogen bonding interaction. Ellipsoids are drawn at 30% probability level.

The second ligand contraposed by forming chelate ring with the second Pd(II) and linked through N_{IP} with the first Pd(II) resulting in a bis-dinuclear complex. At both metal sites, N_{IP} positioned trans to N_{PY}, 4th coordination site was occupied by chloride ion trans to N_{IM} and thus possessed distorted square planar geometry (Figure 2). The Pd–N_{PY} and Pd–N_{IP} bond distances were nearly equidistant while the Pd–N_{IM} length was shorter than them which may be due to its better back bonding ability compared to chloride (Table S4.15–S4.24). The non-bonded Pd···Pd distances were 3.558(2), 4.126(1), 3.532(1), 3.784(1) and 3.776(1) Å in **1** – **5** respectively and an eight-membered tub-shaped metallic cavity was observed connecting Pd1–N_{IM}–C7–N_{IP}–Pd2–N_{IM}–C27–N_{IP} (Figure 2, S4.23–S4.27), believed to be the epicenter of catalytic process.

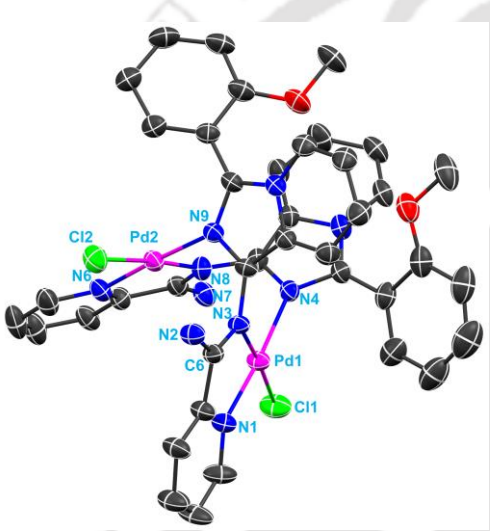

1

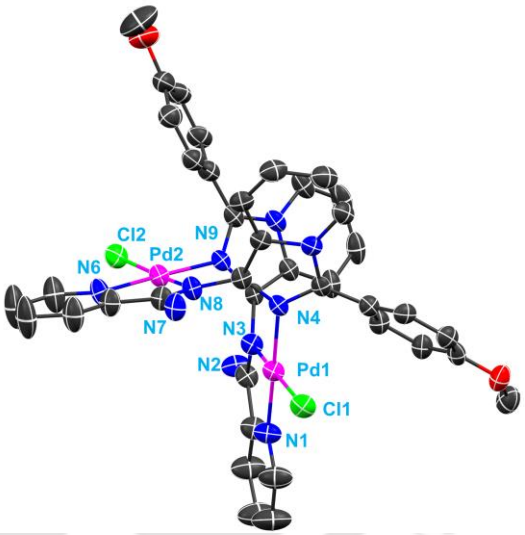

2

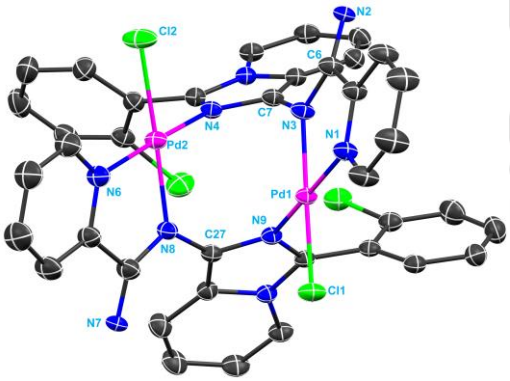

3

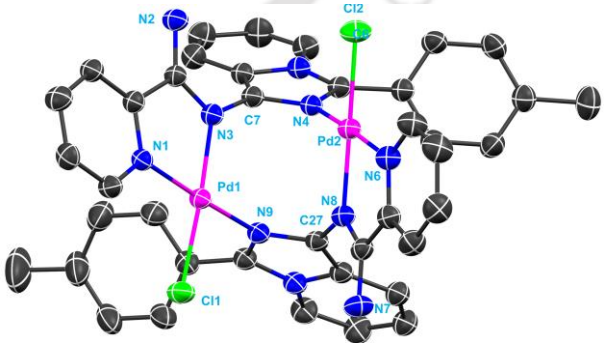

4

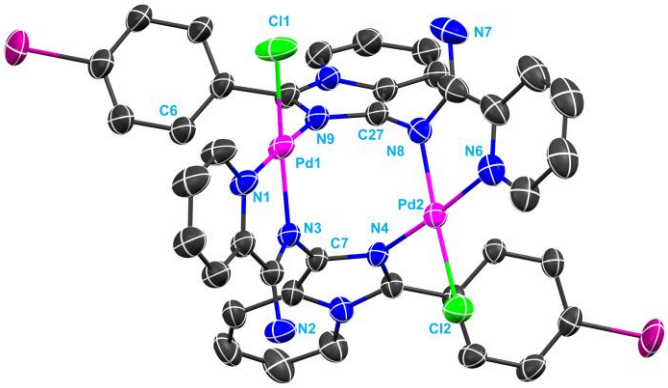

5

Figure 2: Molecular structures of **1** – **5**. Ellipsoids are drawn at 30% probability level and hydrogen atoms and anions are omitted for clarity.

4.2.3 Assessment of catalytic activities of 1 – 5 in Cu-free Sonogashira coupling:

To evaluate the catalytic activity of these dinuclear palladium complexes in C–C cross coupling reaction, complexes were employed as catalyst in copper-free Sonogashira coupling reaction. The reaction condition was screened by altering solvents, bases, time, and temperature. Among several tested solvents, ethanol produced maximum yield in a model reaction of phenylacetylene, 4-bromotoluene, and K_2CO_3 catalyzed by 0.5 mol% of **1** at 80 °C in 10 hours without using any other additives. Similarly, change in the use of bases was carried out with K_2CO_3, NaOH, Et_3N, and ^tBuOK where the maximum product yield was observed with potassium bicarbonate (Table 1, entry1). Then, the effect of temperature was tested using the model reaction at various temperature and highest yield was noted at 80 °C. During time dependency test, the model reaction produced maximum product in 8 hours (Table 1, entry11). Thus, the reaction of 4-bromotoluene, phenylacetylene, and K_2CO_3 at 80 °C catalyzed by 0.5 mol% of **1** yielded 98% of product in 8 hours and concluded as optimum condition. The catalyst loading was also lessened to 0.1 mol% which diminished the product formation to 62% (Table 1, entry16).

Table 1: Optimization table for copper-free Sonogashira coupling reaction

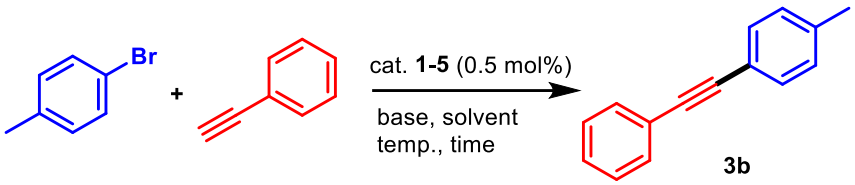

Entry	Catalyst (0.5 mol%)	base	Solvent	T/°C	Time (h)	Yield[#] (%)
1	**1**	K_2CO_3	EtOH	80	10	98
2	**1**	K_2CO_3	Toluene	80	10	87
3	**1**	K_2CO_3	CH_3CN	80	10	79
4	**1**	K_2CO_3	DMF	80	10	72
5	**1**	KOH	EtOH	80	10	84
6	**1**	NaOH	EtOH	80	10	88
7	**1**	Et_3N	EtOH	80	10	74
8	**1**	^tBuOK	EtOH	80	10	90
9	**1**	K_2CO_3	EtOH	80	12	94
10	**1**	K_2CO_3	EtOH	80	4	72
11	**1**	K_2CO_3	EtOH	80	8	99
12	**1**	K_2CO_3	EtOH	110	8	84
13	**1**	K_2CO_3	EtOH	RT	8	12
14	**1**	K_2CO_3	EtOH	50	8	64
15	–	K_2CO_3	EtOH	80	8	00
16	**1**	K_2CO_3	EtOH	80	8	52[a]
17	**2**	K_2CO_3	EtOH	80	8	91
18	**3**	K_2CO_3	EtOH	80	8	98
19	**4**	K_2CO_3	EtOH	80	8	95
20	**5**	K_2CO_3	EtOH	80	8	96

Reaction condition: 4-Bromotoluene (0.5 mmol), phenylacetylene (0.6 mmol), catalyst (0.5 mol%), base (0.75 mmol), and solvent (10.0 mL). Isolated yields. [a] 0.1 mol% catalyst was used.

Also, complexes **2** – **5** effectively catalyzed the model reaction at optimal condition and produced 1-methyl-4-(phenylethynyl)benzene in excellent yield (Table 1, entry17–20). A small deviation in product yield was detected in case of catalysts **1** – **5** that can be attributed to both the presence of substituents on phenyl ring of ligand and the non-bonded Pd···Pd distance. Longer Pd···Pd gap led to diminished the product yield as compared to the shorter gap. The catalytic activity of **1** – **5** followed the order **1** ≈ **3** > **4** ≈ **5** > **2** while the order of non-bonded intramolecular Pd···Pd distance was **1** > **3** > **5** > **4** > **2**. The substrate scope was explored under optimum condition where both electron rich and poor aryl bromides provided excellent yields of the corresponding internal alkynes (Scheme 3). Also, heterocyclic bromides tolerated well and produced good product (**3g**, **3j** and **3l**). Moreover, aliphatic alkynes such as propargylic alcohol and trimethylsilylacetylene also produced desired product in moderate yields. Among the alkynes, molecular structure of **3o** was established using X-ray diffraction. The crystals of **3o** was obtained from slow evaporation of chloroform solution and crystalized in $P2_1/n$ space group.

Further, to understand the mechanistic pathway in these dinuclear complexes, HRMS analysis was carried out on the aliquot taken in the mid of the catalytic reaction of bromobenzene and phenylacetylene catalyzed by **1**. It was observed that the free -NH_2 group played a vital role in stabilization of Pd center *via* internal Lewis's base mechanism during catalytic cycle which was comprehended from the peak observed at *m/z* 449.0344 {for [**1**–4Cl–2H] / $[Pd_2(\mathbf{L1})_2]^{2+}$}, that may be the active catalyst. Similarly, after oxidative addition of C_6H_5Br (during the synthesis of **3a**), phenyl bonded intermediates were detected at *m/z* 1055.0335 $\{[Pd_2(\mathbf{L1})(\mathbf{L1H})(C_6H_5)BrCl–Cl]^+\}$ (IM1), 975.1094 $\{[Pd_2(\mathbf{L1})_2(C_6H_5)Br–Br]^+\}$ (IM2), and 527.0815 $\{[Pd_2(\mathbf{L1H})_2(C_6H_5)_2Br_2–2Br]^{2+}\}$ (IM3) (Figure S4.29–S4.32).

To check the homogeneity nature of these catalysts, a hot filtration test was also carried out with 4-bromotoluene and phenylacetylene under optimal condition using **1** and no significant decline in product yield indicated the homogenous nature of the catalyst.

Scheme 3: Substrate scope in Sonogashira coupling reaction.

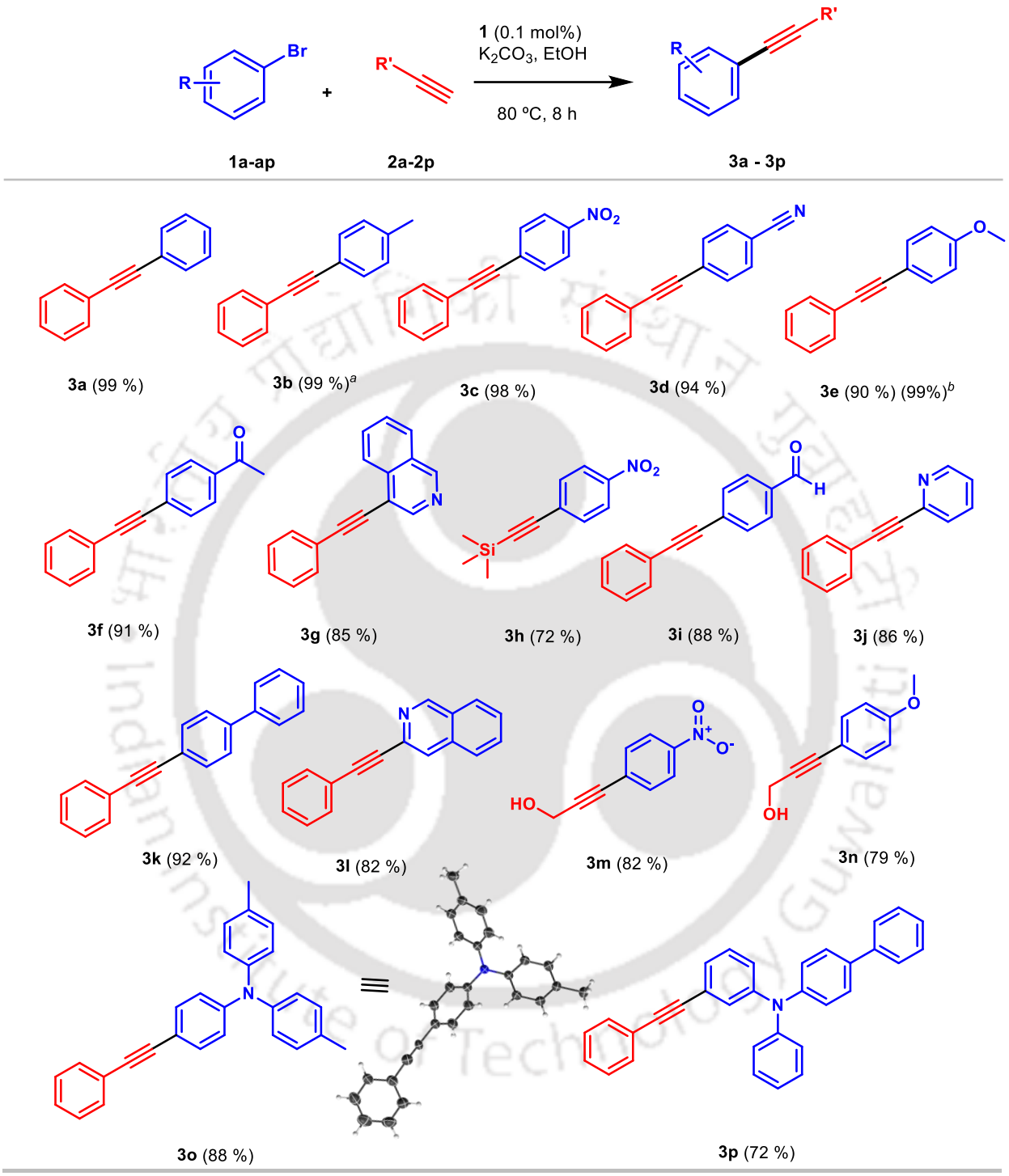

Reaction condition: Aryl bromide/iodide (1.0 mmol), Alkyne (1.2 mmol), catalyst **1** (0.5 mol%), K_2CO_3 (1.5 mmol), ethanol (10 mL), 80 ºC, and 8 h. Isolated yields. [a] NMR yield determined using 1,4-dimethoxybenzne. [b]4-iodoanisole was used.

4.2.4 Assessment of catalytic activities of 1 – 5 in C(sp^2)–P coupling:

The efficiency of these dinuclear Pd(II) catalysts were also employed for the construction of C–P bond and for this, reaction conditions were screened by altering the use of bases, solvents, temperature, and time using catalyst **1** in a model reaction of diethylphosphite and 4-iodoanisole (Scheme 4). Among several tested solvents and bases, ethanol and potassium hydroxide produced highest yield using **1** as catalyst under at 90 °C for 4 hours (Table 2, entry4). Similarly, from temperature and time screening, the best yield of diethyl (4-methoxyphenyl)phosphonate[46] was observed at 90 °C in 10 hours using KOH, catalyst **1** (0.5 mol%) in ethanol and concluded as optimum condition. Here all catalysts **1**–**5** produced diethyl (4-methoxyphenyl)phosphonate in excellent yield (97–99%) (Table 2, entry17–20) under optimal condition, however, the yield lessened to 64 % with the use of bromide analogue.

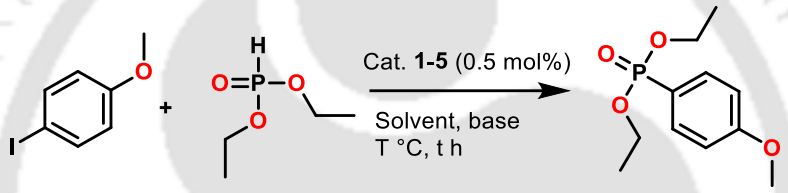

Scheme 4: C(sp^2)–P coupling of diethylphosphite and 4-iodoanisole

Table 2: Optimization table for C–P bond formation reaction

Entry	Catalyst (0.5 mol%)	base	Solvent	T/°C	Time (h)	Yield[#] (%)
1	**1**	K_2CO_3	EtOH	80	10	85
2	**1**	Et_3N	EtOH	80	10	74
3	**1**	^tBuOK	EtOH	80	10	77
4	**1**	KOH	EtOH	80	10	99
7	**1**	KOH	Toluene	80	10	31
8	**1**	KOH	CH_3CN	80	10	20
9	**1**	KOH	DMF	80	10	65
10	**1**	KOH	EtOH	80	7	84
11	**1**	KOH	EtOH	80	12	99
12	**1**	KOH	EtOH	110	10	82
13	**1**	KOH	EtOH	RT	10	00
14	**1**	KOH	EtOH	50	10	35

15	–	KOH	EtOH	80	10	00
16	**1**	KOH	EtOH	80	10	68[a]
17	**2**	KOH	EtOH	80	10	97
18	**3**	KOH	EtOH	80	10	98
19	**4**	KOH	EtOH	80	10	99
20	**5**	KOH	EtOH	80	10	97

Reaction condition: 4-iodoanisole (0.5 mmol), diethylphosphite (0.6 mmol), catalyst (0.5 mol%), base (0.75 mmol), and solvent (10.0 mL). Isolated yields. [a] 0.1 mol% catalyst was used.

4.3 Conclusions

In conclusion, we have reported the synthesis and characterization of five dinuclear palldium(II) complexes of substituted imidazo[1,5-a]pyridinylpicolinimidamides. Single crystal X-ray analysis revealed that the ligands were coordinated with palladium center through pseudo-pincer type mode and the Pd(II) center possessed distorted square planar geometry while an eight-membered metallic cavity was observed in complexes. The complexes were employed as highly active catalyst in copper-free Sonogashira coupling and C–P coupling under mild reaction conditions and produced excellent yield using only 0.5 mol% of catalyst loading. High catalytic activity of these complexes was mainly due to cooperativity and synergic effect of two Pd(II) center present in optimum proximity. The present study thus lays a robust foundation for the deployment of these dinuclear Pd(II) complexes as straightforward yet highly efficacious catalysts, with strong potential for widespread application in the future advancement of metal-catalyzed transformations extending well beyond the explored reactions.

4.3 Experimental Section

4.3.1 General procedure for synthesis of ligands

The ligands were synthesized following a reported procedure with some modification. The corresponding aldehyde, 2-cyanopyridine, and ammonium acetate in 1:2:2 ratio was heat at 100 °C in an oil-bath for 12 h. To the resultant red gummy oil 25 mL of water was added with mechanical stirring for next 12 h. Then, 50 mL dichloromethane was added to the mixture, organic layer was collected and the solid obtained was dried in vacuum over fused $CaCl_2$. The products

were isolated as crystalline fibrous solid after column chromatography using silica gel (60-120 mesh) and ethyl acetate/hexane (1:9) as eluent.

N-(3-(2-methoxyphenyl)imidazo[1,5-*a*]pyridin-1-yl)picolinimidamide **(L1H)**

2-Methoxybenzaldehyde (0.68 g, 0.005 mol) and 2-cyanopyridine (1.04 g, 0.01 mol) was used. Yield: (1.2 g) 70%. ATR-IR (neat, cm^{-1}): 3448, 2922, 2853, 1745, 1616, 1563, 1462, 1380, 1309, 1269, 1238, 1162, 1105, 1077, 956, 759, 729, 747, 711. 466, 427. ^{1}H NMR (400 MHz, DMSO-d_6) δ 9.28 (s, 1H), 8.64 (d, J = 7.9 Hz, 1H), 8.58 (d, J = 5.5 Hz, 1H), 7.92 (d, J = 9.0 Hz, 1H), 7.80 (td, J = 7.8, 1.7 Hz, 1H), 7.68 (dd, J = 7.5, 1.7 Hz, 1H), 7.54 – 7.44 (m, 2H), 7.34 – 7.30 (m, 1H), 7.13 (t, J = 7.9 Hz, 1H), 7.06 (d, J = 8.3 Hz, 1H), 6.69 (dd, J = 9.0, 6.3 Hz, 1H), 6.54 (t, J = 6.8 Hz, 1H), 3.83 (s, 3H). ^{13}C NMR (126 MHz, Chloroform-*d*) δ 157.4, 153.1, 150.1, 148.0, 140.2, 136.4, 132.6, 130.9, 130.5, 125.3, 124.2, 122.5, 121.6, 121.2, 119.7, 119.0, 116.5, 113.2, 111.5, 55.7. UV-Vis (λ, nm (Ɛ, M^{-1} cm^{-1})): 355 (14700), 399 (15700), 417 (15900), 443 (10600). HRMS (ESI) *m/z* calcd for $(C_{20}H_{17}N_5O + H)^+$: 344.1506; found 344.1510.

N-(3-(4-methoxyphenyl)imidazo[1,5-*a*]pyridin-1-yl)picolinimidamide **(L2H)**

4-methoxybenzaldehyde (0.68 g, 0.005 mol) and 2-cyanopyridine (1.04 g, 0.01 mol) was used. Yield: (1.07 g) 63%. UV-Vis (λ, nm (Ɛ, M^{-1} cm^{-1})): 357 (18400), 400(16000), 425 (15260). ATR-IR, NMR and HRMS data were matched well with the literature.

N-(3-(2-chlorophenyl)imidazo[1,5-*a*]pyridin-1-yl)picolinimidamide **(L3H)**

2-chlorobenzaldehyde (0.70 g, 0.005 mol) and 2-cyanopyridine (1.04 g, 0.01 mol) was used. Yield: (1.35 g) 78%. ATR-IR (neat, cm^{-1}): 3460, 2923, 2853, 1738, 1616, 1562, 1467, 1440, 1382, 1324, 1235, 1133, 1033, 992, 727, 709, 453, 420. ^{1}H NMR (400 MHz, Chloroform-*d*) δ 9.18 (s, 1H), 8.62 (d, J = 8.0 Hz, 1H), 8.58 (d, J = 4.8 Hz, 1H), 7.94 (d, J = 9.0 Hz, 1H), 7.80 (td, J = 7.8, 1.7 Hz, 1H), 7.70 – 7.64 (m, 1H), 7.59 – 7.51 (m, 2H), 7.45 – 7.41 (m, 2H), 7.35 – 7.30 (m, 1H), 6.77 – 6.69 (m, 1H), 6.60 (t, J = 7.3 Hz, 1H). ^{13}C NMR (126 MHz, Chloroform-*d*) δ 152.9, 150.8, 148.1, 140.1, 136.5, 134.3, 133.0, 130.5, 130.4, 130.3, 129.7, 127.2, 125.0, 124.3, 121.6, 121.4, 119.4, 117.0, 114.1. UV-Vis (λ, nm (Ɛ, M^{-1} cm^{-1})): 355 (18500), 400 (16100), 427 (15000), 452 (9800). HRMS (ESI) *m/z* calculated for $(C_{19}H_{14}ClN_5+H)^+$: 348.1011; found 348.1026.

N-(3-(4-methylphenyl)imidazo[1,5-*a*]pyridin-1-yl)picolinimidamide **(L4H)**

4-methylbenzaldehyde (0.6 g, 0.005 mol) and 2-cyanopyridine (1.04 g, 0.01 mol) was used. Yield: (1.26 g) 77%. UV-Vis (λ, nm (Ɛ, M^{-1} cm^{-1})): 274 (13330), 361 (12870), 401 (10870), 425 (9900). ATR-IR, NMR and HRMS data were matched well with the literature.

N-(3-(4-bromophenyl)imidazo[1,5-*a*]pyridin-1-yl)picolinimidamide **(L5H)**

4-bromobenzaldehyde (0.92 g, 0.005 mol) and 2-cyanopyridine (1.04 g, 0.01 mol) was used. Yield: (1.33 g) 68%. ATR-IR (neat, cm^{-1}): 3434, 2922, 2852, 1744, 1620, 1528, 1494, 1466, 1371, 1305, 1243, 1075, 994, 948, 832, 798, 709, 502, 470, 442. UV-Vis (λ, nm (Ɛ, M^{-1} cm^{-1})): 236 (18600), 375 (15670), 399(14700), 424 (11830). ^{1}H NMR (400 MHz, Chloroform-*d*) δ 9.21 (s, 1H), 8.62 – 8.58 (m, 2H), 8.16 (d, *J* = 7.2 Hz, 1H), 7.91 (d, *J* = 8.9 Hz, 1H), 7.80 (td, *J* = 7.6, 1.7 Hz, 1H), 7.73 (d, *J* = 8.6 Hz, 2H), 7.65 (d, *J* = 8.6 Hz, 2H), 7.42 (s, 1H), 7.36 – 7.31 (m, 1H), 6.71 – 6.66 (m, 1H), 6.62 (td, *J* = 6.9, 6.5, 1.3 Hz, 1H). ^{13}C NMR (126 MHz, Chloroform-*d*) δ 161.87, 149.59, 148.39, 137.65, 133.72, 132.40, 129.46, 128.95, 127.42, 126.57, 122.87, 122.49, 122.25, 121.62, 120.76, 118.02, 114.25. HRMS (ESI) *m/z* calculated for $(C_{19}H_{14}BrN_5+H)^+$: 392.0505; found 392.0514.

4.3.2 General procedure for synthesis of palladium complexes:

The dinuclear palladium complexes were synthesized by a general procedure. For this, Palladium dichloride (88 mg, 0.5 mmol) was taken in 10 mL acetonitrile and was heated till all $PdCl_2$ dissolved. To the squash colour hot solution, corresponding ligand (**L1H** – **L3H**) (0.5 mmol) was added resulting a deep red/orange colour solution. The mixture was left at ambient temperature with continuous stirring for 12 hours. The solvent was removed, solids were washed with diethyl ether, and dried in vacuo to afford the desired dinuclear palladium complexes (**1** – **3**). Following the similar method, solids obtained from the reaction of $PdCl_2$ with **L4H** and **L5H** were dissolved it methanol, KPF_6 was then added and stirred for about 2 hours at room temperature. Orange solids were precipitated out, filtered, washed with diethyl ether, and dried in vacuo to afford the dinuclear palladium complexes **4** and **5**.

$[Pd_2(\mathbf{L1H})_2Cl_2]Cl_2$ (**1**)

Following the general procedure, complex **1** was synthesized from the reaction of $PdCl_2$ and **L1H**. Yield: (0.385 g) 74%. ATR-IR (neat, cm^{-1}): 2924, 1720, 1645, 1566, 1454, 1250, 1017, 751, 628, 432. UV-Vis (λ, nm (Ɛ, M^{-1} cm^{-1})): 304 (28000), 385 (11800), 440 (6000). ^{1}H NMR (400 MHz,

DMSO-*d*6) δ 9.56 (s, 2H), 9.14 (d, *J* = 5.1 Hz, 2H), 8.61 (s, 2H), 8.57 – 8.50 (m, 4H), 8.46 (t, *J* = 7.7 Hz, 2H), 7.98 (t, *J* = 6.7 Hz, 2H), 7.62 (t, *J* = 7.1 Hz, 2H), 7.39 (d, *J* = 7.2 Hz, 2H), 7.21 (t, *J* = 7.6 Hz, 2H), 7.09 (d, *J* = 8.6 Hz, 2H), 6.96 (s, 4H), 6.80 (dt, *J* = 7.4, 3.7 Hz, 2H), 3.34 (s, 6H). ^{13}C NMR (151 MHz, DMSO-d_6) δ 165.00, 157.53, 152.08, 151.73, 142.64, 133.47, 132.99, 132.31, 130.41, 128.57, 127.79, 126.46, 124.15, 123.02, 120.99, 116.37, 115.52, 114.01, 112.17, 56.32. HRMS (ESI) *m/z* calculated for $[C_{40}H_{34}Cl_4N_{10}O_2Pd_2–2Cl]^{2+}$: 485.0155, found 485.0128; $[C_{40}H_{34}Cl_4N_{10}O_2Pd_2–2Cl–H]^{+}$: 969.0238, found 969.0178.

$[Pd_2(\mathbf{L2H})_2Cl_2]Cl_2$ (**2**)

Following the general procedure, complex **2** was synthesized from the reaction of $PdCl_2$ and **L2H**. Yield: (0.375 g) 72%. ATR-IR (neat, cm^{-1}): 3084, 1651, 1609, 1557, 1456, 1252, 1177, 1025, 839, 795, 748, 575, 523, 440. UV-Vis (λ, nm (Ɛ, M^{-1} cm^{-1})): 311 (19300), 352 (10800), 428 (7600). ^{1}H NMR (400 MHz, Chloroform-*d*) δ 9.77 (s, 2H), 9.09 (d, *J* = 5.0 Hz, 2H), 8.77 (s, 2H), 8.66 (d, *J* = 7.3 Hz, 2H), 8.51 (t, *J* = 7.5 Hz, 2H), 7.97 (dt, *J* = 15.8, 7.4 Hz, 4H), 7.62 (d, *J* = 8.5 Hz, 4H), 7.32 (d, *J* = 9.2 Hz, 2H), 7.17 (d, *J* = 8.6 Hz, 4H), 7.04 – 6.95 (m, 2H), 6.80 (t, *J* = 6.7 Hz, 2H), 3.86 (s, 6H). ^{13}C NMR (151 MHz, DMSO-d_6) δ 165.32, 162.62, 161.06, 152.01, 151.38, 142.34, 134.47, 131.14, 130.10, 128.63, 126.25, 122.83,121.86, 117.34, 117.17, 116.27, 115.04, 55.68. HRMS (ESI) *m/z* calculated for $[C_{40}H_{34}Cl_4N_{10}O_2Pd_2–2Cl]^{2+}$: 485.0155, found 485.0130; $[C_{40}H_{34}Cl_4N_{10}O_2Pd_2–2Cl–H]^{+}$: 969.0238, found 969.0182.

$[Pd_2(\mathbf{L3H})_2Cl_2]Cl_2$ (**3**)

Following the general procedure, complex **3** was synthesized from the reaction of $PdCl_2$ and **L3H**. Yield: (0.446 g) 85%. ATR-IR (neat, cm^{-1}): 3442, 1738, 1626, 1598, 1450, 1354, 1290, 1055, 745, 681, 509, 424. UV-Vis (λ, nm (Ɛ, M^{-1} cm^{-1})): 321 (20600), 366 (14300), 424 (7890). ^{1}H NMR (600 MHz, Chloroform-*d*) δ 9.20 (d, *J* = 5.1 Hz, 2H), 8.76 (d, *J* = 7.6 Hz, 2H), 8.06 (d, *J* = 7.7 Hz, 2H), 7.99 (t, *J* = 7.6 Hz, 2H), 7.54 – 7.51 (m, 2H), 7.50 – 7.47 (m, 2H), 7.47 – 7.44 (m, 2H), 7.34 (d, *J* = 7.4 Hz, 2H), 7.16 (d, *J* = 9.2 Hz, 2H), 7.08 (d, *J* = 7.2 Hz, 2H), 6.73 (dd, *J* = 8.8, 6.9 Hz, 2H), 6.55 – 6.52 (m, 2H). ^{13}C NMR (151 MHz, Chloroform-*d*) δ 169.44, 153.96, 149.74, 139.88, 136.33, 134.87, 134.30, 132.03, 130.26, 129.26, 127.62, 126.89, 126.45, 126.17, 122.89, 121.65, 119.79, 119.57, 114.97. HRMS (ESI) *m/z* calculated for $[C_{38}H_{28}Cl_6N_{10}Pd_2–2Cl]^{2+}$: 489.9652, found 489.9632; $[C_{38}H_{28}Cl_6N_{10}Pd_2–2Cl–H]^{+}$: 978.9231, found 978.9184.

$[Pd_2(\mathbf{L4H})_2Cl_2](PF_6)_2$ (**4**)

Following the general procedure, complex **4** was synthesized from the reaction of $PdCl_2$ and **L4H**. Yield: (0.497 g) 81%. ATR-IR (neat, cm^{-1}): 3086, 1648, 1567, 1384, 1253, 1098, 831, 754, 661, 556, 497, 441. UV-Vis (λ, nm (Ɛ, M^{-1} cm^{-1})):310 (23700), 365 (11500), 426 (8160). ^{1}H NMR (600 MHz, DMSO-d_6) δ 9.66 (s, 2H), 9.10 (d, *J* = 5.0 Hz, 2H), 8.78 (s, 2H), 8.54 (q, *J* = 9.1, 7.8 Hz, 4H), 8.01 (t, *J* = 6.3 Hz, 4H), 7.95 (s, DMF), 7.59 (d, *J* = 7.9 Hz, 4H), 7.44 (d, *J* = 7.8 Hz, 4H), 7.35 (d, *J* = 9.2 Hz, 2H), 6.99 (t, *J* = 7.8 Hz, 2H), 6.82 (t, *J* = 6.8 Hz, 2H), 2.89, (s, DMF), 2.73, (s, DMF), 2.43 (s, 6H). ^{13}C NMR (151 MHz, DMSO-d_6) δ 165.16, 162.33, 151.91, 151.24, 142.22, 140.81, 134.35, 130.02, 129.20, 128.76, 125.99, 122.85, 122.62, 122.22, 121.85, 117.24, 116.21, 35.80, 30.78 (DMF), 21.15 (DMF). ^{31}P NMR (243 MHz, DMSO-d_6) δ -144.19 (sept, *J* = 710.6 Hz). HRMS (ESI) *m/z* calculated for $[C_{40}H_{34}Cl_2F_{12}N_{10}P_2Pd_2–2PF_6]^{2+}$: 469.0206, found 469.0203; $[C_{40}H_{34}Cl_2F_{12}N_{10}P_2Pd_2–2PF_6–H]^{+}$: 937.0240, found 937.0323.

$[Pd_2(\mathbf{L5H})_2Cl_2]$ $(PF_6)_2$ (**5**)

Following the general procedure, complex **5** was synthesized from the reaction of $PdCl_2$ and **L5H**. Yield: (0.516 g) 76%. ATR-IR (neat, cm^{-1}): 3074, 1644, 1563, 1521, 1454, 1069, 1009, 965, 795, 747, 496, 434. UV-Vis (λ, nm (Ɛ, M^{-1} cm^{-1})): 328 (21230), 398 (9950), 432 (7700). ^{1}H NMR (600 MHz, DMSO-d_6) δ 9.69 (s, 1H), 9.12 – 9.07 (m, 1H), 8.79 (s, 1H), 8.55 (q, *J* = 8.1 Hz, 2H), 8.09 (d, *J* = 7.3 Hz, 1H), 8.02 (t, *J* = 6.2 Hz, 1H), 7.86 (d, *J* = 8.4 Hz, 2H), 7.68 (d, *J* = 8.4 Hz, 2H), 7.46 (d, *J* = 9.3 Hz, 1H), 7.10 – 7.04 (m, 1H), 6.89 – 6.83 (m, 1H). ^{13}C NMR (151 MHz, DMSO-d_6) δ 165.34, 151.97, 151.21, 142.23, 133.05, 132.50, 131.24, 129.95, 129.12, 126.04, 124.50, 124.39, 123.16, 123.09, 122.08, 117.08, 116.47. ^{31}P NMR (162 MHz, DMSO-d_6) δ -144.20 (sept, *J* = 711.2 Hz). HRMS (ESI) *m/z* calculated for $[C_{38}H_{28}Br_2Cl_2F_{12}N_{10}P_2Pd_2–2PF_6]^{2+}$: 531.8985, found 531.8982; $[C_{38}H_{28}Br_2Cl_2F_{12}N_{10}P_2Pd_2–2PF_6–H]^{+}$: 1066.8217, found 1066.8212.

4.3.3 Crystallographic data

For the single crystal XRD data collection of the appropriate single crystals of **L1H**, **L3H** and **L5H** was mount on a single source Super Nova CCD System instrument from Agilent Technologies equipped with a fine focus 1.75 kW sealed tube with Mo-Kα radiation was used at room temperature. The data were reduced using CrysAlisPro and Autochem2.1 software.[47] For rest of the ligands and complexes, data was collected at room temperature using a Bruker SMART APEX CCD diffractometer equipped with fine focus 1.75 kW sealed tube of Mo-Kα (λ = 0.71073

Å) X-ray source, with increasing ω (width of 0.3° per frame) at a scan speed of either 3 or 5 s per frame.[48] The SMART software was used for data acquisition and the SAINT software for data extraction. The structure solution and refinement were performed on the Olex2-1.5 using the SHELXT, SHELXL programs.[49,50] All atoms except hydrogen atoms are tuned using anisotropic displacement parameters, whereas hydrogen atoms are tuned using relative isotropic parameters. The disorder in molecular structure of **1g** was fixed using partial occupancies factor, unidentified electron densities were masked using OLEX2 utility.[51] PLATON was used for structure validation and for pictorial visualization of X-ray single crystal data, Mercury and ORTEP software was used.[52–54]

4.3.4 Optimization copper-free of copper-free Sonogashira reaction

A 50 mL round bottom flask equipped with a magnetic stir bar was charged with the 4-bromotoluene (0.5 mmol), base (0.75 mmol), phenylacetylene (0.6 mmol), and catalyst **1** (0.5 mol%) in 10.0 mL absolute ethanol. Then it was stirred at specified temperature for a given time. Then, the reaction was allowed to cool to room temperature, ethyl acetate and H_2O were added and the layers were separated. The aqueous layer was extracted three times with ethylacetate, the combined organic layers were washed with water, dried over Na_2SO4, filtered, and concentrated in vacuo to yield the crude product, which was purified by preparative thin layer chromatography to produce the product.

4.3.5 General procedures for Sonogashira coupling reaction.

A 50 mL round bottom flask equipped with a magnetic stir bar was charged with the aryl bromide (1.0 eq.), K_2CO_3 (1.5 eq.), the terminal alkyne (1.2 eq.), catalyst **1** (0.5 mol%), and 10 mL absolute ethanol. Then it was stirred at 80 °C for 8 hours. The reaction was allowed to cool to room temperature, ethyl acetate and H_2O were added and the layers were separated. The aqueous layer was extracted three times with ethylacetate, the combined organic layers were washed with brine, dried over Na_2SO_4, filtered, and concentrated in vacuo to yield the crude product, which was purified by preparative thin layer chromatography to yield the pure product (see specific procedures for individual purification conditions).

4.3.6 Characterization data for Sonogashira products 3a-3p

1,2-diphenylethyne (3a) [55]

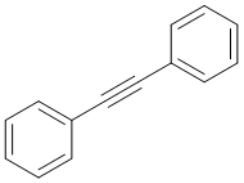

^{1}H NMR (400 MHz, Chloroform-*d*) δ 7.57 – 7.51 (m, 4H), 7.39 – 7.32 (m, 6H). ^{13}C NMR (126 MHz, Chloroform-*d*) δ 132.6, 131.7, 128.5, 123.4, 89.5.

1-methyl-4-(phenylethynyl)benzene (3b) [55]

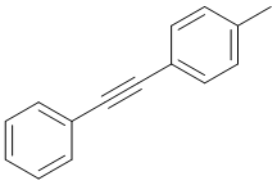

^{1}H NMR (400 MHz, Chloroform-*d*) δ 7.55 – 7.50 (m, 2H), 7.43 (d, *J* = 8.1 Hz, 2H), 7.37 – 7.30 (m, 3H), 7.16 (d, *J* = 7.9 Hz, 2H), 2.37 (s, 3H). ^{13}C NMR (126 MHz, Chloroform-*d*) δ 138.54, 131.70, 131.65, 129.26, 128.46, 128.22, 123.64, 120.3, 89.7, 88.8, 21.7.

1-nitro-4-(phenylethynyl)benzene (3c) [55]

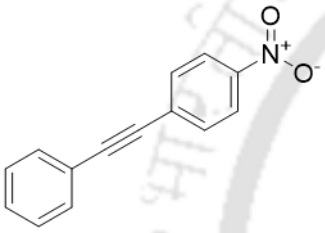

^{1}H NMR (400 MHz, Chloroform-*d*) δ 8.22 (d, *J* = 8.7 Hz, 2H), 7.67 (d, *J* = 8.7 Hz, 2H), 7.61 – 7.53 (m, 2H), 7.43 – 7.36 (m, 3H). ^{13}C NMR (126 MHz, Chloroform-*d*) δ 147.1, 132.4, 132.0, 130.4, 129.4, 128.7, 123.8, 122.3, 94.8, 87.7.

4-(phenylethynyl)benzonitrile (3d)[56]

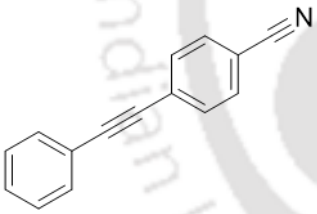

^{1}H NMR (400 MHz, Chloroform-*d*) δ 7.66 – 7.58 (m, 4H), 7.57 – 7.52 (m, 2H), 7.40 – 7.36 (m, *J* = 5.1, 1.8 Hz, 3H).^{13}C NMR (126 MHz, DMSO-d_6) δ 132.2, 132.2, 131.9, 129.3, 128.6, 128.4, 122.3, 118.7, 111.6, 93.9, 87.8.

1-methoxy-4-(phenylethynyl)benzene (3e) [55]

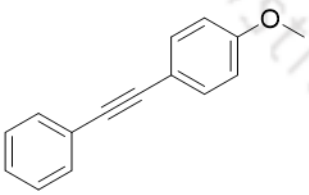

^{1}H NMR (400 MHz, Chloroform-*d*) δ 7.51 (dd, *J* = 7.8, 1.7 Hz, 2H), 7.47 (d, *J* = 8.9 Hz, 2H), 7.38 – 7.29 (m, 3H), 6.88 (d, *J* = 8.9 Hz, 2H), 3.83 (s, 3H). ^{13}C NMR (126 MHz, Chloroform-*d*) δ 159.8, 133.2, 131.6, 128.4, 128.1, 123.7, 115.5, 114.1, 89.5, 88.2, 55.4.

1-(4-(phenylethynyl)phenyl)ethan-1-one (3f) [55]

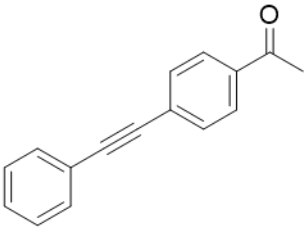

^{1}H NMR (400 MHz, Chloroform-*d*) δ 7.94 (d, *J* = 8.5 Hz, 2H), 7.61 (d, *J* = 8.6 Hz, 2H), 7.55 (dd, *J* = 6.2, 3.4 Hz, 2H), 7.37 (td, *J* = 3.6, 3.2, 2.0 Hz, 3H), 2.62 (s, 3H). ^{13}C NMR (126 MHz, Chloroform-*d*) δ 197.3, 136.2, 131.8, 131.7, 128.8, 128.5, 128.3, 128.2, 122.7, 92.7, 88.6, 26.6.

4-(phenylethynyl)isoquinoline (3g) [57]

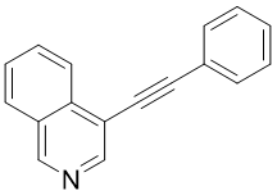

^{1}H NMR (400 MHz, Chloroform-*d*) δ 9.21 (s, 1H), 8.78 (s, 1H), 8.35 (d, *J* = 9.1 Hz, 1H), 8.01 (d, *J* = 8.2 Hz, 1H), 7.82 (ddd, *J* = 8.3, 6.9, 1.2 Hz, 1H), 7.72 – 7.62 (m, 3H), 7.45 – 7.35 (m, 3H). ^{13}C NMR (126 MHz, hloroform-*d*) δ 152.1, 146.6, 135.7, 131.9, 131.3, 129.0, 128.7, 128.1, 128.1, 128.0, 125.3, 123.0, 116.1, 96.9, 84.6.

((p-Nitroxyphenyl)ethynyl)trimethylsilane (3h) [58]

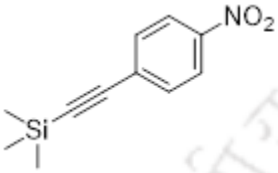

^{1}H NMR (400 MHz, Chloroform-*d*) δ 8.17 (d, *J* = 8.6 Hz, 2H), 7.59 (d, *J* = 8.6 Hz, 2H), 0.27 (s, 9H). ^{13}C NMR (126 MHz, Chloroform-*d*) δ 147.3, 132.8, 130.1, 123.6, 102.9, 100.8, -0.15.

(Phenylethynyl)benzaldehyde (3i) [56]

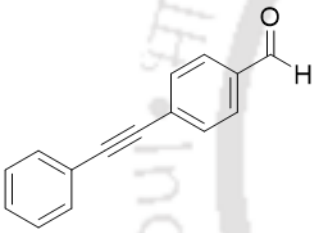

^{1}H NMR (400 MHz, Chloroform-*d*) δ 10.02 (s, 1H), 7.87 (d, *J* = 8.4 Hz, 2H), 7.68 (d, *J* = 8.2 Hz, 2H), 7.60 – 7.53 (m, 2H), 7.38 (p, *J* = 3.1, 2.6 Hz, 3H). ^{13}C NMR (126 MHz, Chloroform-*d*) δ 191.6, 135.5, 132.2, 131.9, 129.7, 129.7, 129.1, 128.6, 122.6, 93.6, 88.6.

2-(phenylethynyl) pyridine (3j) [59]

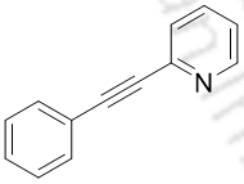

^{1}H NMR (400 MHz, Chloroform-*d*) δ 8.57 (d, *J* = 4.7 Hz, 1H), 7.65 – 7.54 (m, 3H), 7.47 (d, *J* = 7.8 Hz, 1H), 7.37 – 7.28 (m, 3H), 7.21 – 7.14 (m, 1H). ^{13}C NMR (126 MHz, Chloroform-*d*) δ 150.1, 143.5, 136.2, 132.1, 129.0, 128.4, 127.2, 122.8, 122.28, 89.3, 88.7.

4-(phenylethynyl)-1,1'-biphenyl (3k) [56]

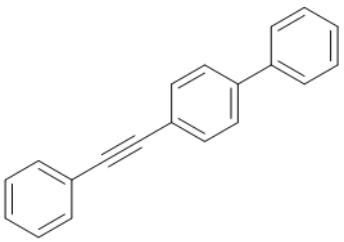

^{1}H NMR (400 MHz, Chloroform-*d*) δ 7.62 (dd, *J* = 8.9, 1.4 Hz, 6H), 7.57 (dd, *J* = 7.6, 2.1 Hz, 2H), 7.46 (t, *J* = 7.5 Hz, 2H), 7.40 – 7.34 (m, 4H). ^{13}C NMR (126 MHz, Chloroform-*d*) δ 141.1, 140.5, 132.2, 131.8, 129.0, 128.5, 128.4, 127.8, 127.2, 123.4, 122.3, 90.2, 89.4.

3-(phenylethynyl)isoquinoline (3l)

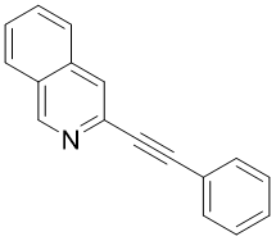

^{1}H NMR (400 MHz, Chloroform-*d*) δ 9.00 (s, 1H), 8.22 (s, 1H), 8.09 (d, *J* = 8.4 Hz, 1H), 7.72 (m, *J* = 8.0, 3.7 Hz, 1H), 7.69 – 7.64 (m, 1H), 7.58 (dd, *J* = 5.2, 2.6 Hz, 2H), 7.53 – 7.48 (m, 1H), 7.38 – 7.32 (m, 3H). ^{13}C NMR (126 MHz, Chloroform-*d*) δ 152.1, 146.8, 138.20 131.7, 130.0, 129.4, 128.8, 128.5, 127.6, 127.2, 127.2, 122.6, 117.4, 86.7. HRMS (ESI) calculated for $[C_{17}H_{11}N+H]^+$: 230.0965, found 230.0960.

3-(4-nitrophenyl) prop-2-yn-1-ol (3m) [60]

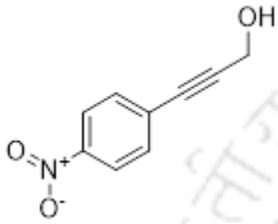

^{1}H NMR (400 MHz, Chloroform-*d*) δ 8.18 (d, *J* = 8.9 Hz, 2H), 7.57 (d, *J* = 8.9 Hz, 2H), 4.54 (s, 2H), 1.86 (s, 1H). ^{13}C NMR (126 MHz, Chloroform-*d*) δ 147.4, 132.6, 129.6, 123.7, 92.6, 83.96, 51.6.

3-(4-methoxyphenyl)prop-2-yn-1-ol (3n)[60]

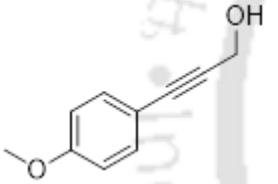

^{1}H NMR (400 MHz, Chloroform-*d*) δ 7.36 (d, *J* = 8.9 Hz, 2H), 6.82 (d, *J* = 8.9 Hz, 2H), 4.47 (s, 2H), 3.79 (s, 3H). ^{13}C NMR (126 MHz, Chloroform-*d*) δ 159.8, 133.3, 114.7, 114.0, 86.0, 85.7, 55.4, 51.7.

4-methyl-N-(4-(phenylethynyl)phenyl)-N-(p-tolyl)aniline (3o)

According to the general procedure, the reaction of 4-bromo-N,N-di-p-tolylaniline (0.5 mmol), phenylacetylene (0.6 mmol), K_2CO_3 (0.75 mmol), catalyst **1** (0.5 mol%) in ethanol for 8 h at 80 °C, affording the title compound as light yellow solid after work-up and chromatography.

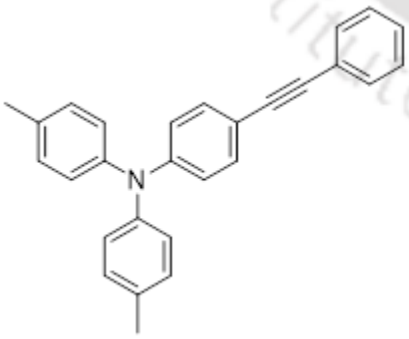

^{1}H NMR (400 MHz, Chloroform-*d*) δ 7.50 (dd, *J* = 7.8, 1.6 Hz, 2H), 7.36 – 7.30 (m, 5H), 7.09 (d, *J* = 8.8 hz, 4H), 7.01 (d, *J* = 8.8 hz, 4H), 6.94 (d, *J* = 8.7 Hz, 2H), 2.32 (s, 6H). ^{13}C NMR (101 MHz, Chloroform-*d*) δ 148.4, 144.8, 133.4, 132.5, 131.57, 130.2, 128.4, 127.9, 125.3, 124.8, 121.2, 115.2, 90.0, 88.4, 21.0. HRMS (ESI) calculated for $[C_{28}H_{23}N+H]^+$: 347.1904, found 347.1904.

N-phenyl-N-(3-(phenylethynyl)phenyl)-[1,1'-biphenyl]-4-amine (3p)

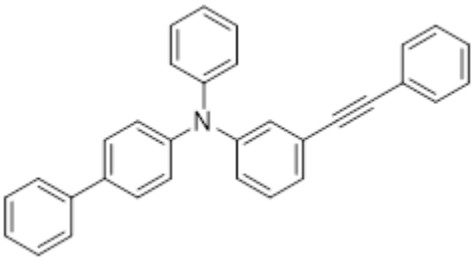

According to the general procedure, the reaction of N-(3-bromophenyl)-N-phenyl-[1,1'-biphenyl]-4-amine (0.5 mmol), phenylacetylene (0.6 mmol), K_2CO_3 (0.75 mmol), catalyst **1** (0.5 mol%) in ethanol for 8 h at 80 °C, affording the title compound as light yellow solid after work-up and chromatography and ^{1}H NMR (400 MHz, Chloroform-*d*) δ 7.61 – 7.55 (m, 2H), 7.50 (td, *J* = 6.0, 5.4, 3.3 Hz, 4H), 7.42 (t, *J* = 7.6 Hz, 2H), 7.35 – 7.26 (m, 7H), 7.25 – 7.18 (m, 2H), 7.18 – 7.13 (m, 4H), 7.13 – 7.05 (m, 2H). ^{13}C NMR (151 MHz, Chloroform-*d*) δ 147.9, 147.5, 147.0, 140.7, 135.7, 131.7, 129.6, 129.5, 128.9, 128.5, 128.4, 128.1, 127.0, 126.9, 126.8, 126.1, 124.8, 124.4, 124.3, 123.4, 89.6, 89.3. HRMS (ESI) calculated for $[C_{32}H_{23}N+H]^+$: 422.1904, found 422.1866.

4.3.7 Optimization of C–P bond formation reaction

4-iodoanisole (0.5 mmol eq.), base (0.75 mmol.), diethylphosphite (0.6mmol), and catalyst **1** (0.5 mol%) were taken in 10.0 mL solvent. Then it was stirred at specified temperature for a given time. The reaction was allowed to cool to room temperature, solvent was removed. Then, ethyl acetate and H_2O were added and the layers were separated. The aqueous layer was extracted three times with ethylacetate, the combined organic layers were washed with water, dried over Na_2SO4, filtered, and concentrated in vacuo to yield the crude product, which was purified flash column chromatography to produce the pure product.

Diethyl (4-methoxyphenyl)phosphonate

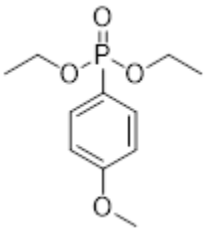

^{1}H NMR (600 MHz, Chloroform-*d*) δ 7.76 – 7.69 (m, 2H), 6.96 (dd, *J* = 8.7, 3.3 Hz, 2H), 4.14 – 3.99 (m, 4H), 3.85 (s, 3H), 1.30 (t, *J* = 7.1 Hz, 6H). ^{13}C NMR (151 MHz, Chloroform-*d*) δ 162.99, 133.93, 133.86, 118.89, 114.22, 114.11, 62.12, 62.08, 55.48, 16.47, 16.42. ^{31}P NMR (243 MHz, Chloroform-*d*) δ 19.73. NMR spectroscopic data matched literature values.[60]

4.3.8 Hot filtration test

Bromotoluene (0.5 mmol), phenylacetylene (0.6 mmol), K_2CO_3 (0.75 mmol), catalyst **1** (0.5 mol%), and ethanol (10.0 mL) was stirred at 90 ºC. After 2 hours, the reaction mixture was filtered through a short pad of celite in hot condition and again stirred for next 6 h. After completion of

the reaction, the mixture was cooled, diluted with ethyl acetate (30.0 mL). Then it was filtered through a short pad of celite and filtrate was removed under reduced pressure. The crude product was purified by preparative thin layer chromatography and the yield of product (**3b**) was 88%.

CCDC No. 2496016–2496026 contain the crystallographic data for all ligands complexes and 4-methyl-N-(4-(phenylethynyl)phenyl)-N-(p-tolyl)aniline (**3o**).

The ATR-IR, NMR, HRMS(ESI), electronic spectra and FESEM images of ligands and complexes, NMR spectra, HRMS spectra (new compounds) of catalytic products, can be found in Appendix III by using the following link:
https://drive.google.com/file/d/1zaFRM0avj7JdeDhpNY-czZtpFMj-cejv/view?usp=sharing

4.4 Reference

1. C. Liu, H. Zhang, W. Shi and A. Lei, *Chem. Rev.*, 2011, **111**, 1780–1824.
2. W. Xu, M. Li, L. Qiao and J. Xie, *Chem. Commun.*, 2020, **56**, 8524–8536.
3. S. E. Hooshmand, B. Heidari, R. Sedghi and R. S. Varma, *Green Chem.,* 2019, **21**, 381-405.
4. C. Torborg and M. Beller, *Adv. Synth. Catal.*, 2009, **351**, 3027–3043.
5. J. Rayadurgam, S. Sana, M. Sasikumar and Q. Gu, *Org. Chem. Front.*, 2021, **8**, 384–414.
6. Z.-Y. Wang, T. Yang, K.-K. Wang, D.-F. Liu, X. Ma, N. Wang, H. Liu, A. Sun and H. Liu, *Green Chem.,* 2023, **25**, *3040-3045*.
7. A. Lashgari, C. K. Williams, J. L. Glover, Y. Wu, J. Chai and J. J. Jiang, *Chem. Euro. J.*, 2020, **26**, 16774–16781.
8. Bratko and M. Gómez, *Dalton Trans*., 2013, **42**, 10664-10681.
9. J. I. Van Der Vlugt, *Eur. J. Inorg. Chem*., 2012, 363–375.
10. J. Park and S. Hong, *Chem. Soc. Rev.*, 2012, **41**, 6931–6943.

11. L. Zhao, O. Akdim, X. Huang, K. Wang, M. Douthwaite, S. Pattisson, R. J. Lewis, R. Lin, B. Yao, D. J. Morgan, G. Shaw, Q. He, D. Bethell, S. McIntosh, C. J. Kiely and G. J. Hutchings, *ACS Catal.*, 2023, **13**, 2892–2903.
12. M. Ramana Reddy, C. M. Darapaneni, R. D. Patil and H. Kumari, *Org. Biomol. Chem.,* 2022, **20**, 3440-3468.
13. M. Alcarazo, S. J. Roseblade, A. R. Cowley, R. Fernández, J. M. Brown and J. M. Lassaletta, *J. Am. Chem. Soc.*, 2005, **127**, 3290–3291.
14. G. A. Ardizzoia, D. Ghiotti, B. Therrien, and S. Brenna, *Inorganica Chim. Acta.*, 2018, **471**, 384-390.
15. T. Scattolin, G. Andreetta, M. Mauceri, F. Rizzolio, N. Demitri, V. Canzonieri and F. Visentin, *J. Organomet. Chem.*, 2021, **952**, 122014.
16. M. S. Sunitha and S. Sarveswari, *Inorganica Chim. Acta.,* 2024, **562**, 121893.
17. Y. Imada, S. Mukai, K. Tahara, N. Kozai, M. Itaya, Y. Yoshida, S. Ueta, Y. Arakawa, K. Minagawa and F. Yagishita, *Inorganica Chim. Acta.*, 2023, **555**, 121584.
18. K. Ramki, R. Selva Kumar, G. Thiruppathi, P. Sundararaj and P. Sakthivel, *J. Photochem. Photobiol. A: Chem.*, 2023, **444**, 115022.
19. A. R. Rayasingh and V. Manivannan, *Dalton Trans.*, 2025, **54**, 7741–7752.
20. M. M. Rahman, J. Zhang, Q. Zhao, J. Feliciano, E. Bisz, B. Dziuk, R. Lalancette, R. Szostak and M. Szostak, *Organometallics*, 2022, **41**, 2281–2290.
21. S. Baweja, T. Gabler, P. Lönnecke and E. Hey-Hawkins, *Dalton Trans.*, 2023, **52**, 6494–6500.
22. R. Chinchilla, C. Nájera, *Chem. Soc. Rev.,* 2011, **40**, 5084-5121.
23. L. M. Zhang, H. Y. Li, H. X. Li, D. J. Young, Y. Wang and J. P. Lang, *Inorg. Chem.*, 2017, **56**, 11230–11243.
24. N. Dehury, N. Maity, S. K. Tripathy, J. M. Basset and S. Patra, *ACS Catal.*, 2016, **6**, 5535–5540.
25. J. Zhu and V. N. G. Lindsay, *ACS Catal.*, 2019, **9**, 6993–6998.
26. M. K. Pal, A.K. Pathak and S. Dey, *New J. Chem.,* 2025, **49**, 15858–15865.
27. S. Demkowicz, J. Rachon, M. Daśko, W. Kozak*, RSC Adv., 2016, **6**, 7101-7112*
28. H. Guo, Y. C. Fan, Z. Sun, Y. Wu, O. Kwon, *Chem. Rev.,* 2018, **118**, 10049–10293.
29. D. Joly, P. Bouit, M. Hissler, *J. Mater. Chem. C,* 2016, **4**, 3686-3698.

30. P. Finkbeiner, J. P. Hehn and C. Gnamm, *J. Med. Chem.*, 2020, **63**, 7081–7107.
31. H. Yorimitsu, *Beilstein J. Org. Chem., 9:143*, 2013, **9**, 1269–1277.
32. D. S. Surry and S. L. Buchwald, *Chem. Sci.*, 2010, **2**, 27–50.
33. Q. Dang, Y. Liu, D. K. Cashion, S. R. Kasibhatla, T. Jiang, F. Taplin, J. D. Jacintho, H. Li, Z. Sun, Y. Fan, J. Dare, F. Tian, W. Li, T. Gibson, R. Lemus, P. D. Van Poelje, S. C. Potter and M. D. Erion, *J. Med. Chem.,* 2011, **54**, 153–165.
34. M. M. Velencoso, A. Battig, J. C. Markwart, B. Schartel and F. R. Wurm, *Angew. Chem. Int. Ed.,* 2018, **57**, 10450–10467.
35. C. Zhou, X. Luo, N. Chen, L. Zhang and J. Gao, *J. Agric. Food Chem.,* 2020, **68**, 3344–3353.
36. T. Baumgartner, *Acc. Chem. Res.,* 2014, **47**, 1613–1622.
37. E. L. Deal, C. Petit and J. L. Montchamp, *Org. Lett.,* 2011, **13**, 3270–3273.
38. D. L. Zhu, S. Jiang, Q. Wu, H. Wang, L. L. Chai, H. Y. Li and H. X. Li, *Org. Lett.*, 2020, **23**, 160–165.
39. M. Kalek, A. Ziadi and J. Stawinski, *Org. Lett.,* 2008, **10**, 4637–4640.
40. O. Berger, C. Petit, E. L. Deal, and J. Montchamp, *Adv. Synth. Catal.*, 2013, **355**, 1361 – 1373
41. Y. Yang, O. Yuen, and C. M. So, *Eur. J. Org. Chem.,* 2025, **28**, e202500084
42. K. Xu, F. Yang, G Zhang, Y. Wu, *Green Chem.,* 2013, **15**, 1055-1060.
43. G. Hu, W. Chen, T. Fu, Z. Peng, H. Qiao, Y. Gao and Y. Zhao, *Org. Lett.,* 2013, **15**, 5362–5365.
44. M. Kalek, M. Jezowska and J. Stawinski, *Adv. Synth. Catal.,* 2009, **351**, 3207–3216.
45. V. K. Fulwa and V. Manivannan, *Tetrahedron*, 2012, **68**, 3927–3931.
46. P. Gong, L. Wang, C. Tian, S. Hao, L. Shi, *Chem. Eur. J.,* 2025, **31**, e202501060.
47. CrysAlis Pro, Agilent Technologies Ltd: Yarnton, Oxfordshire, England, 2010
48. S. Bruker and S. SAINT, *Madison, Wisconsin, USA*.
49. G. M. Sheldrick, *Acta Cryst.,* 2015, **A71**, 3-8.
50. G. M. Sheldrick, *Crystal Structure Communications*, 2015, **71**, 3–8.
51. O. V. Dolomanov, L. J. Bourhis, R. J. Gildea, J. A. K. Howard and H. Puschmann, *urn:issn:0021-8898*, 2009, **42**, 339–341.

52. M. N. Burnett and C. K. Johnson, *Oak ridge national laboratory report ORNL-6895, Oak Ridge, Tennessee*, 1996, preprint.
53. C. F. Macrae, I. J. Bruno, J. A. Chisholm, P. R. Edgington, P. McCabe, E. Pidcock, L. Rodriguez-Monge, R. Taylor, J. V. D. Streek and P. A. Wood, *Applied Crystallography*, 2008, **41**, 466–470.
54. A. L. Spek, *Acta Crystallogr., Sect. D: Biol. Crystallogr*, 2009, **65**, 148–155.
55. Y. Liang, Y. X. Xie and J. H. Li, *J. Org. Chem.*, 2006, **71**, 379–381.
56. Z. Y. Tian, S. M. Wang, S. J. Jia, H. X. Song and C. P. Zhang, *Org. Lett.*, 2017, **19**, 5454–5457.
57. J. He, Y. Shi, W. Cheng, Z. Man, D. Yang and C. Li, *Angew. Chem.*, 2016, **128**, 4633–4637.
58. K. Nozawa-Kumada, M. Inagi and Y. Kondo, *Asian J. Org. Chem.*, 2017, **6**, 63–66.
59. M. Feuerstein, H. Doucet and M. Santelli, *J. Mol. Catal. A Chem.*, 2006, **256**, 75–84.
60. H. Guo, Q. Zhang, W. Pan, H. Yang, K. Pei, J. Zhai, T. Li, Z. Wang, Y. Wang and Y. Yin, *Asian J. Org. Chem.*, 2021, **10**, 2231–2237.

Chapter-5

Zinc(II) Complexes of Some 2-Cyanopyridine Derived Nitrogen-Rich Ligands: Catalysts for Cycloaddition of CO_2 and Epoxide into Cyclic Carbonate

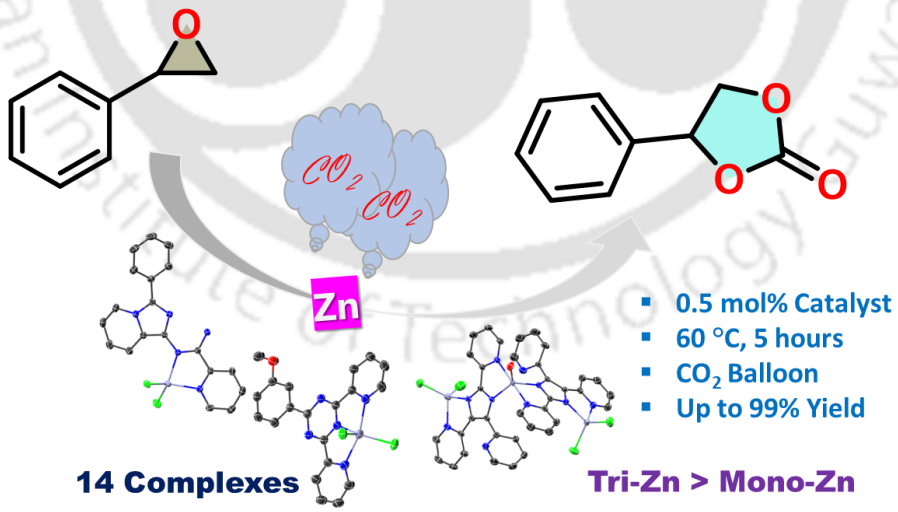

Abstract

A series of zinc(II) complexes were synthesized using some ligands containing imidazo[1,5-*a*]pyridine, triazine, and imidazolylpyridine moieties. Newly synthesised ligands and all zinc complexes were thoroughly characterized using several spectroscopic techniques. Molecular structure of some ligands and all zinc complexes were established by single crystal X-ray diffraction measurements. By controlling the stoichiometry, imidazo[1,5-*a*]pyridines and imidazolylpyridine ligands yielded both mono and trinuclear complexes while the pincer triazine ligands produced only mononuclear complexes. The geometry of tetra coordinated Zn(II) centres were distorted tetrahedral and a distorted square pyramidal environment was observed in penta-coordinated triazine Zn(II) complexes while distorted trigonal bipyramidal geometry was observed in trinuclear Zn(II) imidazolylpyridine complex. All the zinc(II) complexes were employed as catalyst in the conversion of carbon dioxide and styrene epoxide into styrene carbonate, yielded excellently in a mild and solvent free condition using balloon pressure CO_2. Among all the Zn(II) catalysts, trinuclear analogous were found as superior catalyst as compared to their mononuclear congeners.

5.1 Introduction

One of the greenhouse gases[1] is carbon dioxide (CO_2) that is produced in large scale globally due to consumption of fuels. The massive emission of CO_2 leads to serious environmental concern[2–5] including global warming while on other hand, it is readily accessible, cheap, and sustainable C1 source for various synthetic chemistry.[6–10] Thus, fixation of carbon dioxide for the conversion fine chemicals is one of the currently emerging strategies and became a cornerstone goal. Several methods have been developed for the utilization of carbon dioxide in the production of fine chemicals, fuels, and polymeric materials.[11–20] Among these CO_2 fixation methods, formation of cyclic carbonates using epoxides and CO_2 using a catalyst under mild reaction condition is an atom economical efficient strategy.[21,22] The cyclic carbonates have been widely applied as electrolytes,[23,24] solvents,[25–27] and key intermediates for the synthesis of ionic liquids, diols, and polycarbonates.[28–30] Many catalytic systems including organocatalysts,[31–33] metal organic frameworks,[34–36] metal oxides,[37] and transition metal complexes[34,37–40] have been established for the synthesis of cyclic carbonates using carbon dioxide as coupling partner. Basically, presence of a Lewis acidic metal center in these catalytic systems activate the C–O bond of epoxide while a nucleophile co-catalyst such as Br^- from tetrabutyl ammonium bromide (TBAB) executed the ring-

opening process of epoxide.[22] However, many of these systems relied on harsh conditions including high CO_2 pressure, elevated temperature, and high catalyst/co-catalyst loading.[41,42] Thus, development of robust, sustainable catalysts for the cycloaddition of epoxide and CO_2 under mild reaction condition would be significant. In this facet, utilization of zinc complexes as catalyst along with a co-catalyst as dual catalytic platform for the production of cyclic carbonate using epoxide and carbon dioxide have gained popularity due to the non-toxic, readily available, Lewis acidity, and ecofriendly features of zinc.[43,44] Being a d^{10} metal ion, Zn(II) complexes are redox-inert and their reactivity depends on coordination environment which is completely controlled by the ligand framework. The ligand skeleton stabilizes the zinc center, regulate the Lewis acidity, modulate electronic and steric influences at the metal center and thus fine tune the catalytic efficiency of the complex. Thus, development of appropriate ligand systems for the synthesis of Zn(II) complexes have played a vital role in the catalytic application of the complex specifically in cycloaddition of CO_2 and epoxide.

Sun and coworkers reported dinuclear Zn(II) complex **5.1** based on amino phenolate tripodal ligand and employed as catalyst in the reaction of CO_2 and epoxides, produced cyclic carbonate at relatively high temperature and 0.1 MPa CO_2 pressure in the presence of TBAB (Scheme 1).[45] He and coworkers developed [OSSO]-type zinc complexes **5.2**–**5.6** that exhibited catalytic activity in cyclic carbonate formation under mild, solvent-free conditions. The proximity of the two Zn(II) centers enabled synergistic effect, promoting dual activation of CO_2 and epoxide substrates.[46] Zakrzewska et al. reported a series of aryl-BIAN $ZnCl_2$ complexes **5.7**–**5.11** synthesized *via* a green one-pot method.[47] These complexes catalyzed the coupling of CO_2 and various epoxides in the presence of a quaternary ammonium salt as co-catalyst. Among the series, **5.10** displayed the highest activity, achieving good conversions for propylene and styrene oxides. Recently, Christ and coworker worked on some pyrrole Schiff base containing zwitterionic Zn(II) complexes (**5.12**–**5.15**) and used as catalyst in the production of styrene carbonate at 100 °C (Scheme 1).[48]

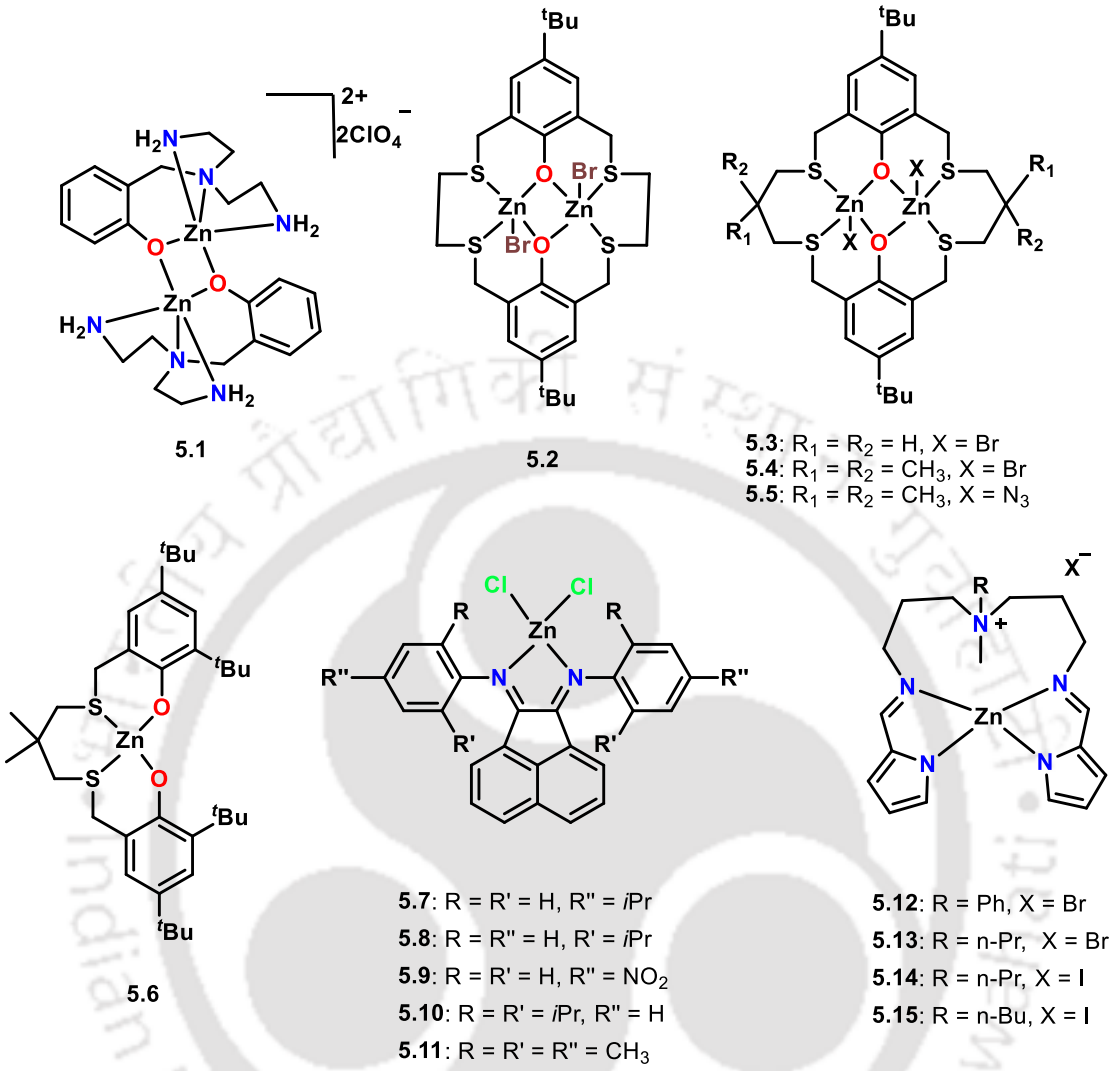

Scheme 1: Some reported zinc catalyst used in the coupling of CO_2 and epoxide

With inspiration from a deep literature survey and owing to use nitrogen rich neutral ligands for the designing of Zn(II) complexes as catalysts in conversion of epoxide and carbon dioxide into cyclic carbonate, this Chapter introduces some imidazo[1,5-*a*]pyridine, triazine, and imidazolylpyridine based ligands, synthesized by using 2-cyano pyridine. Zn(II) complexes bearing these ligand systems were used as catalyst for the first time in cycloaddition of epoxide and CO_2 though their group 10 complexes displayed excellent catalytic activity.

Imidazo[1,5-*a*]pyridine containing compounds have garnered considerable focus because of their captivating biological,[49] photophysical[50] and medicinal properties.[49–54] Ligands having this moiety along with these specific properties enhance the catalytic applications[55] of the resulting metal complexes. Similarly, multi-substituted imidazoles containing metal

complexes have been extensively used in catalysis, biomimetic studies and as photoluminescent materials.[56–58] By regulating the donor capability of imidazole ring, various groups on the imidazole rings was found to be responsible for the catalytic activity of the resulting metal complexes.[59,60]

5.2 Results and discussion

5.2.1 Synthesis and characterization of ligands

Ligands *N*-(3-phenylimidazo[1,5-*a*]pyridin-1-yl)picolinimidamide (**L1H**) and *N*-(3-(2-benzyloxy/2-methoxy/3-methoxy/4-methoxy/4-fluoro/4-methyl/2-methyl)imidazo[1,5-*a*]pyridin-1-yl)picolinimidamide (**L2H** / **L3H** / **L4H** / **L5H** / **L6H** / **L7H** / **L8H**) were prepared from the reaction of 2-cynaopyridine with benzaldehyde, and *N*-(3-(2-benzyloxy / 2-methoxy / 3-methoxy / 4-methoxy / 4-fluoro / 4-methyl / 2-methyl benzaldehyde respectively in presence of ammonium acetate by following a reported procedure with slight modifications (Scheme 2).[61] All ligands were isolated as yellow fibrous solid in good yield and **L2H**, **L4H**, **L6H**, **L8H** were explicitly categorized by ATR-IR, NMR, and High-Resolution Mass spectrometry (HRMS) while spectroscopic data for **L3H** was reported in Chapter 4 and for **L1H**, **L4H** and **L7H** matched well with the reported values. The ^{1}H NMR spectrum of ligands displayed a broad peak around 9.30 ppm (**L2H**, **L4H**) and 9.22 ppm (**L6H**, **L8H**) corresponding to one proton of -NH_2 while the other proton may involve in H-bonding with imidazo[1,5-*a*]pyridine-N and thus was not observed. The methylene, methoxy and methyl protons appeared at 5.08, 3.90, 2.31 ppm for **L2H**, **L4H** and **L8H** respectively while their ^{13}C NMR spectrum contained peaks matched well with total number of calculated carbon atoms. The formation of these new ligands also confirmed from the *m*/*z* peaks corresponding to $[C_{26}H_{21}N_5O+H]^+$ (420.1819), $[C_{20}H_{17}N_5O+H]^+$ (344.1515), $[C_{19}H_{14}FN_5+H]^+$ (332.1294), and $[C_{20}H_{17}N_5+H]^+$ (328.1561) for **L2H**, **L4H**, **L6H**, and **L8H** respectively in their HRMS spectrum.

From the same reaction mixture, triazine ligands **L9** – **L12** were eluted with a mixture of ethylacetate and hexane (9:1) as brown solids (Scheme 2) while imidazolylpyridine ligand (**L13H**) was prepared by following a previously reported procedure. The formation of ligands **L10** and **L12** were established using several spectroscopic techniques and the data obtained for **L9**, **L11** and **L13H** were in congruent with reported values. In the ^{1}H NMR spectrum, the methoxy protons of **L10** resonated at 3.87 ppm while **L12** displayed peaks at 14.00 ppm and 3.98 ppm confirmed

the presence of -OH and -OCH_3 groups and both ligands contained calculated number of carbons in their ^{13}C NMR spectrum. In HRMS spectra, peak rendered at *m/z* 342.1350 and 358.1301 matched with $[C_{20}H_{15}N_5O+H]^+$ (**L10**) and $[C_{20}H_{15}N_5O_2+H]^+$ (**L12**).

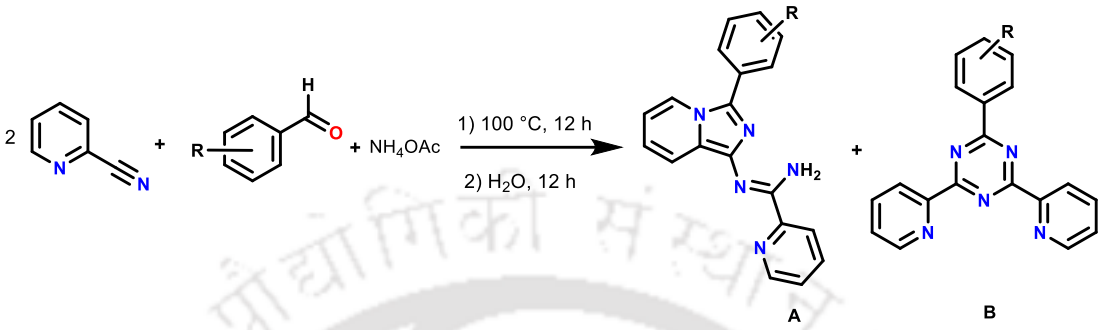

A: R = None (**L1H**, 71%), 2-OBn (**L2H**, 68%), 2-OMe (**L3H**, 70%), 3-OMe (**L4H**, 73%), 4-OMe (**L4H**, 68%), 4-F (**L5H**, 78%), 4-Me (**L7H**, 77%), 2-Me (**L8H**, 74%)
B: R = 4-Br (**L9**, 28%), 3-OMe (**L10**, 24%), 4-OMe (**L11**, 29%), 2-OH, 3-OMe (**L12**, 34%)

Scheme 2: Synthetic route of ligands **L1H** – **L8H** and **L9** – **L12**

5.2.2 Synthesis and characterization of complexes

The reaction of equimolar amounts of **L1H** – **L7H** and $ZnCl_2$ excellently produced mononuclear zinc complexes with composition $[ZnXCl_2]$ {**X** = **L1H** (**1**) – **L7H** (**7**)} in methanol at ambient temperature (Scheme 3). Complexes precipitated as red/orange solids and characterized using various spectroscopic techniques. In high resolution mass spectrometry (ESI, -ve), the base peak at *m/z* 447.9924, 554.0346, 438.0028, 438.0022, 438.0030, 465.9825, and 462.0088 were due to $[ZnXCl_2–H]^-$ (**X** = **L1H** – **L7H**) indicated the existence of mononuclear Zn(II) complex **1** –**7** and the molecular structure of all complexes was confirmed from their X-ray diffraction data. Interestingly, a similar mononuclear complex was not observed from the reaction of $ZnCl_2$ with **L8H**. By changing the stoichiometric ratio of $ZnCl_2$ and **L8H** to 1.5:1, a trinuclear Zn(II) complex Zn_3(**L8**)$_2Cl_4$ (**8**) was isolated while the formation of trinuclear complexes with **L1H** – **L7H** was not succeeded (Scheme 4). The complex **8** rendered a peak at *m/z* 1026.9200 was matched well with the calculated values for $[Zn_3(\mathbf{L8})_2Cl_4+K]^+$ species. Under the same reaction condition used for **1** – **7**, mononuclear pincer Zn(II) complexes of composition $[ZnXCl_2]$ {**X** = **L9** (**9**) – **L12** (**12**)} were prepared from the reaction of pincer triazine ligands **L9** – **L12** and $ZnCl_2$ in 1:1 stoichiometric ratio (Scheme 5). The complexes **9** – **12** produced peaks in their respective HRMS spectrum at *m/z* 489.9227, 440.0261, 440.0272 and 456.0202 were due to the presence of $[C_{19}H_{12}BrClN_5Zn]^+$ (**9**), $[C_{20}H_{15}ClN_5OZn]^+$ (**10**), $[C_{20}H_{15}ClN_5OZn]^+$ (**11**), and $[C_{20}H_{15}ClN_5O_2Zn]^+$ (**12**).

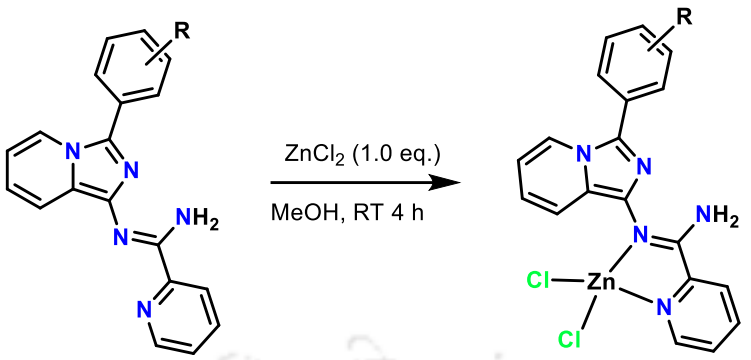

L1H - L7H

R = None (**1**, 81%), 2-OBn (**2**, 84%), 2-OMe (**3**, 91%), 3-OMe (**4**, 95%), 4-OMe (**5**, 85%), 4-Me (**6**, 90%), 4-F (**7**, 87%)

Scheme 3: Synthetic Scheme of mono nuclear zinc complexes **1** – **7**

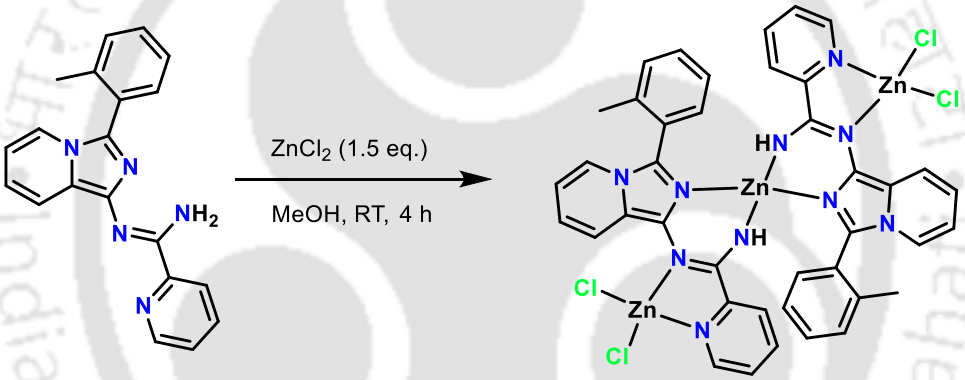

L8H

8 (92%)

Scheme 4: Synthetic Scheme for trinuclear zinc complex **8**

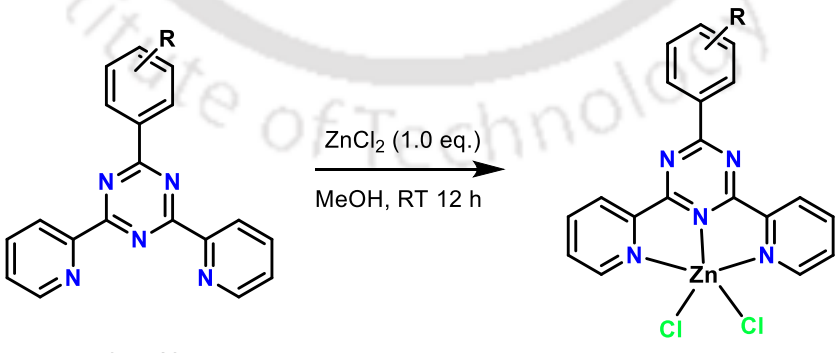

L9 - L12

R = 4-Br (**9,** 75%), 3-OMe (**10,** 74%), 4-OMe (**11,** 78%), 2-OH, 3-OMe (**12,** 71%)

Scheme 5: Synthetic Scheme of pincer mono-nuclear zinc complexes **9** – **12**

Ligand **L13H** has the structural flexibility to act as a tetradentate donor in its neutral state and as a pentadentate donor when deprotonated, offering the potential for various coordination modes and geometries as demonstrated in Chapter 2. Based on this versatility, its reaction with $ZnCl_2$ was anticipated to produce either a dinuclear complex or a coordination polymer, depending on whether the ligand adopts its neutral or anionic (**L13**$^-$) form. But a mononuclear Zn(II) complex Zn(**L13H**)Cl_2 (**13**) was obtained from the reaction of **L13H** with $ZnCl_2$ in 1:1 stoichiometric ratio. Using few drops of triethylamine to facilitate deprotonation and changing the stoichiometry of **L13H** and $ZnCl_2$ to 1.5:1 yielded a trinuclear complex Zn_3(**L13**)Cl_4 (**13**) (Scheme 6). The HRMS (ESI) values and the isotopic pattern of **13** and **14** matched well with the calculated values.

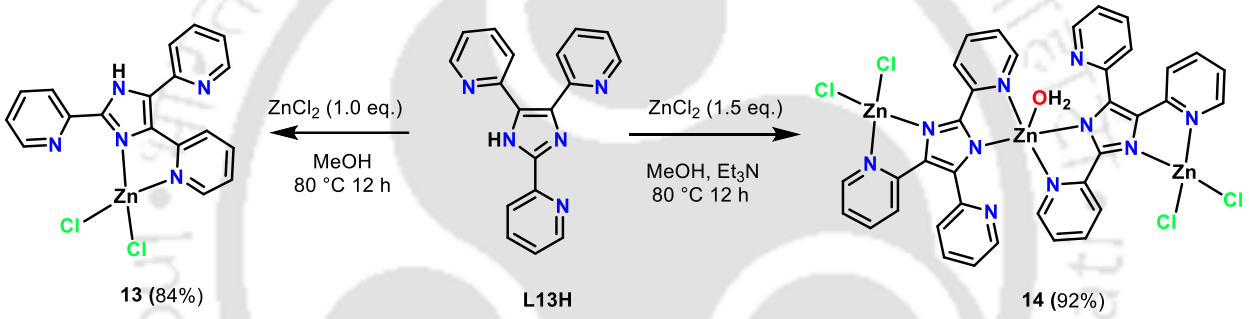

Scheme 6: Synthetic Scheme of mono- and tri- nuclear zinc complexes **13** and **14**

All the complexes **1**–**14** displayed broad peak in their ^{1}H NMR spectra of and thus was not interpretable. Field emission scanning electron microscopy (FESEM) was employed to investigate the surface morphology of all new ligands and zinc complexes. The resulting images revealed smooth, pore-free surfaces, indicative of a densely packed molecular arrangement. This lack of visible porosity suggests a high degree of intermolecular organization, likely driven by strong non-covalent interactions. Such ordered molecular packing reflected the inherent structural rigidity and solid-state stability, which may be beneficial in optoelectronic or catalytic applications. (Figure S5.28).

5.2.3 X-Ray crystallography

Single crystals of ligands **L1H**, **L2H**, **L6H**, and **L8H** obtained by slow evaporation from their dichloromethane solution and crystallized in $P2_1/n$ (**L1H**), Aea2 (**L2H**), $P2_12_12_1$ (**L6H**), and

$P4_12_12$ (**L8H**) space group (Table S5.1 and S5.2). The X-ray structure of ligands disclosed the presence of imine nitrogen (N_{IM}) and amine ($-NH_2$) nitrogen (N_{AM}) as evident from longer C6–N_{AM} bond length by 0.050(3), 0.067(11), 0.054(8) and 0.078(7) Å than C6–N_{IM} distance in **L1H**, **L2H**, **L6H**, and **L8H** respectively (Figure 1). Also, the ligands were engaged in intramolecular hydrogen bonding between imidazo[1,5-*a*]pyridine nitrogen (N_{IP}) and N_{AM} with D–H···A distance of 2.702(2) Å (**L1H**), 2.711(1) Å (**L2H**), 2.783(5) Å (**L6H**), and 2.733(8) Å (**L8H**).

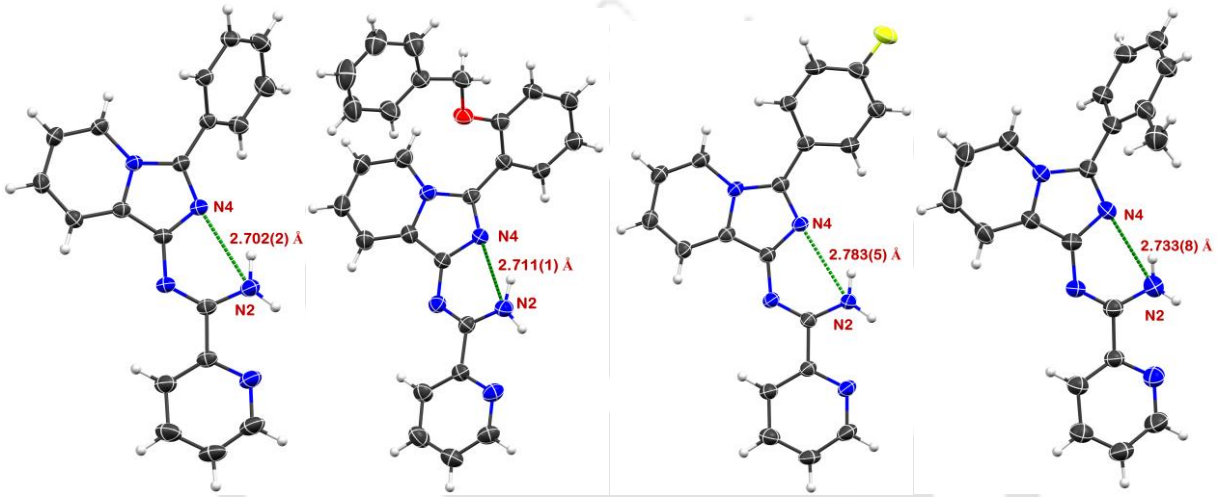

Figure 1: PoV-Ray rendered ORTEP diagram of **L1H**, **L2H**, **L6H**, and **L8H**.

Further, the molecular structure of Zn(II) complexes **1** – **8** were established using X-ray diffraction technique. Crystals of suitable for data collection were harvested from their solution in DMF by slow evaporation method and found to be crystalized in $P2_1/n$ (**1**, **6** and **7**), $P\bar{1}$ (**2** – **5**), and C2/c (**8**) (Table S5.12 and S5.13). In mononuclear complexes **1**–**7**, ligand **L1** – **L7** acted as bidentate donor and coordinated with zinc center through pyridine nitrogen (N_{PY}) and N_{IM} by forming a five member chelate ring. Other two coordination site around zinc center was occupied by chloride ions and thus, a distorted tetrahedral geometry was observed in **1** – **7** as inferred from the bond parameters. The geometry index was calculated in terms of Houser[62] parameter (τ_4) (Table 1) for **1** – **7** and the values nearly equal to 1 which suggested the distortion from ideal tetrahedron. The N_{IP} and N_{AM} remained uncoordinated and engaged in intramolecular hydrogen bonding interaction with D–H···A distance of 2.643(3) Å (**1**), 2.681(1) Å (**2**), 2.671(3) Å (**3**), 2.646(2) Å (**4**), 2.676(2) Å (**5**), 2.642(3) Å (**6**), and 2.632(3) Å (**7**).

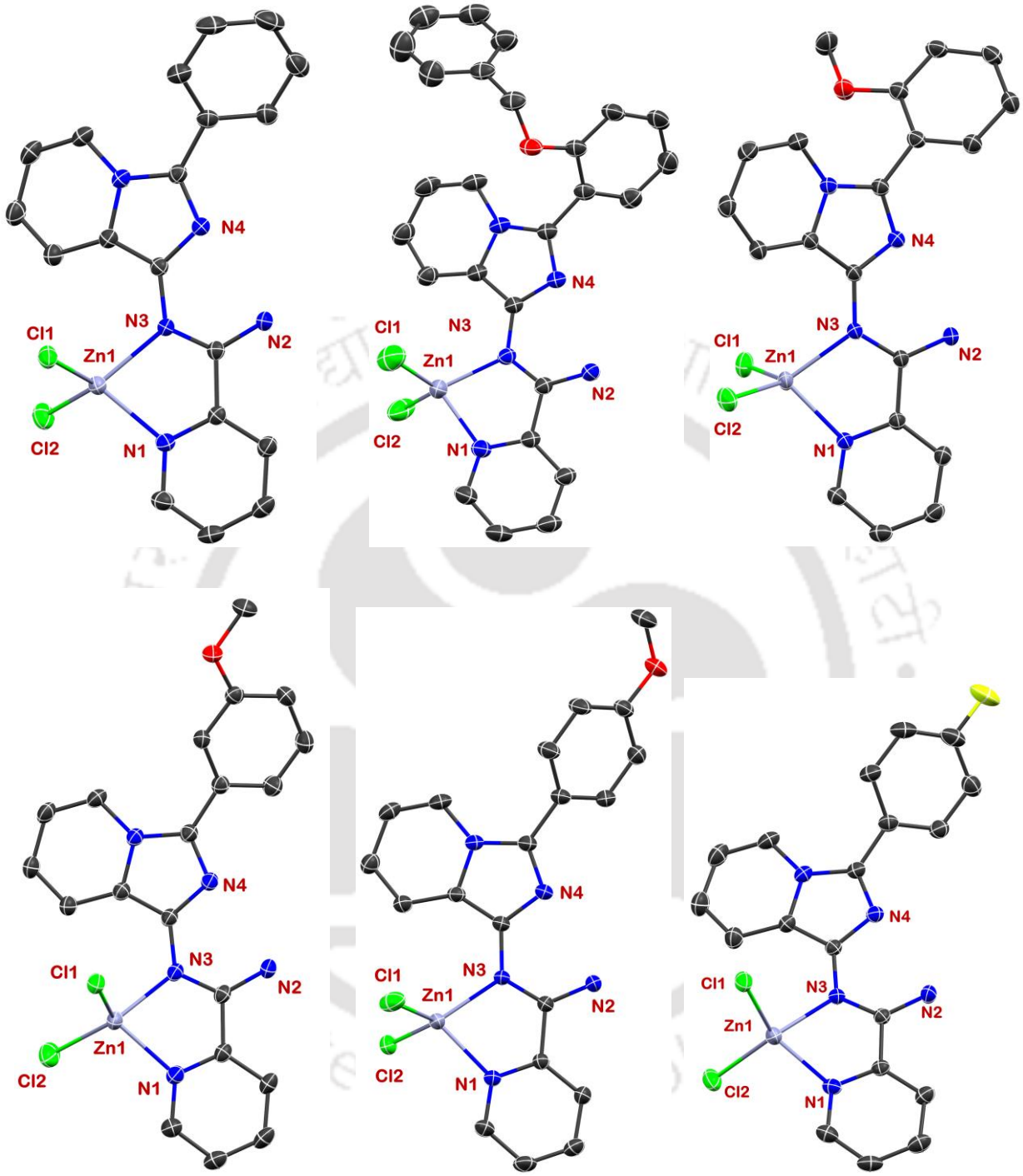

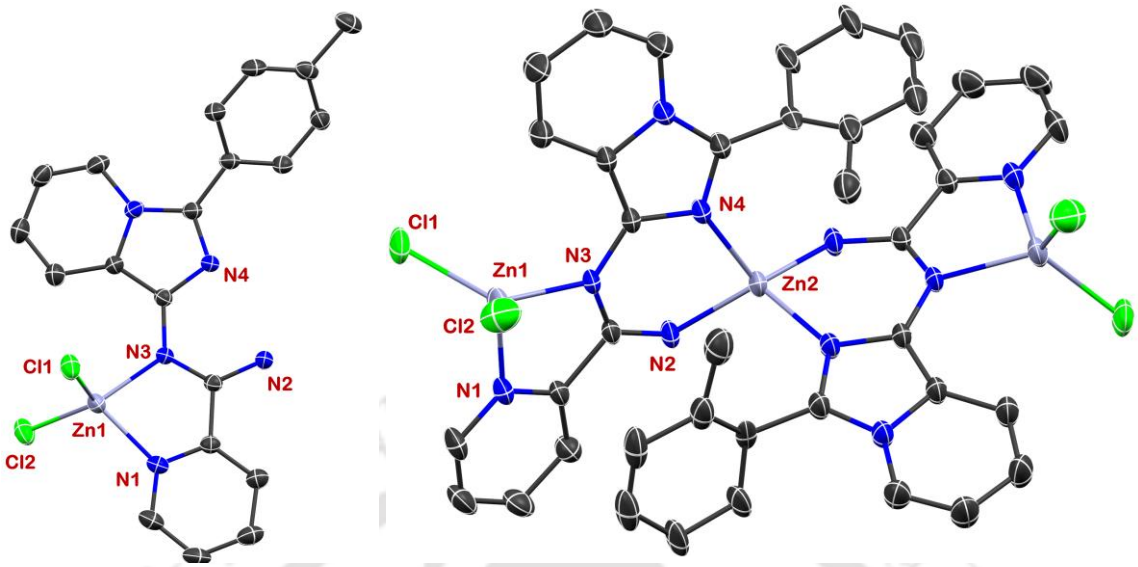

Figure 1: POV-Ray rendered ORTEP diagrams (30% probability level) of **1**–**8**. Hydrogen atoms are omitted for clarity.

Table 1: Geometry index (τ_4) for complexes **1**–**7**

Complexes	**1**	**2**	**3**	**4**	**5**	**6**	**7**
β (deg)	127.49(6)	117.25(5)	126.16(5)	127.72(6)	117.20(6)	127.74(6)	127.43(7)
α (deg)	116.16(7)	115.89(6)	114.92(6)	118.32(3)	114.73(3)	116.23(7)	114.45(7)
τ_4	0.825	0.900	0.844	0.809	0.909	0.823	0.838

$\{\tau_4 = \frac{360-(\alpha+\beta)}{141}$, where β and α are two largest bond angles. τ_4 = 1, tetrahedral; 0, square planar$\}$

In **8**, half of the molecule was in asymmetric unit due to the presence of a 2-fold screw axis and 2-tolyl ring of the ligand possessed rotational disorder which was addressed through partial occupancy factor. The molecule consisted of two ligand units that was found as a tetradentate donor in anionic form (**L8**$^-$) and held three Zn(II) center. Deprotonated N_{AM} and N_{IP} of two **L8**$^-$ units formed a six-membered chelate ring with central zinc in distorted tetrahedral (τ_4 = 0.756) environment while the remaining donor sites coordinated with terminal zinc centers (Zn1, Zn3) using N_{PY}–Zn–N_{IM} chelate and completed the trinucleation. Two chloride ions linked at remaining sites of both terminal Zn(II) center, constructed a similar distorted tetrahedral geometry (τ_4 = 0.879) as in mononuclear complexes **1** – **7** and the Zn–N_{IP} bond distance was 0.068(1) Å longer than that of Zn–N_{AM} may be due to neutral and anionic nature of nitrogen (Figure 3).

Crystals of complexes **9** – **12** were also obtained from DMF solution and **9** crystalized in $P\bar{1}$ while **10** – **12** in $P2_1/c$ space group. The Zn(II) center in **9** – **12** was found in penta-coordination where triazine ligands **L9** – **L12** spanned over three coordination sites around zinc as NNN pincer type binding mode and rest of the coordination location was engaged by two chloride ions. Two five-membered chelate was observed around zinc comprising pyridine nitrogen (N_{PY}) and triazine nitrogen (N_{TZ}). Due to the geometrical constraint, Zn–N_{TZ} distance was shorter than that of Zn–N_{PY} while two chlorides were in equidistant. According to Addison *et al.,*[63] the structural parameter (τ_5) {$\tau_5 = (\beta - \alpha) / 60$, where β and α are two largest bond angle $\beta > \alpha$} for complexes **9** – **12** was 0.044, 0.097, 0.29 and 0.093 respectively and thus proposed distorted square pyramidal geometry around the zinc(II) center. However, the substituents on phenyl ring did not affect the Zn–N_T bond lengths in **9** – **12** may be due to pincer binding mode.

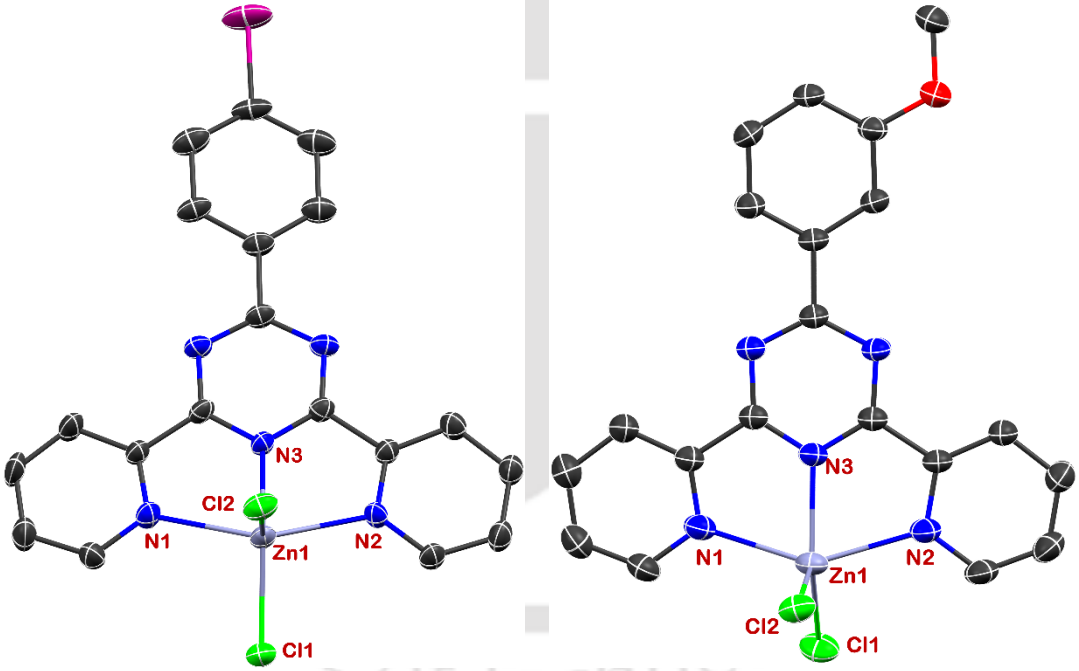

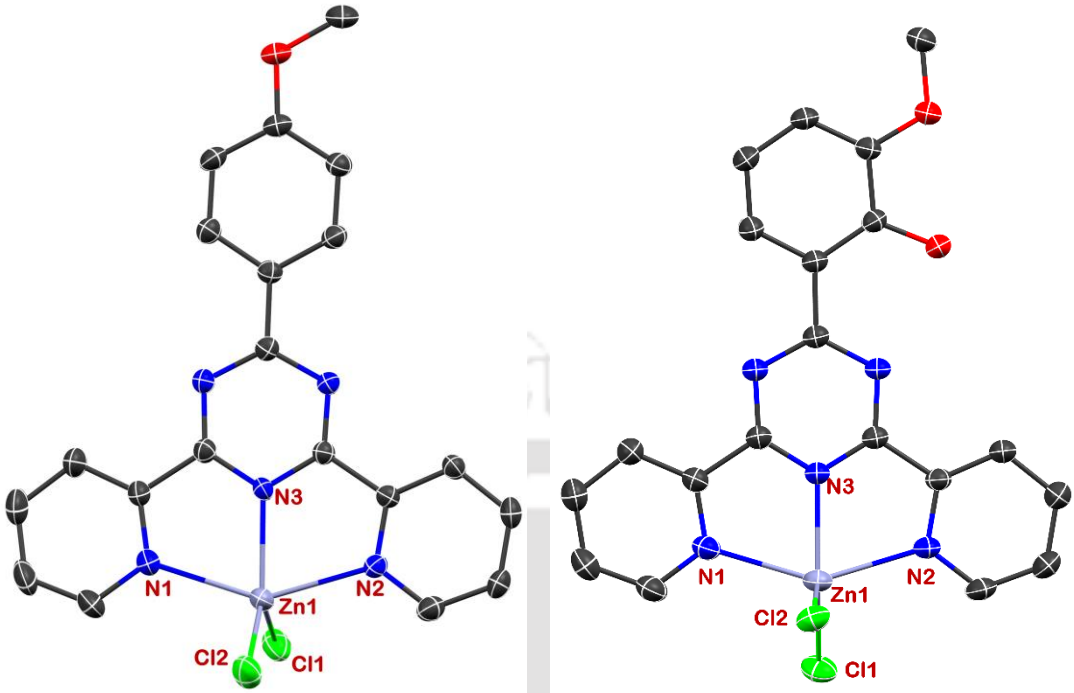

Figure 2: POV-Ray rendered ORTEP diagrams (30% probability level) of **9**–**12**. Hydrogen atoms are omitted for clarity.

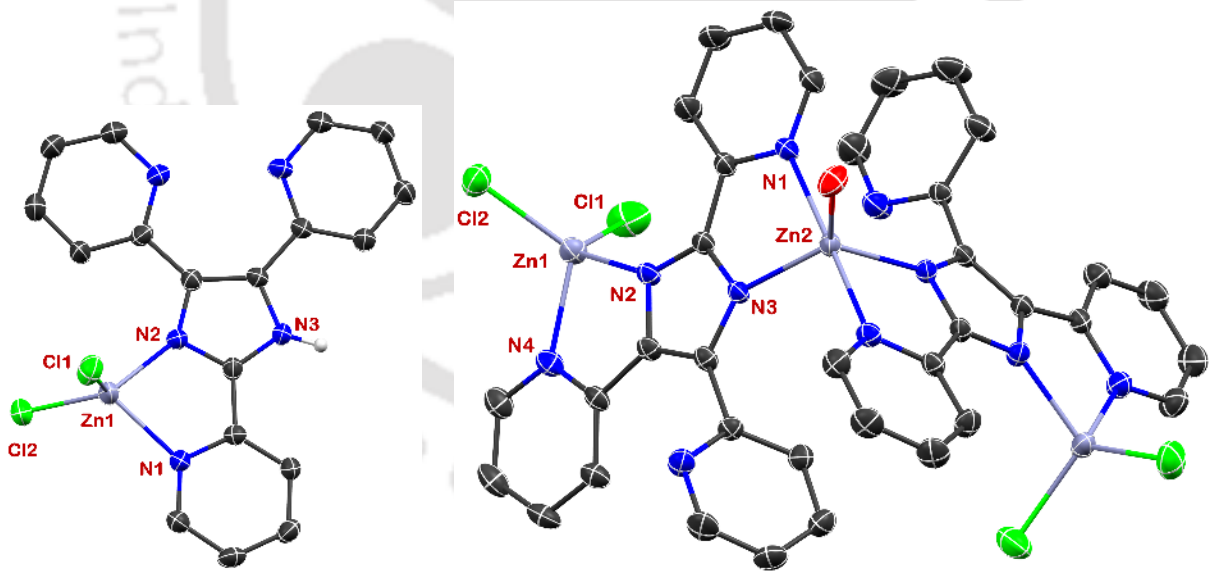

Figure 3: POV-Ray rendered ORTEP diagrams (30% probability level) of **13** and **14**. Hydrogen atoms are omitted for clarity.

Molecular structure of **14** contained two ligand units in anionic form (**L14**$^{-}$) that anchored three zinc(II) centers. Coordination environment of zinc centers in **14** was both tetra- and penta-coordinate. Two anionic ligand **L14**$^{-}$ acted as bis-bidentate ligand, firstly bound to central zinc

(Zn2) by forming two five membered chelate ring using imidazolate-N (N_{IE}) and N_{PY} while the fifth site was occupied by a water molecule. Then both the ligand units used their N_{PY} and N_{IZ} to form a five membered chelate with terminal zinc centers Zn1 and Zn3. These zinc centers were tetra coordinated having two chloride ions, exhibited the similar geometry as in **13**. The geometry index τ_5 = (173.82° - 128.07°) / 60° = 0.76 indicated a distorted trigonal bipyramidal geometry around central zinc (Zn2). Similarly, geometry parameter τ_4 for terminal Zn(II) centers were 0.88 and 0.89, suggested distorted tetrahedral geometry. The equatorial Zn–N_{PY} lengths {2.150(4) and 2.137(4) Å)} were longer than that of Zn–N_{IE} lengths {2.046(3) and 2.064(3) Å)} may be due to strong sigma donor ability of anionic N_{IE} group. The ligand **L14**$^{-}$ engaged it's four nitrogen in coordination with zinc, still one uncoordinated N_{PY} was present in each ligand units and displayed intermolecular discrete hydrogen bonding with oxygen of coordinated water molecule (O_W) with a non-bonded distance of 2.714(5) Å. Also, O_W involved in another discrete H-bonding with oxygen atom of lattice DMF molecule ($O_W \cdots O_{(DMF)}$, 2.658(6) Å).

5.2.4 Catalytic activity of 1–14 in the conversion of CO_2 and epoxide into cyclic carbonates

Considering the excellency of zinc complexes as catalyst in the conversion of CO_2 and epoxides into valuable cyclic carbonates, complexes **1**– **14** were employed as catalyst (Scheme 7). Optimization of reaction was investigated with alteration in solvents, temperature, time, and catalyst/co-catalyst loading (Table 2). Several solvents such as ethanol, acetonitrile, dimethylformamide (DMF), and 1-4 dioxane were tested in a model reaction of the cycloaddition of styrene oxide with carbon dioxide using catalyst **3** (1.0 mol%) and tetra-butyl ammonium bromide (TBAB) (1.0 mol%) at 80 °C for 5 hours. The model reaction condition was also carried in a solvent-free condition. Among all solvents, DMF produce highest yield of 74% but interestingly, the production of styrene carbonate was maximum in solvent-free system and thus, the catalytic conversion was further optimized without using any solvent. Then, the effect of temperature was monitored at various temperature. As the flash point of styrene oxide 76– 69 °C, high temperature condition was avoided and the maximum yield was achieved at 60 °C. Further, the role of reaction time was scrutinized and the progress of reaction was observed by analysing the reaction mixture at different time interval using ^{1}H NMR and ATR-IR spectroscopy (Figure 4). The formation of 4-phenyl-1,3-dioxolan-2-one (styrene carbonate) was confirmed from the peaks at δ = 5.67, 4.79 and 4.33 ppm while peaks at δ = 3.80, 3.08 and 2.75 ppm were for styrene

oxide in their respective ^{1}H NMR spectrum. Peaks corresponding to styrene carbonate were seen to appear within 0.5 h of the reaction and intensity of the peaks were increasing with time. After 5.0 h, the peaks of styrene oxide were nearly disappeared and the maximum yield was noted. A similar trend was also observed in ATR-IR spectral data of reaction mixture at 0.0, 2.0, 3.0 and 5.0 hours (Figure 5). At beginning of the conversion, prominent peaks at 874, 756, 696, 574 and 532 cm^{-1} were due to styrene oxide. As the reaction proceeded, formation of carbonate was identified with the appearance of a new peak at 1782 cm^{-1} which was due to C=O stretching in styrene carbonate. After 5.0 hours, this new peak intensity was high and other peaks were observed at 1162, 1064, 1050, 764, and 697 cm^{-1} while peaks due to styrene oxide disappeared. Then, the effect of catalyst loading on product yield was examined and a decline in production of styrene carbonate was observed with loading of 0.5 mol% of catalyst **3** in the model reaction. Also, a similar lower yield of product was seen with low loading of co-catalyst TBAB and without TBAB carbonate formation was halted while without zinc catalyst, a low yield (24%) was noted. Use of zinc chloride and zinc acetate yielded only 28% and 36% respectively. Thus, the conversion of CO_2 and styrene oxide into styrene carbonate using 1.0 mol% of catalyst **3** and TBAB at 60 °C in 5.0 hours produced maximum yield (94%), concluded as optimum condition and under this condition catalytic activity of other complexes (**1**, **2**, **4**–**14**) were also tested. Imidazo[1,5-*a*]pyridine based mononuclear complexes **1**–**7** produced 82-94 % of styrene carbonate. A little deviation in yield may be attributed to the electronic effect of substituents on phenyl ring. However, the trinuclear complex **8** yielded product excellently even at low catalyst loading (0.5 mol%). The triazine Zn(II) complexes were effectively gave 81–90 % styrene carbonate under optimal condition and the fluctuation in product amount was probably due to the presence of substituents on phenyl ring. Among mono- and tri- nuclear zinc complexes (**13** and **14**) of imidazolyl-pyridine ligand, **13** produced only 82% of styrene carbonate while **14** yielded 98% even using only 0.5 mol% of catalyst loading. Thus, both trinuclear Zn(II) complexes **8** and **14** gave maximum product and acknowledged as superior catalyst among complexes **1**–**14**.

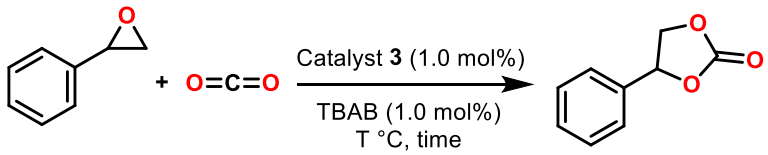

Scheme 7: Synthesis of styrene carbonate using Zn(II) catalysts **3**.

Table 2: Optimization of cyclic carbonates formation using CO2 and epoxide.

Entry	Catalyst (mol %)	Solvent	Cocatalyst	Temp (°C)	Time (h)	Yield (%)
1.	**3** (1.0 %)	EtOH	TBAB	80	5	34
2.	**3** (1.0 %)	MeCN	TBAB	80	5	28
3.	**3** (1.0 %)	1,4-Dioxane	TBAB	80	5	31
4.	**3** (1.0 %)	DMF	TBAB	80	5	67
5.	**3** (1.0 %)	–	TBAB	80	5	86
6.	**3** (1.0 %)	–	TBAB	40	5	82
7.	**3** (1.0 %)	–	TBAB	60	5	94
8.	**3** (1.0 %)	–	TBAB	RT	5	trace
9.	**3** (1.0 %)	–	TBAB	60	0.5	21
10.	**3** (1.0 %)	–	TBAB	60	2	44
11.	**3** (1.0 %)	–	TBAB	60	3	68
12.	**3** (1.0 %)	–	TBAB	60	4	80
13.	**3** (1.0 %)	–	–	60	5	00
14.	–	–	TBAB	60	5	24
15.	**3** (0.5 %)	–	TBAB	60	5	62
16.	**1** (1.0 %)	–	TBAB	60	5	82
17.	**2** (1.0 %)	–	TBAB	60	5	85
18.	**4** (1.0 %)	–	TBAB	60	5	87
19.	**5** (1.0 %)	–	TBAB	60	5	88
20.	**6** (1.0 %)	–	TBAB	60	5	79
21.	**7** (1.0 %)	–	TBAB	60	5	88
22.	**8** (1.0 %)	–	TBAB	60	5	99
23.	**8** (0.5 %)	–	TBAB	60	5	98
24.	**9** (1.0 %)	–	TBAB	60	5	90
25.	**10** (1.0 %)	–	TBAB	60	5	88
26.	**11** (1.0 %)	–	TBAB	60	5	84
27.	**12** (1.0 %)	–	TBAB	60	5	81

28.	**13** (1.0 %)	–	TBAB	60	5	82
29.	**14** (1.0 %)	–	TBAB	60	5	99
30.	**14** (0.5 %)	–	TBAB	60	5	98
31.	$ZnCl_2$	–	TBAB	60	5	28
32.	$Zn(OAc)_2$	–	TBAB	60	5	36

Reaction condition: Styrene oxide (1.0 mmol), catalyst **3** (1.0 mol%), TBAB (1.0 mol%), and CO_2 balloon. Isolated yields.

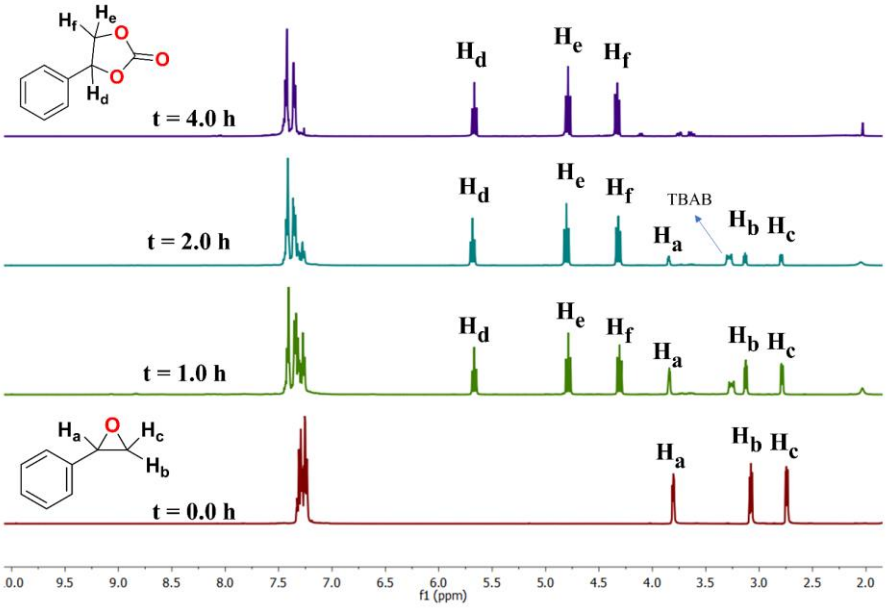

Figure 4: ^1H NMR spectra of reaction mixture (conversion of styrene oxide and CO_2 into styrene carbonate using catalyst **3)** at time interval of 0.0, 0.5, 2.0, 3.0, and 5.0 hours.

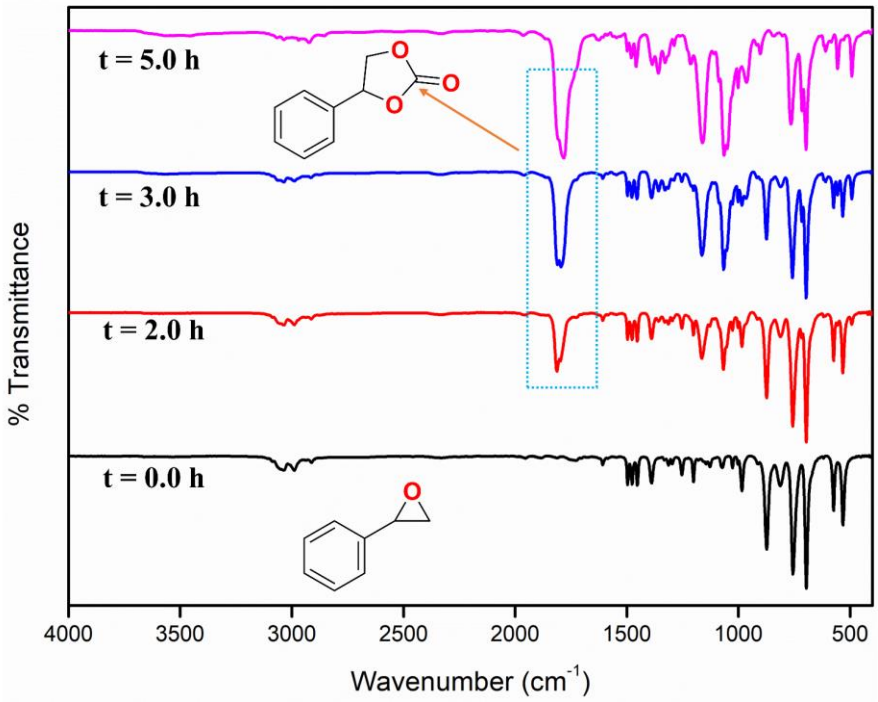

Figure 5: ATR-IR spectra of reaction mixture (conversion of styrene oxide and CO_2 into styrene carbonate using catalyst **3)** at time interval of 0.0, 2.0, 3.0, and 5.0 hours.

5.3 Conclusion

In conclusion, this Chapter unveiled the facile synthesis of a family of zinc(II) complexes **1** – **14** using some nitrogen rich heterocyclic ligands containing imidazo[1,5-*a*]pyridine, triazine, and imidazolylpyridine moieties. Ligands having imidazo[1,5-*a*]pyridine and triazine nucleus were prepared using unified, atom economical one-pot strategy from reaction of 2-cyanopyridine, corresponding aryl aldehydes and ammonium acetate in a single synthetic pathway. The reaction of 2-cyanopyridine and 2-picolylamine yielded imidazolylpyridine ligand. The molecular structure of ligands **L1H**, **L2H**, **L6H**, and **L8H** and all zinc complexes were established by single crystal X-ray diffraction measurements. The disubstituted imidazo[1,5-*a*]pyridine and imidazolylpyridine ligands yielded both mono and trinuclear complexes while the pincer triazine ligands produced only mononuclear complexes. The geometry of tetra coordinated zinc centres in Zn(II) imidazo[1,5-*a*]pyridine and imidazolylpyridine complexes were distorted tetrahedral where their Houser parameter (τ_4) was in the range of 0.8–0.9. A distorted square pyramidal environment with was observed in penta-coordinated Zn(II) triazine complex having 0.044–0.293 Addison parameter (τ_5) while and trinuclear imidazolylpyridine complex **14** displayed both distorted

tetrahedral and trigonal bipyramidal Zn(II) centres with geometry index 0.88 and 0.76. All fourteen zinc(II) complexes were employed as catalyst in the conversion of carbon dioxide and styrene epoxide into styrene carbonate, yielded excellently in a mild and solvent free condition using balloon pressure CO_2. Using 1.0 mol% catalyst, all mononuclear zinc complexes produced styrene carbonate in comparative yield of 81–94% while trinuclear catalysts yielded 98% using 0.5 mol % catalyst loading. The trinuclear analogous were found as superior catalyst as compared to their mononuclear congeners may be due to multisite catalytic pathways.

5.4 Experimental section

5.4.2 Synthesis of Ligands

5.4.2.1 General procedure (A) for synthesis of ligands L1H – L8H

The ligands **L1H – L8H** were synthesized following a reported procedure with some modification.[61] The corresponding aldehyde (1.0 equivalent), 2-cyanopyridine (2.0 equivalent), and ammonium acetate (2.0 equivalent) were heated at 100 °C in an oil-bath for 12 h. The resultant red gummy oil was suspended in 25 mL of water with mechanical stirring for next 12 h. The precipitates were filtered, washed with water, and dried in vacuum over fused $CaCl_2$. If precipitates were not formed, ethyl acetate was added to the aqueous reaction solution and organic layer was separated, washed with copious amount of water, dried with anhydrous sodium sulfate and solvent was removed to produce crude products. The products were isolated as crystalline fibrous solid after column chromatography using silica gel (60-120 mesh) and ethyl acetate/hexane (1:9) as eluent.

N-(3-phenylimidazo[1,5-*a*]pyridin-1-yl)picolinimidamide **(L1H)**

Benzaldehyde (0.53 g, 0.005 mol) and 2-cyanopyridine (1.04 g, 0.01 mol) were used to synthesize **L1H** ($C_{19}H_{15}N_5$). Yield: (1.11 g) 71%. Spectroscopic data were matched well with the literature.[61]

N-(3-(2-benzyloxyphenyl)imidazo[1,5-*a*]pyridin-1-yl)picolinimidamide **(L2H)**

2-Benzyloxybenzaldehyde (1.06 g, 0.005 mol) and 2-cyanopyridine (1.04 g, 0.01 mol) was used to synthesize **L2H** ($C_{26}H_{21}N_5O$). Yield: (1.32 g) 63%. ATR-IR (ν, cm^{-1}): 3427, 2922, 2853, 1616, 1562, 1465, 1447, 1379, 1239, 1107, 1024, 957, 759, 725, 691, 658, 465, 421. ^{1}H NMR (400 MHz, Chloroform-*d*) δ 9.30 (s, 1H), 8.64 (d, *J* = 8.0 Hz, 1H), 8.59 (dd, *J* = 4.8, 1.6 Hz, 1H), 7.92 (d, *J* = 8.1 Hz, 1H), 7.80 (td, *J* = 7.8, 1.7 Hz, 1H), 7.72 (dd, *J* = 7.5, 1.7 Hz, 1H), 7.60 (d, *J* = 7.2 Hz, 1H),

7.44 (td, *J* = 8.1, 1.7 Hz, 1H), 7.32 (dd, *J* = 7.4, 4.9 Hz, 1H), 7.22 (dd, *J* = 5.1, 1.9 Hz, 3H), 7.16 (td, *J* = 7.7, 4.8 Hz, 4H), 6.67 (dd, *J* = 8.8, 6.1 Hz, 1H), 6.47 (t, *J* = 7.4 Hz, 1H), 5.08 (s, 2H). ^{13}C NMR (101 MHz, Chloroform-*d*) δ 156.56, 153.01, 150.47, 148.05, 140.05, 136.52, 136.42, 132.66, 130.88, 130.42, 128.45, 127.85, 127.05, 125.25, 124.20, 122.66, 121.75, 121.52, 120.41, 118.90, 116.65, 113.59, 113.17, 70.87. HRMS (ESI) *m/z* calcd for $[C_{26}H_{21}N_5O+H]^+$: 420.1819; found 420.1813.

N-(3-(2-methoxyphenyl)imidazo[1,5-*a*]pyridin-1-yl)picolinimidamide **(L3H)**

2-Methoxybenzaldehyde (0.68 g, 0.005 mol) and 2-cyanopyridine (1.04 g, 0.01 mol) was used to synthesize **L3H** ($C_{20}H_{17}N_5O$). Yield: (1.2 g) 70%. Spectroscopic data were reported in Chapter 4.

N-(3-(3-methoxyphenyl)imidazo[1,5-*a*]pyridin-1-yl)picolinimidamide **(L4H)**

3-Methoxybenzaldehyde (0.68 g, 0.005 mol) and 2-cyanopyridine (1.04 g, 0.01 mol) was used to synthesize **L4H** ($C_{20}H_{17}N_5O$). Yield: (1.05 g) 61%. ATR-IR (ν, cm^{-1}): 3452, 2925, 1620, 1563, 1467, 1382, 1283, 1252, 1036, 746, 730, 711, 695, 421.^{1}H NMR (600 MHz, Chloroform-*d*) δ 9.28 (s, 1H), 8.60 (dd, *J* = 14.9, 6.6 Hz, 2H), 8.22 (d, *J* = 7.2 Hz, 1H), 7.91 (d, *J* = 9.0 Hz, 1H), 7.79 (t, *J* = 7.7 Hz, 1H), 7.46 – 7.36 (m, 4H), 7.32 (dd, *J* = 8.4, 4.8 Hz, 1H), 6.99 – 6.93 (m, 1H), 6.68 – 6.64 (m, 1H), 6.57 (t, *J* = 7.3 Hz, 1H), 3.89 (s, 3H). ^{13}C NMR (151 MHz, Chloroform-*d*) δ 160.16, 152.87, 150.80, 148.08, 140.51, 136.45, 132.65, 131.85, 130.05, 125.60, 124.30, 121.58, 120.62, 119.92, 119.69, 116.83, 114.63, 113.97, 113.54, 55.56. HRMS (ESI) *m/z* calcd for $[C_{20}H_{17}N_5O+H]^+$: 344.1506; found 344.1515.

N-(3-(4-methoxyphenyl)imidazo[1,5-*a*]pyridin-1-yl)picolinimidamide **(L5H)**

4-Methoxybenzaldehyde (0.68 g, 0.005 mol) and 2-cyanopyridine (1.04 g, 0.01 mol) was used to synthesize **L4H** ($C_{20}H_{17}N_5O$). Yield: (1.08 g) 63%. Spectroscopic data were matched well with the literature.[61]

N-(3-(4-fluorophenyl)imidazo[1,5-*a*]pyridin-1-yl)picolinimidamide **(L6H)**

4-Fluorobenzaldehyde (0.62 g, 0.005 mol) and 2-cyanopyridine (1.04 g, 0.01 mol) were used to synthesize **L5H** ($C_{19}H_{14}FN_5$). Yield, $C_{19}H_{14}FN_5$: (1.22 g) 74%. ATR-IR (ν, cm^{-1}): 3445, 2922, 1739, 1638, 1505, 1377, 1223, 835, 798, 716, 697, 517, 461, 427. ^{1}H NMR (400 MHz, Chloroform-*d*) δ 9.22 (s, 1H), 8.64 – 8.53 (m, 2H), 8.11 (d, *J* = 7.2 Hz, 1H), 7.90 (d, *J* = 9.0 Hz, 1H), 7.80 (dt, *J* =

9.3, 6.4 Hz, 3H), 7.39 (s, 1H), 7.32 (dd, *J* = 7.2, 4.9 Hz, 1H), 7.22 (t, *J* = 8.6 Hz, 2H), 6.66 (dd, *J* = 8.9, 6.3 Hz, 1H), 6.62 – 6.53 (m, 1H). ^{13}C NMR (101 MHz, Chloroform-*d*) δ 163.87, 161.40, 152.81, 150.82, 148.10, 140.48, 136.50, 129.70, 129.62, 124.37, 121.60, 120.16, 119.77, 116.79, 116.27, 116.06, 114.80. HRMS (ESI) *m/z* calcd for $[C_{19}H_{14}FN_5+H]^+$: 332.1306; found 332.1294.

N-(3-(4-methylphenyl)imidazo[1,5-*a*]pyridin-1-yl)picolinimidamide **(L7H)**

4-Methylbenzaldehyde (0.60 g, 0.005 mol) and 2-cyanopyridine (1.04 g, 0.01 mol) were used to synthesize **L6H** ($C_{20}H_{17}N_5$). Yield: (1.26 g) 77%. Spectroscopic data were matched well with the literature.[61]

N-(3-(2-methylphenyl)imidazo[1,5-*a*]pyridin-1-yl)picolinimidamide **(L8H)**

2-Methylbenzaldehyde (0.60 g, 0.005 mol) and 2-cyanopyridine (1.04 g, 0.01 mol) were used to synthesize **L6H** ($C_{20}H_{17}N_5$). Yield: (1.21 g) 74%. ATR-IR (ν, cm^{-1}): 3452, 3306, 2923, 1740, 1615, 1563, 1467, 1374, 1319, 1025, 991, 948, 802, 725, 714, 747, 652, 439, 419. ^{1}H NMR (500 MHz, Chloroform-*d*) δ 9.22 (s, 1H), 8.63 (d, *J* = 7.9 Hz, 1H), 8.58 (d, *J* = 4.7 Hz, 1H), 7.92 (d, *J* = 9.0 Hz, 1H), 7.79 (t, *J* = 7.7 Hz, 1H), 7.60 (d, *J* = 7.1 Hz, 1H), 7.53 (d, *J* = 7.5 Hz, 1H), 7.43 – 7.29 (m, 5H), 6.66 (dd, *J* = 8.9, 6.4 Hz, 1H), 6.52 (t, *J* = 6.7 Hz, 1H), 2.31 (s, 3H). ^{13}C NMR (126 MHz, Chloroform-*d*) δ 152.96, 150.51, 148.05, 139.71, 138.48, 136.43, 132.50, 131.12, 130.15, 129.59, 129.28, 126.10, 124.25, 124.23, 121.51, 120.55, 119.39, 116.61, 114.09, 20.14. HRMS (ESI) *m/z* calcd for $[C_{20}H_{17}N_5+H]^+$: 328.1557; found 328.1561.

5.4.2.2 General procedure for synthesis of ligands L9 – L12

Following the procedures (A), the ligands **L9** – **L12** were isolated as crystalline solid after eluted with 19:1 mixture of dichloromethane and methanol using column chromatography technique (60-120 mesh silica gel).

2-(4-bromophenyl)-4,6-di(pyridin-2-yl)-1,3,5-triazine (**L9**)

4-Bromobenzaldehyde (0.92 g, 0.005 mol) and 2-cyanopyridine (1.04 g, 0.01 mol) was used to synthesize **L9** ($C_{19}H_{12}BrN_5$). Yield: (0.55 g) 28%. The spectroscopic data were matched well with the literature.[64]

2-(3-methoxyphenyl)-4,6-di(pyridin-2-yl)-1,3,5-triazine (**L10**)

The ligand **L10** ($C_{20}H_{15}N_5O$) was synthesized from the reaction of **L4H**. Yield: (0.58 g) 34%. ATR-IR (ν, cm^{-1}): 3377, 2923, 1520, 1363, 1237, 1043, 999, 907, 775, 728, 667, 648, 624, 478.^{1}H NMR (600 MHz, Chloroform-*d*) δ 8.91 (d, *J* = 4.3 Hz, 2H), 8.79 (d, *J* = 7.8 Hz, 2H), 8.38 (d, *J* = 7.7 Hz, 1H), 8.30 (s, 1H), 7.94 (t, *J* = 7.7 Hz, 2H), 7.51 (dd, *J* = 7.2, 4.9 Hz, 2H), 7.47 (t, *J* = 7.9 Hz, 1H), 7.15 (dd, *J* = 8.1, 2.4 Hz, 1H), 3.94 (s, 3H). ^{13}C NMR (151 MHz, Chloroform-*d*) δ 172.72, 171.62, 160.09, 153.40, 150.40, 137.26, 136.90, 129.88, 126.55, 125.00, 122.04, 119.20, 114.20, 55.64. HRMS (ESI) *m/z* calcd for $(C_{20}H_{15}N_5O+H)^+$: 342.1350; found 342.1350.

2-(4-methoxyphenyl)-4,6-di(pyridin-2-yl)-1,3,5-triazine (**L11**)

The ligand **L11** ($C_{20}H_{15}N_5O$) was synthesized from the reaction of **L5H**. Yield: (0.53 g) 31%. The spectroscopic data were matched well with the literature.[64]

2-(4,6-di(pyridin-2-yl)-1,3,5-triazin-2-yl)-6-methoxyphenol (**L12**)

2-hydroxy-3-methoxybenzaldehyde (0.76 g, 0.005 mol) and 2-cyanopyridine (1.04 g, 0.01 mol) was used to synthesize **L12** ($C_{20}H_{15}N_5O_2$). Yield: (0.68 g) 38%. ATR-IR (ν, cm^{-1}): 3371, 2923, 1738, 1527, 1457, 1374, 1246, 771, 736, 691, 673, 624. ^{1}H NMR (600 MHz, Chloroform-*d*) δ 14.00 (s, 1H), 8.92 (d, *J* = 4.2 Hz, 2H), 8.77 (d, *J* = 7.8 Hz, 2H), 8.34 (d, *J* = 8.1 Hz, 1H), 7.96 (t, *J* = 7.6 Hz, 2H), 7.57 – 7.52 (m, 2H), 7.12 (d, *J* = 7.8 Hz, 1H), 6.97 (t, *J* = 8.0 Hz, 1H), 3.98 (s, 3H). ^{13}C NMR (151 MHz, Chloroform-*d*) δ 173.02, 170.49, 153.64, 152.48, 150.75, 149.50, 137.30, 127.00, 125.07, 121.42, 118.63, 117.29, 116.72, 56.44. HRMS (ESI) *m/z* calcd for $(C_{20}H_{15}N_5O_2+H)^+$: 358.1299; found 358.1278.

2,2',2"-(1H-imidazole-2,4,5-triyl)tripyridine (**L13H**)

From the reaction of 2-cyanopyridine, 2-picolylamine, and ammonium acetate, ligand **L13H** ($C_{18}H_{13}N_5$) was synthesized by following a reported procedure. The spectroscopic data were in congruent with the reported values.[65]

5.4.2.3 General procedure (A) for synthesis of Zinc(II) complexes 1 – 7:

The mononuclear zinc complexes **1** – **7** were synthesized by a general procedure (B). For this, zinc dichloride (0.0025 mol) was taken in 5.0 mL absolute ethanol, corresponding ligand (**L1H** – **L7H**) (0.0025 mol) in 5.0 mL absolute ethanol was added, resulting a deep red/orange color solution. The mixture was left at ambient temperature with continuous stirring for 12 hours. The solids were

filtered, washed with diethyl ether, and dried in vacuo to afford the desired zinc complexes (**1** – **7**).

[Zn(**L1H**)Cl_2] (**1**)

Following the general procedure (A), complex **1** was synthesized from the reaction of $ZnCl_2$ and **L1H**. Yield: (0.91 g) 81%. Anal. calcd for $C_{19}H_{15}Cl_2N_5Zn$: C, 50.75%; H, 3.36%; N, 15.58%; found: C, 50.82%; H, 3.39%; N, 15.47%. ATR-IR (ν, cm^{-1}): 3349, 3017, 2970, 1740, 1601, 1446, 1368, 1216, 720, 752, 696, 542, 469, 427. HRMS (ESI) *m/z* calcd for $[C_{19}H_{15}Cl_2N_5Zn–H]^-$: 447.9895; found 447.9924.

[Zn(**L2H**)Cl_2] (**2**)

Following the general procedure (A), complex **2** was synthesized from the reaction of $ZnCl_2$ and **L2H**. Yield: (1.16 g) 84%. Anal. calcd for $C_{26}H_{21}Cl_2N_5OZn$: C, 56.19%; H, 3.81%; N, 12.60%; found: C, 56.27%; H, 3.84%; N, 12.53%. ATR-IR (ν, cm^{-1}): 3369, 1633, 1599, 1451, 1215, 1101, 983, 750, 697, 649, 533, 424. HRMS (ESI) *m/z* calcd for $[C_{26}H_{21}Cl_2N_5OZn–H]^-$: 554.0315; found 554.0346.

[Zn(**L3H**)Cl_2] (**3**)

Following the general procedure (A), complex **3** was synthesized from the reaction of $ZnCl_2$ and **L3H**. Yield: (1.08 g) 91%. Anal. calcd for $C_{20}H_{17}Cl_2N_5OZn$: C, 50.08%; H, 3.57%; N, 14.60%; found: C, 50.18%; H, 3.60%; N, 14.54%. ATR-IR (ν, cm^{-1}): 3369, 3148. 1636, 1602, 1508, 1461, 1445, 1274, 1244, 1101, 1007, 768, 746, 731, 716, 648, 540, 461, 428. HRMS (ESI) *m/z* calcd for $[C_{20}H_{17}Cl_2N_5OZn–H]^-$: 478.0001; found 478.0028.

[Zn(**L4H**)Cl_2] (**4**)

Following the general procedure (A), complex **4** was synthesized from the reaction of $ZnCl_2$ and **L4H**. Yield: (1.13 g) 95%. Anal. calcd for $C_{20}H_{17}Cl_2N_5OZn$: C, 50.08%; H, 3.57%; N, 14.60%; found: C, 50.14%; H, 3.60%; N, 14.55%. ATR-IR (ν, cm^{-1}): 3348, 3139, 1637, 1602, 1577, 1371, 1287, 1237, 1038, 786, 734, 724, 700, 650, 555, 423. HRMS (ESI) *m/z* calcd for $[C_{20}H_{17}Cl_2N_5OZn–H]^-$: 478.0001; found 478.0030.

[Zn(**L5H**)Cl_2] (**5**)

Following the general procedure (A), complex **5** was synthesized from the reaction of $ZnCl_2$ and **L5H**. Yield: (1.01 g) 85%. Anal. calcd for $C_{20}H_{17}Cl_2N_5OZn$: C, 50.08%; H, 3.57%; N, 14.60%; found: C, 50.15%; H, 3.61%; N, 14.52%. ATR-IR (ν, cm^{-1}): 3353, 3143, 1739, 1640, 1604, 1526, 1376, 1234, 1162, 1140, 854, 798, 753, 727, 622, 551, 515, 471, 438, 418. HRMS (ESI) *m/z* calcd for $[C_{20}H_{17}Cl_2N_5OZn–H]^-$: 478.0001; found 478.0029.

[Zn(**L6H**)Cl_2] (**6**)

Following the general procedure (A), complex **6** was synthesized from the reaction of $ZnCl_2$ and **L6H**. Yield: (1.00 g) 87%. Anal. calcd for $C_{19}H_{14}Cl_2FN_5Zn$: C, 48.80%; H, 3.02%; N, 14.98%; found: C, 48.92%; H, 3.07%; N, 14.91%. ATR-IR (ν, cm^{-1}): 3350, 1599, 1553, 1522, 1374, 1151, 1007, 854, 784, 751, 726, 592, 548, 513, 437, 416. HRMS (ESI) *m/z* calcd for $[C_{19}H_{14}Cl_2FN_5Zn–H]^-$: 465.9800; found 465.9825.

[Zn(**L7H**)Cl_2] (**7**)

Following the general procedure (A), complex **7** was synthesized from the reaction of $ZnCl_2$ and **L7H**. Yield: (1.04 g) 90 %. Anal. calcd for: C, 51.81%; H, 3.70%; N, 15.10%; found: C, 51.92%; H, 3.78%; N, 15.00%. ATR-IR (ν, cm^{-1}): 3350, 3105, 1638, 1603, 1321, 1047, 957, 832, 796, 736, 726, 552, 505, 431, 409. HRMS (ESI) *m/z* calcd for $[C_{20}H_{17}Cl_2N_5Zn–H]^-$: 462.0051; found 462.00887.

[Zn_3(**L8**)$_2Cl_4$] (**8**)

Zinc dichloride (0.54 g, 0.004 mol) was taken in 10 mL absolute ethanol. To this, ligand **L8H** (0.82 g, 0.0025 mmol) was added resulting a dark orange color solution. The mixture was left at ambient temperature with continuous stirring for 12 hours. The solids were filtered, washed with diethyl ether, and dried in vacuo to afford the trinuclear zinc complex **8**. Yield: (1.13 g) 92%. Anal. calcd for $C_{40}H_{32}Cl_4N_{10}Zn_3$: C, 48.49%; H, 3.26%; N, 14.14%; found: C, 48.58%; H, 3.32%; N, 14.10%. ATR-IR (ν, cm^{-1}): 3358, 1669, 1546, 1451, 1385, 1330, 1093, 1033, 932, 771, 654, 568, 446, 418. HRMS (ESI) *m/z* calcd for $[C_{40}H_{32}Cl_4N_{10}Zn_3+K]^+$: 1026.9011; found 1026.9826.

[Zn(**L9**)Cl_2] (**9**)

Following the general procedure (B), complex **9** was synthesized from the reaction of $ZnCl_2$ and **L9**. Yield: (0.58 g) 75%. Anal. calcd for $C_{19}H_{12}BrCl_2N_5Zn$: C, 43.34%; H, 2.30%; N, 13.30%;

found: C, 43.48%; H, 2.34%; N, 13.24%. ATR-IR (ν, cm^{-1}): 3340, 1739, 1636, 1555, 1527, 1410, 1378, 1217, 1066, 1006, 955, 828, 779, 748, 555, 494, 435, 408. HRMS (ESI) *m/z* calcd for $[C_{19}H_{12}BrCl_2N_5Zn+H]^+$: 489.9226; found 489.9227.

[Zn(**L10**)Cl_2] (**10**)

Following the general procedure (B), complex **10** was synthesized from the reaction of $ZnCl_2$ and **L10**. Yield: (0.61 g) 74%. Anal. calcd for $C_{20}H_{15}Cl_2N_5OZn$: C, 50.29%; H, 3.17%; N, 14.66%; found: C, 50.35%; H, 3.22%; N, 14.60%. ATR-IR (ν, cm^{-1}): 1740, 1556, 1528, 1370, 1236, 1094, 1009, 893, 775, 661 632, 409. HRMS (ESI) *m/z* calcd for $[C_{20}H_{15}Cl_2N_5OZn+H]^+$: 440.0251; found 440.0261.

[Zn(**L11**)Cl_2] (**11**)

Following the general procedure (B), complex **11** was synthesized from the reaction of $ZnCl_2$ and **L11**. Yield: (0.64 g) 78%. Anal. calcd for $C_{20}H_{15}Cl_2N_5OZn$: C, 50.29%; H, 3.17%; N, 14.66%; found: C, 50.34%; H, 3.21%; N, 14.58%. ATR-IR (ν, cm^{-1}): 3445, 1736, 1602, 1554, 1512, 1374, 1253, 1177, 1011, 835, 784, 753, 666, 633, 599, 518, 413. HRMS (ESI) *m/z* calcd for $[C_{20}H_{15}Cl_2N_5OZn+H]^+$: 440.0251; found 440.0231.

[Zn(**L12**)Cl_2] (**12**)

Following the general procedure (B), complex **12** was synthesized from the reaction of $ZnCl_2$ and **L12**. Yield: (0.52 g) 52%. Anal. calcd for $C_{20}H_{15}Cl_2N_5O_2Zn$: C, 48.66%; H, 3.06%; N, 14.19%; found: C, 48.73%; H, 3.12%; N, 14.12%. ATR-IR (ν, cm^{-1}): 3388, 1738, 1638, 1533, 1472, 1382, 1252, 1078, 793, 776, 735, 527, 428. HRMS (ESI) *m/z* calcd for $[C_{20}H_{15}Cl_2N_5OZn$ $C_{20}H_{15}Cl_2N_5O_2Zn+H]^+$: 456.0200; found 456.0202.

[Zn(**L13H**)Cl_2] (**13**)

Ligand **L13H** (0.75 g, 0.0025 mol) was taken in 10.0 mL absolute ethanol and reflux till all ligand dissolved. Solid $ZnCl_2$ (0.34 g, 0.0025 mol) was added to it and the mixture was stirred at 80 °C for 12 hours. The ivory-colored solids were filtered, washed with diethyl ether, and dried in vacuo to afford the mononuclear zinc complex **13**. Yield: (0.91 g) 77%. Anal. calcd for: C, 49.63%; H, 3.01%; N, 16.08%; found: C, 49.76%; H, 3.08%; N, 16.00%. ATR-IR (ν, cm^{-1}): 1598, 1500, 1485, 1449, 1022, 795, 781, 754, 719, 697, 642, 553, 511, 419. HRMS (ESI) *m/z* calcd for $[C_{18}H_{13}Cl_2N_5Zn+H]^+$: 398.0145; found 398.0120.

$[Zn_3(\mathbf{L13})_2Cl_4(H_2O)]$ (**14**)

Ligand **L13H** (0.75 g, 0.0025 mol) was taken in 10.0 mL absolute ethanol and reflux till all ligand dissolved. Solid $ZnCl_2$ (0.54 g, 0.004 mol) was added to it followed by few drops of triethylamine and the mixture was stirred at 80 °C for 12 hours. The tan-colored solids were filtered, washed with diethyl ether, and dried in vacuo to afford the trinuclear zinc complex **14**. Yield: (1.1 g) 92%. Anal. calcd for $C_{36}H_{26}Cl_4N_{10}OZn_3$: C, 45.39%; H, 2.75%; N, 14.70%; found: C, 45.51%; H, 2.82%; N, 14.62%. ATR-IR (ν, cm^{-1}): 3500, 3061, 1739, 1607, 1489, 1460, 1373, 1230, 1158, 1024, 790, 747, 714, 646, 550, 503, 413. HRMS (ESI) *m/z* calcd for $[C_{36}H_{26}Cl_4N_{10}OZn_3-H_2O-Cl]^+$: 898.9049; found 898.8994.

5.4.1 Crystallographic data collection

For the single crystal XRD data collection of the appropriate single crystals of **L8H**, **8**, **9** and **14** was mount on a single source Super Nova CCD System instrument from Agilent Technologies equipped with a fine focus 1.75 kW sealed tube with Mo-Kα radiation was used at room temperature. The data were reduced using CrysAlisPro and Autochem2.1 software.[66] For rest of the ligands and complexes, data was collected at room temperature using a Bruker SMART APEX CCD diffractometer equipped with fine focus 1.75 kW sealed tube of Mo-Kα (λ = 0.71073 Å) X-ray source, with increasing ω (width of 0.3° per frame) at a scan speed of either 3 or 5 s per frame.[67] The SMART software was used for data acquisition and the SAINT software for data extraction. The structure solution and refinement were performed on the Olex2-1.5 using the SHELXT, SHELXL programs.[68,69] All atoms except hydrogen atoms are tuned using anisotropic displacement parameters, whereas hydrogen atoms are tuned using relative isotropic parameters. The disorder in molecular structure of **L8H** and **8** were fixed using partial occupancies factor, unidentified electron densities were masked using OLEX2 utility.[70] PLATON was used for structure validation and for pictorial visualization of X-ray single crystal data, Mercury and ORTEP software was used.[71–73]

5.4.3 Optimization of cycloaddition of styrene oxide with carbon dioxide

Styrene oxide (1.0 mmol eq.), TBAB (0.01 mmol.), catalyst **3** (0.5 mol%) were stirred at specified temperature for a given time in presence of carbon dioxide gas supplied from a balloon. The reaction was allowed to cool to room temperature, diluted with ethyl acetate, filtered and and concentrated in vacuo to yield the crude product which was analysed using ^1H NMR spectroscopy.

The pure product 4-phenyl-1,3-dioxolan-2-one (styrene carbonate) was obtained by using preparative thin layer chromatography.

4-phenyl-1,3-dioxolan-2-one

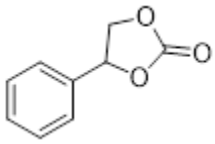

Styrene oxide (1.0 mmol), TBAB (0.01 mmol.), catalyst **3** (0.5 mol%) were stirred at 60 °C for 5.0 hours. The reaction mixture was cooled cool to room temperature, diluted with ethyl acetate, filtered and concentrated in vacuo to yield the crude product. The pure 4-phenyl-1,3-dioxolan-2-one (styrene carbonate) was obtained by using preparative thin layer chromatography (hexane/ethylacetate, 1:9). ^{1}H NMR (400 MHz, Chloroform-*d*) δ 7.47 – 7.40 (m, 3H), 7.37 – 7.33 (m, 2H), 5.67 (t, *J* = 8.0 Hz, 1H), 4.79 (t, *J* = 8.4 Hz, 1H), 4.37 – 4.29 (m, 1H). ^{13}C NMR (101 MHz, Chloroform-*d*) δ 154.98, 135.86, 129.78, 129.28, 125.96, 78.09, 71.24. NMR spectroscopic data matched literature values.[74]

CCDC No. 2496030 – 2496047 contain the crystallographic data for ligands **L1H**, **L2H**, **L6H**, **L8H** and complexes **1**–**14** studied in this Chapter.

The ATR-IR, NMR, HRMS spectra and FESEM images of ligands and complexes, NMR spectra of catalytic product, and crystallographic data, refinement parameters, bond parameters, and ORTEP diagrams can be found in Appendix IV by using the following link:

https://drive.google.com/file/d/1-39P8oyGNv1MI5jG3z9Nzu4bE-in0gsA/view?usp=sharing

5.5 References

1. R. K. Pachauri, M. R. Allen, V. R. Barros, J. Broome, W. Cramer, R. Christ, J. A. Church, L. Clarke, Q. Dahe and P. Dasgupta, Climate Change 2014: Synthesis Report. Contribution of Working Groups I, II and III to the Fifth Assessment Report of the Intergovernmental Panel on Climate Change, IPCC, Geneva, Switzerland, 2015.

2. J. Artz, T. E. Müller, K. Thenert, J. Kleinekorte, R. Meys, A. Sternberg, A. Bardow and W. Leitner, *Chem. Rev.*, 2017, **118**, 434–504.
3. K. S. Lackner, S. Brennan, J. M. Matter, A. H. A. Park, A. Wright and B. Van Der Zwaan, *Proc. Natl. Acad. Sci. U.S.A.*, 2012, **109**, 13156–13162.
4. G. Centi and S. Perathoner, *Catal. Today*, 2009, **148**, 191–205.
5. B. Yu and L. N. He, *ChemSusChem*, 2015, **8**, 52–62.
6. M. Aresta, A. Dibenedetto and A. Angelini, *Chem. Rev.*, 2013, **114**, 1709–1742.
7. A. Sternberg, C. M. Jens and A. Bardow, *Green Chem.*, 2017, **19**, 2244-2259.
8. Q. W. Song, Z. H. Zhou and L. N. He, *Green Chem.*, 2017, **19**, 3707–3728.
9. I. Omae, Coord. Chem. Rev., 2012, **256**, 1384– 1405
10. M. M. F. Hasan, L. M. Rossi, D. P. Debecker, K. C. Leonard, Z. Li, B. C. E. Makhubela, C. Zhao and A. Kleij, *ACS Sustainable Chem. Eng.***,** 2021, ***9***, 12427–12443.
11. R. R. Shaikh, S. Pornpraprom and V. D'Elia, *ACS Catal.*, 2017, **8**, 419–450.
12. X. B. Lu and D. J. Darensbourg, *Chem. Soc. Rev.*, 2012, **41**, 1462–1484.
13. V. Aomchad, À. Cristòfol, F. Della Monica, B. Limburg, V. D'Elia and A. W. Kleij, *Green Chem.*, 2021, **23**, 1077–1113.
14. W. Guo, J. E. Gómez, À. Cristòfol, J. Xie and A. W. Kleij, *Angew. Chem. Int. Ed.*, 2018, **57**, 13735–13747.
15. A. Modak, P. Bhanja, S. Dutta, B. Chowdhury and A. Bhaumik, *Green Chem.,* 2020, **22**, 4002-4033.
16. M. Peters, B. Köhler, W. Kuckshinrichs, W. Leitner, P. Markewitz and T. E. Müller, *ChemSusChem.***,** 2011**, 4**, 1216–1240.
17. Q. Liu, L. Wu, R. Jackstell and M. Beller, *Nat. Commun.*, 2015, **6**, 1–15.
18. M. Cokoja, C. Bruckmeier, B. Rieger, W. A. Herrmann and F. E. Kühn, *Angew. Chem. Int. Ed.*, 2011, **50**, 8510–8537.
19. C. Kim, C. J. Yoo, H. S. Oh, B. K. Min and U. Lee, *J. CO2 Util.*, 2022, **65**, 102239.
20. D. D. Suppiah, W. M. A. W. Daud and M. R. Johan, *Energy Fuels*, 2021, **35**, 17261–17278.
21. L. Guo, K. J. Lamb and M. North, *Green Chem.*, 2021, **23**, 77–118.
22. C. Martín, G. Fiorani and A. W. Kleij, *ACS Catal.*, 2015, **5**, 1353–1370.
23. C. Zhao, X. Luo, C. Chen and H. Wu, *Nanoscale*, 2016, **8**, 9511–9516.

24. C. C. Su, M. He, R. Amine, Z. Chen, R. Sahore, N. Dietz Rago and K. Amine, *Energy Storage Mater.*, 2019, **17**, 284–292.
25. B. Schäffner, F. Schäffner, S. P. Verevkin and A. Börner, *Chem. Rev.*, 2010, **110**, 4554–4581.
26. M. Sathish, K. J. Sreeram, J. Raghava Rao and B. Unni Nair, *ACS Sustain. Chem. Eng.*, 2016, **4**, 1032–1040.
27. J. H. Clements, *Ind. Eng. Chem. Res.*, 2003, **42**, 663–674.
28. V. Laserna, G. Fiorani, C. J. Whiteoak, E. Martin, E. Escudero-Adán and A. W. Kleij, *Angew. Chem. Int. Ed.*, 2014, **53**, 10416–10419.
29. T. Sakakura and K. Kohno, *Chem. Commun.*, 2009, **1312**, 1330.
30. M. North, R. Pasquale and C. Young, *Green Chem.*, 2010, **12**, 1514–1539.
31. M. E. Wilhelm, M. H. Anthofer, M. Cokoja, I. I. E. Markovits, W. A. Herrmann, F. E. Kühn,] M. E. Wilhelm, M. H. Anthofer, M. Cokoja, I. I. E. Markovits, W. A. Herrmann and F. E. Kühn, *ChemSusChem*, 2014, **7**, 1357–1360.
32. H. Song, Y. Wang, M. Xiao, L. Liu, Y. Liu, X. Liu and H. Gai, *ACS Sustain. Chem. Eng.*, 2019, **7**, 9489–9497.
33. G. Fiorani, W. Guo and A. W. Kleij, *Green Chem.*, 2015, **17**, 1375–1389.
34. L. Liu, S. Jayakumar, J. Chen, L. Tao, H. Li, Q. Yang and C. Li, *ACS Appl. Mater. Interfaces*, 2021, **13**, 29522–29531.
35. K. Huang, J. Y. Zhang, F. Liu and S. Dai, *ACS Catal.*, 2018, **8**, 9079–9102.
36. R. Luo, M. Chen, F. Zhou, J. Zhan, Q. Deng, Y. Yu, Y. Zhang, W. Xu and Y. Fang, *J. Mater. Chem. A*, 2021, **9**, 25731–25749.
37. H. Yasuda, L. N. He, T. Sakakura and C. Hu, *J. Catal.*, 2005, **233**, 119–122.
38. J. A. Castro-Osma, K. J. Lamb and M. North, *ACS Catal.*, 2016, **6**, 5012–5025.
39. J. W. Comerford, I. D. V. Ingram, M. North and X. Wu, *Green Chem.*, 2015, **17**, 1966–1987.
40. A. Decortes, A. M. Castilla and A. W. Kleij, *Angew. Chem. Int. Ed.*, 2010, **49**, 9822–9837.
41. R. R. Shaikh, S. Pornpraprom and V. D'Elia, *ACS Catal.*, 2017, **8**, 419–450.
42. S. Changsong, R. Xu, T. Suo and R. Yun, *Chem. Commun.*, 2023, **59**, 9904–9906.
43. C. Y. Li, Y. C. Su, C. H. Lin, H. Y. Huang, C. Y. Tsai, T. Y. Lee and B. T. Ko, *Dalton Trans.*, 2017, **46**, 15399–15406.
44. M. Reiter, S. Vagin, A. Kronast, C. Jandl and B. Rieger, *Chem. Sci.*, 2017, **8**, 1876–1882.

45. D. Zhao, X. H. Liu, Z. Z. Shi, C. D. Zhu, Y. Zhao, P. Wang and W. Y. Sun, *Dalton Trans.,* 2016, **45**, 14184-14190.
46. J. Chen, X. Wu, H. Ding, N. Liu, B. Li and L. He, *ACS Sustainable Chem. Eng.,* 2021, **9**, 16210−16219
47. M. E. Zakrzewska, P. J. L. Andre ´, C. S. B. Gomes, A. V. M. Nunes and V. Rosa, *New J. Chem.,* 2023, **47**, 6551–6562.
48. M. A. Pena, L. Merzoudb, D. Busse-Cote, A. Tuel, C.e Morell, H. Chermette, L. Christ, *Mol. Catal.,* 2024. **553**, 113746.
49. T. Scattolin, G. Andreetta, M. Mauceri, F. Rizzolio, N. Demitri, V. Canzonieri and F. Visentin, *J. Organomet. Chem.*, 2021, **952**, 122014.
50. N. Kundu, S. M. T. Abtab, S. Kundu, A. Endo, S. J. Teat and M. Chaudhury, *Inorg. Chem.*, 2012, **51**, 2652–2661.
51. G. Volpi, G. Magnano, I. Benesperi, D. Saccone, E. Priola, V. Gianotti, M. Milanesio, E. Conterosito, C. Barolo and G. Viscardi, *Dyes Pigm.*, 2017, **137**, 152–164.
52. C. Garino, T. Ruiu, L. Salassa, A. Albertino, G. Volpi, C. Nervi, R. Gobetto and K. I. Hardcastle, *Eur. J. Inorg. Chem.*, 2008, **3587**, 3591.
53. S. Pischedda, S. Stoccoro, A. Zucca, G. Sciortino, F. Ortu and G. J. Clarkson, *Dalton Trans.*, 2021, **50**, 4859–4873.
54. Y. Imada, S. Mukai, K. Tahara, N. Kozai, M. Itaya, Y. Yoshida, S. Ueta, Y. Arakawa, K. Minagawa and F. Yagishita, *Inorg. Chim. Acta*, 2023, **555**, 121584.
55. G. A. Ardizzoia, D. Ghiotti, B. Therrien and S. Brenna, *Inorg. Chim. Acta*, 2018, **471**, 384–390.
56. Y. Qin, Y. Chen, J. Liu, J. Zhao, D. Gao, Y. Li, W. Liu and W. Li, *Inorg. Chem. Commun.*, 2015, **56**, 58–61.
57. R. G. Gámez-Heredia, A. Cruz-Enríquez, R. Aceves, H. Höpfl, M. Parra-Hake, R. E. Navarro and J. J. Campos-Gaxiola, *Inorg. Chim. Acta*, 2019, **486**, 377–386.
58. Y. Zhan, X. Wang, Y. Wang and Y. Xu, *Dyes Pigm.*, 2019, **167**, 1–9.
59. A. O. Eseola, D. Geibig, H. Görls, W. H. Sun, X. Hao, J. A. O. Woods and W. Plass, *J. Organomet. Chem.*, 2014, **754**, 39–50.
60. A. R. Rayasingh and V. Manivannan, *Dalton Trans.*, 2025, **54**, 7741–7752.
61. V. K. Fulwa and V. Manivannan, *Tetrahedron*, 2012, **68**, 3927–3931.

62. L. Yang, D. R. Powell, and R. P. Houser, *Dalton Trans.,* 2007, 955-964.
63. A. W. Addison, T. N. Rao, J. Reedijk, J. Rijn and G. C. Verschoor, *J. Chem. Soc., Dalton Trans.,* 1984, 1349-1356
64. E. A. Medlycott, K. A. Udachinb and G. S. Hanan, *Dalton Trans.,* 2007, 430–438
65. V. K. Fulwa, R. Sahu, H. S. Jena and V. Manivannan, *Tetrahedron Lett.*, 2009, **50**, 6264–6267.
66. Pro, CrysAlis, Agilent Technologies Ltd: Yarnton, Oxfordshire, England, 2010
67. S. Bruker and S. SAINT, *Madison, Wisconsin, USA*.
68. G. M. Sheldrick, *Acta Cryst.,* 2015, **A71**, 3-8.
69. G. M. Sheldrick, *Crystal Structure Communications*, 2015, **71**, 3–8.
70. O. V. Dolomanov, L. J. Bourhis, R. J. Gildea, J. A. K. Howard and H. Puschmann, *urn:issn:0021-8898*, 2009, **42**, 339–341.
71. M. N. Burnett and C. K. Johnson, *Oak ridge national laboratory report ORNL-6895, Oak Ridge, Tennessee*, 1996, preprint.
72. C. F. Macrae, I. J. Bruno, J. A. Chisholm, P. R. Edgington, P. McCabe, E. Pidcock, L. Rodriguez-Monge, R. Taylor, J. V. D. Streek and P. A. Wood, *Applied Crystallography*, 2008, **41**, 466–470.
73. A. L. Spek, *Acta Crystallogr., Sect. D: Biol. Crystallogr*, 2009, **65**, 148–155.
74. S. Ravi, P. Puthiaraj, D. W. Park, and W. S. Ahn, *New J. Chem.,* 2018, **42**, 12429–12436.

Thesis Summary

This thesis covers five chapters.

Chapter 1 provides a comprehensive overview of the recent advancements in the synthesis and applications of divalent Group 10 and zinc complexes, tracing their development from historical discoveries to contemporary progress. It highlights the evolution of palladium-based catalysts in C–C cross-coupling reactions, emerging trends in nickel catalysis, and the biological activities of Pd(II) and Pt(II) complexes. The Chapter also discusses significant progress in carbon dioxide fixation employing zinc(II) complexes as catalysts. Additionally, the general methods, materials, and instrumentation used in experimental works are given in this Chapter.

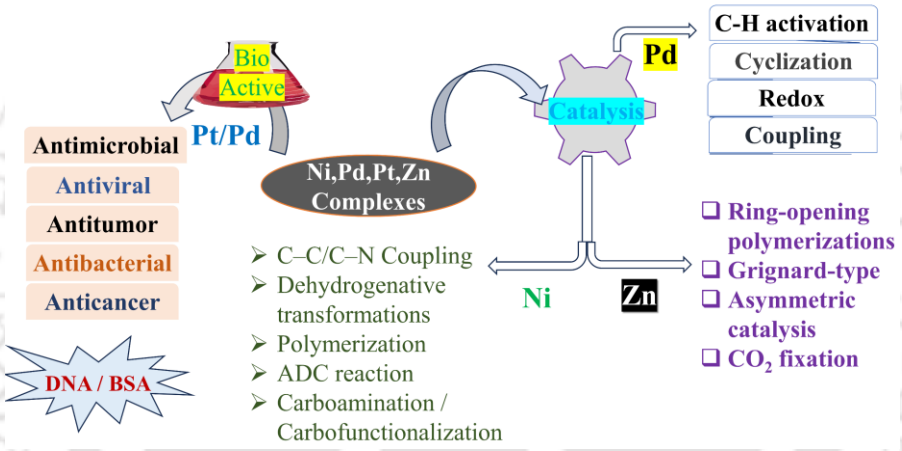

Chapter 2 deals with synthesis and characterization of a series of mono-, di-, tri-, and tetranuclear Pd(II) complexes along with one Pt(II) analogue using two nitrogen-rich ligands with imidazo[1,5-a]pyridine and imidazolyl-pyridine moieties. the denticity of **L1H** was bis-bidentate or tridentate coordinated through nitrogen atoms with controlled stoichiometry and reaction conditions. The exceptional coordination mode with formation of a seven membered chelate was observed in trinuclear Pd(II) complex (**4**) and a tetranuclear complex was synthesized by reversing the molar ratio of ligand and $PdCl_2$. Based on X-ray diffraction study and spectroscopic results, the geometry around palladium center was observed to be distorted square planar. The Pd(II) complexes were proved as versatile and potent catalysts in Suzuki cross-coupling, transfer hydrogenation reaction, and alkyne homocoupling under environmentally apposite conditions by taking only 0.1 mol% of tetranuclear Pd(II) complex (**5**) as catalyst. The interaction of all Pd(II) and Pt(II) complexes with calf thymus DNA were examined wherein all displayed intercalative mode of binding and showed

high binding affinity with bovine serum albumin (BSA). Further, ADMET calculations and molecular docking study of two bioactive molecules **3s** and **3t** obtained from Suzuki reaction using catalyst **5** were performed towards LTA_4H inhibition.

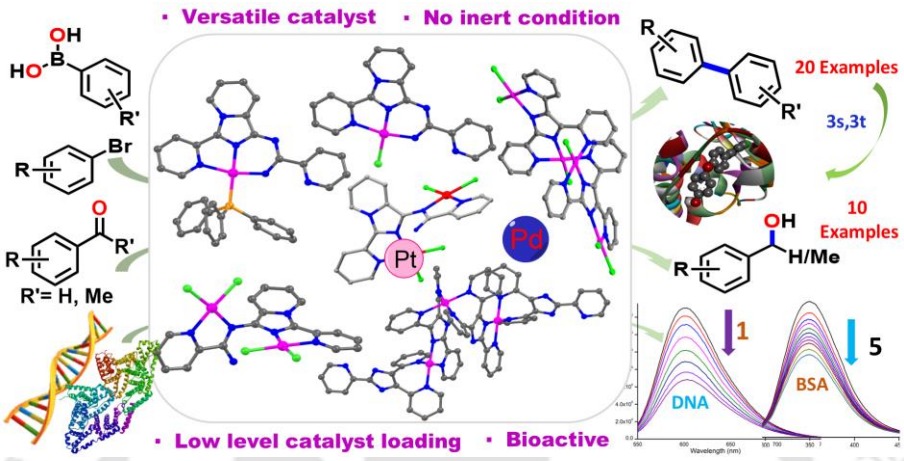

Chapter 3 outlines the synthetic procedure of a series of Ni(II), Pd(II) and Pt(II) complexes of various ligands bearing benzothiazole hydrazone, coumarin fused pyrrole and imidazo[1,5-*a*]pyridine moieties. All the ligands and complexes were characterized thoroughly using various spectroscopic techniques, molecular structures were confirmed by single crystal X-ray diffraction method and computational investigation was also performed to optimize the geometry and calculate energies. The nickel(II) complexes were employed as catalysts in synthesis of imines/diimines via acceptorless dehydrogenative coupling of alcohols and amines/diamine. Among all Ni(II) complexes, **1a** gave maximum yield of 99% in 12 h using only 1.0 mol% catalyst loading offered a cost-effective and sustainable alternative to existed noble metal catalysts. The catalytic activity of Pd(II) complexes was assessed in Heck coupling reaction, effectively produced 1-methylstilbene in ethanol at 90 ºC and 8 hours, surpassing many existing conventional systems relying on DMF or DMSO solvent at high temperature. The pincer Pd(II) complex **2h** was superior catalyst among all, with a yield of 98% using only 1.0 mol% catalyst loading. Furthermore, the versatility of Pd(II) catalysts was tested in cross-dehydrogenative coupling of thiophene-2-carboxaldehyde and formed the product in good yield. The platinum complexes of all ligands were inspected for their interaction with biomolecules such as CT-DNA and BSA and among all Pt(II) complexes, **3e** displayed the highest binding constants with these two biomolecules. Molecular docking study was also carried out to visualize the interaction of **3e** with CT-DNA and BSA,

showed high binding free energy and intercalative binding mode with CT-DNA which was in congruence with experimental findings.

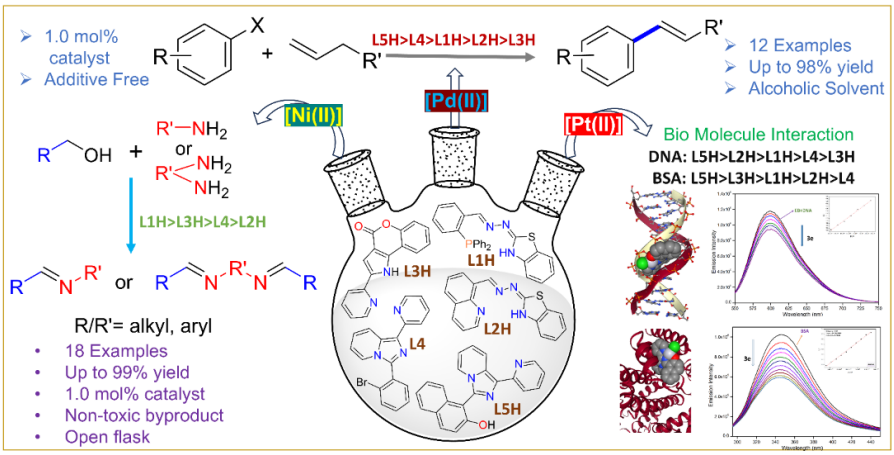

Chapter 4 describes the synthesis and characterization of five dinuclear palldium(II) complexes of substituted imidazo[1,5-a]pyridinylpicolinimidamides. Single crystal X-ray analysis revealed that the ligands were coordinated with palladium center through pseudo-pincer type mode and the Pd(II) center possessed distorted square planar geometry while an eight-membered metallic cavity was observed in all complexes. The complexes were employed as highly active catalyst in copper-free Sonogashira coupling and C–P coupling under mild reaction conditions and produced excellent yield using only 0.5 mol% of catalyst loading. High catalytic activity of these complexes was mainly due to cooperativity and synergic effect of two Pd(II) center present in optimum proximity.

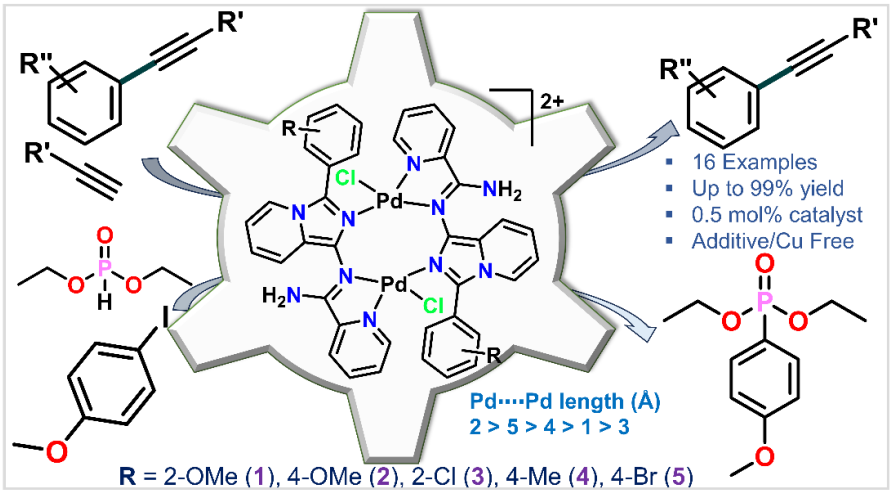

Chapter 5 unveils the synthetic methods of fourteen well characterized zinc(II) complexes of nitrogen rich heterocyclic ligands containing imidazo[1,5-*a*]pyridine, triazine, and imidazolylpyridine moieties. Ligands having imidazo[1,5-*a*]pyridine and triazine nucleus were prepared using unified, atom economical one-pot strategy from the reaction of 2-cyanopyridine, corresponding aryl aldehydes and ammonium acetate in a single synthetic pathway. The molecular structure of ligands **L1H**, **L2H**, **L6H**, and **L8H** and all zinc complexes were established by single crystal X-ray diffraction measurements. The disubstituted imidazo[1,5-*a*]pyridine and imidazolylpyridine ligands yielded both mono and trinuclear complexes while the pincer triazine ligands produced only mononuclear complexes. The geometry of tetra coordinated zinc centres in Zn(II) imidazo[1,5-*a*]pyridine and imidazolylpyridine complexes were distorted tetrahedral where their Houser parameter (τ_4) was in the range of 0.8–0.9. A distorted square pyramidal environment was observed in penta-coordinated Zn(II) triazine complexes having Addison parameter (τ_5) 0.044–0.293 while trinuclear imidazolylpyridine complex **14** displayed both distorted tetrahedral and trigonal bipyramidal Zn(II) centres with geometry index 0.88 and 0.76. All fourteen zinc(II) complexes were employed as catalyst in the conversion of carbon dioxide and styrene epoxide into styrene carbonate, yielded excellently in a mild and solvent free condition using balloon pressure CO_2. Using 1.0 mol% catalyst, all mononuclear zinc complexes produced styrene carbonate in comparative yield of 81–94% while trinuclear catalysts yielded 98% using 0.5 mol % catalyst loading.

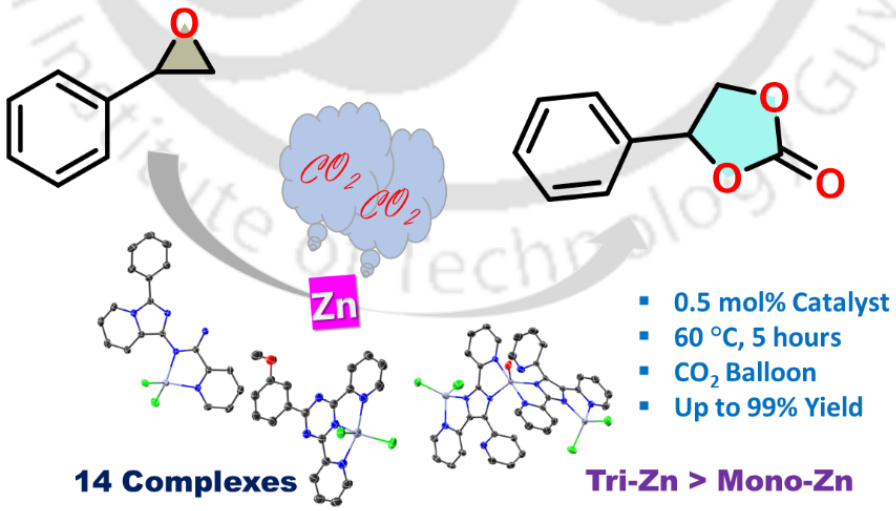

Future Perspectives

The current thesis explored divalent Ni, Pd, Pt, and Zn complexes of ligands containing various nitrogen-rich nuclei, including imidazo[1,5-a]pyridine. All complexes other than Pt(II) effectively catalyzed various organic transformations, while palladium and platinum complexes interacted well with CT-DNA and BSA. The present study thus lays a robust foundation for a versatile platform for the development and deployment of group 10 and zinc complexes as efficacious catalysts and further investigations for *in vitro* anticancer activities. Though the study covered several metal-catalyzed conversions and biomolecule interactions using these metal complexes, there are still more possibilities for future investigation to address the following points.

1. Earth-abundant metal complexes can be synthesized using these ligands for sustainable, cost-effective, and valuable catalysis.
2. Pt(II) complexes can be tested for *in vitro* anticancer activities, aiming for biomedical applications.
3. The Pd(II) and Ni(II) complexes can be used for other value-added organic transformations under green chemistry conditions.
4. These imidazo[1,5-a]pyridines and their complexes can be tested for optoelectronic and luminescent properties. Also, the design of lanthanide complexes using these ligands can be utilized for this purpose.
5. These catalysts or using other metals with these ligands can be applied in photo/electro-catalysis.
6. Dinuclear Pd(II) complexes given in Chapter 4 can be used to synthesize dual metal centers of specific distances.
7. Mononuclear Zn(II) complexes of imidazo[1,5-a]pyridines may be used as precursors for synthesis of hetero bimetallic complexes.
8. These zinc complexes can be used for other catalysis, including ring opening of lactides and polymer synthesis.

List of Publications:

1. A. R. Rayasingh and V. Manivannan, Palladium(II) and Platinum(II) Complexes of Disubstituted Imidazo[1,5-a]Pyridine and Imidazolylpyridine: Coordination Chemistry, Versatile Catalysis, and Biophysical Study, *Dalton Trans.,* 2025, ***54*** (19), 7741–7752.
2. A. R. Rayasingh and V. Manivannan, Group 10 Complexes of Benzothiazolehydrazone and Imidazo[1,5-*a*]pyridine based Ligands: Structural Artistry, Biophysical Study, and Catalytic activity, *Accepted for publication in Dalton Trans.* https://doi.org/10.1039/D5DT02077H
3. A. R. Rayasingh and V. Manivannan, Dinuclear Pd(II) Complexes of N-(imidazo[1,5-a]pyridin-1-yl)picolinimidamides: Pd‧‧‧Pd distance vs Reactivity in C-C/P Bond Formation, "*To be Communicated Soon".*
4. A. R. Rayasingh and V. Manivannan, Zinc(II) Complexes of Some 2-Cyanopyridine Derived Nitrogen-Rich Ligands: Catalysts for Cycloaddition of CO_2 and Epoxide into Cyclic Carbonate, "*To be Communicated Soon".*